TESIS DE LA UNIVERSIDAD DE ZARAGOZA

2023

170

Adrián Begué Gracia

Magnetic and magnetoelastic properties of FeGa epitaxial thin films for low-power Magnetoelectronics

Director/es

Ciria Remacha, Miguel Ángel

Arnaudas Pontaque, José Ignacio

ISSN 2254-7606

Prensas de la Universidad Universidad Zaragoza

ISSN 2254-7606

Universidad Zaragoza
1542

Tesis Doctoral

MAGNETIC AND MAGNETOELASTIC PROPERTIES OF FEGA EPITAXIAL THIN FILMS FOR LOW-POWER MAGNETOELECTRONICS

Autor

Adrián Begué Gracia

Director/es

Ciria Remacha, Miguel Ángel
Arnaudas Pontaque, José Ignacio

UNIVERSIDAD DE ZARAGOZA
Escuela de Doctorado

Programa de Doctorado en Física

2022

UNIVERSIDAD DE ZARAGOZA

INSTITUTO DE NANOCIENCIA Y MATERIALES DE ARAGON

DEPARTAMENTO DE FISICA DE LA MATERIA CONDENSADA

Magnetic and magnetoelastic properties of FeGa epitaxial thin films for low-power magnetoelectronics

Author:

Adrián Begué Gracia

Thesis advisors:

Prof. José Ignacio Arnaudas Pontaque
Dr. Miguel Ángel Ciria Remacha

To my family
to Irene

Contents

Chapter 1

Introduction

Technological innovation is reshaping the world faster than ever before. The information era is reaching its end, while the nanotechnology era is rising up [1]. The nanotechnology starts with the famous lecture of Richard Feynman at the 1959 Annual Meeting of the American Physical Society called "There's Plenty of Room at the Bottom" [2]. Nanotechnology involves structures and systems in which at least one dimension is less than 100 nm. That is, reducing 1, 2 or 3 dimensions of a bulk material to the nanometer scale produces nanometer thick 2D layers, 1D nanowires, or 0D nanoclusters, respectively. Several applications take advantage of nanotechnology like electronics, spintronics, hyperthermia treatment, energy harvesting, and wireless communications among other applications [3–6]. Nowadays the use of nanotechnology is massive (Meta, Twitter among other applications), and therefore, the electrical energy needed to feed the processing of information increases hugely every year. It is considered that by 2030, the 20% of the electricity generated will supply only technological applications [7]. So, approaches to make devices more efficient energetically are one of the most promising fields in nanotechnology. The digital information is processed in a binary system as 1 and 0 states. Nowadays, the energy dissipated during the change of state in a transistor is $\sim 100\,\mathrm{aJ}$ [8, 9]. It seems few energy, but in millions of bits needed to write and rewrite is a lot of energy. New technologies based in the use of magnetoelastic couplings can make the energy needed to write a bit lower than 1 aJ [10–12]. One of these technologies is called straintronics, and it is based on a multiferroic heterostructure in which ferroelectricity and magnetostriction are combined [13–16]. A ferroelectric material presents two states of polarization, depending on the bias of application of an external electric field, that are related to two states of strain. A magnetostrictive material is able to modify its shape in presence of an external magnetic field, or vice

versa, changes the orientation of its magnetization in presence of an external stress (Villari effect). When both materials are coupled, the strain in the ferroelectric may be able to modify the magnetization of the magnetic material by the magnetoelastic coupling. The study of magnetostrictive thin films to optimize its magnetic properties at room temperature is one of the main topics discussed in this thesis.

Not only straintronics is the field of application of magnetostrictive materials. There are many applications where magnetostrictive materials are used: active and passive vibration control, spintronic devices, patterned media for magnetic storage, energy harvesting, and torque sensing [17]. All of these applications motivate the quest for materials with large magnetostriction at room temperature at low magnetic field. Over the last decades, an alloy based on Fe is attracting a lot of attention [18]: the iron-gallium alloy presents a tenfold increase of the iron magnetostrictive values when a fraction of Fe atoms are replaced by Ga [19]. Although other materials like Terfenol-D ($Tb_xDy_{1-x}Fe_2$) present higher values of magnetostriction ~ 2000 ppm, respect to iron-gallium ~ 400 ppm, iron-gallium alloys are rare-earth free which are more eco-friendly and cheaper to produce [20]. From now on, we will refer to iron-gallium alloys as FeGa. FeGa exhibit high magnetostriction under very low magnetic fields ~ 20 mT, and they have demonstrated high tensile strength (~ 500 MPa), and limited variation in magnetomechanical properties for temperatures between -20 and 80 °C [21–23]. For alloys with Ga content lower than 19%, they are machinable [24], ductile, weldable, and they can be deposited over crystalline substrates [25]. They present high Curie temperature [19] (675 °C for Ga 19%), small magnetic anisotropy coefficients [26] and are corrosion resistant [27], as well as biodegradable [28].

In this thesis the variable x is referred to the atomic Ga content in the alloy, being the composition of the alloy: $Fe_{100-x}Ga_x$.

1.1 Magnetoelastic coupling and thin films

Anisotropic magnetostriction describes the change of the dimensions of a magnetic sample due to the magnetization. The coefficient λ_s is used to describe the rotation of the magnetization M of an isotropic material:

$$\lambda_s = \frac{\Delta l}{l} \tag{1.1}$$

Two magnetostrictive coefficients are relevant for cubic materials [29]:

$$\lambda_{100} = -\frac{2}{3}\frac{B_1}{(c_{11}-c_{12})} \tag{1.2}$$

$$\lambda_{111} = -\frac{1}{3}\frac{B_2}{c_{44}} \tag{1.3}$$

where λ_{100} and λ_{111} are the relative change in length that is measured along [100] and [111] with M along [100] and [111], for each coefficient respectively. c_{11}, c_{12} and c_{44} are the stiffness elastic constants, and, B_1 and B_2 the magnetoelastic coupling coefficients which are the magnetic stress causing the magnetoelastic strain. B_1 is related to tetragonal distortions, whereas B_2 is related to rhombohedral distortions. For B_1 positive, when the material is magnetized along a cubic axis is contracted, and, for B_1 negative is expanded. Most experimental data on the magnetoelastic coupling coefficients are obtained from measurements of the magnetostrictive strains λ_s of bulk samples, and the B_i coefficients are calculated from eqs. 1.2 and 1.3. The presence of elastic coefficients is due to the fact that, the sample lower its energy by changing its length l until elastic forces balance the magnetostrictive stress given by the B's.

In the discussion of magnetoelastic coupling in bulk samples, B and λ are often used as synonyms. However, in thin films the equivalence between magnetoelastic coupling and magnetostrictive strain has been criticized [30]. In contrast to bulk samples, the in-plane strains of a film are clamped by the substrate, and cannot freely adjust to minimize the energy of the system. Therefore, the use of λ seems not suitable for the study of the magnetoelasticity due to the dependence on the elastic constants. The magnetoelastic coefficients B_1 and B_2 are the subject of our investigations because are intrinsic to the material. The section 2.5 presents the procedure to determine both, B_1 and B_2, in thin films, and chapter 4 shows an application of magnetostrictive films in straintronic heterostructures.

1.2 FeGa system

Phase diagram

Before to explain the magnetostrictive behavior of the FeGa alloy as a function of the Ga content, it is necessary to introduce the phase diagrams for the thermodynamic equilibrium and metastable scenario (obtained by quenching) see Fig. 1.1 . In both of them, the crystal structures found are the same, although they are located at different ranges of temperatures, or Ga concentrations.

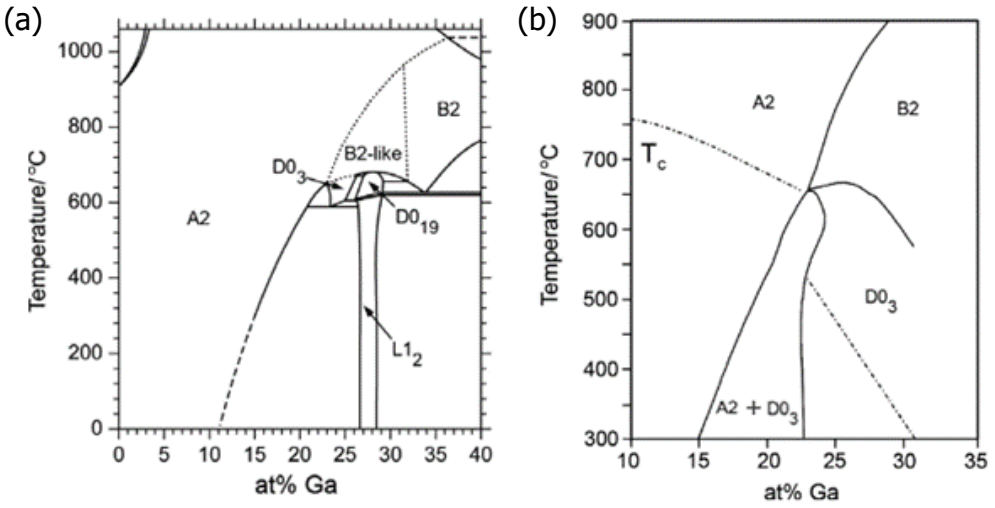

Figure 1.1: Phase diagram for bulk FeGa alloy. (a) Equilibrium [31], (b) Metastable [32].

The crystal structures are depicted in Fig. 1.2 . The A2 structure is *bcc*, where Ga and Fe atoms are distributed randomly in any crystal position. B2 is a cubic structure where Ga atoms are in the body-centered sites. $D0_3$ is an ordered cubic structure with unit cell expanding twice [33]. In this superstructure, Ga atoms are occupying body-centered sites, but, their four next nearest cells are occupied by body-centered Fe atoms. Modified $D0_3$ implies that the Ga *bcc* cells are aligned along some crystallographic direction ($\langle 010 \rangle$ in the example). $L1_2$ is a *fcc* structure with Ga atoms at face-centered sites, and Fe atoms at the corner sites. The $D0_{22}$ crystal structure is a superstructure based on $L1_2$ *fcc* structure, where Ga atoms are at the face-centered sites of the intermediate layer of the superstructure.

Magnetostriction

The FeGa alloy has become very famous because of the strong increment of λ_{100} for $x = 19$ and $x = 28$ [18]. According to [34], the magnetostriction λ_{100} can be divided in four regions depending on the behavior of the magnetostriction. Fig. 1.3 shows the four regions of magnetostriction for slow-cooled and quenched samples.

- Region 1: The strain monotonically increases up to $x \sim 17.9 - 20.6$. The composition of the maximum depends clearly on thermal history for alloys: in slow-cooled conditions (10 °C/min from 1000 °C), the first maximum occurs at ~ 320 ppm and $x = 17.9$. For quenched conditions, the maximum occurs at ~ 390 ppm and $x = 20.6$ [35].

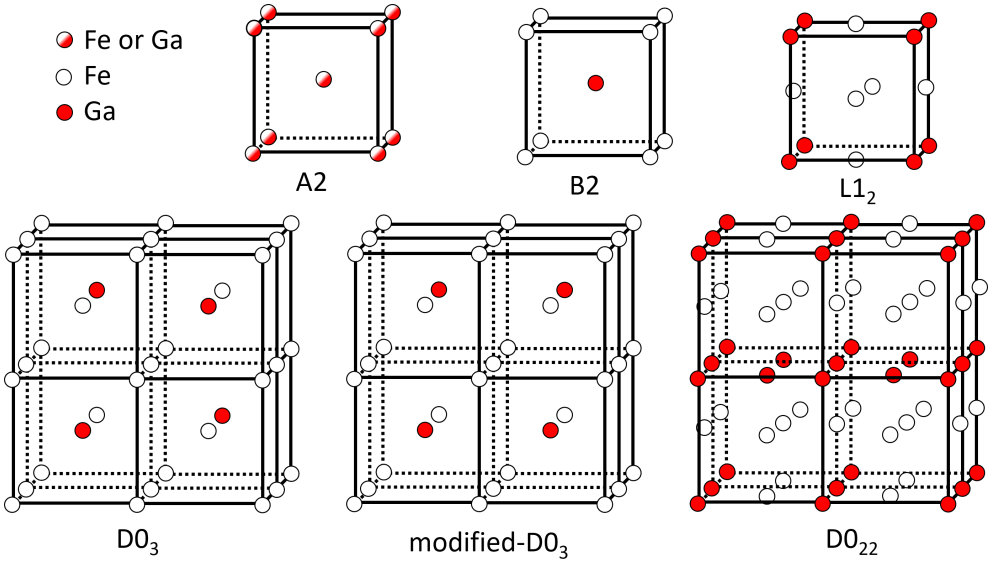

Figure 1.2: Crystal structures of FeGa alloys. Half white/red circles are for Fe or Ga randomly distributed, white and red circles are Fe and Ga atoms, respectively. *bcc* structures A2 and B2. *fcc* structure $L1_2$. Superstructures $D0_3$, modified-$D0_3$, and $D0_{22}$.

- Region 2: From $x = 17.9 - 20.6$ to $x = 22.5$, the strain decreases, reaching a minimum ~ 250 ppm at $x = 22.5$.
- Region 3: Between $x = 22.5$ and $x = 28.5$, λ_{100} increases again, up to ~ 380 ppm for slow-cooled alloys and 440 ppm for quenched alloys at $x = 28.5$.
- Region 4: For compositions $x > 28.5$, the magnetostriction decreases sharply with the Ga content [18, 35].

The origin of the two magnetostrictive peaks has been an open topic of discussion. Two models [36, 37] have been proposed to explain its origin. A first principles computational approach used to calculate the magnetocrystalline anisotropy suggests that spin-orbit coupling plays a crucial role in the enhacement of magnetoelastic coupling [36]. The model introduces the idea of non-uniform Ga site occupancies where are forming pairs. When Ga pairs are added to Fe matrix, the density of states and band structure changes significantly, and leads to a high dependence of magnetocrystalline anisotropy on strain. However, the results observed from calculations performed by different groups disagree in fundamental issues. Qu's calculations state that λ_{100} is negative for the $D0_3$ phase and positive for the a B2-like, and the nucleation of $D0_3$ pairs correlates with the drop of λ_{100} [38]. Recent work made by Julie B.

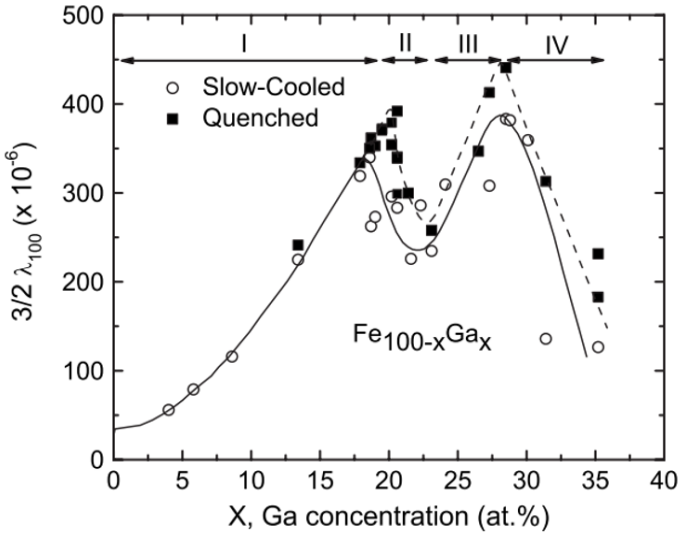

Figure 1.3: Saturation magnetostriction λ_{100} of FeGa alloy at room temperature as a function of gallium concentration showing four regions I–IV. Slow-cooled samples at 10 °C/min from 1000 °C. Quenched samples from 1000 °C. Taken from [18].

Staunton's group conclude that the $D0_3$ phase is not detrimental for λ_{100} with values more than twice that of the measured peak [39]. The second approach argues that the enhancement of magnetostriction is due to extrinsic sources: tetragonal Ga-rich nanoclusters within the Fe matrix [37]. Several models have proposed that the formation, distribution and size of these nanoclusters are controlled by a displacement in the vicinity of the solubility limits of the disordered *bcc* phase and $L1_2$ phase. For the first peak, the model suggests a transformation from α-Fe to $L1_2$ via the intermediate multivariant phase $D0_{22}$. The source of strain in this model comes from the formation of the $D0_{22}$ state. When a magnetic field is applied, the reorientation of the variants to a single variant leads to field-induced strains whose values are related to the tetragonality of the $D0_{22}$ structure. Then, the strain observed is indicating the amount of $D0_{22}$ present during the formation of $D0_3$ phase. This phenomenological model explain the observed thermal history effects because the volume fraction of $D0_3$ depends on vacancy concentration. But, up to date, no experimental observations of $D0_{22}$ were found.

Neither of the previous models provides an adequate fit of the entire range of experimental magnetostriction data in FeGa alloys [35]. However, both models agree in that the structural phases are the source of the magnetoelastic behavior. However, the actual crystal phase distribution in each region of the magnetostriction diagram (Fig. 1.3) is not clear, due to mixtures between

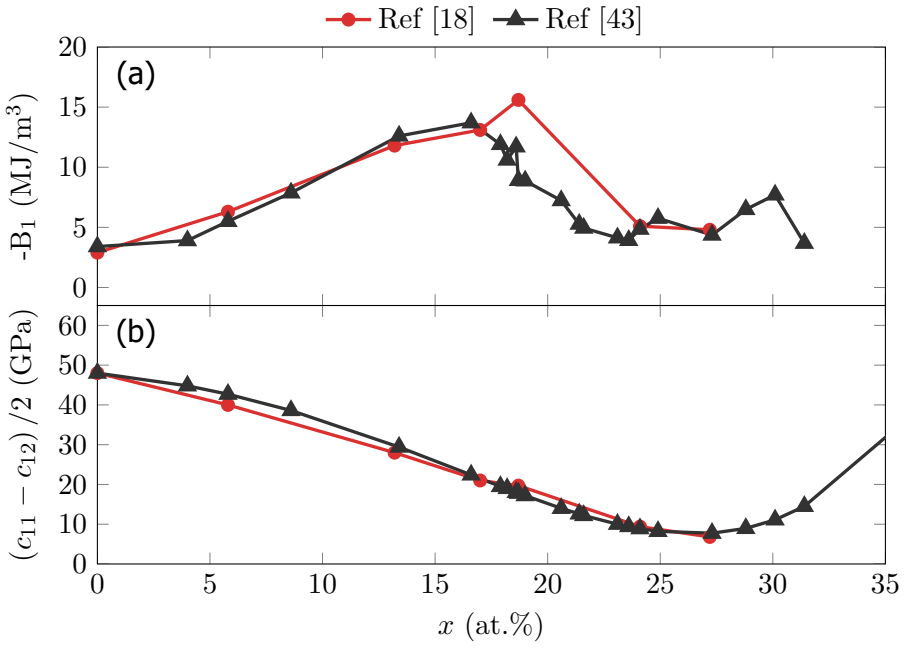

Figure 1.4: Data for FeGa bulk at room temperature as a function of Ga atomic content. (a) Magnetoelastic coupling coefficient $-B_1$. (b) Shear modulus $(c_{11} - c_{12})/2$.

phases. So, the determination of which phase causes an increase of λ_{100} is not straightforward. Microstructural studies together with magnetostriction measurements [40–42] are unfinished. The magnetostriction follows a metastable phase diagram [31], rather than the equilibrium phase diagram [32]. Fig. 1.1 a shows the equilibrium phase diagram for FeGa alloys. We will focus the analysis at room temperature. The single-phase A2 exists up to $x \sim 10$, and a mixture of A2 and $L1_2$ is present in the range $x = 10$ – 26.7. The single-phase $L1_2$ is, then, obtained for $x = 26.7$ – 27.4. However, the ranges here presented do not correspond to the observed magnetoelastic behavior. On the other hand, the metastable phase diagram shown in Fig. 1.1 b presents a better agreement with the experimental magnetostriction values, and with the models. XRD data support that at $x = 19.5$ the phase is 100% A2 for quenched samples, but a mixture of 67% A2 + 33% $D0_3$ is found for slow-cooled ones [41]. The portion of each phase can be tuned by the growing process. In this thesis, the samples are grown at 150 °C, which is similar to work with quenched samples. By this means, we can achieve, according to the theory, the highest values in magnetostriction.

As we have discussed before, in thin films study, λ_s is not the relevant parameter to study the magnetostriction. The magnetoelastic coupling B_i is

the relevant one because it does not depend on the elastic constants. Fig. 1.4 shows data for slow cooled bulk FeGa at room temperature. Comparing the magnetostriction (Fig. 1.3) and magnetoelastic coefficient B_1 (Fig. 1.4 a) we can identify the first peak at $x \sim 19$. Therefore, it can be concluded that the first magnetostriction peak can be linked to an increment of $|B_1|$. On the other hand, see Fig. 1.4 a, there is no peak at $x \sim 28$ for B_1, which excludes the direct link between B and λ_s for that composition. Observing the eq. 1.2, it is noted that λ_{100} depends inversely on elastic constants. Fig. 1.4 b shows the values of $(c_{11} - c_{12})/2$ reaching its minimum *vs* the gallium content, which reaches a minimum for $x \sim 28$. Then, the second magnetostrictive peak is due to a softening in the shear modulus and not by an increment of the magnetocoupling coefficient.

Chapter 2

Experimental methods

2.1 Thin film fabrication

Epitaxial FeGa thin film samples are grown by Molecular Beam Epitaxy (MBE). M600 DCA system is the equipment employed (see sketch in Fig. 2.1). MBE is a versatile technique that allows obtaining samples with specific crystal structures, compositions, thicknesses, and heterostructures with layer-by-layer control with high quality. Thin film fabrication takes place in a chamber in ultra-high-vacuum (UHV), which is less than 10^{-9} Torr. This requirement is essential to obtain better-quality crystal structures. The deposition is performed by heating bulk material. When the material is at a specific temperature, it starts to evaporate and is emitted to a substrate held at a temperature controlled with SiC heater. The flux of evaporation is supervised to make the growth by atomic layers. When growing films, we can measure *in situ* the evaporation flux rate and take RHEED patterns.

The mean free path of elements is inversely proportional to pressure. At UHV, the mean free path is in the order of kilometers. That means that the evaporated material reaches the substrate without colliding with other particles. So, the sample is grown mostly by the evaporated material without impurities in the environment. A lower vacuum means better-quality samples because the mean free path increases. Base pressure achieved in the main chamber of the equipment is 10^{-11} Torr. The main chamber of MBE connects with three pumps (rotary, turbomolecular, and ionic) and the load-lock is connected to two pumps (rotary and turbomolecular). Each pump has a different working pressure. Rotary pumps assist turbomolecular pumps. A rotary pump reaches 10^{-4} Torr. When this vacuum is reached, the turbo pump can be switched on and eventually reach 10^{-8} Torr. Ionic pump needs a base pressure of 10^{-6} Torr to start working and helps to reach a pressure of 10^{-9} Torr. To get the lowest

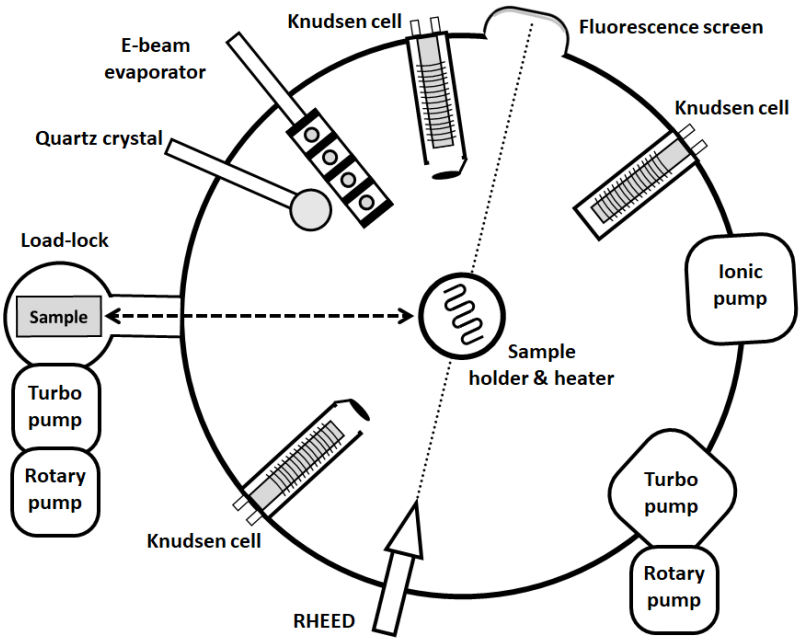

Figure 2.1: Scheme of the MBE M600 DCA equipment used to grow all the samples in this thesis.

pressure (10^{-11} Torr), the chamber is baked at 150 °C for two days to eliminate molecules that are trapped at the chamber surfaces (mainly H_2O).

Knudsen cells and e-beam evaporator are used to perform the evaporation process. The equipment contains three Knudsen cells and one e-beam with four crucibles. The combination of cells and e-beam allows the creation of samples of up to seven different materials. Also, it is possible to co-evaporate materials for two cells or one cell and the e-beam evaporator to make alloys or doping. Knudsen cells and e-beam have closed cooling water systems to secure the integrity of the equipment due to the high temperatures that that the materials used in this thesis require to reach reasonable evaporation rates. The refrigeration system also stabilized the temperature of the chamber to avoid desorption of residual particles remaining at the chamber surfaces.

A Knudsen cell (Fig. 2.2 a) contains a crucible filled with the desired material to evaporate and it is surrounded by a metallic wire (W, Ta) which acts a resistive heater. Also, tantalum radiation layer provides radiation shielding of the heater to extend its lifetime. The coil acts as a resistance that is heated up by the intensity applied. The flux of evaporated material depends on the temperature. A thermocouple located close to the crucible is used to controls the temperature of the cell. To calibrate the evaporation flux of a Knudsen cell,

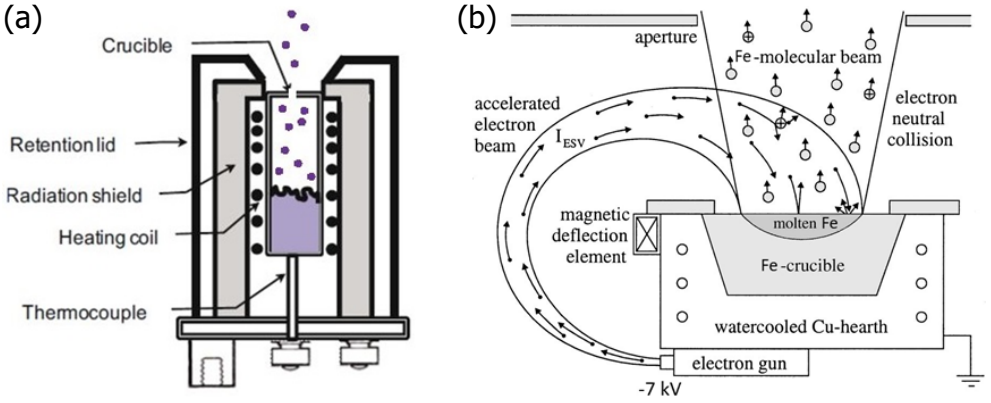

Figure 2.2: Schemes of the evaporation equipment in MBE: (a) Knudsen cell, (b) e-beam evaporator.

we use *ex situ* measures such as x-ray reflectometry (XRR). We evaporate at a constant temperature for a specific time. Afterward, we measure the thickness of the thin film by XRR. The evaporation flux rate is the quotient between the thickness and time. Note that for each temperature, a calibration by *ex situ* means needs to be accomplished.

The e-beam evaporator uses electrons to heat the material (Fig. 2.2 b). A tungsten filament emits the electrons that are deflected by permanent magnets. The filament is located under the crucibles to prevent it from being damaged by the evaporation jet. The e-beam evaporator used in this thesis is a multipocket Telemark model with room for 4 crucibles, with 15 cm^2 volume for all of them. Only one crucible can evaporate material at a time by this method. A magnetic field bends the electron beam to reach the material inside of the crucible. A second coil magnetic field, generated by a set of coils, is used to focus with precision the electron beam onto the crucible. Also, the equipment allows sweeping large areas of the evaporant by adding a sinusoidal wave. By this swept, the material gets homogeneously heated by the electrons. We accelerate the electron beam by using a voltage of 7kV. The intensity of the electron beam controls the temperature of the material. Typical ranges of intensity are $5 - 400$ mA. Evaporation flux is measured *in situ* by a quartz crystal microbalance. When evaporating, the quartz crystal is vibrating at a specific frequency. The deviation of the frequency concerning resonance frequency indicates the incoming flux of evaporated material. The resonance frequency changes as layers of materials are accumulated on the crystal. The calibration of these changes for each materials is done with XRR and provide values of the rate and accumulated thickness during the growth of a layer.

A typical fabrication of a sample by MBE is detailed as follows. First, we pro-

ceed to isolate the load-lock from the main chamber by the guillotine damper of a UHV gate valve until the load-lock reaches atmospheric pressure. Then, we insert a substrate in the holder. Once the substrate is inserted, the pumps of the load-lock start to increase the vacuum. Once the pressure in the load-lock is in the 10^{-7} Torr or better, we open the guillotine damper. Then, the substrate is transferred to the center of the main chamber. At the center there is a holder that traps the substrate. This holder can heat the substrate up to 1000 °C. To clean the substrate, usually, we hold it at 800 °C for at least 2 hours to ensure the cleanness of the surface. This cleanness is monitored by *in situ* RHEED patterns. After the cleaning procedure, the temperature of the substrate is changed to a growing temperature, usually 150 °C. This temperature plays a crucial role in obtaining specific phases. FeGa grows *bcc* at 150 °C, while FeGa grown at 600 °C is *fcc* [44]. To fabricate a thin film of an alloy like FeGa, we use the Knudsen cell to evaporate Ga and the e-beam evaporator to evaporate Fe in sync. By controlling the flux of each element the desired composition of the alloy can be obtained. After the deposition, we take RHEED images to characterize the sample obtained. Before extracting it, we usually deposit a layer of Mo by e-beam evaporator to prevent the sample from oxidation.

2.2 Structural characterization

2.2.1 Reflection High-Energy Electron Diffraction (RHEED)

Reflection High-Energy Electron Diffraction (RHEED) is used to characterize the texture structure of thin films. This technique is based on obtaining diffraction patterns with electrons, instead of x-ray as the XRD technique does. The scattering cross section for electrons in solids is much larger than that for x-rays. For example, the electron scattering from Mo at 10 keV is 10^{-19} m^2 [45] and for 1 keV photon, the cross-section from Pb is 10^{-22} m^2 [46]. The mean free path of electrons is a few nanometers to tens of nanometer in solids. This means that the electrons will mostly diffract with the surface for the gracing incidence configuration. However, charged surfaces can deflect electrons due to their electrical charge and cause them not to interact with the surface. The RHEED setup is inside the MBE main chamber to take advantage of the ultra-high vacuum to study the growth of thin films *in situ*.

To understand the patterns of RHEED is necessary to work in the reciprocal space. We use a geometric construction called the Ewald sphere to analyze the diffraction patterns. Fig. 2.3 shows schematically the Ewald sphere and the relevant wavevectors that play a role in the diffraction. k_0 is the wavevector of the incident electron wave. For elastic scattering, the diffracted waves, such as

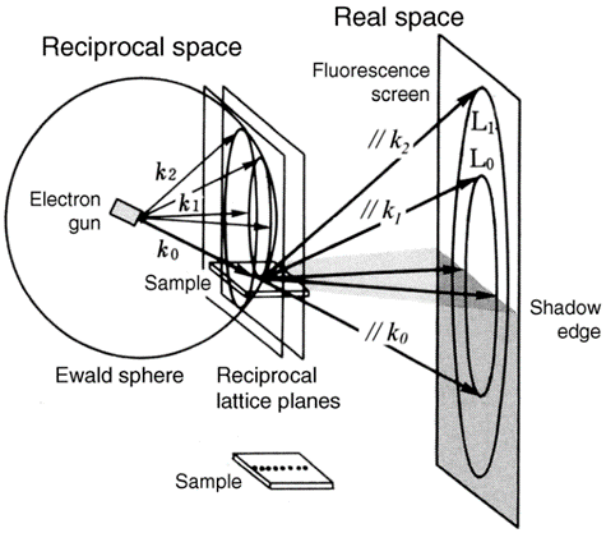

Figure 2.3: Direct space and reciprocal space of RHEED. Image taken from[47]

k_1 and k_2 have the same amplitude as the wavevector k_0. So, if we draw these vectors from the same origin, they form a sphere with radius $|k_0|$. That is the Ewald sphere. If the atoms are in an equidistant fashion along the incident beam, the Fourier transform of this atom row is a series of equidistant planes perpendicular to the atom row. The intersection between the Ewald sphere and the reciprocal planes is a series of concentrical circumferences. These circumferences are observed experimentally on a fluorescence screen.

For crystalline materials, depending on the texture structure, can be observed several patterns. In Fig. 2.4 we show the three most relevant patterns that cover this thesis. Fig. 2.4 a shows the pattern for a smooth single-crystal material. In this geometry, the electrons are reflected from the top layers. The reciprocal lattice of a single-crystal is the intersection between the reciprocal planes generated by the distribution of the atoms. This is called, reciprocal rods. The RHEED patterns generated by the intersection of the Ewald sphere and the reciprocal rods are vertical streaks. Fig. 2.4 b shows single-crystal islands. Electrons are transmitted and not reflected. Electrons enter by one side of the island and leave it from the other side. The reciprocal lattice, in this case, are points. The diffraction pattern is a set of sharp spots. This pattern indicates that the thin film is growing by islands and is not perfectly flat. Fig. 2.4 c shows polycrystalline diffraction. The reciprocal lattice consists of a set of concentric spherical shells. The intersection with the Ewald sphere leads to continuous rings in the diffraction pattern.

For single crystals, there is a phenomenon in which the RHEED pattern may display extra lines. These extra lines are called Kikuchi lines(Fig. 2.4 d). When

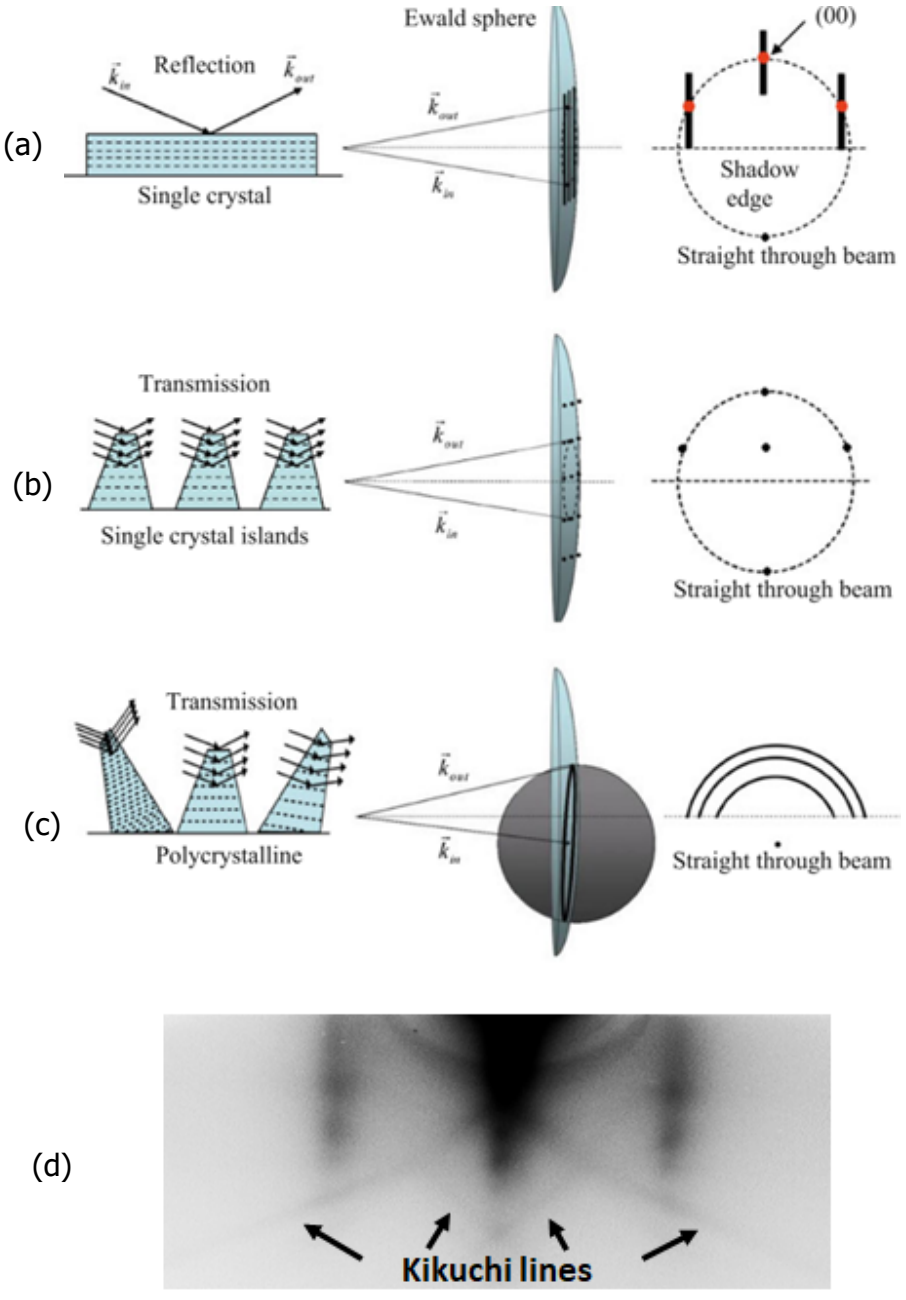

Figure 2.4: RHEED configurations for: (a) Single crystal, (b) Single-crystal islands, (c) Polycrystalline islands. First column: Electron geometry. Second column: Ewald sphere. Third column: RHEED pattern. Images taken from[48]. (d) Kikuchi lines taken on one MgO crystal used in this thesis.

a perfect crystal is irradiated by an electron beam, an incoherent scattering is followed by a coherent scattering originated by Bragg condition [49]. After the scatterings, the resulting pattern displays a lines due to the absorption of the material. As the Kikuchi lines depends on coherent scattering, the presence of these lines is used as an indicator of flatness and purity of the surface studied.

2.2.2 Transmission Electron Microscopy (TEM)

Transmission electron microscopy (TEM) is used to get information on the morphological, structural, and chemical nanoscale. The resolution of TEM is given by the electron wavelength. Typically, the resolution of TEM is 0.2 nm but for corrected aberration TEM it can reach 0.05 nm. Electrons are emitted by a tungsten filament at high voltage (20 kV) in a high-vacuum chamber to increase their mean free path. The beam of electrons is guided through the electromagnetic lenses of the system until is transmitted through the sample and is finally detected. The information obtained by TEM can be separated in two categories: imaging and analytical. In this thesis TEM experiments are used mainly for imaging.

TEM detects transmitted electrons, so it is desirable to minimize the scattered electrons when are passing through the sample. Then, to get high resolution images the thickness of the samples has to be < 100 nm. Our samples have to be thinned perpendicular to the growth direction because the atom columns need to be from the same element to be correctly studied. For our samples the method to get a perpendicular thin foil is by focused ion beam (FIB) extraction. FIB uses Ga ion milling to lithography samples. Our sample is milled until a thin foil is obtained. Then is extracted and carried to the microscope. The most common mode of TEM imaging is bright field image. The images are in grayscale. In this mode, we obtain a 2D projection of the 3D structure of the sample. When the sample has heavy and light atoms, the first are going to absorb more electrons than the light ones. This variation of intensity is reflected in the image with dark and light pixels.

To study the crystallinity of our samples we use High-Resolution TEM (HRTEM). This technique is the only known method to probe locally the crystalline structure of a nanostructure. HRTEM uses the phase of the electrons to generate images. The phase of the electrons changes when they are passing through the material. In a periodic crystal, the atomic potential interferes constructive or destructive with the electron wave. The image produced is a phase-contrast 2D projection of the crystalline structure. This image shows defects, dislocations or strain in the lattice [50]. This image from the real space can be converted to the reciprocal space by applying a Fourier transform (Fig. 2.5). In reciprocal space, planes and crystallographic

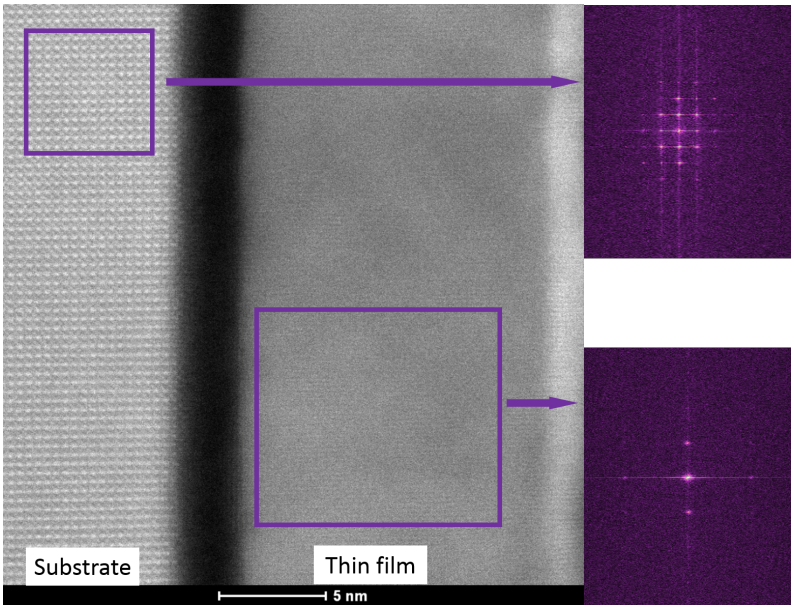

Figure 2.5: TEM image of a thin film of FeGa grown over a substrate of MgO. In purple is shown the Fourier transform of the selected areas.

directions can be indexed. This study is very interesting in epitaxial films, where thin films may have grown with a different interplanar distance to accommodate the lattice parameter of the substrate.

2.2.3 X-Ray Diffraction (XRD)

X-Ray Diffraction (XRD) allows us to study the structural properties of a crystal without damaging it. Some of the properties studied are lattice parameters, crystal structure, indexing planes, and directions. It relies on Bragg's law (Fig. 2.6 a). When an incident electromagnetic wave reaches the crystal structure there is an interference between lattice planes separated by the interplanar distance d. The constructive interference gives information about d because the diffracted waves are in phase. The Bragg condition for this phenomenon is:

$$2d \sin\theta = n\lambda \tag{2.1}$$

where θ is the angle of incidence, n an integer, and λ the wavelength of the x-rays.

The wavelength has to be in the range of the interplanar distance to observe the constructive interference. Two diffractometer were used, Bruker D8 Advance and Rigaku Rotaflex Ru-300, both uses Cu K-alpha wavelength $\lambda = 1.5418$Å. Typically, we measure using the $2\theta - \theta$ configuration (Bragg-Brentano ge-

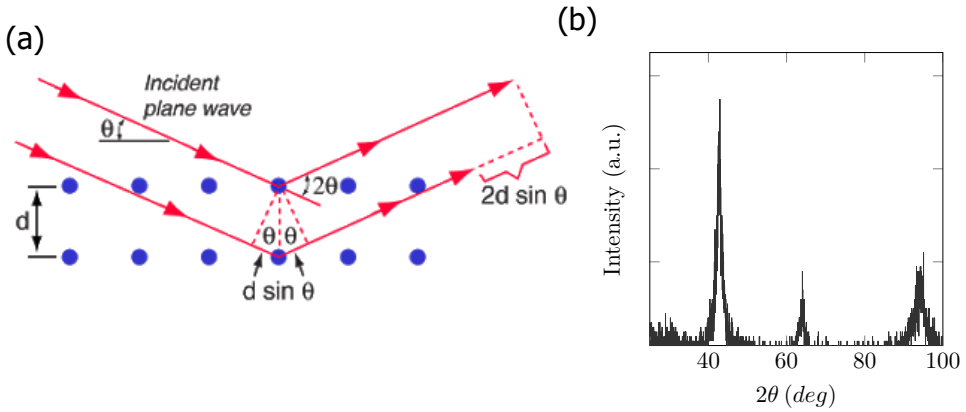

Figure 2.6: (a) X-ray diffraction in a crystal structure according to Bragg's law. (b) XRD pattern in $2\theta - \theta$ configuration.

ometry). In this geometry, the source of x-rays and the detector are at the same distance and angle from the surface of the sample. The x-ray source is stationary while the sample and detector move synchronously by an angle θ and 2θ respectively. In this configuration, we achieve the Bragg condition Eq. 2.1, and the interplanar distance d is obtained. In a $2\theta - \theta$ pattern, there are peaks with high intensity when the interference is constructive. But, some peaks cannot be detected due to systematic extinctions. This happens when the structure factor, $F(h,k,l) = \sum_{j=1}^{n} f_j e^{2\pi i[hx+ky+lz]}$, for certain crystal structures is zero. For example, the systematic extinctions for *bcc* structures happen when $h+k+l$ is odd, and for *fcc* structures are when h,k,l have mixed parity.

In this thesis, the crystal structures studied are cubic. Fig. 2.6 b shows a typical XRD pattern for a cubic structure. For these structures, the interplanar distances fulfill that

$$d = \frac{a}{\sqrt{h^2+k^2+l^2}} \tag{2.2}$$

where a is the lattice parameter. To index a peak is useful to know approximately the lattice parameter of the material studied. Once the peak is indexed, the lattice parameter is defined by the experimental measure. The lattice parameter may indicate if the thin film is relaxed or stressed.

2.2.4 X-Ray Reflectivity (XRR)

It is a similar technique to XRD but is used to obtain the thickness of thin films. The equipment used is the same as for XRD, Bruker D8 Advance. The configuration, in this case, is with an x-ray source and detector nearly parallel to the surface. X-rays are reflected from the sample by total internal reflection.

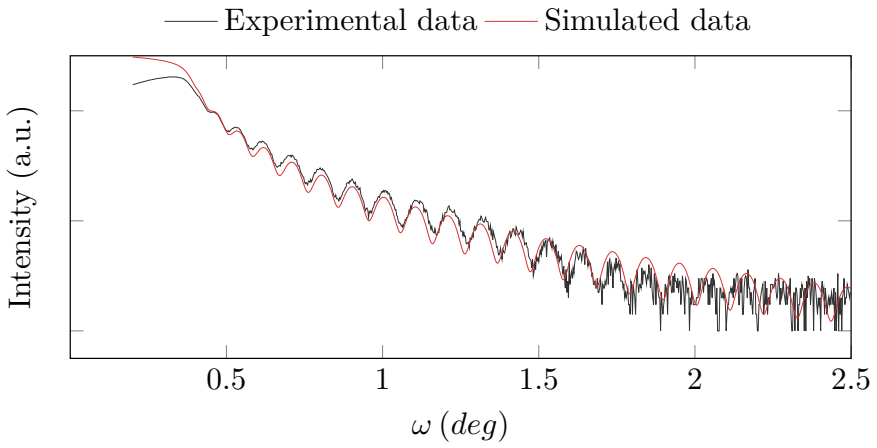

Figure 2.7: Typical XRR pattern of a thin film on a substrate. The thickness can be obtained by the period of oscillations.

This happens below a critical angle, usually $\omega < 5\,°$. The pattern obtained shows oscillations (Fig. 2.7). The period of the oscillations is related to the thickness of the film by the formula:

$$m\lambda = 2D\sqrt{\sin^2(\omega_i) - \sin^2(\omega_c)} \tag{2.3}$$

where m is the index of oscillation, λ is the wavelength of x-rays, D is the layer thickness, ω_i is the angle of the oscillation, and ω_c is the critical angle at which the first oscillations begin. Experimentally we use the program Leptos to simulate a curve that fits the oscillations precisely.

2.3 Chemical characterization

2.3.1 Energy-Dispersive X-ray spectroscopy (EDX)

Energy-dispersive x-ray spectroscopy (EDX), also called EDS, or EDAX is a tool inside a Scanning Electron Microscope (SEM) that allows us to identify the present elements in a sample. It is based on the specific relation between the x-ray and the elements of the sample (Fig. 2.8 a). The x-ray stimulation happens if enough energy is provided externally to kick-out. The empty place generated by this electron is filled with another electron of a higher-energy shell. The energy difference between the higher-energy shell and the lower-energy shell is released as an x-ray. For an atom, there are different emitted waves. These waves are $k\alpha$, $L\alpha$, $k\beta$ (Fig. 2.8 a). The wavelength of the emitted x-ray is characteristic for each element. We compare the wavelengths emitted by a sample with the values predicted by Moseley's law to analyze the spectra.

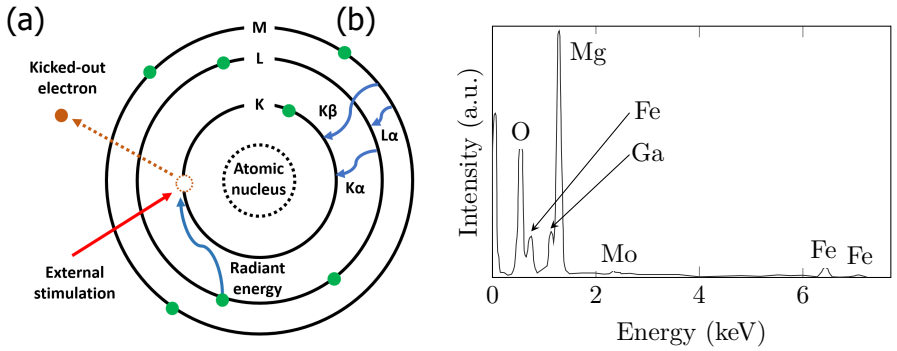

Figure 2.8: (a) Mechanism of x-ray generated by EDX. First, the external stimulation kicks out an electron, leaving behind a hole. Second, the hole is filled by another electron from a higher energy shell, and the characteristic X-ray is emitted. (b) EDX pattern for a sample. The elements Mg, O, Fe and Ga are detected.

In Fig. 2.8 b there is an example of EDX spectrum with some elements identified such as Fe, Ga, Mg, O, and C. The relative intensity between the peaks in the electromagnetic emission spectrum is related to the atomic weight. This data is important in alloys such as FeGa to identify the percentage of each element in a sample.

The equipment used is FEI Inspect F50 located at Laboratorio de Microscopías avanzadas (LMA) in Zaragoza. As this technique is non-invasive, the sample is very little damaged after the measurements. The acceleration voltage used to pump-out electrons is decisive to characterize precisely the percentage weight of the elements in the samples. Lower voltages characterize the surface, and higher voltages generate a larger volume of interaction, which is deep enough to interact with the substrate. For this work, an acceleration voltage of 10 keV is used in samples of thickness $10 - 50$ nm to minimize the interaction with the substrate.

2.4 Magnetic characterization

2.4.1 Vibrating-Sample Magnetometer (VSM)

This magnetometer allows us to obtain the magnetic properties of magnetic samples such as hysteresis, saturation, coercivity, and anisotropy. The magnetometer uses Faraday's law of induction to measure the electromotive force, $\mathcal{E}$, induced in a coil,

$$\mathcal{E} = -N\frac{d}{dt}\left(BA\cos(\phi)\right) \tag{2.4}$$

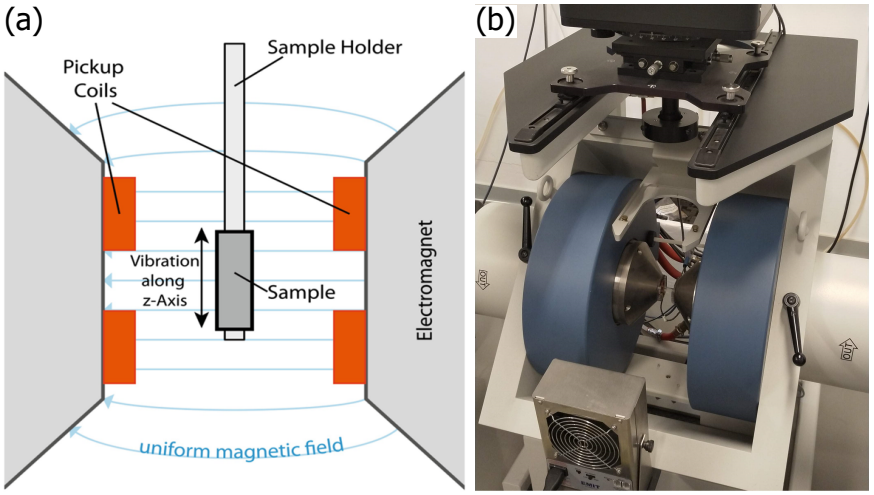

Figure 2.9: VSM setup. (a) Elements of the VSM (b) General view of the Lakeshore 7407 equipment.

where N is the number of wire turns in the coil, A is the coil turn area, and ϕ is the angle between the B field and the direction normal to the coil surface. Experimentally (Fig. 2.9 a), the sample is placed at the end of a rod between two detection coils. This rod vibrates at a given frequency ν. The detection coils are mounted on a electromagnet, which can apply a magnetic field depending on the DC current that goes through its coils. The oscillatory motion of the magnetic sample induces a voltage in the detection coils given by eq. 2.4. This induced voltage is proportional to B and, hence to the magnetization, M. We use a sphere of Ni to calibrate the equipment. At $H = 5\,\mathrm{kOe}$ the saturation magnetization is $M = 6.92\,\mathrm{emu}$. This calibration gives the equipment the relation between $\mathcal{E}$ and M. For hysteresis loops, when the sample is vibrating, the electromagnets apply a magnetic field for a period long enough to assure that the magnetic domains stay in the stationary phase. The change in the magnetization of the sample modifies the electromagnetic force, which is detected by the coils. The experimental setup used here is a LakeShore 7407 model (Fig. 2.9 b), which can apply a magnetic field up to 20kG. The magnetic measure is performed along the direction of the applied magnetic field, $M \parallel H$. The head of the VSM can be rotated, and hysteresis loops at any in-plane angle with respect to sample direction can be performed. To apply magnetic field in the film plane or perpendicularly to the surface specific glass sample-holders are used.

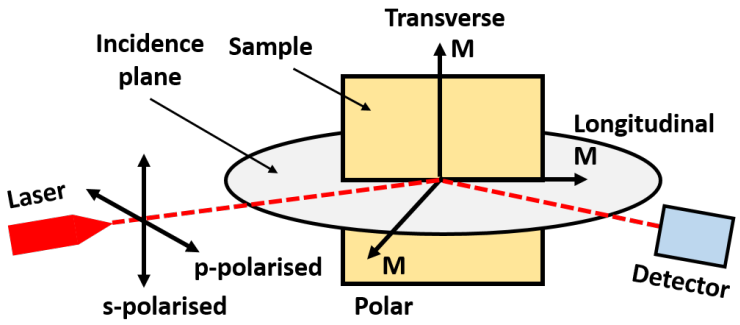

Figure 2.10: Scheme of MOKE geometry. Laser emits polarized light (p-polarised or s-polarised). The incidence plane contains the laser beam. Three different configurations depending on the **M** can be studied: longitudinal, transverse and polar.

2.4.2 Magneto-Optic Kerr Effect (MOKE)

The Kerr effect is a magneto-optic phenomenon. It happens when a magnetic material reflects polarised light. Therefore, this technique is useful for the study of metallic films, for which the surface of the sample has to be optically reflective. The interaction between the polarised light and the magnetization of the sample leads to a rotation in the polarization vector of the reflected light. The angle of rotation is related to the magnetization vector of the surface of the sample. The basic experimental setup include a laser and a photodetector sensor. being the diameter of the laser spot on the micron range. So, the measures are locally focused on the surface, unlike VSM. The plane that contains the laser beam and the normal is the incidence plane.

There are three configurations to study the Kerr effect (Fig. 2.10):

- Longitudinal: When **M** is parallel both to the surface of reflection and incidence plane.
- Transverse: When **M** is perpendicular to the incidence plane and parallel to the reflection surface.
- Polar: When **M** is perpendicular to the surface of reflection and parallel to the incidence plane.

In MOKE, for a plane polarised emitted light, there are two different polarizations (Fig. 2.10):

- p-polarised light: **E** is in the incidence plane.
- s-polarised light: **E** is perpendicular to the incidence plane.

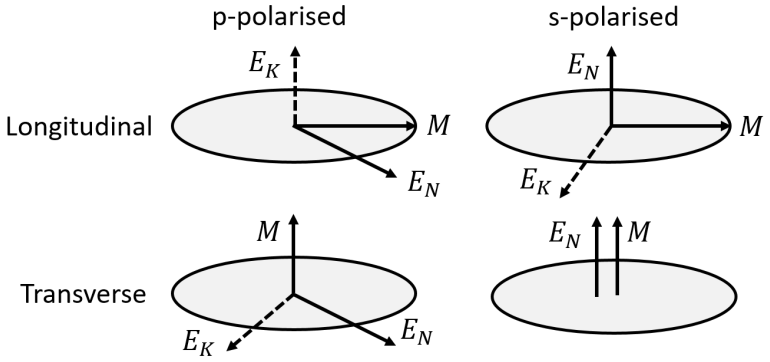

Figure 2.11: MOKE interactions according to the Lorentz force. The incidence plane is drawn as a grey ellipse. $\mathbf{E}_K$ is the induced component on the wave after the reflection. $\mathbf{E}_N$ is the polarization vector of the incident wave. $\mathbf{M}$ is the magnetization of the film. Adapted from [52].

For this thesis, the magnetic samples are mostly in-plane magnetized. Longitudinal and transverse are the main configurations to be used. To study interaction of the polarization of light with a ferromagnetic material after the reflection happens, we need to use the Lorentz force, $\mathbf{F} = q\mathbf{v} \times \mathbf{B}$. In our case, $\mathbf{B}$ is related to the magnetization of the film, $\mathbf{v}$ can be seen as the vector of the emitted electromagnetic wave that oscillate parallel to the polarised plane, and $\mathbf{F}$ as the induced force after the reflection. We can rewrite the Lorentz Force for this case as $\mathbf{E}_K \propto \mathbf{E}_N \times \mathbf{M}$. Being $\mathbf{E}_K$ the induced Kerr component that arises in the electromagnetic wave after the reflection, $\mathbf{E}_N$ the polarization vector of the emitted wave, and $\mathbf{M}$ the magnetization vector of the surface of the sample. Fig. 2.11 shows the effect of the Lorentz force in p-polarised and s-polarised light for longitudinal and transverse configurations.
For longitudinal configuration, p or s-polarised light, the component $\mathbf{E}_K$ makes the vector $\mathbf{E}_N$ rotate around the incidence plane. The resultant vector after the reflection, $\mathbf{E}_K + \mathbf{E}_N$, generates an elliptic electromagnetic wave with the major axis rotated [51]. The rotation of this wave is the Kerr rotation θ.
For transverse configuration, p-polarised light induces a $\mathbf{E}_K$ component in the incidence plane. There is no elliptic wave because $\mathbf{E}_K + \mathbf{E}_N$ is in the plane of incidence. The reflected wave only changes its amplitude. For s-polarised light, the polarization vector and magnetization are parallel, so there is no Lorentz force. Therefore, for transverse configuration there are no quadratic contributions in the reflected wave. To study MOKE in transverse configuration, we detect changes in the intensity of the light. The measured signal of transverse configuration modifies the reflectivity, R, of the film.

The experimental setup is the commercial equipment NanoMOKE3. The res-

olution of the laser spot is 2 μm and the laser light is p-polarized. It has a quadrupolar electromagnet to apply magnetic field in-plane up to 1kOe. The software LXPro 2 allows us to automatize the measurement and export the results. In this work, NanoMOKE3 is used to study the magnetic anisotropy of the samples. To study a certain crystallographic direction, the sample has to be fixed in the way that the crystallographic direction is in the incidence plane of the laser beam. Next, the laser beam is focused in the desired area. Then, the quadrupolar magnet applies a sinusoidal magnetic field. The final hysteresis loop is the result of averaging the signal obtained from a certain number of magnetic field cycles. By this means, we can obtain a M-H loop of the focused area along the chosen crystallographic direction.

MOKE symmetric M-H loops

Usually, Kerr rotation is described as proportional to the magnetization, which is called linear MOKE (LMOKE). But some materials have a quadratic MOKE (QMOKE) coexisting with LMOKE. In this thesis, the studied films are from FeGa, and it is reported that epitaxial Fe films present strong values of QMOKE [53]. So, we need to consider this quadratic effect to process the results. We can express the Kerr rotation, θ, according to [54] as:

$$\theta = \theta^L m_L + \theta^{LT} m_L m_T + \theta^{TT} m_T^2 \tag{2.5}$$

where m_L and m_T are the normalized longitudinal and transverse components of the magnetization. θ^L is the LMOKE contribution. θ^{LT} and θ^{TT} are the contributions of QMOKE.

Experimentally, the quadratic contribution tends to make asymmetric loops with non-linear saturation and anomalous dips. To obtain magnetic parameters of the samples as coercivity, remanence and magnetic anisotropy energy we need symmetric loops. These symmetric loops can be obtained cancelling the QMOKE contributions from Eq. 2.5.
When reversing the magnetization, m_L changes its sign, but $m_L m_T$ and m_T^2 stay constant [55]. Thus, the Kerr rotation for a generic magnetization m and its reversal $-m$ is:

$$\theta(m) = \theta^L m_L + \theta^{LT} m_L m_T + \theta^{TT} m_T^2 \tag{2.6}$$

$$\theta(-m) = -\theta^L m_L + \theta^{LT} m_L m_T + \theta^{TT} m_T^2 \tag{2.7}$$

LMOKE terms can be obtained as:

$$\frac{\theta(m) - \theta(-m)}{2} = \theta^L m_L \tag{2.8}$$

By this means, we can avoid quadratic contributions and obtain symmetric loops. Fig. 2.12 shows an experimental case of Kerr rotation symmetrization.

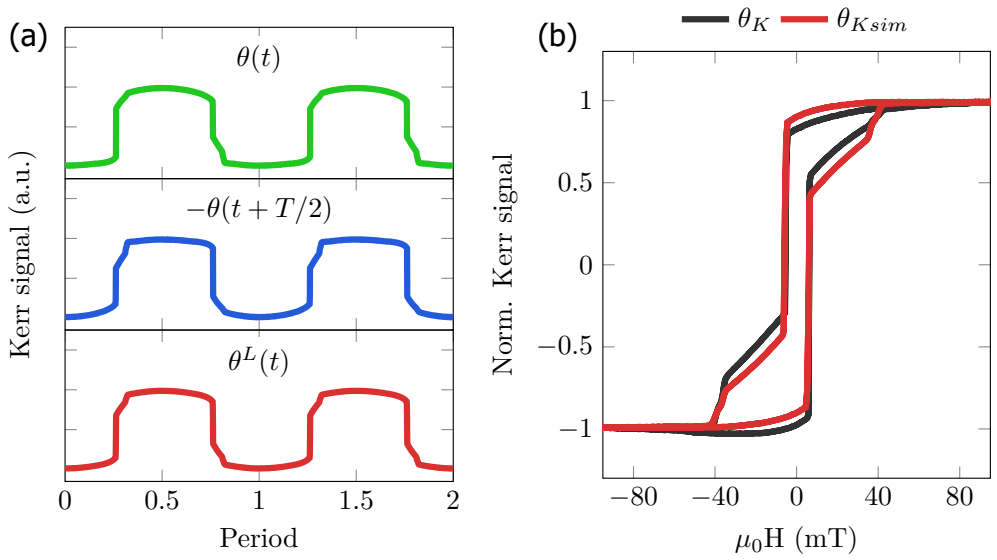

Figure 2.12: (a) Measured Kerr rotation, $\theta(t)$. Minus Kerr rotation shifted half a period, $-\theta(t+T/2)$. Linear Kerr rotation, $\theta^L m_L(t)$. (b) Comparison between symmetric and non-symmetric Kerr rotation in a normalized M-H loop.

Here, for computing simplicity, the time variable is used instead the magnetic field value to analyze θ. T is the time used to make an hysteresis loop. The Kerr rotation is considered as a function that depends on time $\theta(t)$ (Fig. 2.12 a green). To get $\theta(t)$ symmetric, the function is shifted half of a period of the measurement. Each $T/2$ the magnetic applied field has the same amplitude, but the sign is the opposite. The equation that describes this shift is $-\theta(t+T/2)$ (Fig. 2.12 a blue). Then, $\theta(m) = \theta(t)$ and $\theta(-m) = \theta(t+T/2)$ and the LMOKE contribution $\theta^L m_L$ (Fig. 2.12 a red) is obtained. To express it as a normalized M-H loop, it is necessary to normalize by the amplitude of the linear contribution θ^L.

$$m_L(t) = \frac{\theta(t) - \theta(t+T/2)}{2\theta^L} \tag{2.9}$$

By this mathematical treatment, we obtain m_L corresponding to LMOKE contribution, which is symmetric by definition. Fig. 2.12 b shows a comparison between θ and m_L in a M-H loop. The quadratic terms tends to make a non-linear saturation, while with symmetrization, saturation is linear. The effect of QMOKE is relatively small, but enough to make M-H loops asymmetric and distort the procedure of obtaining magnetic parameters.

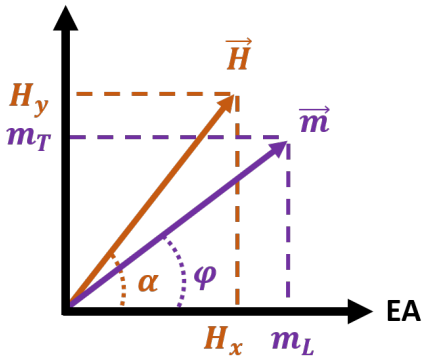

Figure 2.13: (a) Scheme of the relevant vectors in MOKE analysis.

MOKE angular measurements

For samples with local magnetic inhomogeneities, MOKE measurements allows us to characterize these specific local areas. Nevertheless, obtaining M-H loops for several directions in the same area is a hard task to achieve. The experimental configuration of NanoMOKE3 allows us to rotate the sample to get a specific crystallographic direction aligned with the incidence plane and measure it in longitudinal configuration. However, when the sample is rotated, usually, the laser spot is not exactly in the same position as before. For this reason, we developed a method in this thesis to obtain the M-H loops for all in-plane directions without moving the sample. This method is based on conjugate Kerr rotation ($\propto m_L$), and reflectivity ($\propto m_T$) as orthogonal vectors to obtain $\mathbf{m}$ in our samples, but avoiding quadratic effects.

The equipment detects Kerr rotation θ and reflectivity R. Kerr rotation is originated by the longitudinal configuration, this means that the magnetization is parallel to the incidence plane (Fig. 2.10). Reflectivity variation occurs in transverse MOKE, this is when the magnetization is perpendicular to the incidence plane (Fig. 2.10). We can write the magnetization unit vector of the sample as $\mathbf{m} = (m_L, m_T)$ if we take the Cartesian axes parallel to the longitudinal and transverse directions (Fig. 2.13). m_T is obtained directly of the normalized reflectivity measure, $R = R^T m_T$, because the transverse MOKE effect has no quadratic contributions with R^T being the amplitude of the loop made by m_T. But, obtaining m_L is not direct because θ has quadratic contributions that mix m_L and m_T (Eq. 2.5). In this case, unlike symmetrization, we want to obtain the QMOKE terms of θ. We consider that this terms are constant for all directions of the sample in the specific area of measure. So, a calibration measure is needed to characterize our sample.

First, we need to obtain two hysteresis loops with the magnetic field along the

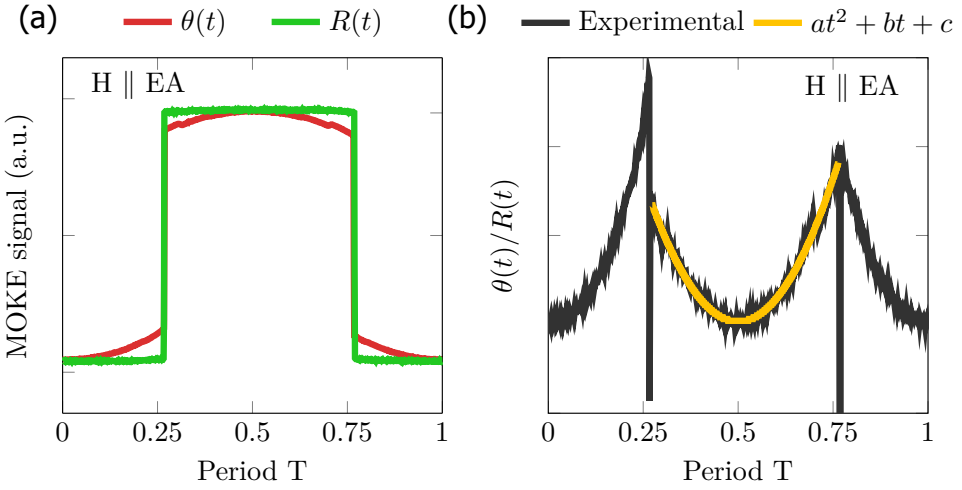

Figure 2.14: (a) Kerr rotation $\theta(t)$ (red), and reflectivity $R(t)$ (green), data from an easy magnetic axis. (b) Quotient between Kerr rotation and reflectivity (black) fitted by the quadratic function $at^2 + bt + c$ (yellow).

easy direction. One of them is done by transverse configuration, and the other one is done in the longitudinal configuration. Fig. 2.14a shows an example of the two loops as a function of time. For easy axis, the magnetization changes abruptly from $+m$ to $-m$ as the reflectivity measure does and the H field and M become parallel. This step-like behavior is not replicated for the longitudinal configuration. If the Kerr rotation did not have quadratic terms, both loops should be identical. Fig. 2.14b shows the quotient between the two loops, $\theta(t)/R(t)$. There are three sectors, where quadratic functions can be used to fit the data. In the figure appears as example the sector $T/4$ to $3T/4$. This quadratic pattern is used as calibration curve to obtain the QMOKE terms.

For each quadratic function we have this relation between Kerr rotation and reflectivity at the easy axis:

$$\frac{\theta(t)}{R(t)} = at^2 + bt + c \tag{2.10}$$

where a, b, and c can be experimentally fitted. Now, we will show the relation between these coefficients and QMOKE terms as a function of time.

Considering that for measurements, H is applied along the easy direction, m_T can be equaled with m_L. Then, $R = R^T m_L$ is used instead of $R = R^T m_T$.

Then, $\theta(t)/R(t)$ with H along the same axis:

$$\frac{\theta(t)}{R(t)} = \frac{\theta^L m_L(t) + \theta^{LT} m_L(t) m_T(t) + \theta^{TT} m_T^2(t)}{R^T m_L(t)} \tag{2.11}$$

$$= \frac{\theta^L}{R^T} + \frac{\theta^{LT}}{R^T} m_T(t) + \frac{\theta^{TT}}{R^T} \frac{m_T^2(t)}{m_L(t)} \tag{2.12}$$

The magnetization unit vectors can be written as $m_L = \cos\varphi$ and $m_T = \sin\varphi$, where φ is the angle that forms m with the easy axis (Fig. 2.13).

In this configuration, the easy axis is parallel to both, longitudinal axis and the applied magnetic field. The magnetization is mainly parallel to the longitudinal axis, except when it switches from m to $-m$ abruptly. Therefore, we can make the approximation at first order of $\varphi \to 0$.

$$m_L = \lim_{\varphi \to 0} \cos\varphi = 1 \tag{2.13}$$

$$m_T = \lim_{\varphi \to 0} \sin\varphi = \varphi \tag{2.14}$$

Introducing these values of magnetization in Eq. 2.12.

$$\frac{\theta(t)}{R(t)} = \frac{\theta^L}{R^T} + \frac{\theta^{LT}}{R^T} \varphi(t) + \frac{\theta^{TT}}{R^T} \varphi^2(t) \tag{2.15}$$

The angle φ moves as the same rate as the magnetic field is applied, $H = H_0 \cos(\omega t)$, where H_0 is the amplitude of magnetic field, and ω is the frequency. The magnetic field starts at saturation, that is $\varphi = 0$ at $t = 0$. And, when $H = 0$ at $T/4$, φ is maximum. So, φ describes a sinusoidal wave as a function of time, $\varphi(t) = \sin(\omega t)$. Taking a first order approximation, $\varphi(t) \to \omega t$.

And, substituting $\varphi(t)$ into 2.15

$$\frac{\theta(t)}{R(t)} = \frac{\theta^L}{R^T} + \frac{\theta^{LT}}{R^T} \omega t + \frac{\theta^{TT}}{R^T} \omega^2 t^2 \tag{2.16}$$

By direct comparison between 2.10 and 2.16, we can obtain the QMOKE terms from the fitted a, b, and c coefficients.

$$a = \frac{\theta^{TT}}{R^T} \omega^2 \quad b = \frac{\theta^{LT}}{R^T} \omega \quad c = \frac{\theta^L}{R^T} \tag{2.17}$$

As we consider that these coefficients are constant for the sample, we can obtain m_L for any Kerr rotation measurement.

Eq. 2.10 was written for the specific case of applied field along easy axis, but, if we generalize to a situation where M and H are not collinear (Fig. 2.13) :

$$\frac{\theta(t)}{A^L m_L(t)} = at^2 + bt + c \tag{2.18}$$

$$\frac{\theta(t)}{at^2 + bt + c} = A^L m_L(t) \tag{2.19}$$

We can obtain any m_L with an amplitude of A^L by making the quotient between the Kerr rotation and the calibration curve. Then, the magnetization unit vector is the sum of its components:

$$m = \frac{A^L m_L + R^T m_T}{A^L + R^T} \tag{2.20}$$

Note that $A^L + R^T$ is used to normalize the values of m.

Experimentally, to obtain a M-H loop at a specific angle (α), we apply field H_x and H_y as $\alpha = \tan^{-1}(H_y/H_x)$. So, the total applied field to the sample is $H = \sqrt{H_x^2 + H_y^2}$. Once Kerr rotation and reflectivity signals are recorded, we apply the calibration function to Kerr rotation (Eq. 2.19). The M-H loop is calculated by using Eq. 2.20 and is shown in Fig. 2.15 a. This loop corresponds to $\alpha = 160°$ direction. This indirect method to measure directions that are mixed between longitudinal and transversal configurations is compared with a direct measure in longitudinal configuration symmetrized. As we can notice, both loops are nearly equal, proving the validity of the approximations made.

By using the method of MOKE angular measurements developed in this thesis, we can present in great detail, the squareness, S_k, for each loop as:

$$S_k = \frac{\theta_r}{\theta_s} \tag{2.21}$$

where θ_r is the remanent Kerr signal, and θ_s is the saturated Kerr signal. So, S_k is similarly to talk about remanent magnetization. Values of S_k close to 1 indicate easy axis, and lower values may indicate non-easy axis, but further analysis is needed for those cases.

The study of S_k is particularly relevant to identify anisotropies in samples. Fig. 2.15 b shows a squareness polar plot comparing a direct measurement and an indirect measurement. Both curves are nearly equal proving that the indirect method proposed is a valid approximation. For samples with cubic magnetic anisotropy (as Fig. 2.15), the polar plot displays a 4-fold symmetry, whereas for uniaxial magnetic anisotropy, displays 2-fold symmetry.

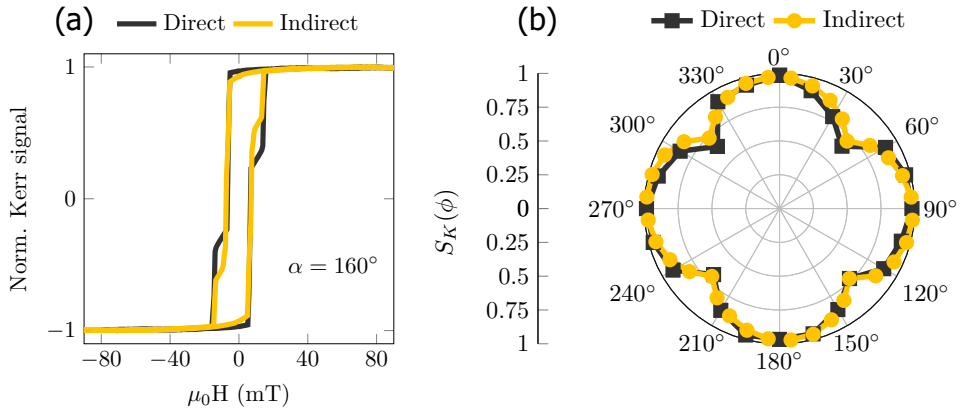

Figure 2.15: (a) Comparison between a direct measurement at longitudinal configuration (black), and a measure taken at 160° from longitudinal axis applying the indirect method explained in this section. (b) Squareness polar plot of a sample with cubic anisotropy. Direct measurement (black squares), and indirect measurement (yellow circles).

2.4.3 Cubic anisotropy, K_1

FeGa alloys present cubic anisotropy [56]. We can write the cubic energy as a function of two constants, K_1 and K_2. The magnetocrystalline energy per unit volume of a cubic system is given by [57]:

$$e_{cubic} = K_1\left(\alpha_1^2\alpha_2^2 + \alpha_2^2\alpha_3^2 + \alpha_3^2\alpha_1^2\right) + K_2\alpha_1^2\alpha_2^2\alpha_3^2 \tag{2.22}$$

where α_1, α_2, and α_3 are the direction cosines of the magnetization relative to the three crystal axes, [100], [010] and [001] respectively.

The easy axis depends on the values of K_1 and K_2. In general, for $K_1 > 0$, the easy axes are the $\langle 100\rangle$ directions. For $K_1 < 0$ depending on the value of K_2, the magnetic easy axes are $\langle 111\rangle$ or $\langle 110\rangle$ [58].

For samples with anisotropy in-plane (001), as FeGa, we have $\alpha_3 = 0$. As the cubic system has an orthogonal axis, $\alpha_1^2 = 1 - \alpha_2^2$. Then, we can write $\alpha_2^2 = \sin^2\phi$ with ϕ, the angle that form M and the [100] direction we obtain:

$$e_{(001)} = \frac{K_1}{4}\sin^2(2\phi) \tag{2.23}$$

To obtain K_1, we recall the magnetic energy per unit volume of a ferromagnet in an applied magnetic field [57]:

$$e = \mu_0 \int H(M)dM \tag{2.24}$$

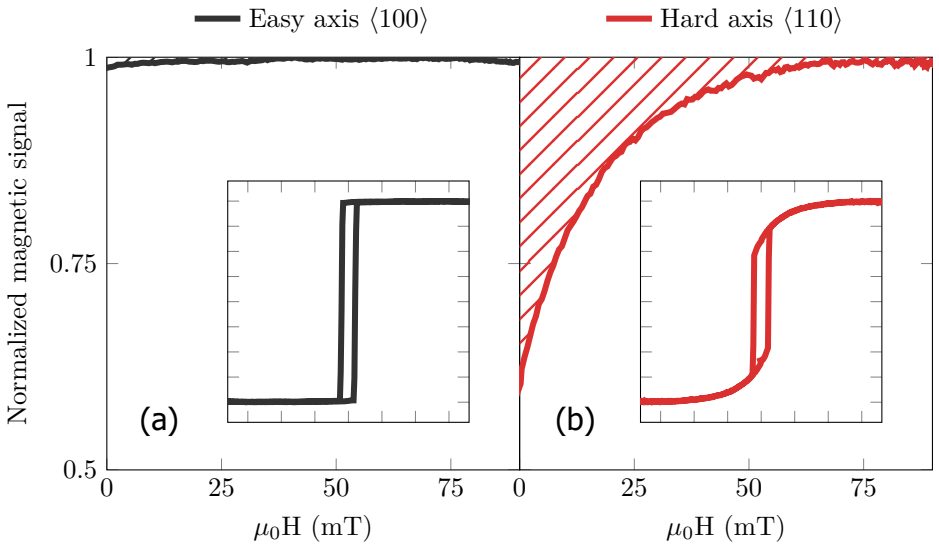

Figure 2.16: M-H loops of a FeGa film with H along the easy and hard axis. Ticks of inset plots are at the same scale as main plots. (a) Easy axis. Inset of the full loop. (b) Hard axis. Inset of the full loop. Dashed area is the integral $A = \int_{m_r}^{1} H(m)dm$ used to calculate K_1.

As we usually work with MOKE and VSM equipment, we cannot obtain M because we need a fine calibration procedure to obtain M_s. So, magnetic hysteresis loops are usually presented as normalized magnetic signal in the range ± 1. We can consider that, at first approximation [59], the data obtained from MOKE are proportional to M by a factor equal to the saturation magnetization, M_s. If we call m to the normalized data measured, we have:

$$\frac{M}{M_s} = m \tag{2.25}$$

$$dM = M_s dm \tag{2.26}$$

Subsituting 2.26 into 2.24:

$$e = \mu_0 M_s \int_{m_r}^{1} H(m)dm = \mu_0 M_s A \tag{2.27}$$

where the limits of the integral are given by the remanent magnetization in the normalized system, m_r, and saturation, which is 1 in a normalized loop. We recall the integral A because it represents an area of integration. An example is shown in Fig. 2.16 where the m(H) curve is obtained by averaging the hysteresis loop branches.

In a cubic system, the value of K_1 can be obtained from the difference between in-plane easy and hard axis measurements [56]. We will illustrate it with experimental data of a system in which the easy axis is parallel to $\langle 100 \rangle$, as FeGa with $x < 19$. Fig. 2.16 a shows a M-H loop for an easy axis. The energy is ~ 0 because M_r and M_s are nearly equal. But, for the hard axis, the area is bigger (Fig. 2.16 b). The hard axis is at the in-plane $\langle 110 \rangle$ directions ($\phi = \pi/4$). Substituting the values of ϕ in eq. 2.23 for easy and hard axis, we obtain:

$$e_{\langle 100 \rangle} - e_{\langle 110 \rangle} = 0 - \frac{K_1}{4} \tag{2.28}$$

Note that if the easy axis of the system is at $\langle 110 \rangle$ directions, the sign of eq. 2.28 will be the opposite.

To evaluate the value of K_1 from a M-H loop we consider that all of the energy is due to the magnetic domain rotation. By this argument, the energy of the eqs. 2.27 and 2.28 is equal. Finally, K_1 can be obtained:

$$K_1 = -4\mu_0 M_s \left[A_{\langle 100 \rangle} - A_{\langle 110 \rangle} \right] \tag{2.29}$$

where $A_{\langle 100 \rangle}$ and $A_{\langle 110 \rangle}$ are the areas obtained from the M-H loops along $\langle 100 \rangle$ and $\langle 110 \rangle$, respectively. Experimentally, we obtain the value of the integral from M-H loop (dashed area in Fig. 2.16 b). M_s can be obtained either from VSM measurements or from the literature.

2.4.4 Magnetic Force Microscopy (MFM)

Magnetic force microscopy (MFM) is based on the mechanism of atomic force microscopy (AFM). AFM technique obtains the topography of almost any type of surface with a resolution in the scale of nanometers. AFM uses a sharp tip of about 50 nm in diameter attached to a cantilever. The resolution and noise of AFM images depend on the diameter of the chosen tip. There are two modes to measure topography with AFM: contact mode and tapping mode (Fig. 2.17 a). For contact mode, the cantilever is displaced until the tip touches the surface. When the equipment detects a certain pressure, the downwards movement is stopped. Then, the scan starts. The tip is in contact with the surface and replicates the topography with their displacements upwards and downwards. The AFM measures this displacement by focusing a laser beam on the tip with a photodiode as shown in Fig. 2.17 a. This displacement is proportional to the bending of the cantilever induced by the topography of the surface. For tapping mode, the tip is closer to the surface and oscillates at its resonance frequency. We choose this mode to obtain the images in this thesis because the tip preserves the surface, and it is more difficult to damage the tip while scanning. Fig. 2.17 b shows an example of nanoelements studied

by AFM in tapping mode. Also, the cleanliness of the tip is more assured in tapping mode. If a small impurity is attached to the tip, the produced image will be full of artifacts that sometimes are hard to detect.

While the basis of the AFM technique is the measure of the amplitude of deflection of the cantilever, the basis of the MFM technique is the measure of the variation in the oscillation frequency of the cantilever. The tip must be magnetic because it needs to interact with the stray magnetic field of the surface. In this mode, the tip is not in contact with the surface, but it needs to be close enough to interact magnetically with it (Fig. 2.17 a). Typically, the distance between tip and surface is around 30 nm. The magnetic force that the tip experiences by the surface by a distance Δz:

$$F_z = c\Delta z \tag{2.30}$$

where c is the cantilever spring constant in the z-direction. For small deflections, we consider the cantilever as a damped harmonic oscillator. It can be modeled by an ideal spring of elastic constant c, a mass m, and damping D. When an external oscillating force $F_z = F_0 \cos(\omega t)$ is applied to the cantilever, the resulting displacement is harmonic, but it has a phase shift, $z = z_0 \cos(\omega t + \theta(\omega))$. This force can be applied directly to the end of the cantilever, for example, by electrostatic means. The variation in the frequency caused by the magnetic surface is:

$$\Delta f = f_n^{'} - f_n \approx -\frac{f_n}{2c}\frac{\partial F_z}{\partial z} \tag{2.31}$$

The approximation is accurate for $\Delta f \ll f_n$, which is always the case in MFM [60]. The sign in Δf indicates that when the tip is attracted towards the sample, the force is negative, and the force derivative is positive. So for attracting forces, the resonance frequency of the cantilever decreases. Note that these forces are in z-direction, in-plane magnetization is undetected by the tip, so the images have to be interpreted as a landscape of out-of-plane magnetization.

The MFM measurements have been performed with an NT-MDT Scanning probe microscope using the two-pass method. In the first scan, the topography is determined by the tapping mode. In the second pass, the cantilever is lifted to certain height, and the scan is made using the stored topography without the feedback. Therefore the tip-sample separation during second pass is kept constant. During the second pass, the short-range forces are not detected because they decay faster than the long-range magnetic force. During second pass the phase shift between the cantilever oscillation and the drive excitation wave is sensitive to the magnetic signal. The result is a magnetic image taken

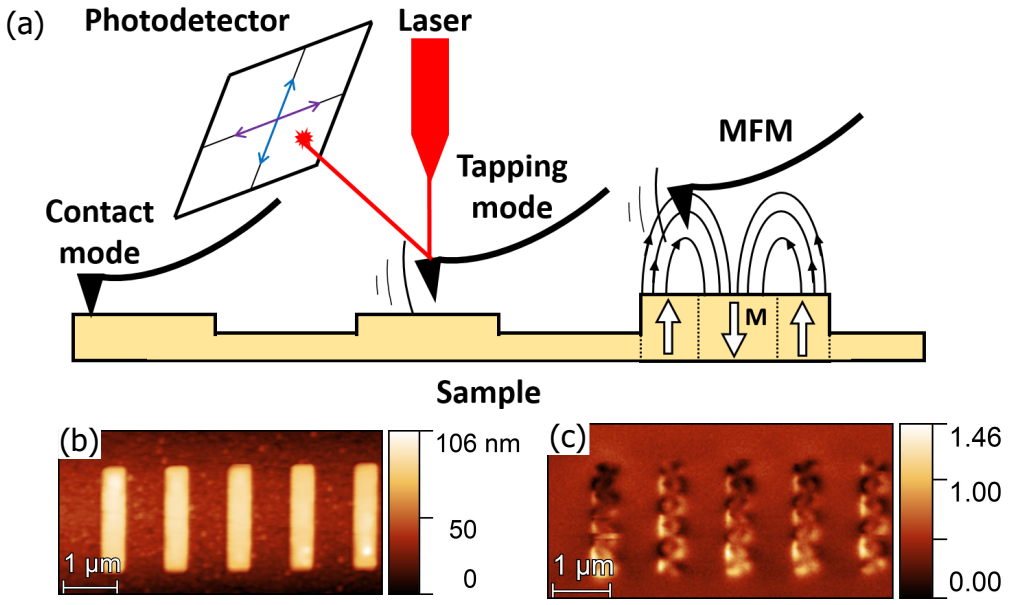

Figure 2.17: (a) AFM and MFM schemes of working. For contact mode, the tip is in contact with the surface. For tapping mode, the tip is oscillating and touches intermittently the surface. For MFM, the system measures the change in the oscillation phase due to the interaction with the magnetization field. (b) AFM and (c) MFM image of rectangular nanoelements.

simultaneously with the topography of the sample. An example is shown in Fig. 2.17 b and Fig. 2.17 c. In (b) appears the topography while in (c) appears the magnetic contrast. Both images are from the same nanoelements, but give us complementary information.

Some measurements were performed in vacuum to maximize the resolution of the MFM technique. We achieve low vacuum by using a rotary pump and vacuum o-rings to seal the chamber. The quality factor of the cantilever can increases up to 50 times [61] because of the decreasing damping constant. We can detect small magnetic contributions that noise masks when the experiment is performed at atmospheric pressure. The inconvenience is that the resonance frequency of the cantilever shifts because of the damping. Depending on the pressure, the damping is different, and the resonance frequency shifts. When a scan is in process, we disconnect the rotary pump because it disturbs the measurement. So, when we finish a scan, the resonance frequency is different, and it needs a correction after each measure.

2.5 Magnetoelastic stress measurements: Cantilever method

Measuring directly the magnetoelastic (ME) stress in thin films is not an easy task. For bulk materials, the standard methods for measuring the anisotropic magnetostriction are the strain gauge and the capacitive cell. The strain gauge is a resistive band that changes the value of the resistance when the dimensions of the material are modified for a given direction. Strain gauge is glued to the magnetic material. When a magnetic field is applied, the sensor can detect the average deformation of the sample, for instance, parallel and perpendicular to the magnetic field direction. For thin films, this standard method is not suitable because of the substrate. Capacitive methods are more sensitive to determine strain. But, in bulk samples designs, the variation of the gap is proportional to the length of the magnetic sample, which for thin films is very small. The sample is made of an active element (thin film) and a passive element (substrate). The elastic properties of the substrate play an essential role in determining the magnetostriction of the film. When the magnetic field is applied to the sample, the magnetic film tends to change its shape, but the substrate is a rigid element that limits the strain. The thickness of the substrate is $\sim$ 1000 times the thickness of the film. This massive volume of rigid element leads to indirect ways of measuring magnetostriction instead of direct measures, such as the strain gauge.

In 1976 Klokholm [62] observed the deflection of the end of a bimorph when magnetized. When a sample made of a magnetostrictive film deposited onto a substrate is acting as a cantilever under a magnetic field, it bends. Depending on the magnetostrictive sign, the bending occurs upwards o downwards and it is proportional to the strength of the magnetoelastic energy. Higher the bend, higher is the magnetostrictive constant. We will refer to this indirect technique of measuring the magnetostriction as the cantilever method.

The bending of the cantilever is related to its ME constants. So, if we can measure the bending, the ME constants can be determined. The technique used to measure the bending is based on a plane-parallel capacitor (Fig. 2.18). The capacitor is made by a fixed plate and the sample. When the sample bends due to magnetostriction, the capacitance of the system will change. As one can foresee, this bend is extremely small as well as the resulting variation of capacitance. In this section we will show the design and fabrication of the measurement system that involves a high precision capacitance cell that allows to measure changes with a precision in the order of attoFarads (aF).

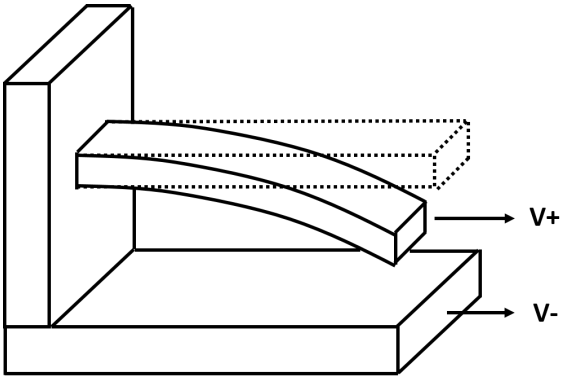

Figure 2.18: Schematics of cantilever method. Cantilever bends under magnetic field (from dashed to solid line) due to magnetostriction. Capacitor made by sample (positive voltage) and fixed plate (negative voltage). Magnetostrictive constants are determined by the capacitance measured.

2.5.1 Flexure of the substrate-thin film bimorph

To determine the ME constants the mathematical model for bimorph is presented in this section. The model use the curvature of the cantilever as a common element between magnetostriction and capacitance. First, we calculate the curvature of a cantilever. Afterwards, we relate the curvature to the ME constants by minimizing the total energy of the sample. Finally, the curvature is related to the capacitance.

Curvature of the cantilever

The strain-stress tensors are related by:

$$\begin{pmatrix} \varepsilon_{xx} \\ \varepsilon_{yy} \\ \varepsilon_{zz} \\ \varepsilon_{yz} \\ \varepsilon_{zx} \\ \varepsilon_{xy} \end{pmatrix} = \begin{pmatrix} s_{11} & s_{12} & s_{13} & s_{14} & s_{15} & s_{16} \\ s_{21} & s_{22} & s_{23} & s_{24} & s_{25} & s_{26} \\ s_{31} & s_{32} & s_{33} & s_{34} & s_{35} & s_{36} \\ s_{41} & s_{42} & s_{43} & s_{44} & s_{45} & s_{46} \\ s_{51} & s_{52} & s_{53} & s_{54} & s_{55} & s_{56} \\ s_{61} & s_{62} & s_{63} & s_{64} & s_{65} & s_{66} \end{pmatrix} \begin{pmatrix} \sigma_{xx} \\ \sigma_{yy} \\ \sigma_{zz} \\ \sigma_{yz} \\ \sigma_{zx} \\ \sigma_{xy} \end{pmatrix} \tag{2.32}$$

where ϵ_{ij} are the strain components, s_{ij} are the elastic compliance constants, and σ_{ij} are the stress components of the material.

The s_{ij} matrix has 36 independent coefficients. To reduce the difficulty of this problem, we will make some assumptions [63]. First, we consider that the material will deform continuously. Thus, both stresses and strains are symmetric, which is $\varepsilon_{ij} = \varepsilon_{ji}$ and $\sigma_{ij} = \sigma_{ji}$. This assumption reduces the independent coefficients to 21. If the material is isotropic, which means that

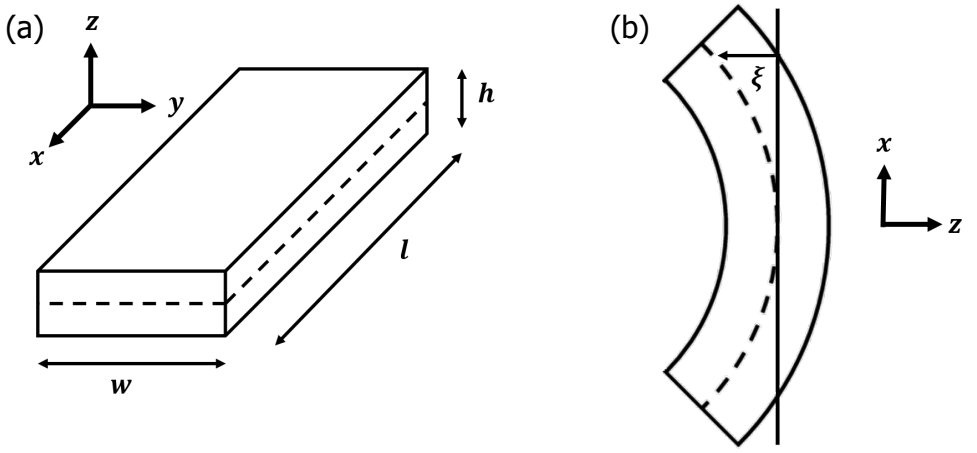

Figure 2.19: Axis coordinate system for the cantilever, long axis parallel to x. Dashed line indicates the neutral surface. (a) Dimensions of the cantilever. (b) Bent state, the displacement component z is taken as $\xi = -u_z$.

when is deformed it has the same behavior in any orientation, the independent coefficients is reduced to 2. The elastic compliance constants s_{11}, s_{12} and s_{44} are the only ones required to characterize the system. The elastic constants are intrinsic to materials, hence, the values of s_{11}, s_{12} and s_{44} will be taken from the literature.

To evaluate the stress of the cantilever we consider a rectangular plate. The dimensions of the plate are l, w and h (Fig. 2.19 a). The axes are chosen as follows: $x \parallel l$, $y \parallel w$ and $z \parallel h$. When the plate bends, the convex face suffers tension and the concave face suffers compression (Fig. 2.19 b). There is a layer between the faces that suffers no tension nor compression. This layer is called neutral surface (dashed line in Fig. 2.19). We consider that the lateral faces keep flat during the bending process. So, the planes xz and yz are normal to neutral surface [64]. No shear strain will be produced $\sigma_{xy} = 0$. Also, we consider that any point of the neutral surface is displaced by a distance ξ perpendicular to the xy plane. The displacement inside of the neutral surface is second order term respect to ξ [65], so, it will not be considered for the model. When an external force bends a plate, usually it does not alter locally the plate. The internal stresses of the cantilever are higher than the external force. Thus, we consider that $\sigma_{iz} = 0$ for $i = x, y, z$ [65].

The relation between strain and stress taking previous assumptions is:

$$\begin{pmatrix} \varepsilon_{xx} \\ \varepsilon_{yy} \\ \varepsilon_{zz} \\ \varepsilon_{yz} \\ \varepsilon_{zx} \\ \varepsilon_{xy} \end{pmatrix} = \begin{pmatrix} s_{11} & s_{12} & s_{12} & 0 & 0 & 0 \\ s_{12} & s_{11} & s_{12} & 0 & 0 & 0 \\ s_{12} & s_{12} & s_{11} & 0 & 0 & 0 \\ 0 & 0 & 0 & s_{44} & 0 & 0 \\ 0 & 0 & 0 & 0 & s_{44} & 0 \\ 0 & 0 & 0 & 0 & 0 & s_{44} \end{pmatrix} \begin{pmatrix} \sigma_{xx} \\ \sigma_{yy} \\ 0 \\ 0 \\ 0 \\ 0 \end{pmatrix} \tag{2.33}$$

The strain components, ϵ_{ij}, are related to the displacement vector $\overrightarrow{u} = (u_x, u_y, u_z)$ as:

$$\varepsilon_{ij} = \frac{1}{2}\left(\frac{\partial u_i}{\partial x_j} + \frac{\partial u_j}{\partial x_i}\right) \tag{2.34}$$

To obtain the vector displacement $\overrightarrow{u}$, we will use the shear strain components, ε_{ij} with $i \neq j$. By matching eqs. 2.34 and 2.33 for ε_{zx} we obtain:

$$\varepsilon_{zx} = \frac{1}{2}\left(\frac{\partial u_z}{\partial x} + \frac{\partial u_x}{\partial z}\right) = 0 \tag{2.35}$$

We integrate by z to solve the differential equation:

$$\frac{\partial u_x}{\partial z} = -\frac{\partial u_z}{\partial x} \tag{2.36}$$

$$u_x = -\frac{\partial u_z}{\partial x} z = \frac{\partial \xi}{\partial x} z \tag{2.37}$$

where $u_z = -\xi$ (Fig. 2.19 b). We can rewrite ε_{xx} as the partial derivative respect to x of eq. 2.37

$$\frac{\partial u_x}{\partial x} = \varepsilon_{xx} = \frac{\partial^2 \xi}{\partial x^2} z \tag{2.38}$$

The relation between the displacement, ξ, and the curvature $\kappa = 1/R$ (Fig. 2.20 a), is defined as [66]:

$$\kappa_x = \frac{\dfrac{\partial^2 \xi}{\partial x^2}}{\sqrt{1 + \left(\dfrac{\partial^2 \xi}{\partial x^2}\right)^2 + \left(\dfrac{\partial^2 \xi}{\partial y^2}\right)^2}} \simeq \frac{\partial^2 \xi}{\partial x^2} \tag{2.39}$$

The approximation taken is that the quadratic deformations are negligible compared to 1:

$$1 \gg \left(\frac{\partial^2 \xi}{\partial x^2}\right)^2 + \left(\frac{\partial^2 \xi}{\partial y^2}\right)^2 \tag{2.40}$$

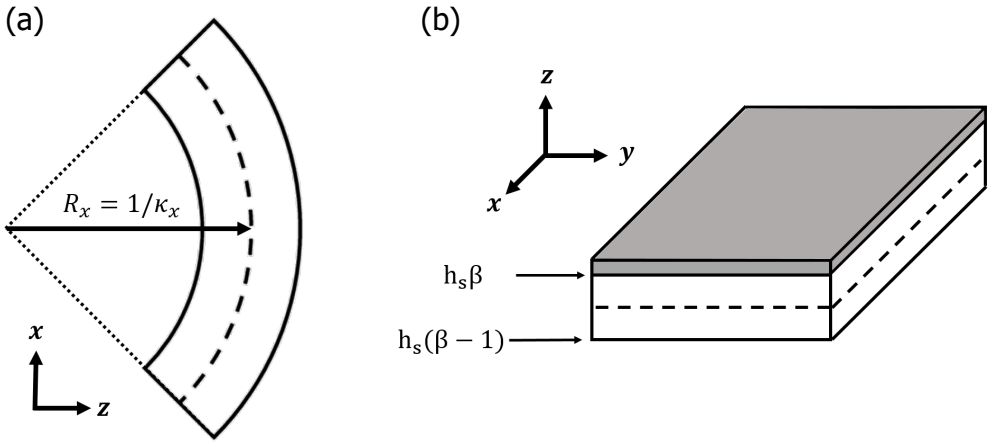

Figure 2.20: (a) Curvature of the neutral surface, κ_x. (b) Limits of β variable for volume integral of the substrate. Gray surface is the thin film.

So, by eqs. 2.38 and 2.39 the strain can be expressed as follows:

$$\varepsilon_{xx} = z\kappa_x \tag{2.41}$$

Alternatively, we can obtain the displacement vector u_y, and the strain ε_{yy} using the previous argumentation. From eq. 2.35, studying ε_{yz} instead of ε_{zx}, we get:

$$u_y = \frac{\partial \xi}{\partial y} z \tag{2.42}$$

$$\varepsilon_{yy} = z\kappa_y \tag{2.43}$$

Energy of the substrate

The cantilever is mainly made by the substrate. Thus, the energy of the substrate is ruled by the elastic contribution. The strain that the substrate will suffer when bending can be calculated from eqs. 2.33, 2.41, and 2.43:

$$\epsilon_{xx} = s_{11}\sigma_{xx} + s_{12}\sigma_{yy} = z\kappa_x \tag{2.44}$$

$$\epsilon_{yy} = s_{11}\sigma_{yy} + s_{12}\sigma_{xx} = z\kappa_y \tag{2.45}$$

Solving the system of equations for σ_{xx} and σ_{yy}:

$$\sigma_{xx} = \frac{s_{11}}{s_{11}^2 - s_{12}^2} z\kappa_x + \frac{s_{12}}{s_{12}^2 - s_{11}^2} z\kappa_y \tag{2.46}$$

$$\sigma_{yy} = \frac{s_{11}}{s_{11}^2 - s_{12}^2} z\kappa_y + \frac{s_{12}}{s_{12}^2 - s_{11}^2} z\kappa_x \tag{2.47}$$

We define the following constants:

$$S_\gamma = \frac{s_{11}}{s_{11}^2 - s_{12}^2} \tag{2.48}$$

$$S_{\gamma'} = \frac{s_{12}}{s_{12}^2 - s_{11}^2} \tag{2.49}$$

s_{11} and s_{12} values depends on the crystallographic direction of the substrate. The sub-index γ is refereed to specific directions, i.e. $S_{[100]}$ or $S_{[110]}$.

The eqs. 2.46, and 2.47 are simplified as:

$$\sigma_{xx} = \left(S_\gamma \kappa_x + S_{\gamma'} \kappa_y\right) z \tag{2.50}$$

$$\sigma_{yy} = \left(S_\gamma \kappa_y + S_{\gamma'} \kappa_x\right) z \tag{2.51}$$

$$\tag{2.52}$$

The elastic energy density is defined as:

$$e_{elas} = \frac{1}{2} \sigma_{ij} \varepsilon_{ij} \tag{2.53}$$

The elastic energy density of the substrate is:

$$e_{elas}^{subs} = \frac{1}{2} \left(S_\gamma \left(\kappa_x^2 + \kappa_y^2 \right) + 2 S_{\gamma'} \kappa_x \kappa_y \right) z^2 \tag{2.54}$$

The origin of our system of coordinates is taken at the interface between substrate and thin film. As we do not know where is the position of the neutral surface inside of the cantilever, we will use an auxiliary variable, β. The neutral surface only can move along z axis due to the symmetry of the problem. We redefine z variable as $z = \beta h_s$. Fig. 2.20 b shows how the β indicates the fraction of the cantilever where the neutral surface is located. For example, $\beta = 0.5$ indicates that the neutral surface is exactly on the middle of the substrate thickness.

To obtain the elastic energy we need to make a volume integral of the eq. 2.54. The limits of dz will be expressed as a function of β.

$$\begin{aligned} E^{subs} &= \int_{-l/2}^{l/2} \int_{-w/2}^{w/2} \int_{h_s(\beta-1)}^{h_s \beta} e_{elas}^{subs} \, dx \, dy \, dz = \\ &= \frac{A h_s^3}{6} \left(S_\gamma \left(\kappa_x^2 + \kappa_y^2 \right) + 2 S_{\gamma'} \kappa_x \kappa_y \right) \left(3\beta^2 - 3\beta + 1 \right) \end{aligned} \tag{2.55}$$

where A is the area of the sample ($l \times w$), and h_s is the thickness of the substrate.

Energy of the thin film

The total energy of the thin film considered here is the sum of two contributions: magnetoelastic and elastic ones. When the material is inside of a magnetic field, the magnetoelastic stress tries to change its shape. Also, this strain affects the elastic energy of the material because it is not in rest position, it is deformed. So, both contributions are studied to obtain the equilibrium energy, the one that minimises the energy.

We need to define the coordinate axis of our model. As the structure of FeGa is cubic, the Cartesian axes are chosen parallel to the axes of the cubic cell. The relation is: $x \parallel [100]$, $y \parallel [010]$ and $z \parallel [001]$. The magnetoelastic energy density for a cubic magnetostrictive material is defined as [67]:

$$\begin{aligned} e_{mel}^{cub} = B_0 \left(\epsilon_{xx} + \epsilon_{yy} + \epsilon_{zz}\right) + B_1 \left(\alpha_x^2 \epsilon_{xx} + \alpha_y^2 \epsilon_{yy} + \alpha_z^2 \epsilon_{zz}\right) + \\ + B_2 \left(\alpha_x \alpha_y \epsilon_{xy} + \alpha_y \alpha_z \epsilon_{yz} + \alpha_z \alpha_x \epsilon_{zx}\right) \end{aligned} \tag{2.56}$$

where B_i are the ME constants, ε_{ij} are the components of the strain tensor, and α_i are the direction cosines of $\mathbf{M}$ with respect to the cubic axes.

The elastic energy density for a cubic crystal is defined as [68]:

$$\begin{aligned} e_{elas}^{cub} = \frac{1}{2} c_{11} \left(\epsilon_{xx}^2 + \epsilon_{yy}^2 + \epsilon_{zz}^2\right) + c_{12} \left(\epsilon_{xx}\epsilon_{yy} + \epsilon_{yy}\epsilon_{zz} + \epsilon_{zz}\epsilon_{xx}\right) + \\ + \frac{1}{2} c_{44} \left(\epsilon_{xy}^2 + \epsilon_{yz}^2 + \epsilon_{zx}^2\right) \end{aligned} \tag{2.57}$$

where c_{ij} are the elastic stiffness constants.

The total energy density of the film is the sum of the magnetoelastic and elastic contributions, $e^{film} = e_{mel}^{cub} + e_{elas}^{cub}$. As the film is in the cantilever system, we can use the previous results to simplify the expression. We take $\epsilon_{xy} = \epsilon_{yz} = \epsilon_{zx} = 0$. Also, the magnetization will be applied in the plane of the film, so $\alpha_z = 0$.

$$\begin{aligned} e^{film} = B_0 \left(\epsilon_{xx} + \epsilon_{yy} + \epsilon_{zz}\right) + B_1 \left(\alpha_x^2 \epsilon_{xx} + \alpha_y^2 \epsilon_{yy}\right) + \frac{1}{2} c_{11} \left(\epsilon_{xx}^2 + \epsilon_{yy}^2 + \epsilon_{zz}^2\right) + \\ + c_{12} \left(\epsilon_{xx}\epsilon_{yy} + \epsilon_{yy}\epsilon_{zz} + \epsilon_{zz}\epsilon_{xx}\right) \end{aligned} \tag{2.58}$$

The equilibrium is reached when the strain out-of-plane is minimum.

$$\frac{\partial e^{film}}{\partial \varepsilon_{zz}} = B_0 + c_{11}\varepsilon_{zz} + c_{12} \left(\varepsilon_{xx} + \varepsilon_{yy}\right) = 0 \tag{2.59}$$

The strain ε_{zz} can be described as a function of longitudinal strains, ε_{xx} and ε_{yy}.

$$\varepsilon_{zz} = -\frac{B_0 + c_{12} \left(\varepsilon_{xx} + \varepsilon_{yy}\right)}{c_{11}} \tag{2.60}$$

Strain components obtained in 2.41 and 2.43 are now defined as a function of β by substituting $z = \beta h_s$.

$$\varepsilon_{xx} = h_s \beta \kappa_x \tag{2.61}$$

$$\varepsilon_{yy} = h_s \beta \kappa_y \tag{2.62}$$

Substituting in eq. 2.58 the expressions 2.60, 2.61 and 2.62. The energy density of the film can be described as a function of the curvature (κ_x, κ_y) and the position of the neutral surface (β).

$$\begin{aligned} e^{film} = & -\frac{B_0^2}{2c_{11}} + \frac{B_0 h_s \beta}{c_{11}} (c_{11} - c_{12}) (\kappa_x + \kappa_y) + B_1 h_s \beta \left(\alpha_x^2 \kappa_x + \alpha_y^2 \kappa_y \right) + \\ & + h_s^2 \beta^2 \left(\frac{c_{11}}{2} \left(\kappa_x^2 + \kappa_y^2 \right) + c_{12} \kappa_x \kappa_y - \frac{c_{12}^2}{2c_{c_{11}}} \left(\kappa_x^2 + \kappa_y^2 + \kappa_x \kappa_y \right) \right) \end{aligned} \tag{2.63}$$

The energy of the film is the volume integral $E^{film} = \iiint_V e^{film}$

$$\begin{aligned} E^{film} = A h_f \Bigg[& -\frac{B_0^2}{2c_{11}} + \frac{B_0 h_s \beta}{c_{11}} (c_{11} - c_{12}) (\kappa_x + \kappa_y) + B_1 h_s \beta \left(\alpha_x^2 \kappa_x + \alpha_y^2 \kappa_y \right) + \\ & + h_s^2 \beta^2 \left(\frac{c_{11}}{2} \left(\kappa_x^2 + \kappa_y^2 \right) + c_{12} \kappa_x \kappa_y - \frac{c_{12}^2}{2c_{c_{11}}} \left(\kappa_x^2 + \kappa_y^2 + \kappa_x \kappa_y \right) \right) \Bigg] \end{aligned} \tag{2.64}$$

where A is the area of the sample, and h_f is the thickness of the film.

Magnetostriction and curvature

The total energy of the system is the sum of the substrate and the film, $E^{total} = E^{subs} + E^{film}$

$$\begin{aligned} E^{total} = & \frac{A h_s^3}{6} \left(S_\gamma \left(\kappa_x^2 + \kappa_y^2 \right) + 2 S_{\gamma'} \kappa_x \kappa_y \right) \left(3\beta^2 - 3\beta + 1 \right) + \\ & + A h_f \Bigg[-\frac{B_0^2}{2c_{11}} + \frac{B_0 h_s \beta}{c_{11}} (c_{11} - c_{12}) (\kappa_x + \kappa_y) + B_1 h_s \beta \left(\alpha_x^2 \kappa_x + \alpha_y^2 \kappa_y \right) + \\ & + h_s^2 \beta^2 \left(\frac{c_{11}}{2} \left(\kappa_x^2 + \kappa_y^2 \right) + c_{12} \kappa_x \kappa_y - \frac{c_{12}^2}{2c_{c_{11}}} \left(\kappa_x^2 + \kappa_y^2 + \kappa_x \kappa_y \right) \right) \Bigg] \end{aligned} \tag{2.65}$$

To obtain the position of the neutral surface, we minimise the total energy respect to β. This is $\dfrac{\partial E^{total}}{\partial \beta} = 0$. The value of β obtained is described as a

ratio between two expressions, P_1 and P_2.

$$\beta = \frac{P_1}{P_2} \tag{2.66}$$

$$\begin{aligned} P_1 = & -2B_0 h_f \left(c_{11} - c_{12}\right)\left(\kappa_x + \kappa_y\right) - 2B_1 c_{11} h_f \left(\alpha_x^2 \kappa_x + \alpha_y^2 \kappa_y\right) + \\ & + c_{11} h_s^2 \left[S_\gamma \left(\kappa_x^2 + \kappa_y^2\right) + 2S_{\gamma'} \kappa_x \kappa_y\right] \end{aligned} \tag{2.67}$$

$$\begin{aligned} P_2 = & 2h_f h_s \left[\left(c_{11}^2 - c_{12}^2\right)\left(\kappa_x^2 + \kappa_y^2\right) + 2\kappa_x \kappa_y \left(1 + c_{11} c_{12}\right)\right] + \\ & + 2c_{11} h_s^2 \left[S_\gamma \left(\kappa_x^2 + \kappa_y^2\right) + 2S_{\gamma'} \kappa_x \kappa_y\right] \end{aligned} \tag{2.68}$$

In our system $h_s/h_f \sim 10^4$. So, we consider that $h_s \gg h_f$. Then, eq. 2.66 can be simplified:

$$\beta = \frac{c_{11} h_s^2 \left[S_\gamma \left(\kappa_x^2 + \kappa_y^2\right) + 2S_{\gamma'} \kappa_x \kappa_y\right]}{2c_{11} h_s^2 \left[S_\gamma \left(\kappa_x^2 + \kappa_y^2\right) + 2S_{\gamma'} \kappa_x \kappa_y\right]} = \frac{1}{2} \tag{2.69}$$

The value of $\beta = 0.5$ indicates that the neutral surface is exactly at the middle of the substrate thickness.

To obtain the curvature in x direction, we need to calculate the minimum of the energy for κ_x ($\partial E^{total}/\partial \kappa_x = 0$). The result of the partial derivation and the substitution of $\beta = 0.5$ is:

$$\kappa_x = -\frac{6B_0 h_f \left(c_{11} - c_{12}\right) + 6B_1 c_{11} h_f \alpha_x^2 + \kappa_y h_s \left[S_{\gamma'} c_{11} h_s + 3h_f c_{12} \left(c_{11} - c_{12}\right)\right]}{S_\gamma c_{11} h_s^2 + 3h_f h_s \left(c_{11}^2 - c_{12}^2\right)} \tag{2.70}$$

If it can be assumed that $\kappa_y \simeq 0$, it is due to the cantilever clamped in the yz plane, and the large L/w ratio. The main curvature is given by κ_x. Also, the previous condition of using $h_s \gg h_f$. Taking these approximations the curvature κ_x is:

$$\kappa_x = -\frac{6B_0 h_f \left(c_{11} - c_{12}\right)}{S_\gamma c_{11} h_s^2} - \frac{6B_1 h_f \alpha_x^2}{S_\gamma h_s^2} \tag{2.71}$$

The curvature of the cantilever in x direction is the sum of a constant term and other proportional to B_1. To obtain B_1 we need to define two values of the curvature. When the magnetic field is applied parallel to x ($\alpha_x = 1$), the curvature is called $\kappa_{x\|}$. When the magnetic field is applied perpendicular to x, this is y direction because at the beginning of the model we consider that the magnetic field is applied in-plane ($\alpha_z = 0$). This curvature is called

$\kappa_{x\perp}(\alpha_x = 0)$.

$$\kappa_{x\parallel} = -\frac{6B_0 h_f\,(c_{11}-c_{12})}{S_\gamma c_{11} h_s^2} - \frac{6B_1 h_f}{S_\gamma h_s^2} \tag{2.72}$$

$$\kappa_{x\perp} = -\frac{6B_0 h_f\,(c_{11}-c_{12})}{S_\gamma c_{11} h_s^2} \tag{2.73}$$

Finally, we can obtain B_1 from the difference between the curvature obtained when the magnetic field is parallel and perpendicular to the long axis of the cantilever.

$$\kappa_{x\parallel} - \kappa_{x\perp} = -\frac{6B_1 h_f}{S_\gamma h_s^2} \tag{2.74}$$

$$B_1 = -\frac{S_\gamma h_s^2}{6h_f}\left(\kappa_{x\parallel} - \kappa_{x\perp}\right) \tag{2.75}$$

One important note about eq. 2.75 is that the coordinate axes are parallel to the cubic coordinates of the crystalline thin film. B_1 is related to the deformation along the cubic coordinates, i.e. FeGa[100]. In our case, the epitaxy satisfies that FeGa[100] ∥ MgO[110]. This means that if we want to measure B_1, the substrate direction parallel to x has to be [110].

Thin film rotated axes

B_2 is related to shear strain under applied magnetic field. But, due to the cantilever constraints, B_2 can not be obtained if the cubic coordinates are parallel to the system coordinate (FeGa[100] ∥ x). If the thin film is grown in such way that FeGa[110] is parallel to x direction it will not be affected by the cantilever constraints and B_2 will be obtained. This fact can be achieved experimentally by using substrates with the direction MgO[100] ∥ x.

To calculate B_2 we proceed to obtain the curvature of the cantilever as the previous section. But first, we need to rotate the thin film coordinates. The new axes of the thin film are called x'. The strain matrix in this rotated system is made by a change of basis [69].

$$[\varepsilon_{ij}] = [R_z]^T [\varepsilon_{i'j'}][R_z] \tag{2.76}$$

being R_z the rotation matrix

$$R_z(\theta) = \begin{pmatrix} \cos(\theta) & -\sin(\theta) & 0 \\ \sin(\theta) & \cos(\theta) & 0 \\ 0 & 0 & 1 \end{pmatrix} \tag{2.77}$$

Substituting $\theta = 45°$ in eq. 2.76:

$$\begin{pmatrix} \varepsilon_{xx} & \varepsilon_{xy} & \varepsilon_{xz} \\ \varepsilon_{xy} & \varepsilon_{yy} & \varepsilon_{yz} \\ \varepsilon_{zx} & \varepsilon_{yz} & \varepsilon_{zz} \end{pmatrix} = \begin{pmatrix} \frac{1}{\sqrt{2}} & \frac{1}{\sqrt{2}} & 0 \\ -\frac{1}{\sqrt{2}} & \frac{1}{\sqrt{2}} & 0 \\ 0 & 0 & 1 \end{pmatrix} \begin{pmatrix} \varepsilon_{x'x'} & \varepsilon_{x'y'} & \varepsilon_{x'z'} \\ \varepsilon_{x'y'} & \varepsilon_{y'y'} & \varepsilon_{y'z'} \\ \varepsilon_{z'x'} & \varepsilon_{y'z'} & \varepsilon_{z'z'} \end{pmatrix} \begin{pmatrix} \frac{1}{\sqrt{2}} & -\frac{1}{\sqrt{2}} & 0 \\ \frac{1}{\sqrt{2}} & \frac{1}{\sqrt{2}} & 0 \\ 0 & 0 & 1 \end{pmatrix} \tag{2.78}$$

The strain components are now defined by the new axes.

$$\varepsilon_{xx} = \frac{1}{2}\left(\varepsilon_{x'x'} + \varepsilon_{y'y'}\right) + \varepsilon_{x'y'} \tag{2.79}$$

$$\varepsilon_{yy} = \frac{1}{2}\left(\varepsilon_{x'x'} + \varepsilon_{y'y'}\right) - \varepsilon_{x'y'} \tag{2.80}$$

$$\varepsilon_{xy} = \frac{1}{2}\left(-\varepsilon_{x'x'} + \varepsilon_{y'y'}\right) \tag{2.81}$$

$$\varepsilon_{zx} = \frac{\sqrt{2}}{2}\left(\varepsilon_{z'x'} + \varepsilon_{y'z'}\right) \tag{2.82}$$

$$\varepsilon_{yz} = \frac{\sqrt{2}}{2}\left(-\varepsilon_{z'x'} + \varepsilon_{y'z'}\right) \tag{2.83}$$

$$\varepsilon_{zz} = \varepsilon_{z'z'} \tag{2.84}$$

The cosine directors of magnetization are also rotated 45º.

$$\alpha_x = \frac{1}{\sqrt{2}}\alpha_{x'} + \frac{1}{\sqrt{2}}\alpha_{y'} \tag{2.85}$$

$$\alpha_y = \frac{-1}{\sqrt{2}}\alpha_{x'} + \frac{1}{\sqrt{2}}\alpha_{y'} \tag{2.86}$$

$$\alpha_z = \alpha_{z'} \tag{2.87}$$

The assumptions taken in our model are the same as explained in the previous section.

$$\varepsilon_{x'y'} = 0 \tag{2.88}$$

$$\varepsilon_{z'x'} = 0 \tag{2.89}$$

$$\varepsilon_{y'z'} = 0 \tag{2.90}$$

$$\alpha_{z'} = 0 \tag{2.91}$$

The energy density of the rotated thin film is:

$$\begin{aligned} e^{film}_{\theta=45°} = {} & B_0\left(\varepsilon_{x'x'} + \varepsilon_{y'y'} + \varepsilon_{z'z'}\right) + \frac{B_1}{2}\left(\varepsilon_{x'x'} + \varepsilon_{y'y'}\right)\left(\alpha_x^2 + \alpha_y^2\right) + \\ & + \frac{B_2}{2}\left(\varepsilon_{x'x'} - \varepsilon_{y'y'}\right)\left(\alpha_x^2 - \alpha_y^2\right) + \frac{c_{11}}{4}\left(\left(\varepsilon_{x'x'} + \varepsilon_{y'y'}\right)^2 + 2\varepsilon_{z'z'}^2\right) + \\ & + \frac{c_{12}}{4}\left(\left(\varepsilon_{x'x'} + \varepsilon_{y'y'}\right)^2 + 4\varepsilon_{z'z'}\left(\varepsilon_{x'x'} + \varepsilon_{y'y'}\right)\right) \end{aligned} \tag{2.92}$$

The total energy of the system is calculated as $E^{total} = E^{subs} + E^{film}_{\theta=45^\circ}$. The neutral surface obtained is $\beta = 0.5$, as before. When the energy is minimised respect to curvature in x, the constant B_2 is obtained:

$$B_2 = -\frac{S_\gamma h_s^2}{6h_f}\left(\kappa_{x\parallel} - \kappa_{x\perp}\right) \tag{2.93}$$

B_2 can be obtained when the cubic axes are rotated 45º respect to the coordinate system of the cantilever. We only need to measure the difference between the curvature when the magnetic applied field is parallel and perpendicular to the long axis of the cantilever.

$\mathbf{S}_\gamma$ for MgO substrate

The value of S_γ is essential to obtain B_1 and B_2. S_γ indicates the elastic compliance of the cantilever in the γ direction.

For our system, the elastic compliance constants s_{ij} satisfies that [68]

$$s_{11} = \frac{1}{E_\gamma} \tag{2.94}$$

$$s_{12} = -s_{11}\nu_\gamma = -\frac{\nu_\gamma}{E_\gamma} \tag{2.95}$$

where E_γ and ν_γ are the Young's modulus and Poisson's ratio in the γ direction, respectively.

We recall the definition of S_γ, and we substitute the expression with E_γ and ν_γ

$$S_\gamma = \frac{s_{11}}{s_{11}^2 - s_{12}^2} = \frac{E_\gamma}{1-\nu_\gamma^2} \tag{2.96}$$

The elastic compliance constant of the cantilever is now described as a function of the Young's modulus and Poisson's ratio. The general form for these constants is [68]:

$$E_\gamma = \frac{1}{s_{11} - \left[2\left(s_{11} - s_{12}\right) - s_{44}\right]\Gamma} \tag{2.97}$$

$$\nu_\gamma = -\frac{2s_{12} + \left[2\left(s_{11} - s_{12}\right) - s_{44}\right]\Gamma}{2\left\{s_{11} - \left[2\left(s_{11} - s_{12}\right)\right]\Gamma\right\}} \tag{2.98}$$

where $\Gamma = u^2v^2 + v^2w^2 + w^2u^2$. Being, u, v and w the unit vectors.

Young's modulus and Poisson's ratio for [100] direction ($\Gamma = 0$) is:

$$E_{[100]} = \frac{1}{s_{11}} \tag{2.99}$$

$$\nu_{[100]} = -\frac{s_{12}}{s_{11}} \tag{2.100}$$

Young's modulus and Poisson's ratio for [110] direction ($\Gamma = 0.25$) is:

$$E_{[110]} = \frac{-1}{s_{11} - 2s_{12} - s_{44}} \tag{2.101}$$

$$\nu_{[110]} = \frac{2s_{11} - s_{44}}{2s_{11} - 4s_{12} - 2s_{44}} \tag{2.102}$$

Usually, the experimental data taken from articles are the elastic stiffness constants, c_{ij}, instead of the elastic compliance constants, s_{ij}. The relations between the relevant s_{ij} and c_{ij} are given by:

$$s_{11} = \frac{c_{11}^2 - c_{12}^2}{c_{11}^3 - 3c_{11}c_{12}^2 + 2c_{12}^3} \tag{2.103}$$

$$s_{12} = \frac{-c_{12}\left(c_{11} - c_{12}\right)}{c_{11}^3 - 3c_{11}c_{12}^2 + 2c_{12}^3} \tag{2.104}$$

$$s_{44} = \frac{1}{c_{44}} \tag{2.105}$$

The values S_γ calculated for MgO are shown in Table 2.1. These values allows us to calculate the B_1 and B_2 constants. The unique value to be experimentally determined is the curvature in x.

$$B_1 = -\frac{S_{[110]}h_s^2}{6h_f}\left(\kappa_{x\parallel} - \kappa_{x\perp}\right) \tag{2.106}$$

$$B_2 = -\frac{S_{[100]}h_s^2}{6h_f}\left(\kappa_{x\parallel} - \kappa_{x\perp}\right) \tag{2.107}$$

c_{11}	c_{12}	c_{44}	$E_{[100]}$	$\nu_{[100]}$	$E_{[110]}$	$\nu_{[110]}$	$S_{[100]}$	$S_{[110]}$
300	93.6	147	255.48	0.24	313.25	0.18	270.79	323.56

Table 2.1: Data for MgO. All units are GPa. c_{ij} is taken from [70]. E_γ, ν_γ and S_γ are calculated from eqs. 2.99 - 2.102 and 2.96, respectively.

Capacitance

The curvature of the cantilever is measured by the capacitance technique. The cantilever has two states, relaxed and bent. The cantilever is relaxed when

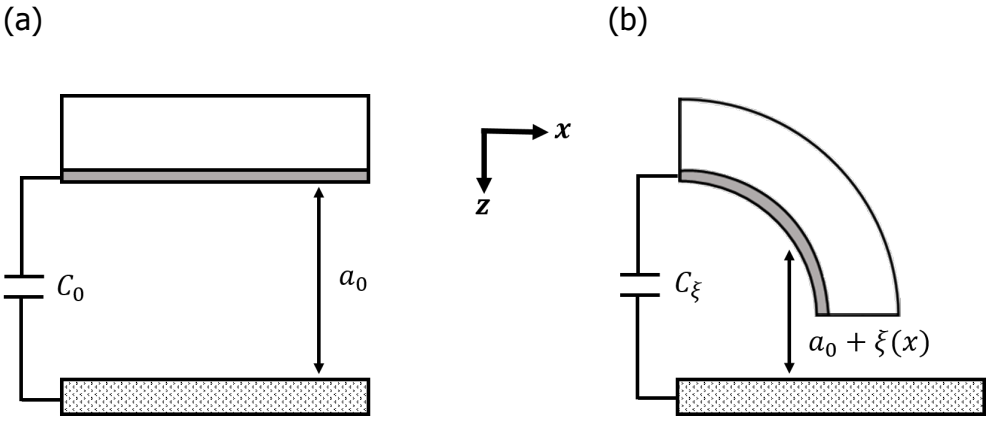

Figure 2.21: Two states of cantilever. (a) Relaxed state, the distance between thin film (gray) and fixed plate (dashed) is a_0. The capacitance measured is C_0. (b) Bent state, the distance between plates is $a_0 + \xi(x)$. The capacitance is C_ξ.

there is no applied magnetic field (Fig. 2.21 a), and bent when it is applied (Fig. 2.21 b). We can use the thin film as a plate of a plane-parallel capacitor. The difference in capacitance between the two states can be related to the curvature in x direction.

The capacitance of a plane-parallel capacitor is defined as:

$$C_0 = \int_0^{L_x} \int_0^{L_y} \frac{\varepsilon_0}{a_0}\, dx\, dy = \frac{\varepsilon_0 A}{a_0} \tag{2.108}$$

where ϵ_0 is the vacuum permittivity, A is the area of the capacitor, and a_0 is the distance between the plates. C_0 is considered the capacitance for relaxed position.

The initial distance between plates can be obtained from eq.2.108

$$a_0 = \frac{\varepsilon_0 A}{C_0} \tag{2.109}$$

For bent state, we recall eq.2.39 where the curvature is related to the z displacement. Curvature of the cantilever faces is considered the same as the neutral surface. We can obtain the deflection of the cantilever along x direction by integration.

$$\frac{\partial^2 \xi}{\partial x^2} = \kappa_x \tag{2.110}$$

$$\xi(x) = \frac{\kappa_x}{2} x^2 \tag{2.111}$$

For bent state, the distance between plates is $a_0 + \xi(x)$. The capacitance for this state is:

$$\begin{aligned} C_\xi &= \int_0^{L_x}\int_0^{L_y} \frac{\varepsilon_0}{a_0+\xi}\,dx\,dy = \int_0^{L_x}\int_0^{L_y} \frac{\varepsilon_0}{a_0+\frac{\kappa_x}{2}x^2}\,dx\,dy = \\ &= L_y\varepsilon_0\sqrt{\frac{2}{a_0\kappa_x}}\tan^{-1}\left(\frac{L_x^2\kappa_x}{2a_0}\right) \end{aligned} \tag{2.112}$$

The curvature is small enough to do a Maclaurin series of $\tan^{-1}$ at 3rd order.

$$\tan^{-1}\left(\sqrt{\frac{L_x^2\kappa_x}{2a_0}}\right) \simeq \sqrt{\frac{L_x^2\kappa_x}{2a_0}} - \frac{1}{3}\left(\sqrt{\frac{L_x^2\kappa_x}{2a_0}}\right) \tag{2.113}$$

Substituting eqs.2.109 and 2.113 into 2.112 we obtain:

$$C_\xi = \frac{6a_0 - L_x^2\kappa_x}{6a_0^2}A\varepsilon_0 = C_0 - \frac{C_0^2L_x^2\kappa_x}{6\varepsilon_0 A} \tag{2.114}$$

We can define the difference in capacitance between bent and relaxed state as $\Delta C_x = C_\xi - C_0$. The curvature calculated is:

$$\kappa_x = -\frac{6\varepsilon_0 A\Delta C_x}{L_x^2C_0^2} \tag{2.115}$$

The expression of κ_x allows us to determine the ME constants by substituting 2.115 into eqs.2.106 and 2.107.

$$B_1 = -\frac{S_{[110]}h_s^2\varepsilon_0 A}{h_f L_x^2C_0^2}\left(\Delta C_{x\parallel} - \Delta C_{x\perp}\right) \tag{2.116}$$

$$B_2 = -\frac{S_{[100]}h_s^2\varepsilon_0 A}{h_f L_x^2C_0^2}\left(\Delta C_{x\parallel} - \Delta C_{x\perp}\right) \tag{2.117}$$

Experimentally, the ME constants can be obtained by measuring the difference in capacitance between applied magnetic field parallel and perpendicular to the cantilever. B_1 is obtained by using a MgO substrate with [110] parallel to x direction. For B_2, it is done but MgO[100] $\parallel x$.

2.5.2 Experimental method: capacitive technique

The cantilever is experimentally mounted on a capacitance cell. The complexity on the design of the capacitance cell relies on the excessive sensitivity

needed to measure the curvature of the cantilever. As one can think, the curvature produced by a 20 nm film is extremely small. We can rewrite eq.2.116 by using eq. 2.109 as:

$$\left(\Delta C_{x\parallel} - \Delta C_{x\perp}\right) = -\frac{B_1 h_f \varepsilon_0 A}{S_{[110]} h_s^2} \left(\frac{L_x}{a_0}\right)^2 \tag{2.118}$$

To measure easily ΔC_x we need to maximize its value. Thus, the distance a_0 needs to be minimized and L_x maximized. Intuitive, a cantilever closer to the fixed plate increases the value of capacitance, and longer cantilever leads to major curvature. Experimentally, a closer a_0 leads to a risk of dead short if the film touches the fixed plate, and longer samples depend on the manufacturer. Taking approximations, maximum B_1 for FeGa is $-15.6\,\mathrm{MJ/m^3}$ [18] and for our capacitance cell $a_0 = 60\,\mu\mathrm{m}$ and $L_x = 9\,\mathrm{mm}$. The result indicates that ΔC_x is in the order of $\sim 100\,\mathrm{aF}$ if FeGa is in its maximum peak of magnetostriction. For the design of the capacitance cell is essential to avoid or minimize the effect due to parasitic capacitance. If this parasitic capacitance is greater than $10^{-5}\,\mathrm{pF}$ the signal is masked and the obtained signal is noise. This effect appears between the electrodes of the capacitance cell and the ground. Also, the coaxial wires that joint the electrodes to the capacitance bridge (system of detection) can present parasitic capacitance.

The cell has two main parts: clamping and fixed plate. The clamping part is used to hold the sample in such a way that it stays as a cantilever. This part also needs to lead positive voltage to the thin film. The fixed plate needs to stay at negative voltage and avoid border effects from the difference between the areas of sample and cell. The capacitance is measured between film and fixed plate.

The first experimental capacitance cell built in this lab was made by Dr. M. Ciria [71]. The material used was copper. This cell was designed to work at temperatures from 3.2 K to 300 K, and high applied magnetic field, 0 to 12 T. Afterwards, the cell was revised by Dr. C. Abadía [72] using copper deposited over fused quartz. The last improvement in capacitance cells was made by Dr. L. Benito [73]. The cell was built in MACOR® a machinable glass ceramic. This ceramic has a coefficient of thermal expansion more similar to Cu than fused quartz. MACOR® improves the quartz capacitance cell performance because is able to bear more cycles of changing temperatures without the detaching of deposited copper.

For this thesis, a new capacitance cell was specifically designed and built. The previous cell has a disadvantage related to the MACOR® piece. This piece was glued to a plinth of aluminium, so it was not strongly fixed and oscillated around the equilibrium position. Besides, the piece was too high respect to its

base, leading to considerable angle of inclination. The distance a_0 is strongly dependent on the inclination of MACOR® piece. Thus, some measures were not reproducible because the MACOR® piece was not always in the same position, which was undesirable.

Fig. 2.22 a shows the experimental capacitance cell built. It consists in two blocks mounted over a plinth of aluminium. There is one block called active, which is the responsible to lead the voltage to the sample. The other block is called passive, which has the fixed plate of the capacitor. The blocks were designed in a printed circuit board (PCB). PCB was chosen due to several factors: the metal top layer is copper, is machinable, and the flatness of its surface. The copper has a high conductivity, which is essential to reduce the resistance present in the circuit. Also, PCB is prepared to be welded easily. Thus, there are no adhesives in the capacitance cell, all elements are welded or screwed more easily than by using a MACOR® piece.

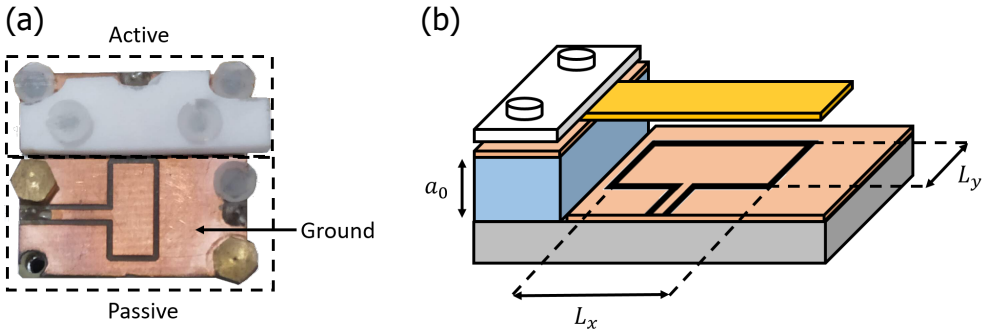

Figure 2.22: (a) Photo of the experimental capacitance cell. Active and passive blocks are marked in dashed lines. Ground voltage is also pointed. (b) Schematic representation of the capacitance cell. The colors indicate the material used: orange for cantilever, brown for copper, gray for aluminium plinth, blue for separator and white for MACOR® . The distance a_0 (exaggerated for clarity) and area, A, of the capacitor ($L_x \times L_y$) are also noted.

Fig. 2.22 b shows the parts that made each block. The plinth of aluminium is mechanized to align its screws with the holes of the PCB. The active block has four holes. Two of them are designed to fix the active block to the plinth of aluminium. The other holes are designed to fix a piece of MACOR® . This piece is used to clamp the sample and ensure that the metallic surface of the sample is homogeneously in contact with the copper of the active block. The copper is welded to the positive bias of the capacitance bridge. The distance a_0 is achieved by intercalating a separator of $\sim 60\,\mu$m between the active block and the plinth.

The passive block has a lithographed design. It is a rectangle of area $A = 9\,\text{mm} \times 4\,\text{mm} = 36\,\text{mm}^2$ ($A = L_x \times L_y$). This is the fixed plate of the capacitor. The area has to be equal or smaller respect to the area of the cantilever. This condition ensures that the capacitor uses all the area of its fixed plate. The voltage is leaded to this area by a thin line outside of the measurement area, welded to the negative bias of the capacitance bridge. The capacitor made by the sample and the fixed plate is influenced by the electrostatic border effect. To reduce this effect, the rectangular area is surrounded by a bucking electrode, but the sample not. The electric field is not perfectly straight from the borders of the sample to the fixed plate. The lines are curved in these parts. For example, the border effects of a capacitor of $A = 300\,\text{mm}^2$ and $a_0 = 50\,\mu\text{m}$, can change the value of the capacitance between 5% and 3% [74, 75].

Another effect to keep in mind is the thermal stability. When we manipulate the cell to place a sample, the sample is at a different temperature with respect to the cell. A slight difference in temperature can lead to, for example, a closer distance between the sample and the fixed plate. So, the value of C_0 will be time-dependent as the temperature of the sample reaches the temperature of the capacitance cell. This effect is predominantly linear with time. So, if we start to measure from the beginning, the values of ΔC will be over a linear function because the reference value C_0 is varying. To ensure that the system is in thermal equilibrium, we usually wait for 15 minutes before the measure. By this means, we consider that C_0 and ΔC have their stationary values.

During the capacitance measurements, the cell is near to other metallic objects. To avoid external electrical effects that can disturb the capacitance measurement, a metallic capsule was designed and fabricated to shield the cell (Fig. 2.23 a). The capsule is made by aluminium. It is designed to connect the cell to coaxial wires from the capacitance bridge. The whole capsule is grounded. The parasitic currents are reduced because the coaxial wires, cell and capsule share a circuit with no electrical loops. Fig. 2.23 b shows the capacitance cell inside the capsule, the volume available is a cylinder with a radius of 14 mm and a height of 25 mm. It is designed to connect easily different cells. Capacitance cells of different A or a_0 can be interchangeable to study samples at different conditions. Also, at its base there is a holder that allows the capsule to be screwed to optical equipment. As we need to put the capacitance cell inside a magnetic field and keep it stabilised, an optical equipment was used.

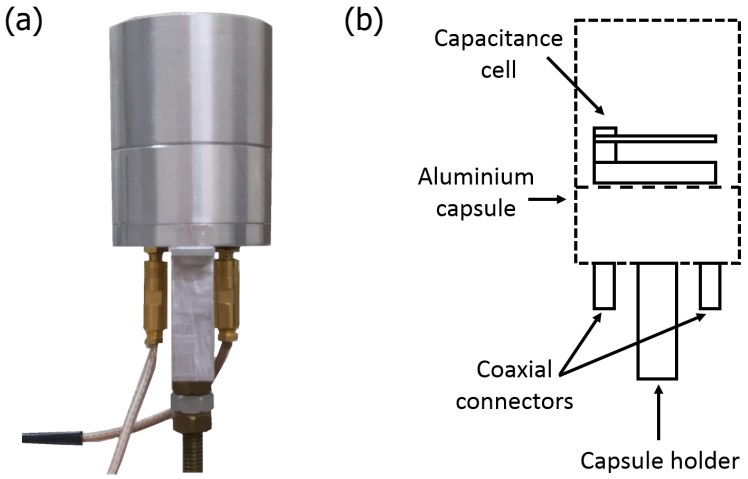

Figure 2.23: (a) Photo of the experimental aluminum capsule. (b) Schematic section view of the aluminum capsule. The capacitance cell is mounted parallel to its base. Inside of the base there are wires that connect the capacitance cell to coaxial connectors. Capsule holder is perpendicular to the base and can be screwed to optical equipment.

Capacitance bridge

There are several methods to measure capacitance: oscillating, resonant, charge-discharge, and AC bridge [76]. In this thesis, we use the AC bridge method because of its high resolution and low sensitivity to parasitic capacitances.

Fig. 2.24 shows the configuration scheme of the ideal AC bridge employed (Andeen-Hagerling moel AH2500A) [77]. Where Z_p is the unknown impedance. C_p is the capacitance that we need to measure, R_p is the value of the resistive component, C_{ref} is a variable capacitor standard and R_{ref} is a variable resistance standard. These references are needed to obtain the values of C_p and R_p in absolute units. Other two branches are at voltages V_1 and V_2, respectively. When the bridge is at equilibrium (this is when $Z_p = Z_{ref}$), the voltage in the detector is zero and the values of C_p and R_p are:

$$C_p = \frac{V_1}{V_2} C_{ref} \tag{2.119}$$

$$R_p = \frac{V_2}{V_1} R_{ref} \tag{2.120}$$

Fig. 2.25 shows the electronic block diagram of the experimental set-up. An exhaustive description can be found in [74]. The basis of operation of this

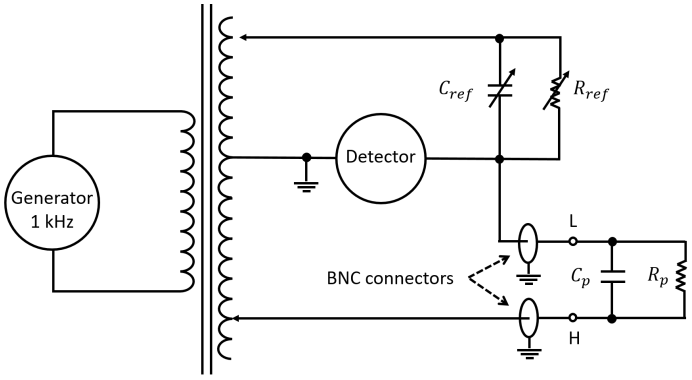

Figure 2.24: Scheme of an ideal capacitance bridge.

bridge consists in employing as the reference signal, the same as the used to feed the passive branches of the bridge. The disequilibrium signal is carried to the detector. The first stage is the preamplification. The current is amplified and, then, goes through a phase detector. The detection enables the possibility of compare the in-phase and quadrature signal respect to the reference signal. Z_p and the resistivity losses are obtained by this method. The system used to equilibrate the signal and the reference signal can be external. The number of coils in S_1 and S_2 can be changed to vary the voltage of each active branch. The change in the number of coils can be made automatic by a microprocessor. When the coils of a transformer are strongly coupled between them, the output impedance is low. Then, the effect of the parasitic impedances between both output transformer terminals and ground, the coaxial wires, and between ground and the electrodes of the capacitance cell is only noticeable if the coaxial wires are long. We use coaxial wires of 20 cm to minimize this parasitic capacitance induced.

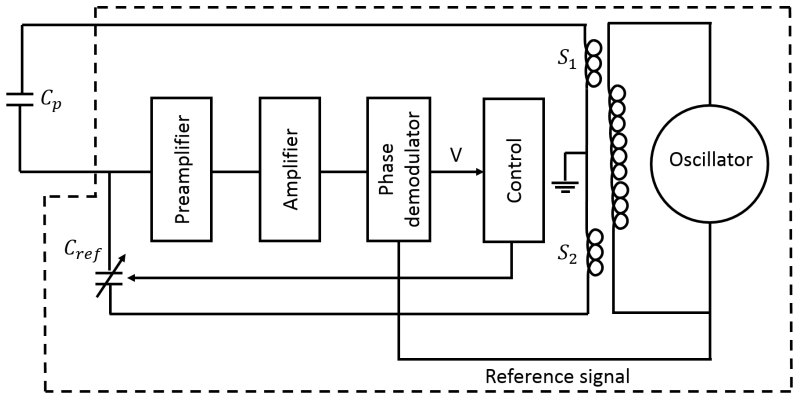

Figure 2.25: Electronic block diagram of the capacitance bridge set-up.

The capacitance bridge used is Andeen-Hagerling model AH2500A. This model incorporates internal capacitors thermostatted, automatic equilibrium system, remote control (port IEEE and RS-232) and simultaneous measure of resistive and capacity components of Z_p. This bridge works in equilibrium by the system control of a specific configuration of internal standards. The voltage is the same in each passive branch, which permits to increase the accuracy in C_p.

Magnetic set-up

The capacitance cell needs applied magnetic field to bend the cantilever due to the magnetostriction. The magnetic field needed to saturate FeGa is $\sim$ 500 Oe. At the beginning of this thesis, the magnetic field was applied by an electromagnet. Later on, a new set-up was designed and fabricated to enhance the magnetostriction measurements. This set-up consists on two permanent ferrite magnets in a dipole configuration mounted over a rotary plate. By using this set-up, the measurements were more reliable and precise than with the previous electromagnet set-up.

- **Electromagnet set-up**

Fig. 2.26 a shows the set-up, which consists in an electromagnet and a hall sensor. The electromagnet can apply magnetic field up to 2.5 KOe sinusoidally. The Hall sensor measures H and transfers that information to the acquisition card of the computer. The acquisition program was coded in LabVIEW. The program needs two inputs: capacitance (obtained by capacitance bridge), and applied magnetic field (obtained by Hall sensor). The user's interface can be seen in Fig. 2.26 b. We can delay the start to ensure thermal stabilization. Also, the acquisition velocity is set to make plots with the density points desired. The program automatically plots the data in the graph allowing to analyse in real time the measure.

The capacitance cell is placed between the magnetic poles by using an optical arm. There are two measures needed, parallel and perpendicular to the magnetic field generated by the electromagnet. Fig. 2.27 shows a typical measure made by using the electromagnet. The magnetoelastic stress is measured at saturation as we have seen, $\alpha_x = 1$ for parallel and $\alpha_y = 1$ for perpendicular. To obtain B_1 and B_2, the only experimental value needed is the difference between the two configurations at saturation, $\Delta C_{x\parallel} - \Delta C_{x\perp}$ (Fig. 2.27 orange arrow).

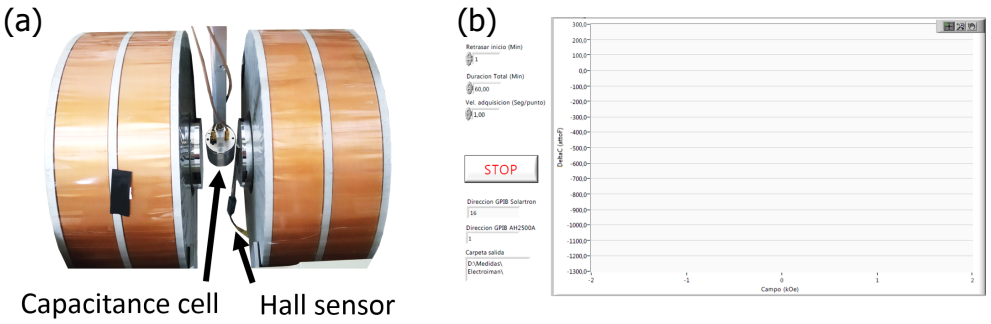

Figure 2.26: (a) Photo of electromagnet set-up. Arrows indicate the capacitance cell and hall sensor positions. (b) User's interface of the LabVIEW program.

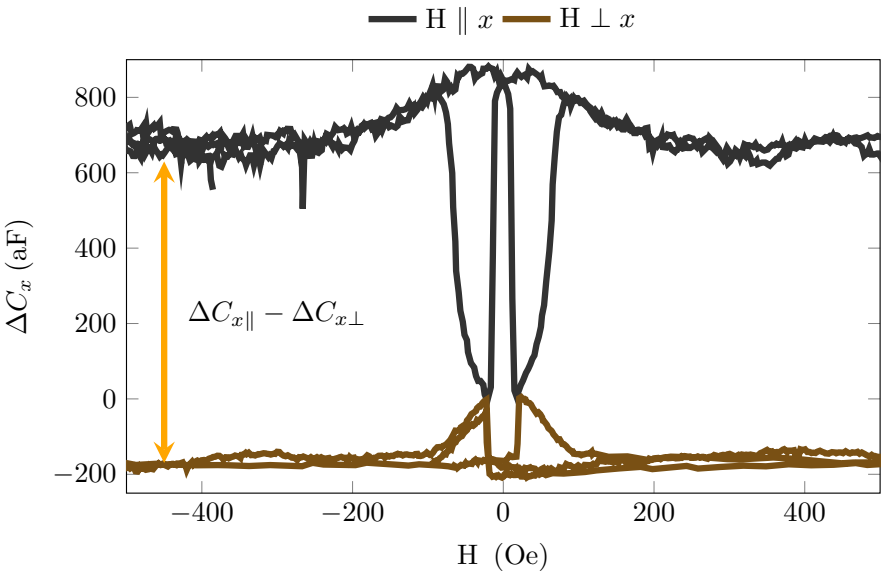

Figure 2.27: Typical magnetostriction plot for electromagnet set-up. $\Delta C_x = C_\xi - C_0$, being the difference between bent (C_ξ) and relax state (C_0) for the cantilever. Two measures are plot: applied magnetic field parallel (black line) and perpendicular (dark ochre) to the cantilever long axis. Orange arrow indicates the difference between two configurations at saturation.

- **Dipole set-up**

In the work of improving the previous techniques used to measure magnetostriction, we designed and fabricated a new magnetic set-up. This set-up consists in two ferrite permanent magnets in a dipole configuration. The magnetic field inside of the dipole is $\sim 1\,\mathrm{kOe}$, enough to saturate FeGa samples. The magnetic field is also homogeneous between the magnets. Fig. 2.28 a shows the capacitance cell in the middle of the dipole set-up. The dipole is mounted over a rotary stage. The stage allows the dipole to rotate around the capacitance cell (Fig. 2.28 b). By this means, the capacitance cell is remaining still while the magnetic field rotates around it. The positions of cantilever parallel and perpendicular to H are easily achieved in one loop. A typical measurement of this set-up is shown in Fig. 2.29 . The value of ΔC_x is displayed versus the period, T, which is the duration of a complete rotation of the dipole set-up. The capacitance oscillates as the dipole is rotating and also reflects the symmetry of the magnetic field. Maxima and minima correspond to $\Delta C_{x\parallel}$ and $\Delta C_{x\perp}$ respectively, if the ME constant is positive. The difference between a maximum and a minimum is $\Delta C_{x\parallel} - \Delta C_{x\perp}$. By using this set-up we can obtain quite a large number of cycles and determine more accurately parallel and perpendicular configurations. Thus, we can obtain a more accurate value of $\Delta C_{x\parallel} - \Delta C_{x\perp}$ by averaging. Usually, we take 24 oscillations to average. Also, the capacitance cell is remaining still, which avoids the 90 ° rotation required by using the electromagnet and any mechanical vibration that lead to capacitance fluctuations. The improvement compared to the electromagnet set-up, in addition to the aforementioned, is the alignment of H with respect to the cantilever. As the magnetic field is rotating, all positions are covered. But, when the measure is made by the electromagnet set-up a few degrees of misalignment may be present between H and the cantilever.

A LabVIEW program was coded to control the angular velocity of the rotary stage dipole set-up in addition to take measurements of the capacitance cell. Lower velocities permit to represent more points and make the domain rotation smoother. The capacitance is obtained from the capacitance bridge and the time from the internal clock of the computer. The program can subtract a second order polynomial to make the oscillations centred at $\Delta C_x = 0$. The second order polynomial is associated to the thermal stability of the capacitance cell. The user's interface is nearly the same as for the electromagnet set-up (Fig. 2.26 b), but the x-axis shows time instead of H.

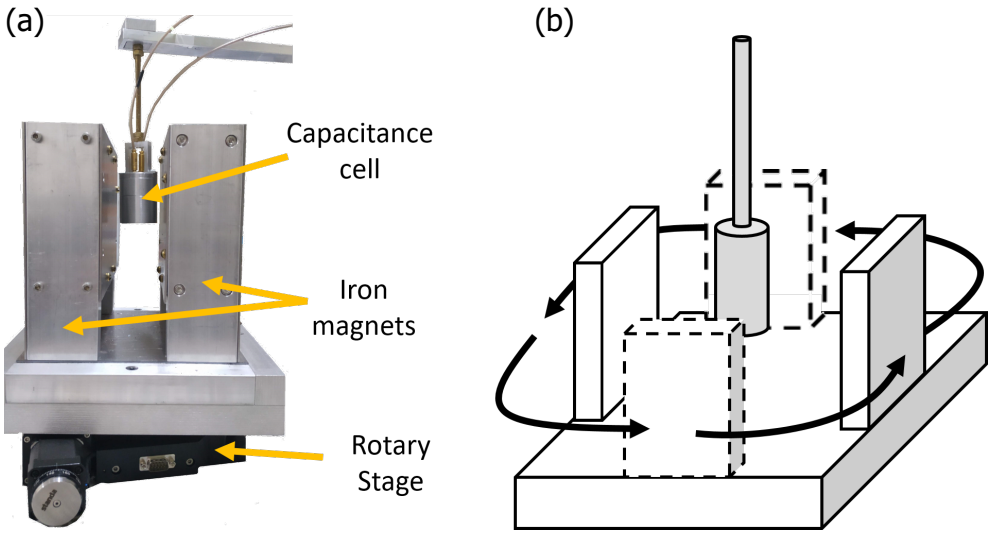

Figure 2.28: (a) Photo of dipole set-up. Capacitance cell is between the iron magnets. The dipole is mounted over a rotary stage. (b) Scheme of rotation. Capacitance cell remains still while the dipole rotates. Dashed magnets indicate the motion of original magnets (solid line) according to the arrows.

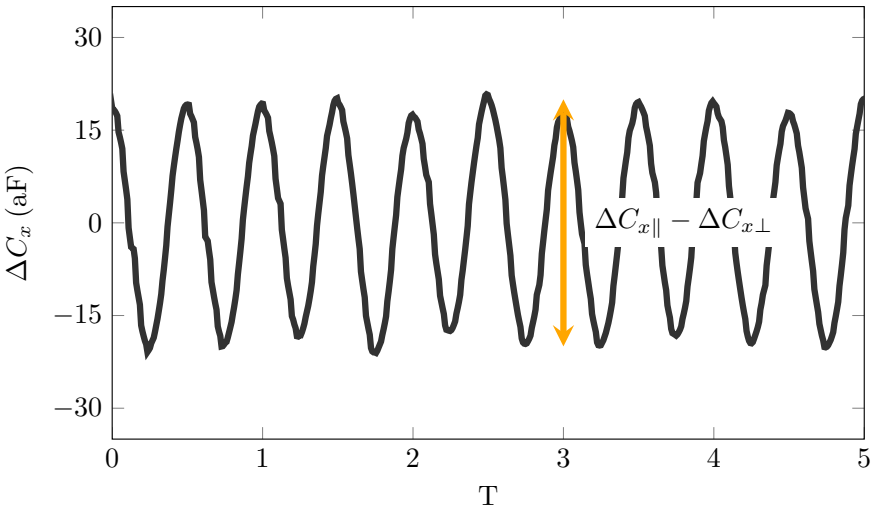

Figure 2.29: Typical magnetostriction plot for dipole set-up. $\Delta C_x = C_\xi - C_0$, being the difference between bent (C_ξ) and relax state (C_0) for the cantilever. T is the period of the rotatory stage. The plot shows oscillation between parallel and perpendicular configuration, maximums and minimums. The yellow arrow inidcates the amplitude of oscillation, which is $\Delta C_{x\parallel} - \Delta C_{x\perp}$.

Calibration

Capacitance cell measurements are in the order of aF. Thus, a measure can be masked by undesirable signals higher than aF easily. The first step to ensure that the cell is measuring correctly the curvature of the cantilever is to calibrate it by using non-magnetostrictive thin films. Non-magnetostrictive metals such as copper are used as a cantilever. When the cell is put in the dipole set-up the plot has to be linear, $\Delta C_x = 0$. By this method we debugged the cell until the parasitic currents were smaller than aF, and the measures were linear.

To ensure that the obtained ME constants are quantitatively relevant, the system needs a calibration. To calibrate the capacitance cell we used Fe thin films grown over MgO as a cantilever. ME constants of Fe are well-known: $B_1 = -2.9\,\mathrm{MPa}$ and $B_2 = 7.4\,\mathrm{MPa}$ [18]. By using the same substrate, all constants are the same for Fe and FeGa. The calibration factor F_i is inserted in ME equations proportionally.

$$B_1 = -F_1 \times \frac{S_{[110]} h_s^2 \varepsilon_0 A}{h_f L_x^2 C_0^2} \left(\Delta C_{x\parallel} - \Delta C_{x\perp} \right) \tag{2.121}$$

$$B_2 = -F_2 \times \frac{S_{[100]} h_s^2 \varepsilon_0 A}{h_f L_x^2 C_0^2} \left(\Delta C_{x\parallel} - \Delta C_{x\perp} \right) \tag{2.122}$$

A total of six samples of Fe/MgO were used to calibrate both F_1 and F_2. The experimental calibration factors are $F_1 = 0.97$ and $F_2 = 1.15$. The results indicate that the cantilever model developed in this thesis is reasonably exact and provides values for B_1 and B_2 close to the experimental ones, being necessary to correct the expressions by means of calibration constants not too far from 1.

Chapter 3

FeGa/MgO(001) epitaxial thin films

3.1 Introduction

This chapter describes the fabrication process carried out to grow FeGa thin films by MBE, and its subsequent structural and magnetic characterization. The samples analyzed in this chapter are FeGa/MgO(001). By using MgO(001) substrate the epitaxial grown is guaranteed, as RHEED images display. During the growing process, two parameters play an important role, which are the evaporation flux, and the temperature of the substrate (T_s) to achieve specific crystal structures and magnetic anisotropies in the samples. The control of evaporation flux rules the composition of the FeGa alloy, and it is determined by the vapor pressure of Fe and Ga elements. The temperature of the substrate while Fe/Ga are being deposited establishes the crystal structure of the thin film. At composition $x = 24$, *bcc* crystals are found for $T_s = 150 - 700\,°C$, but, *fcc* structures are only found for $T_s = 400 - 700\,°C$. Also, RHEED and XRD measurements indicate that for $x > 18$ a superorder between Fe and Ga atoms is formed in the crystalline structure. The study of samples grown in the range $T_s = 150 - 700\,°C$ shows that the magnetic anisotropy diminishes as T_s increases, while the applied magnetic field needed to saturate the sample increases. For the composition study, it is found a spin reorientation in the samples grown at $T_s = 150\,°C$ with $x > 19$. The easy axis changes from [100] to [110] as the Ga content increases. The origin of the spin reorientation can be explained by the ordering of Ga atoms in the Fe matrix.

MFM study of the samples grown at $T_s = 150\,°C$ shows that a magnetic corrugation occurs for $x > 20$. This corrugation is an indicator of a slight out-of-plane magnetization. As the samples are not thick enough, the stripe

model do not predict out-of-plane magnetization for the samples. The results obtained by high-field magnetization loops agree with the simulations of the ferromagnetic wandering axis model. So, it is argued that a random magnetic anisotropy is behind the magnetic corrugation observed.

An investigation on the enhancement of ME coefficients by adding third elements was carried out. Two elements are proposed to enhance the magnetostriction of FeGa: Tb and Cu. The results for doping with Tb indicate that the ME coefficients are not affected, and remain at the same values as the FeGa undoped samples. Nevertheless, the ternary alloy FeGaCu presents a detrimental in the ME coefficients. TEM experiments indicate that the ω phase is formed in the film. It is discussed that the lower values of $|B_1|$ and $|B_2|$ are due to the superorder lattice ω.

3.2 Samples growth procedure

The samples consist in a thin film deposited over a single crystalline substrate. In this thesis, all the samples are grown by MBE technique. By this means, we can obtain high-crystalline samples at the desired thickness and composition. When working in high-crystalline films, we need to attend to the epitaxy of the growth. Differences of the lattice parameters between film and substrate need to be low to ensure an epitaxial growth. For *bcc* $Fe_{100-x}Ga_x$, the range of the lattice parameter is $a_{FeGa} = 0.286$ – $0.290\,nm$ for a composition in the range $x = 0$ – 24, respectively [44]. The substrate chosen to deposit FeGa is MgO(001). The lattice parameter of MgO is $a_{MgO} = 0.421\,nm$, which is near to $\sim \sqrt{2}a_{FeGa} = 0.410\,nm$. This means that it is expected that FeGa grows rotated 45° to achieve epitaxy with MgO [78], being the misfit between them:

$$\eta_{FeGa/MgO} = \frac{\sqrt{2}a_{FeGa} - a_{MgO}}{a_{MgO}} = -2.58\% \tag{3.1}$$

The misfit value is low enough to achieve the epitaxial growing, and the minus sign indicates that the film grows enlarged in the plane. The epitaxal relationships between the film and the MgO(001) are:

$$\text{FeGa(001)/MgO(001)} \tag{3.2}$$

$$\text{FeGa[100]} \parallel \text{MgO[110]} \tag{3.3}$$

$$\text{FeGa[110]} \parallel \text{MgO[100]} \tag{3.4}$$

Several steps are required to deposit epitaxial FeGa films on MgO. Fig. 3.1 a depicts the process. The substrate is introduced inside the main chamber at room temperature. Then, the substrate is heated until a temperature of

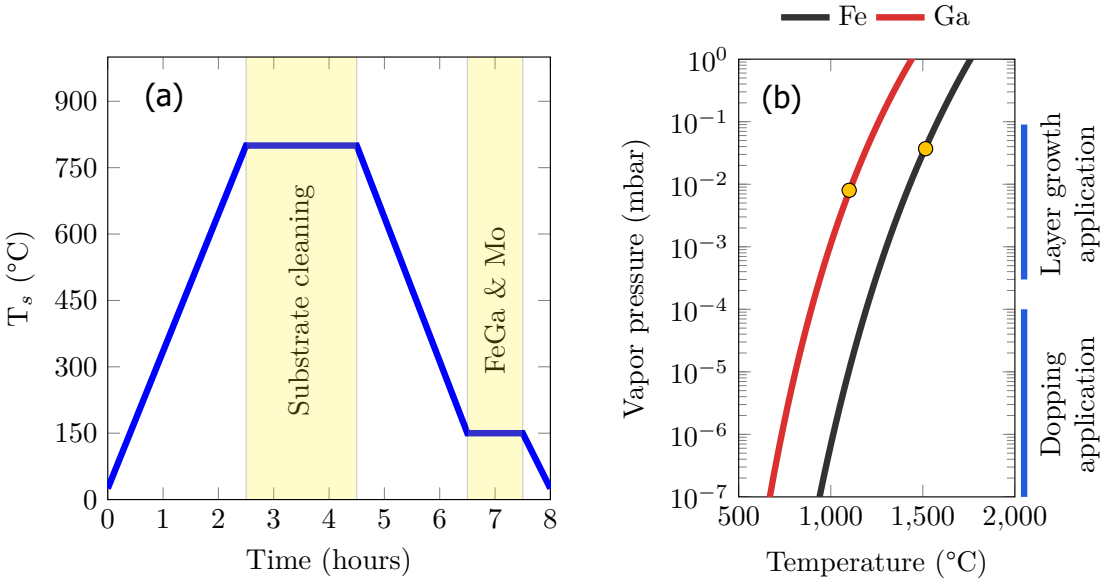

Figure 3.1: (a) Temperature of the substrate along the growing stages. Substrate cleaning at $T_s = 800\,°C$, and deposition of FeGa and Mo at $T_s = 150\,°C$. (b) Vapor pressure curves for Fe and Ga. Orange dots indicates the values used in MBE. Apapted from [79].

$T_s = 800\,°C$ is achieved and it is held at $T_s = 800\,°C$ for 2 hours in ultra high vacuum conditions to eliminate adsorbates (as RHEED pattern indicates Fig. 3.3). Next, a temperature ramp is programmed to lead the substrate to the temperature of deposition. The majority of the samples in this thesis are grown at $T_s = 150\,°C$, but in this chapter we also analyze samples grown at different temperature to study its structural and magnetic changes as a function of the deposition temperature.

The evaporation of FeGa alloy is carried out by e-beam evaporator and Knudsen cell for Fe and Ga, respectively. To know approximately the temperature of evaporation that we need for each element we use the equation that relates pressure and temperature:

$$\mathrm{P(mbar)} = 10^{A - B/T(K)} \tag{3.5}$$

where A and B are the phenomenological coefficients: $A_{\mathrm{Fe}} = 10.353$, $B_{\mathrm{Fe}} = 21038\,\mathrm{K}$, $A_{\mathrm{Ga}} = 8.558$, and $B_{\mathrm{Ga}} = 14658\,\mathrm{K}$ [79]. Fig. 3.1 b shows the vapor pressure curves for Fe and Ga, and the evaporation temperature used in this thesis by an orange dot. Usually, we set the evaporation rate of Fe at $\sim 1.4\,\mathrm{nm/min}$, which is a temperature of $\mathrm{T_{Fe}} \simeq 1500\,°C$, and we vary the Ga temperature to make the alloy. For example, to obtain $Fe_{80}Ga_{20}$, the va-

por pressure of Fe is $P_{Fe} = 0.034\,\text{mbar}$, so the vapor pressure needed of Ga is $P_{Ga} = P_{Fe}/4 = 0.0085\,\text{mbar}$, which corresponds to $T_{Ga} \simeq 1100\,°\text{C}$. Experimentally (by using EDX), we found that the Ga temperature needed for $Fe_{80}Ga_{20}$ is $T_{Ga} = 1120\,°\text{C}$, which is a light deviation from the theoretical temperature because of the geometrical set-up that involves e-beam evaporator and Knudsen cell. The range of Ga temperatures used to grow FeGa alloys in the range $x = 0 - 35$ is $T_{Ga} = 1050 - 1200\,°\text{C}$.

The time of evaporation rules the thickness of the film. Typically, a film of 40 nm (determined by XRR) is grown in $\sim 25\,\text{min}$. After the deposition of FeGa, we deposit a capping layer of Mo to prevent the sample from oxidation. As Mo is a refractory metal, we need high temperatures to achieve enough vapor pressure to deposit a layer of 2 nm. By using the e-beam evaporator, we reach a temperature of $T_{Mo} \simeq 2300\,°\text{C}$ to deposit the layer in $\sim 15\,\text{secs}$. Once the FeGa and Mo are deposited, the sample is extracted from the main chamber to characterize it by ex-situ techniques.

In sections 3.3 and 3.4, we use the code $\#_x^{T_s}$ to indicate the composition of the sample and the temperature of the substrate while the deposition was carried out.

To calibrate the deposition parameters of MBE we use two ex-situ techniques: EDX for composition, and XRR for film thickness. The composition of the alloy is determined by the temperature of the Ga cell because the Fe evaporation flux is intentionally always the same and controlled with a quartz balance. At first approximation, we use the pressure vapor of Ga to set a range of temperatures that are close to the searched composition. Fig. 3.2 a shows two EDX patterns for samples with $x = 15, 26$. For the elements Fe and Ga, the sample is scanned with an electron beam of 5 keV to detect the L_α x-ray lines. Higher energies probe more volume of the sample, but MgO is detected and the quantification of Fe and Ga is disturbed. As low energy is used, more surface is studied and Mo L_α is detected. Then, using L_α peaks is sufficient to study our samples [80]. The relative intensity between the Fe L_α and Ga L_α is used to determine the relative content of each element. In the pattern of Fig. 3.2 a is noticeable how Fe L_α peak has the same amplitude for both samples, but Ga L_α peak is higher for the sample with $x = 26$. By this analysis we can calibrate the temperature of the Knudsen cell to achieve the desired concentration of Fe and Ga.

The thickness of the samples is controlled by the time of Fe and Ga deposition. As the flux evaporation rate of Fe is constant, by using XRR we can make a correspondence between time and thickness. Fig. 3.2 b shows a XRR pattern for a sample with thickness 40.41 nm. The oscillations are clearly visible indicating a flat surface. The simulated curve is obtained by LEPTOS

software.

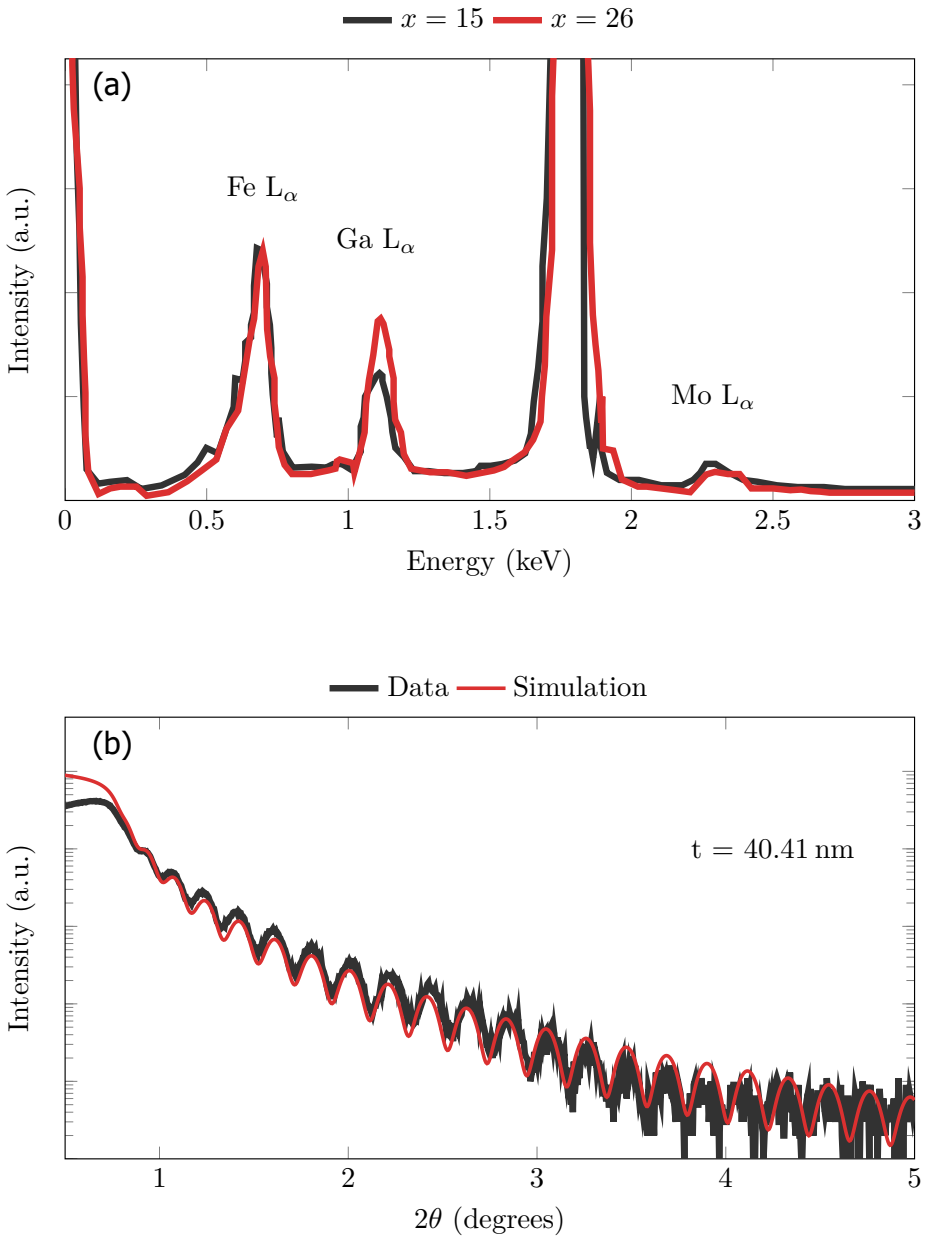

Figure 3.2: Ex-situ techniques used to calibrate MBE parameters. (a) EDX pattern for samples at different Ga content. An electron beam of 5 keV is used. (b) XRR pattern for a sample with t= 40.41 nm.

3.3 Structural characterization

3.3.1 RHEED

In situ RHEED technique provides an initial evaluation of the growth mechanism and the crystal structure present in the sample. Fig. 3.3 shows the evolution of the RHEED pattern while FeGa is being deposited at $T_s = 150\,°C$ along FeGa[100] direction. At $t = 0\,s$, the MgO(001) substrate presents diagonal sharp lines (Kikuchi lines) that denote the cleanness of the surface after the thermal cleaning process. As time goes, the MgO pattern changes its shape to display light spots ($t = 120\,s$) indicating a single-crystal islands growth. After this time, the growing changes from islands to a flat single-crystal surface as the layers are being completed. The spots start to enlarge until vertical streaks are noticeable at $t = 390\,s$. At $t = 600\,s$ the characteristic RHEED pattern for FeGa grown with several monolayers is shown.

By analyzing the intensity of the RHEED spots with the time, we can measure the monolayer growth rate. Fig. 3.4 shows the intensity *vs* time after the island growing. The graph shows periodic oscillations of the intensity. The maxima corresponds to a full monolayer (ML) deposited, and the minima are for a half-completed monolayer. The period of growing a ML is $\sim 12\,s$, that yields a growth rate of $\sim 1.45\,nm/min$ for FeGa with $a_{FeGa} = 0.29\,nm$.

RHEED patterns obtained for FeGa present symmetry. Two characteristic patters are observed with an angular separation of 90 degrees (Fig. 3.5 a-b). Also these two patters happen at azimuth angles separated by 45 degrees. The distance between two symmetrical streaks for these patterns is marked (red arrows) as d_1 and d_2. The ratio $d_1/d_2 \sim 0.7$, which is the same as the produced by FeGa reciprocal space vectors: $2\pi/a_{200}$ and $2\pi/a_{220}$, $\sqrt{2^2+0^2+0^2}/\sqrt{2^2+2^2+0^2} \sim 0.7$. Then, Fig. 3.5 a and Fig. 3.5 b correspond to FeGa[100] and FeGa[110] directions, respectively.

The RHEED pattern presents surface reconstruction as the Ga content increases indicating a superlattice (SL) order. Fig. 3.5 a-b and Fig. 3.5 c-d shows the RHEED patterns for $x = 14$ and $x = 26$, respectively. For $x = 26$, a surface reconstruction in the RHEED pattern is seen between the main streaks. For FeGa[100] direction arises one SL streak, and for FeGa[110] arise two SL streaks between main streaks (orange arrows). As these SL streaks are not clearly visible, an intensity plot is shown in Fig. 3.5 e-f for FeGa[100] and FeGa[110] directions respectively. The orange arrows mark the change in the intensity that corresponds to the SL streaks.

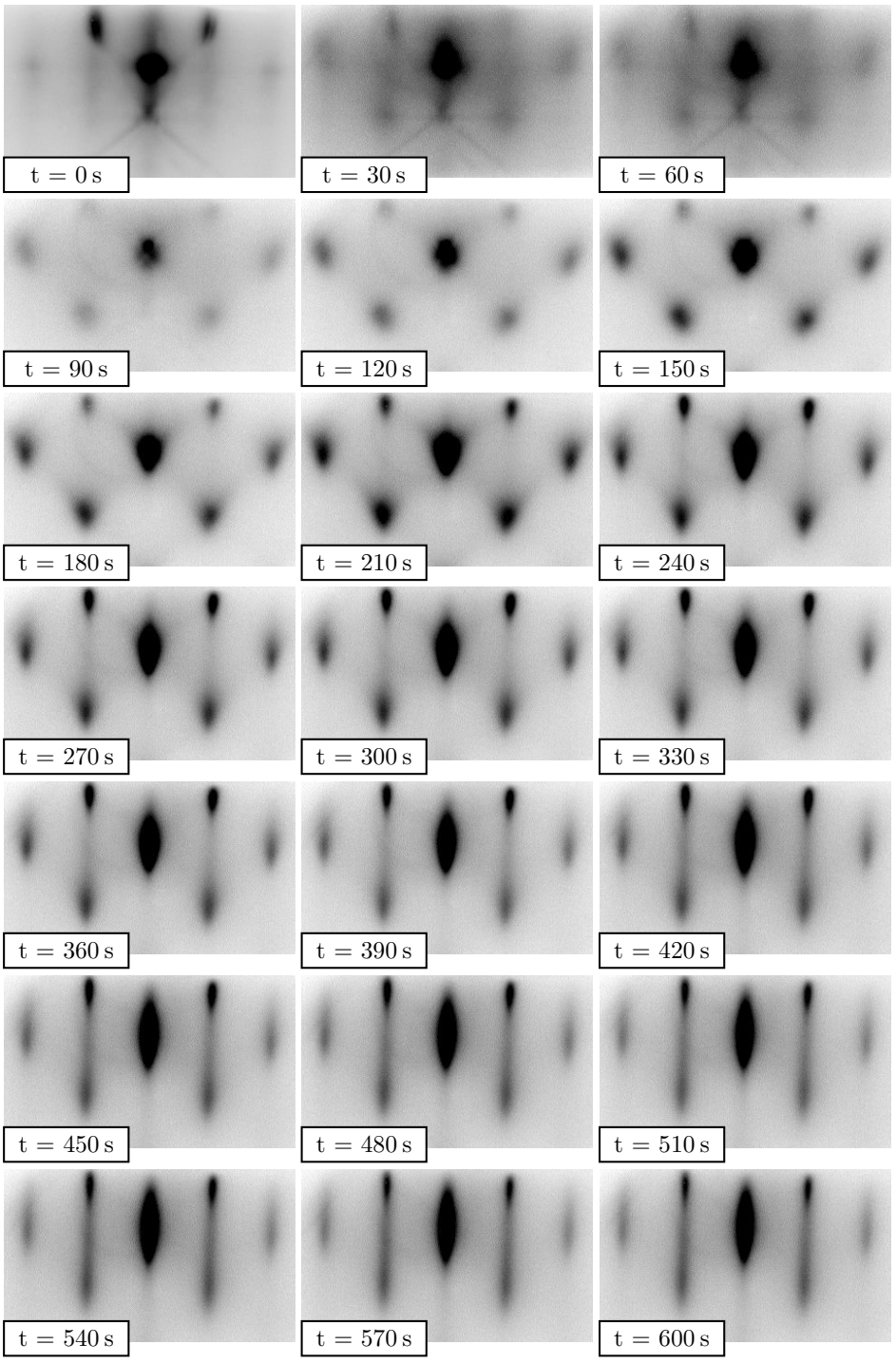

Figure 3.3: RHEED pattern evolution for *bcc* FeGa grown over MgO(001) taken at $T_s = 150\,^{\circ}\mathrm{C}$ along FeGa[100] direction.

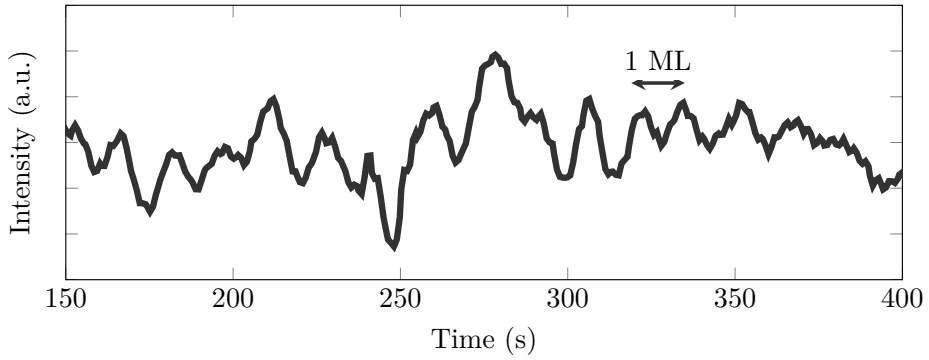

Figure 3.4: Intensity of a RHEED spot from Fig. 3.3 along the deposition time. The time between two maxima gives the growth rate of the monolayer .

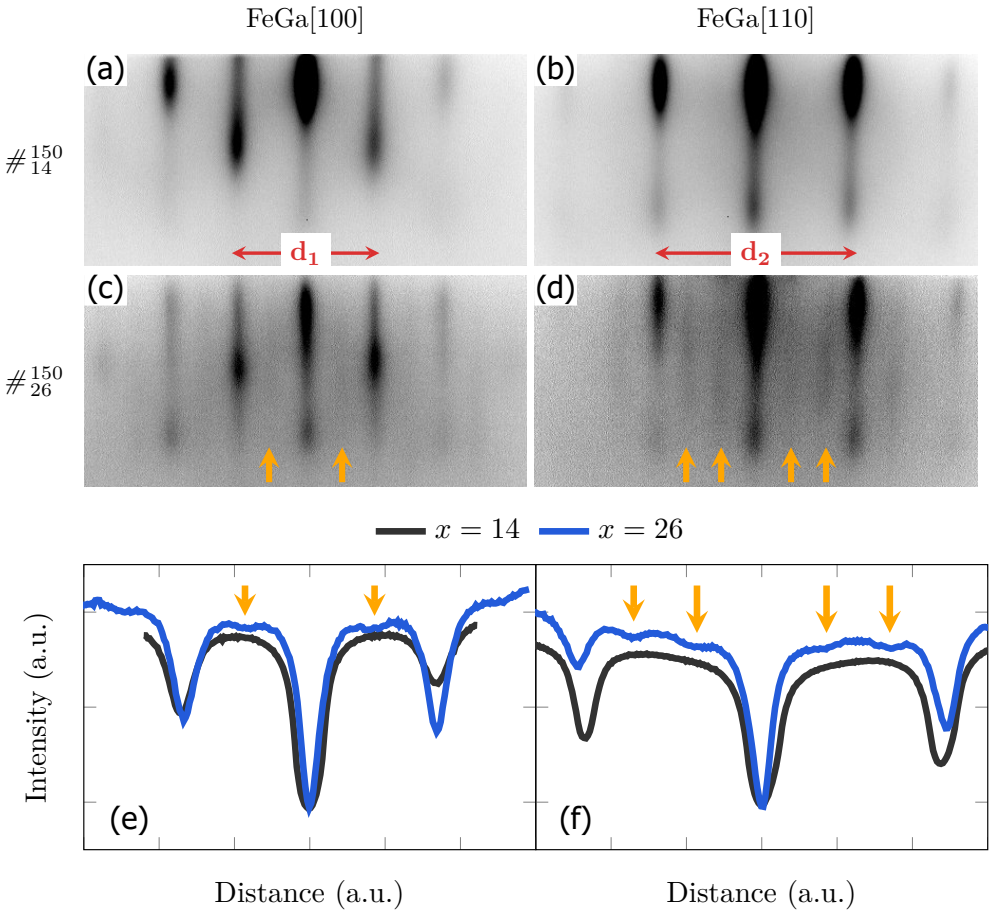

Figure 3.5: RHEED patterns for samples grown at $T_s = 150\,°C$. Rows are for samples at the same composition: (a) and (b) for $x = 14$, whereas (c) and (d) for $x = 26$. Columns indicate the direction at which the RHEED pattern is taken: (a) and (c) for FeGa[100], whereas (b) and (d) for FeGa[110]. (e) and (f) are the intensity plots of FeGa[100] and FeGa[110], respectively. Orange arrows indicate the streaks that can be interpreted as a surface reconstruction.

The interpretation of SL streaks is explained by a surface reconstruction due to a superlattice phase. Fig. 3.5 e shows the SL streaks exactly at middle position between main streaks. The SL patterns suggest the presence of domains with several reconstruction unit cells. We propose that one of them looks to be the superstructure $(2 \times 1) + (1 \times 2)$ due to the lack of superlines at the middle points between the main streaks along [110] directions (see Fig. 3.5 d,f for $x = 26$). We propose that the reconstruction (2×1) may be generated by a small amount of Ga pairs with a periodicity of 2a in real space. The fact that the SL streaks are not observed for films with low x may indicate that the number of Ga pairs is low, or are randomly distributed in the Fe matrix.

Another RHEED pattern was found in some samples grown at $T_s > 300\,°C$. Fig. 3.6 c-d shows the pattern observed in a sample $T_s = 600\,°C$ in comparison with the previous one, $T_s = 150\,°C$ (Fig. 3.6 a-b). Both samples have the same composition, $x = 24$, but their difference lies in the temperature of the substrate during the deposition on the film. As we will see in the XRD section, the patterns Fig. 3.6 a-b and Fig. 3.6 c-d indicate *bcc* and *fcc* crystal structure, respectively. The reconstruction is also visible in the *fcc* structure indicating that a superstructure is also formed.

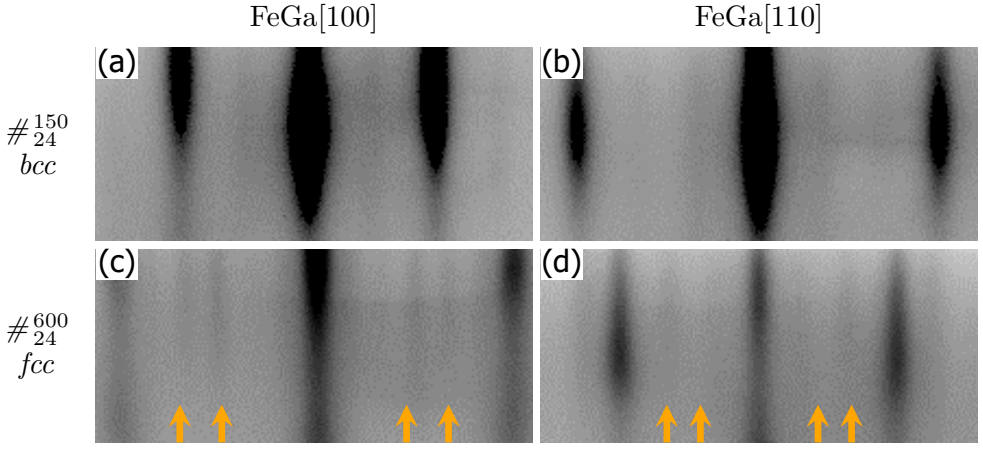

Figure 3.6: Comparison between RHEED patterns for *bcc* and *fcc* structures. Both samples have the same composition $x = 24$. Rows are for samples at the same T_s: (a) and (b) for $T_s = 150\,°C$, whereas (c) and (d) for $T_s = 600\,°C$. Columns indicate the direction at which the RHEED pattern is taken: (a) and (c) for FeGa[100], whereas (b) and (d) for FeGa[110]. Orange arrows indicate the streaks that can be interpreted as a surface reconstruction.

3.3.2 XRD

Fig. 3.7 shows the XRD pattern for *bcc* and *fcc* FeGa samples grown. The *bcc* structure is assigned to samples with the main peak at $2\theta \approx 65°$, that corresponds to a bcc(002) reflection with a lattice parameter around 0.29 nm [33]. The *fcc* structure is associated to samples with the main peak at $2\theta \approx 49°$, which is the fcc(002) peak with the lattice constant value around 0.37 nm, the value reported for the $L1_2$ phase [33]. The superlattice peak (001) is found for *bcc* and *fcc* structures. For *bcc* is located at $2\theta \approx 31°$, while for *fcc* is at $2\theta \approx 24.5°$. No evidences of other peaks are found in the scans.

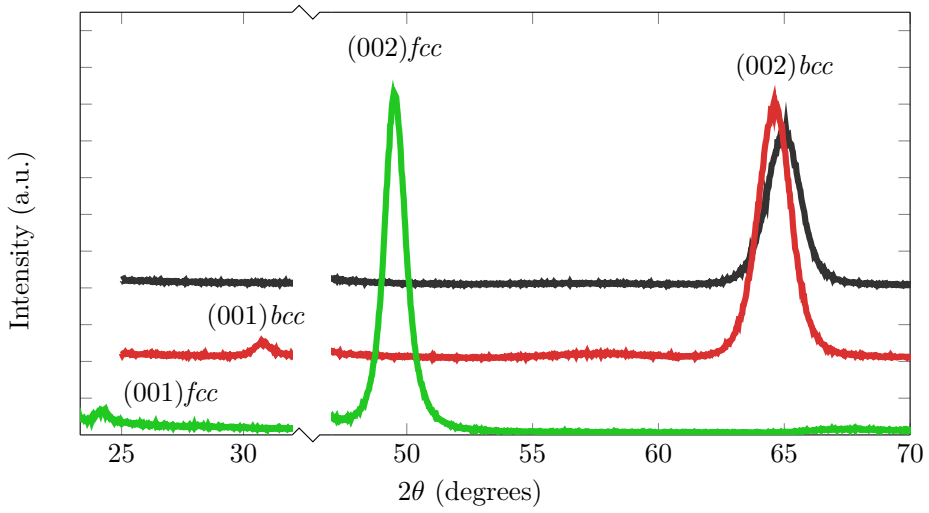

Figure 3.7: XRD pattern for samples $\#_{13}^{150}$ (black), $\#_{24}^{150}$ (red), and $\#_{24}^{600}$ (green).

For *bcc* structures, the peak (001) is extincted for some compositions, but it is clearly visible in the sample $x = 24$. The A2 structure with atoms randomly distributed cannot present the (001) superlattice peak. But, *bcc* B2 and $D0_3$ structure can explain the (001) SL peak [33] meaning that a large range order is present in the film at that composition. The origin of the long range order can be explained by the Ga ordering that suffers FeGa from the A2 disordered matrix to an ordered matrix as Ga content increases. We cannot confirm that the order is due to a $D0_3$ phase because its signature peak, (1/2 1/2 1/2), is not detected.

The perpendicular lattice parameter for samples grown at $T_s = 150\,°C$ as a function of x is shown in Fig. 3.8 a. The values obtained are in agreement with the bulk ones [33]. A tendency line is plotted to show that the lattice parameter increases as the Ga content does. However, the values are dispersed

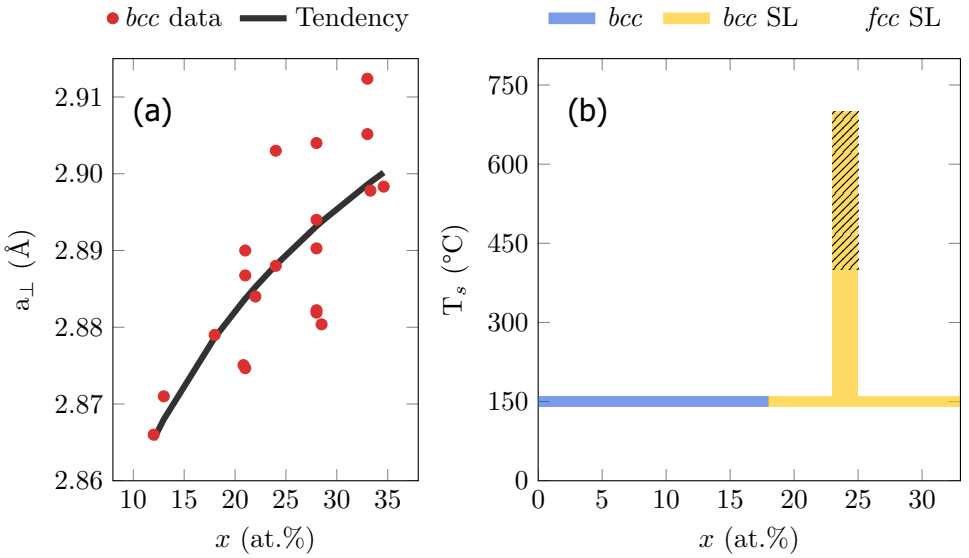

Figure 3.8: (a) Perpendicular lattice parameter obtained from (002) *bcc* peak, $T_s = 150\,°C$ samples. Tendency line indicates the increase in $a_\perp$ as Ga content increases. (b) Phase diagram for the samples studied by XRD and RHEED. A superlattice (SL) structure appears for $x > 18$. *bcc* and *fcc* structures coexist at $x = 24$, $T_s > 400\,°C$.

with respect to the tendency because the thickness factor is not considered.

For *fcc* structures, the origin of the (001) SL peak can be explained similarly to the *bcc* one. The SL peak may have its origin in an ordered Ga matrix. For *fcc*, the crystal structure that satisfies a long range order between Ga atoms is the $L1_2$ one. The phase $L1_2$, according to the FeGa diagram phase [31, 32], is present at the range of temperatures where the samples with *fcc* peaks have been observed.

The perpendicular lattice parameter of *fcc* samples agrees with the bulk values $\sim 0.368\,nm$ [33]. As the *fcc* samples studied are grown at the same composition, $x = 24$, there is no tendency study in its lattice parameters.

We can conclude that the SL peak (001) is related to the composition, and T_s to the crystal structure of the thin film. A phase diagram of the studied samples is shown in Fig. 3.8 b. Samples grown at $T_s = 150\,°C$ always display a *bcc* structure. At $x = 18$, XRD and RHEED indicate a change in the structural order, and a superlattice is formed. The thermal study done at $x = 24$ concludes that both *bcc* and *fcc* structures coexist at $T_s > 400\,°C$. The nucleation of each phase can be induced by a minute fluctuation in the composition.

3.3.3 AFM

Fig. 3.9 shows topographic images of two samples grown at different temperature with *bcc* crystal structure [44]. The greyscale bar indicates the height of the said images. The sample grown at $T_s = 150\,°C$ (Fig. 3.9 a) presents a high flatness with steps as high as 0.4 nm (thick black line) along the MgO[100] edges. However, the samples grown at $T_s = 600\,°C$ (Fig. 3.9 b) present a 3D islands growing. The transition from 2D to 3D growing has been reported for pure Fe films grown on MgO [81]. The height of the islands is in the $50-80$ nm range.

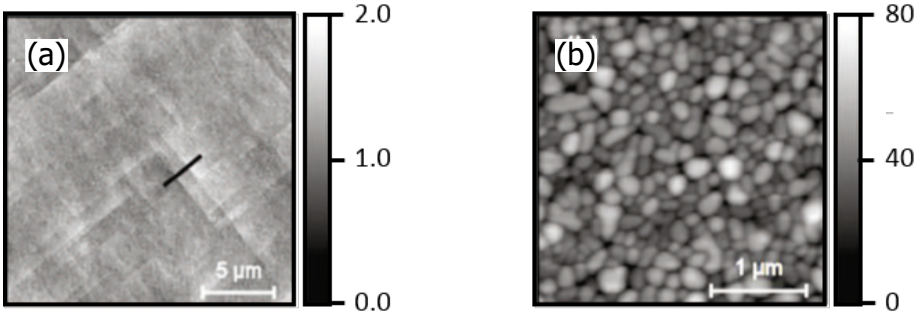

Figure 3.9: Topographic images taken at different T_s. Greyscale bar units are nm. (a) Sample grown at $T_s = 150\,°C$. (b) Sample grown at $T_s = 600\,°C$. The height of the steps along the thick line in panel (a) are about 0.4 nm.

3.3.4 TEM

Fig. 3.10 a shows the TEM image for a sample grown at $T_s = 150\,°C$ with composition $Fe_{76}Ga_{24}$. The image is taken with the planes MgO(100) and FeGa(110) perpendicular to electron beam. The columns of atoms are clearly visible confirming an epitaxial growth between MgO and FeGa.

The FFT image of the FeGa film is shown in Fig. 3.10 b. The zone axis for FeGa in this direction is the [110] one. Thus, the spots are indexed according to a *bcc* [110] zone axis. The spots indexed as (002) and (110) indicate the growing and the in-plane direction, respectively. $D0_3$ structures present a SL peak at (1/2 1/2 n/2) position [82]. But, no peak is observed for any value of n, either odd or even. The reflection (001) presents a splitting that appears as a double spot. The splitting of the double spot varies from point to point of measure and it is related to anti-phase boundaries [83] caused by a superlattice structure, or by the oxidation of the sample [50].

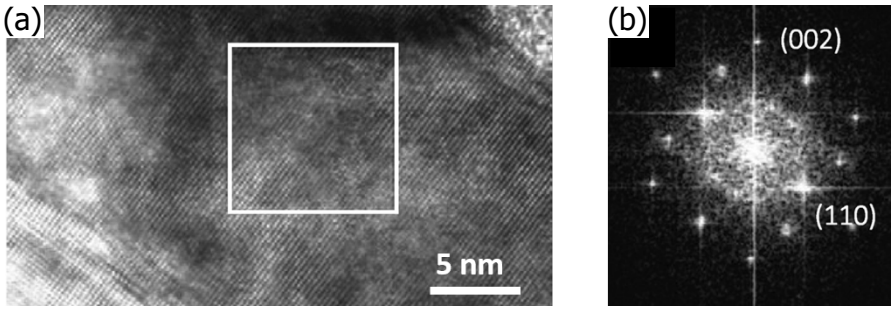

Figure 3.10: TEM measurements. (a) TEM image for FeGa/MgO(001). (b) FFT image of FeGa corresponding to the white rectangle in (a).

3.4 Magnetic characterization

3.4.1 T_s dependency

The temperature of the substrate while the alloy is being deposited not only affects the crystal structure, their magnetic properties are affected too. Samples with $x = 24$ are analyzed attending to its crystal structure. Fig. 3.11 shows the evolution of *bcc* films as a function of T_s. Sample $\#_{24}^{150}$ (Fig. 3.11 a) presents magnetic cubic anisotropy, where the easy axis is FeGa[110] and the hard axis is FeGa[100]. As the temperature of deposition increases (Fig. 3.11 b-c), the hysteresis loops for each direction become similar, indicating that the magnetic anisotropy is weakening. Sample $\#_{24}^{700}$ (Fig. 3.11 d) presents an isotropic magnetic behavior in which both loops are approximately equal, and the applied magnetic field necessary to saturate the sample is increased from $\sim 90\,\mathrm{mT}$ to $\sim 250\,\mathrm{mT}$.

For *fcc* samples, the behavior is similar to *bcc* ones. Fig. 3.12 a-b shows M-H loops for samples $\#_{24}^{400}$ and $\#_{24}^{600}$, respectively. Both crystalline directions, FeGa[100] and FeGa[110], present similar loops indicating an absence of magnetic anisotropy. For these films, the magnetic field needed to saturate the sample is higher for $T_s = 400\,^{\circ}\mathrm{C}$ than for $T_s = 600\,^{\circ}\mathrm{C}$ ($\sim 200\,\mathrm{mT}$ *vs* $\sim 90\,\mathrm{mT}$).

In this thesis, we are focused in searching magnetic applications for FeGa thin film alloys. The results obtained at different T_s allows us to discern the best structures and temperatures to work with. The magnetic anisotropy plays a crucial role in the development of magnetic applications [84, 85]. Samples grown at $T_s = 150\,^{\circ}\mathrm{C}$ present higher magnetic anisotropy than other films grown at higher temperature. The magnetic saturation is also an important value to keep in mind because MOKE set-up, and the magnetic dipole used to measure magnetostrictive coefficients can apply at most around 100 mT.

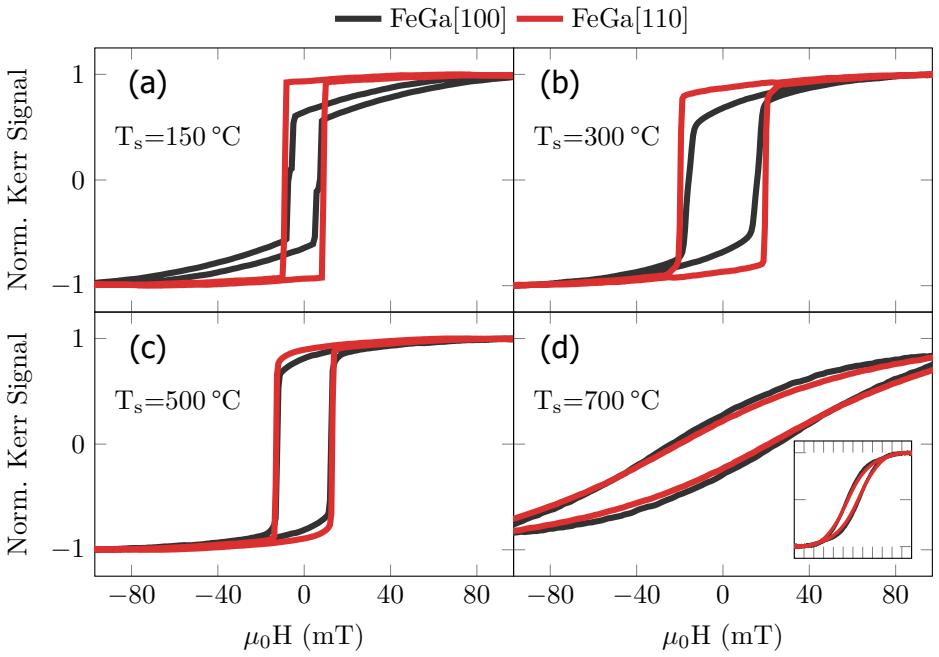

Figure 3.11: MOKE M-H loops for *bcc* samples grown at several T_s. Samples are: (a) $\#_{24}^{150}$, (b) $\#_{24}^{300}$, (c) $\#_{24}^{500}$, (d) $\#_{24}^{700}$. Inset panel shows the full loop ranging H= 240 mT.

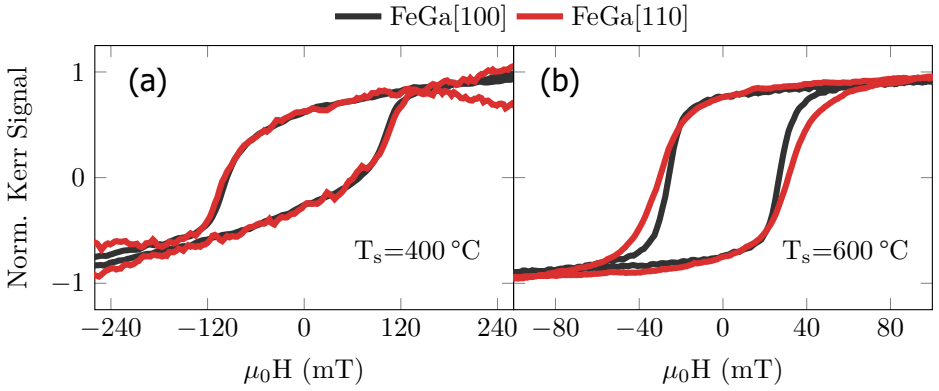

Figure 3.12: MOKE M-H loops for *fcc* samples grown at several T_s. Samples are: (a) $\#_{24}^{400}$, (b) $\#_{24}^{600}$.

Films grown at higher temperatures have magnetic saturation values above the magnetic field that we can apply in the lab, so we need to discard those films in order to have reliable measurement. From now on, the samples studied are grown at $T_s = 150\,°C$. All of this samples present *bcc* crystal structure because *fcc* structures are only found at higher T_s (Fig. 3.8 b).

3.4.2 Ga content dependency

An investigation of the easy axis dependence on Ga composition was performed by VSM. Fig. 3.13 a-b shows M-H loops for FeGa[100] and FeGa[110] directions, respectively. At low x, the easy axis is along FeGa[100] direction. However, above certain composition in the range $x = 14 - 19$ there is a spin reorientation and the easy axis becomes the FeGa[110] direction. The results are not affected by the thickness of the films, at least in films ranging $t = 15 - 50\,nm$.

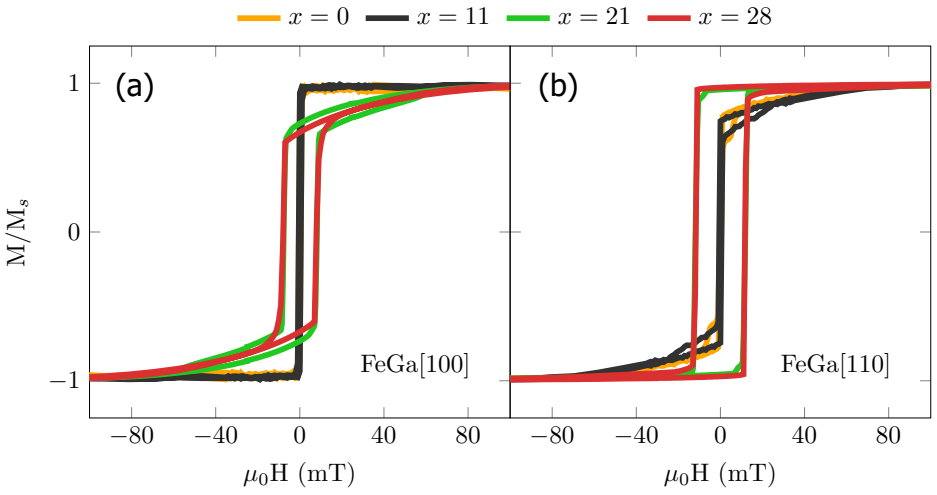

Figure 3.13: VSM M-H loops for samples grown at $T_s = 150\,°C$ at several compositions. Two crystallographic directions are studied: (a) FeGa[100] and (b) FeGa[110].

By using the method of MOKE angular measurements developed in this thesis, we can plot the squareness, S_k, in a polar plot. The squareness is calculated in a Kerr loop as:

$$S_k = \frac{\theta_r}{\theta_s} \tag{3.6}$$

where θ_r is the remanent Kerr signal, and θ_s is the saturated Kerr signal. So, S_k determination is similar to talk about magnetic remanence. Values of S_k

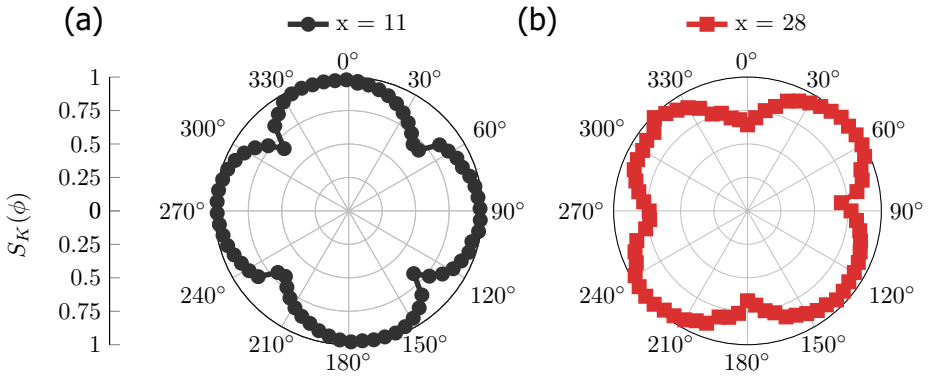

Figure 3.14: Squareness polar plot of samples (a) $\#_{11}^{150}$ and (b) $\#_{28}^{150}$. The polar axes correspond to 0° ∥ FeGa[100] and 90° ∥ FeGa[010].

close to 1 indicate easy axis, and lower values may indicate non-easy axis, but further analysis is needed for those cases.

Fig. 3.14 a-b shows the S_k polar plot for $\#_{11}^{150}$ and $\#_{28}^{150}$, respectively. For both samples, plot indicates a magnetocrystalline anisotropy with 4-fold symmetry. This symmetry has a periodicity of 90°, which corresponds to a cubic magnetic anisotropy. The relation between the polar plot and crystallographic axes is 0° ∥ FeGa[100] and 90° ∥ FeGa[010]. The results obtained by this method are equivalent to those obtained by VSM loops. Nevertheless, we can observe the magnetic anisotropy landscape of each sample, and it is more noticeable the magnetic switching from easy to hard axis as the Ga content increases.

The reorientation of the easy axis can be seen by the dependency of K_1 *vs* composition. $K_1 > 0$ indicates that the easy axis is along [100] direction, and $K_1 < 0$ indicates that the easy axis is along [110] direction. Fig. 3.14 shows our K_1 values obtained by analyzing VSM loops for several compositions. The transition from positive to negative K_1 occurs at some point in the range $x = 14 - 19$. The magnetic saturation, $\mu_0 H_s$, for each composition used to calculate K_1 is obtained from [86, 87].

The values of K_1 obtained are different to those of the literature [56, 86]. The difference between our work and the references is that our samples are thin films, and the references correspond to measurements in bulk samples [56] and theoretical bulk calculations [86]. We can notice how FeGa thin films present smaller K_1 values for the $K_1 > 0$ regime. But, after the spin reorientation $|K_1|$ is greater with respect to bulk. Our samples conserve the cubic anisotropy instead of becoming isotropic, as the bulk ones. It is also noticeable that our samples present a constant value of $K_1 \sim -22\,\mathrm{kJ/m^3}$ for the $K_1 < 0$ regime.

The atomic ordering of Ga atoms seems to play a crucial role in the spin reori-

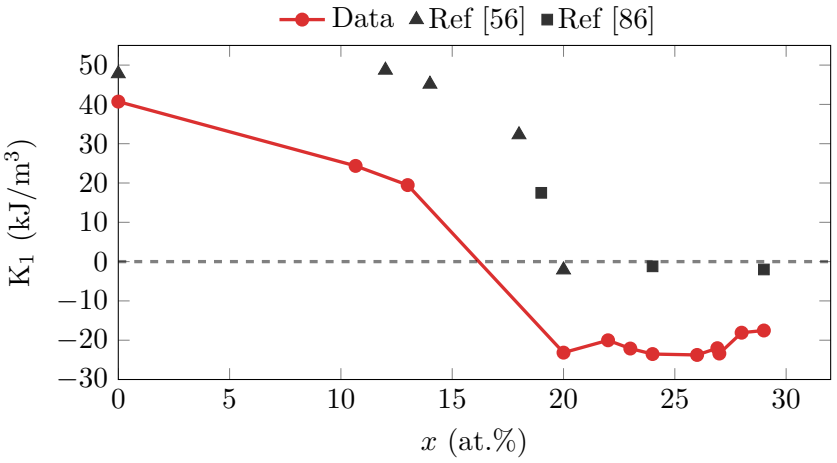

Figure 3.15: K_1 values as a function of x. Our data in red circles, and reference data for bulk [56] (black triangles) and theoretical bulk calculations [86] (black squares). The spin reorientation occurs in the range $x = 14 - 19$ for thin films.

entation because it occurs in the range of compositions where the alloy changes from A2 to an ordered structure. The superstructure $D0_3$ is discarded because XRD and TEM do not shown the (1/2 1/2 1/2) reflection. But, long-range order is present because of (001) reflection obtained by XRD. Modified-$D0_3$ or Ga-pairs distributed randomly in the Fe matrix could explain the long-range order observed. But, to confirm our guesses we need further structural experiments like extended x-ray absorption fine structure (EXAFS) to determine the vicinity of Ga atoms and discern if they are forming pairs or not. Also, computational simulations are required to study the energy density of the sample for several scenarios of Ga ordering.

3.5 Magnetic ripple domain structure

This section describes the investigation of the ripple domain structure observed in FeGa films with $x > 20$, and thicknesses below 60 nm. The samples studied were grown by MBE at $T_s = 150\,°C$ to avoid 3D growing that may affect the MFM imaging. The hysteresis loops show how the magnetization of thin films lie in-plane for $x < 20$ and the contrast in the MFM images is due to Bloch domain walls. For $x > 20$, MFM images show a magnetic corrugation in the magnetic signal with a periodicity of ~ 300 nm that is associated to a oscillation or ripple of M. High-field magnetization loops and XRD experiments were performed to clarify the mechanism behind the ripple observed. We discuss the origin of these magnetic structures from two points of view: perpendicular magnetic anisotropy, and a random magnetic anisotropy

superimposed to the cubic coherent anisotropy.

3.5.1 Magnetic force microscopy results

MFM images of samples grown at $T_s = 150\,°C$ with different thicknesses and compositions are shown in Fig. 3.16 . The code used to name every sample of the set in this section is denoted by $\#_x^t$, where x is the composition and t is the thickness of the thin film. The samples are in remnant state after applying magnetic field in-plane. Fig. 3.16 a-d are images taken in air, Fig. 3.16 e-f images are taken in low vacuum.

Sample $\#_{13}^{17}$ (Fig. 3.16 a) presents some lines that can be interpreted as as magnetic domain walls (some tip-induced features are also observed). The domain walls separate areas without contrast, indicating that **M** lies in-plane and that the domain walls are pointing out-of-plane (Bloch domain walls [57]). When Ga content is increased, from $x = 14$ (Fig. 3.16 a) to $x > 21$ (Fig. 3.16 b-d) a magnetic corrugation structure appears. The strength of this ripple in air is in the order of the Bloch domain wall (± 0.3 degrees). Air MFM image of the sample $\#_{21}^{16}$ is not shown because the ripple is very weak. The ripple observed in all samples is seen after several scans, so, an induced out-of-plane magnetization from the tip is discarded.

To increase the sensitivity of the measures, some MFM images were taken at low-vacuum. The quality factor of the cantilever is increased (resonance curve is sharper) because the viscosity of the medium is lower (lower damping). Fig. 3.16 e shows a MFM image taken at low-vacuum for the sample $\#_{13}^{17}$. The image shows a similar magnetic structure respect to the air image (Fig. 3.16 a). No magnetic ripple is observed between the domain walls. Fig. 3.16 f shows the low-vacuum image for the sample $\#_{21}^{16}$. In this image the magnetic ripple is clearly visible. Comparing both vacuum MFM images we can see that the strength of the domain wall (± 7 degrees) is higher than the ripple structure (± 1.5 degrees). Inset of Fig. 3.16 f represents an image of the sample $\#_{21}^{16}$ in the same range as the Fig. 3.16 e (± 7 degrees). By this way, we can compare the strength of the ripple respect to a domain wall. **M** is not pointing as perpendicular as a domain wall, so, it can be pointing slightly out-of-plane.

The period of the ripple structures is $\sim 300\,nm$ for $\#_{24}^{20}$, $\#_{28}^{56}$ and $\#_{28}^{21}$. For the sample $\#_{21}^{16}$, the period between domain walls is $\sim 900\,nm$.

Bulk samples that are quenched in water [88], or slowly cooled [89], present a similar magnetic structure respect to our samples with $x < 21$: there is no magnetic ripple, and the only contrast comes from domain walls. To obtain bulk samples with some similar magnetic ripple, a post-growing treatment is necessary [88]. This treatment originates stresses and other surface defects.

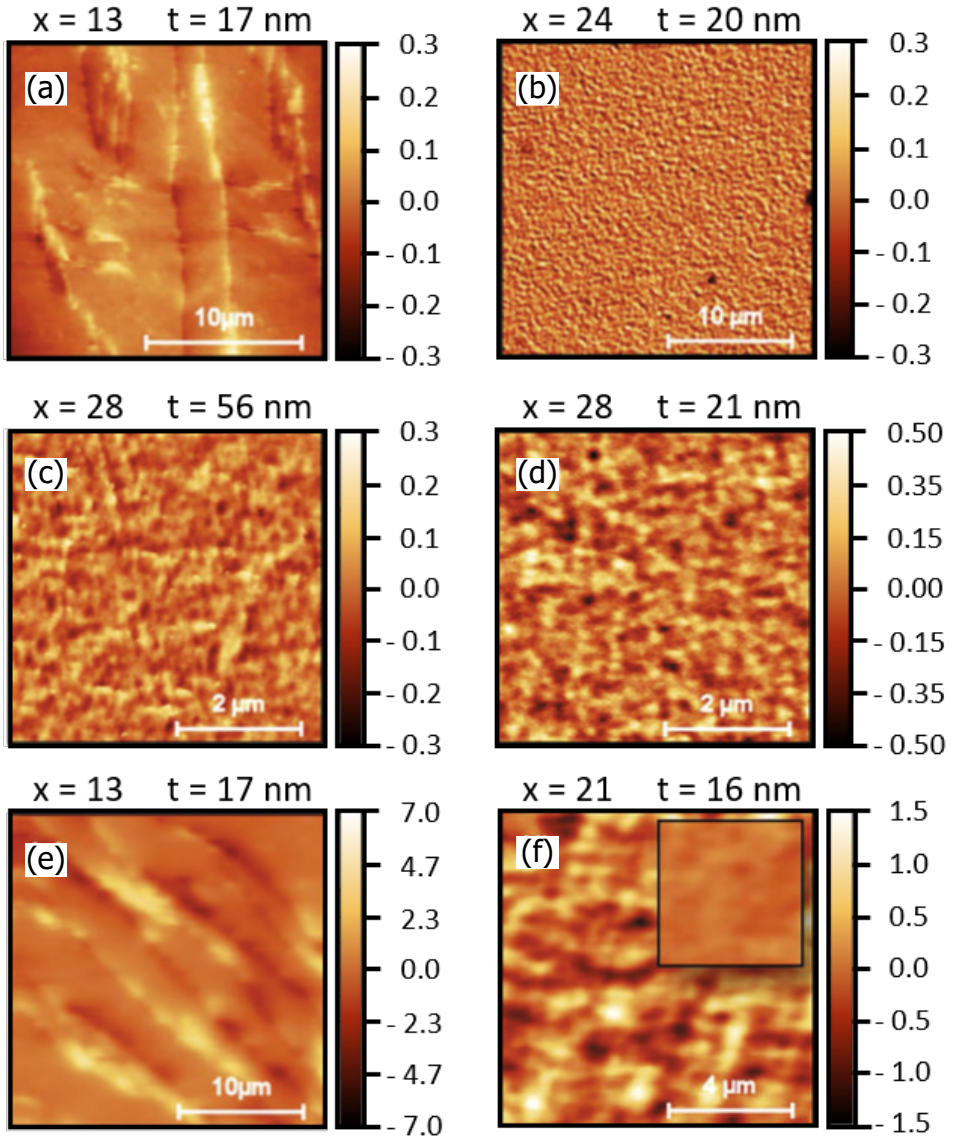

Figure 3.16: Magnetic force microscopy images taken in air for films (a) $\#_{13}^{17}$ (b) $\#_{24}^{20}$ (c) $\#_{28}^{56}$ and (d) $\#_{28}^{21}$. Low vacuum measurements for films (e) $\#_{13}^{17}$ and (f) $\#_{21}^{16}$, the color scale for the inset is ± 7 degrees.

However, our samples have not been treated after growth and, therefore the observed magnetic ripple cannot been attributed to any post-growing processing.

3.5.2 Magnetization loops

Typically, the easy axis in this type of samples is in-plane [56, 90]. If there is some out-of-plane component of **M**, as the magnetic ripple indicates, the remanent magnetization, M_r, will be lower than the saturation value, M_s [91–93].

A detailed M-H loop of the sample $\#^{56}_{28}$ along the easy axis in-plane is shown in Fig. 3.17. The equipment used is the VSM installed in PPMS platform, which can apply a maximum magnetic field of 9 T. By this means, we can correct the linear diamagnetic/paramagnetic contributions present in this type of measurements which produces a linear dependency of M *vs* H. The slope of the diamagnetic contribution was calculated from the values of m in the range $6 - 9$ T. The remanence obtained is $M_r \simeq 0.95 M_s$. The difference between values can be interpreted as if the easy axis is not exactly in that direction. The easy axis can be slightly out-of-plane in agreement with the ripple observed.

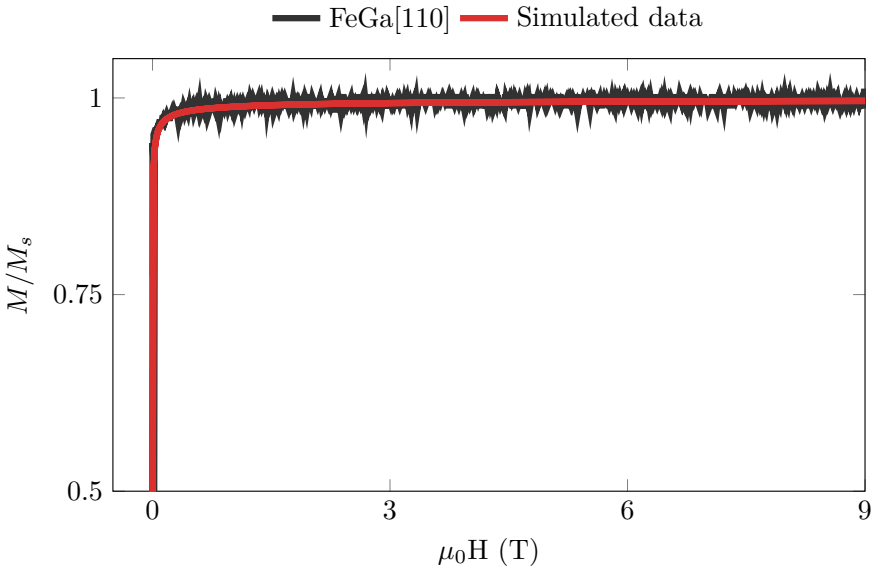

Figure 3.17: M-H loop for sample $\#^{56}_{28}$ along [110] direction (easy axis). Simulated data is calculated according to the ferromagnetic wandering axis model described in the text.

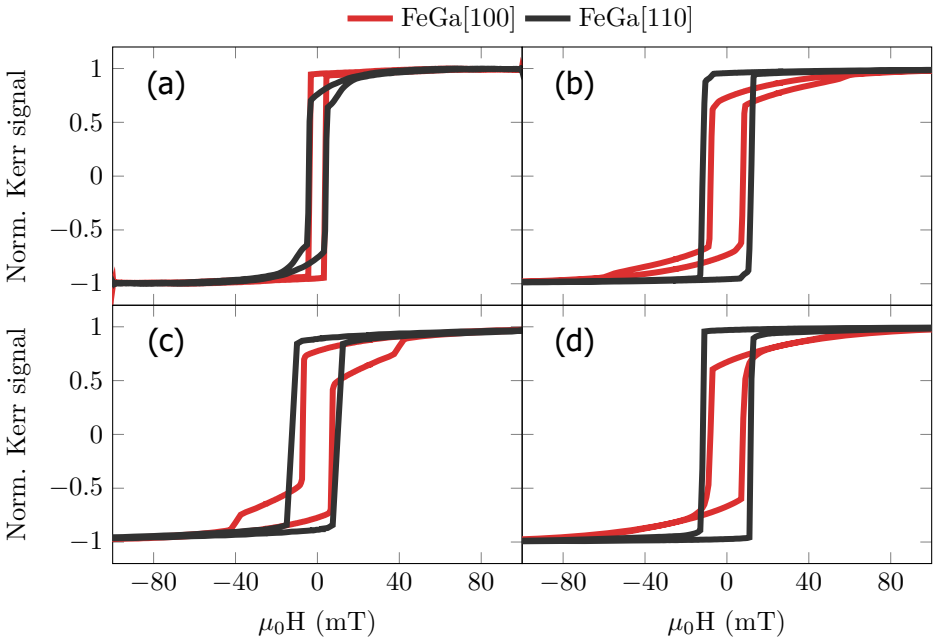

Figure 3.18: MOKE loops along FeGa[100] (red) and FeGa[110] (black) directions. The samples shown are (a) $\#^{17}_{13}$, (b) $\#^{16}_{21}$, (c) $\#^{20}_{24}$, (d) $\#^{56}_{28}$.

MOKE measurements of samples $\#^{17}_{13}$, $\#^{16}_{21}$, $\#^{20}_{24}$, and $\#^{56}_{28}$ in the $\pm 100\,\mathrm{mT}$ range are shown in Fig. 3.18, although the maximum applied magnetic field is 150 mT and the subtracted slope due to the diamagnetic contribution is obtained from the range $80 - 150\,\mathrm{mT}$. The sensitivity of the equipment used is not as high as that of the PPMS, so the value of the remanence obtained is $M_r \simeq M_s$ for all the loops measured along the easy axis.

For films with $x = 28$, we obtain that $K_1 = -10\,\mathrm{kJ/m^3}$. The need of a large magnetic field to reach a full saturation cannot be explained by misorientation between sample and magnetic field since the magnitude of the anisotropy constant is small. Therefore, the lack of magnetization at low fields can be associated with the presence of the domain structure observed in MFM images.

3.5.3 X-ray diffraction

A XRD experiment was performed in this set of samples as a routinary characterization tool and it is used in this section to extract further structural information using the Williamson-Hall method [68]. Fig. 3.19 shows a scan done by using synchrotron radiation to sample $\#^{56}_{28}$. The wavelength used is $\lambda = 0.062\,\mathrm{nm}$ and $K = 2\sin\theta/\lambda$. The out-of-plane and in-plane lattice pa-

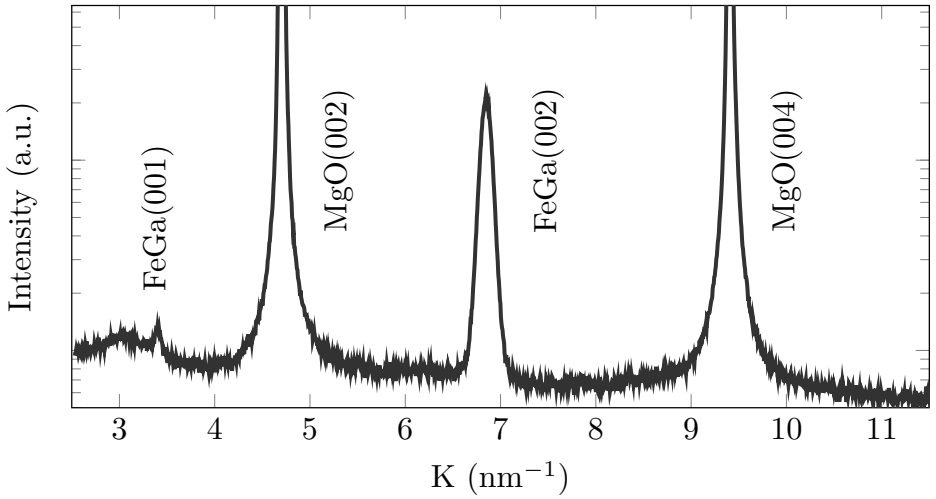

Figure 3.19: XRD pattern for sample $\#^{56}_{28}$, measured by using synchrotron radiation light with $\lambda = 0.062\,\text{nm}$ perpendicular to film plane. K is defined as $K = 2\sin\theta/\lambda$.

rameter value decreases and increases, respectively, with respect to the bulk value because of the effect of the epitaxial strain due to the MgO substrate [44]. The superlattice(001) peak observed is due to the ordering of Ga and Fe atoms. This peak is observed for $x > 20$. The (002) peak is due to the *bcc* structure. The width $\Delta K_{(00n)}$ of those peaks is fitted using gaussian functions. The values obtained from XRD for the different samples are shown in Table 3.1.

For the measurements obtained with K_α radiation, the effect on the FeGa peak width due to the presence of $\text{K}_{\alpha,1}$ and $\text{K}_{\alpha,2}$ components can be quantified by considering the splitting of the MgO substrate (002) and (004) reflections, which increases with K. Thus, the correction to the width values of the FeGa peaks can be estimated resulting in negligible changes of $\Delta\text{K}_{(100)}$ and $\Delta\text{K}_{(200)}$.

The fact that $\Delta\text{K}_{(002)}$ is larger than $\Delta\text{K}_{(001)}$ (Table 3.1) implies the presence of inhomogeneous strain [94]. Sources for this contribution are dislocations, non-uniform distortions, or antiphase domain boundaries [94]. This strain is superimposed to that obtained by the evaluation of the lattice parameters by means of the measurement of the Bragg reflections.

The Williamson-Hall method allows us to obtain the average crystallite size L and strain ϵ in the film.

$$\Delta K^2_{(n00)} = \left(\frac{0.9}{L}\right)^2 + \left(2\epsilon K_{(n00)}\right)^2 \tag{3.7}$$

x	t	$K_{(100)}$	$\Delta K_{(100)}$	$K_{(200)}$	$\Delta K_{(200)}$	L	ϵ
± 1	± 0.5	± 0.008	$\pm 4 \times 10^{-4}$	± 0.030	± 0.001	± 2	$\pm 4 \times 10^{-4}$
(% Ga)	(nm)	(nm^{-1})	(nm^{-1})	(nm^{-1})	(nm^{-1})	(nm)	
13	17	–	–	6.967	0.156	–	–
21	16	3.438	0.143	6.925	0.185	7.1	0.010
24	20	3.468	0.107	6.930	0.172	12.1	0.011
28	21	3.451	0.081	6.912	0.132	16.6	0.009
28	56	3.406	0.099	6.848	0.146	11.7	0.010

Table 3.1: Composition (x) and thickness (t) for samples grown at $T_s = 150\,°C$. Reciprocal space position (K) and Full Width at Half Height (ΔK) for (001) and (002) reflections obtained by Gaussian fits. Average crystallite size, L, and strain values, ϵ, are obtained by performing the fit of (001) and (002) reflections with the Williamson-Hall model described in the text.

L and ϵ are obtained as:

$$\epsilon^2 = \frac{\Delta K^2_{(200)} - \Delta K^2_{(100)}}{4\left[K^2_{(200)} - K^2_{(100)}\right]} \tag{3.8}$$

$$L^2 = \frac{0.9^2\left[K^2_{(200)} - K^2_{(100)}\right]}{K^2_{(200)}\Delta K^2_{(100)} - K^2_{(100)}\Delta K^2_{(200)}} \tag{3.9}$$

The values obtained for L and ϵ are in Table 3.1. The values obtained for L are not limited by the film thickness. The values for strain ϵ are in the range of 10^{-2}, indicating that the strain in the films is inhomogeneous.

The misfit between film and substrate can increment ϵ. However, the misfit between FeGa and MgO decreases with x. The lattice parameter for MgO is $a = 4.21\,Å$ [95], and the lattice parameter for FeGa at $x = 28$ is $\sqrt{2}a_{FeGa} = 4.19\,Å$ [44]. This fact discards the nucleation of misfit dislocations as the origin for an increment of ϵ. The (001) peak suggests that the film is formed by crystal regions with ordered and random distribution of Fe/Ga species. The corresponding phases are A2 and $D0_3$. This phases have slightly different lattice parameters [33] that contribute to enlarge inhomogenous strain in the film as x increases.

3.5.4 Analysis

Perpendicular magnetic anisotropies

MFM images indicate an out-of-plane component of **M**. The origin of the microscopic modulation may be a competition between perpendicular and shape

anisotropies. To study the perpendicular magnetic anisotropy (PMA) we recall the equation of effective magnetic anisotropy, K_{eff}, to observe the terms involved in PMA. The sign of K_{eff} indicates if the anisotropy is in-plane (negative) or out-of-plane (positive) [96].

$$K_{\text{eff}} = K_u + \frac{2K_s}{t} \tag{3.10}$$

where K_u is the volume anisotropy, and K_s is the surface/interface anisotropy. This two terms will be discussed in this section as a possible origin of the perpendicular anisotropy observed.

Volume magnetic anisotropy

In the analysis of magnetic structures it is usual to define the quality factor Q. The development of perpendicular magnetization in a stripe phase is related to Q values. For $Q > 1$, perpendicular magnetization appears spontaneously. But, for $Q < 1$, the developing of a stripe phase occurs when the film thickness is larger than a critical value, $t > t_c$ [97]. Fig. 3.20 a shows an example of stripe phase MFM images for Co(0001) thin films [98]. Q-factor for this films is $Q = 0.4$ and a stripe phase is weakly visible at 25 nm. For $t = 50$ nm the stripe phase is dominating the magnetic structure. We need to study if the ripple observed in our samples is due to a weak stripe phase.

Q-factor relates a relevant anisotropy energy density and the maximum possible energy density (shape demagnetization field). For our analysis, we want to obtain the Q-factor for the perpendicular magnetic anisotropy constant, K_u.

$$Q = \frac{2K_u}{\mu_0 M_s^2} \tag{3.11}$$

To evaluate K_u, a perpendicular M-H loop is needed. In the literature, the reported values for $\mu_0 M_s$ are ranging from 1.15 T [33, 99] to 1.4 T [100] for compositions around $x = 28$. We consider $\mu_0 M_S = 1.25$ T for our data. A simple estimation of K_u can be done as:

$$K_u = \frac{\mu_0 M_s (M_s - H_a)}{2} \tag{3.12}$$

To calculate K_u we proceed as follows. Fig. 3.21 shows the perpendicular loop for the sample $\#^{21}_{28}$. The black line is the experimental data and the red line is a linear fit of $\mathbf{M}$. The linear fit allows us to evaluate the anisotropy field, H_a, of the sample. The intersection between the linear fit and the saturation is $\mu_0 H_a = 1$ T. We obtain $Q = 0.2$ for samples with $x = 28$ by using eq. 3.11.

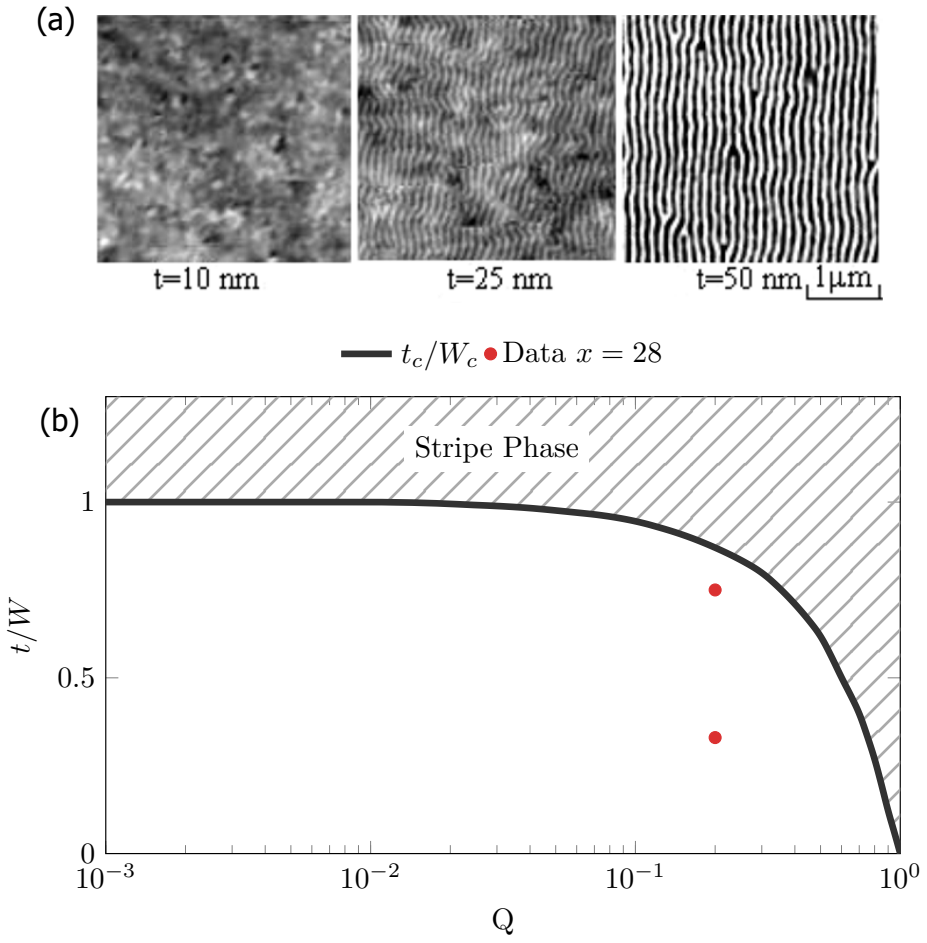

Figure 3.20: (a) MFM images of stripe domain structures developing in epitaxial Co(0001) thin films. Images are shown for a strong stripe structure (t = 50 nm), a weak stripe structure (t = 25 nm) and an in-plane magnetized film (t = 10 nm). Images taken from [98]. (b) Stripe phase Q dependence at remanence. t_c/W_c is the ratio between the critical thickness and the critical domain width, respectively. Above the critical line, the stripe phase occurs (dashed area). Our samples are in the non-stripe phase (points). Graph adapted from [97]

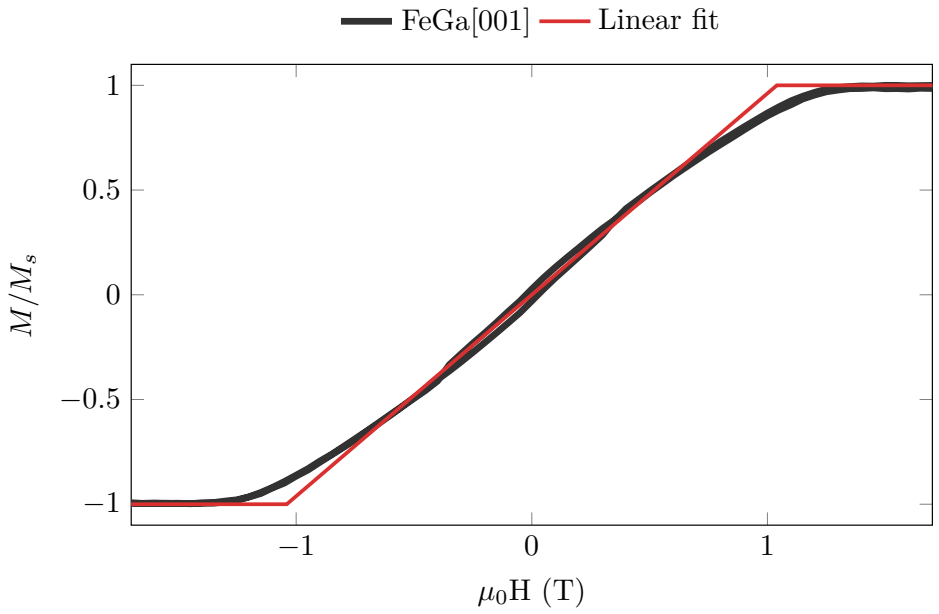

Figure 3.21: M-H loop performed by VSM perpendicular to the surface's sample $\#^{21}_{28}$. The red line indicates a linear approximation of the loop. The intersection between linear fit and saturation is the anisotropy field $\mu_0 H_a \sim 1\,\mathrm{T}$.

To complete the analysis of perpendicular magnetic structure, we need to calculate the expected domain width, W.

$$W = 2\pi\sqrt{\frac{A}{K_u}} \tag{3.13}$$

where A is the exchange stiffness constant, typically $A = 15\,\mathrm{pJ/m}$ for $x = 28$.

Fig. 3.20 b shows an adapted graph [97] to evaluate stripe phase including our data for $x = 28$. The ratio between the thickness of our samples (t) and its domain width (W) along with its Q-factor is marked on Fig. 3.20 b by points. The region of our data is clearly under the stripe transition. Therefore, a simple estimation for the volume perpendicular anisotropy, if it were present in the films, does not explain the domain structure observed as the gallium content increases.

Interface magnetic anisotropy

The samples have two interface contributions: FeGa/MgO and Mo/FeGa. These contributions can be large enough to explain the perpendicular magnetization observed. Previous experiments have shown how a large K_s can tilt **M** out-of-plane. Fe layers sandwiched by MgO blocks [101] and canting

M in Fe/MgO films [102] give values of $K_s = 2\,\mathrm{mJ/m^2}$. First principles calculations obtained $K_s = 3\,\mathrm{mJ/m^2}$ for an ideal Fe/MgO interface [103]. For Fe/Mo interfaces, K_s is probably large because a value of $K_s \sim 2\,\mathrm{mJ/m^2}$ is reported for Mo/CoFeB layers [104]. Thus, we can consider that both interfaces have nearly the same value of K_s. Using a value of $K_s = 2.5\,\mathrm{mJ/m^2}$, and the anisotropy obtained from the previous section $K_u = -124\,\mathrm{kJ/m^3}$. We obtain that for a film with thickness $t = 21\,\mathrm{nm}$, the effective anisotropy is $K_{\mathrm{eff}} = -5.29\,\mathrm{kJ/m^3}$. This value is negative, which indicates that the in-plane anisotropy dominates over perpendicular.

Some micromagnetic models [105, 106] predict canting on the magnetization. The tilting angle changes along the axial direction and it is uniform on each film plane. The models do not consider magnetic domains, but their results can be used as a starting point to evaluate the role of interfacial anisotropy in our samples. When the canting occurs, the magnetization vary from tilted at the interface, to in-plane at a certain thickness. The thickness at which the magnetization lies in-plane is the critical thickness. In Ref. [106] a phase diagram is presented for symmetric and asymmetrical structures. For $\mu_0 M_s = 1.25\,\mathrm{T}$ and $A = 15\,\mathrm{pJ/m}$, the model yields a canted state for films with thicknesses between 4.6 and 5.5 nm. These values are below of the thickness of our samples. So, although K_s is large, it is not enough to tilt **M** to point out-of-plane for samples with thicknesses above 6 nm.

Random magnetic anisotropy

Random local magnetic fields can destroy long-range order of ferromagnetic crystal materials [107]. The orientation and strength of this field varies with position, hence it is called random magnetic anisotropy (RMA). This local crystal field can be expressed as a uniaxial term of value K_{loc} [108]. The orientation of the uniaxial axis fluctuates along a length l determined by the local structure. The strength of this field can be noticed in macroscopic magnetic behaviors. Fig. 3.22 a shows an example of how the uniaxial anisotropy points randomly along the position x of the material. The local magnetic moments are coupled with each other by an exchange interaction or stiffness A. Depending on the strength of K_{loc}, it can compete with the strength of the exchange. Two distances are related to local fields, the correlation length L and l. Fig. 3.22 b shows the behavior of a strong K_{loc} where $L \sim l$. The spin system changes randomly each l length. For a system with a weak K_{loc} as Fig. 3.22 c, the lengths satisfies that $L \gg l$. The exchange stiffness can maintain a local orientation despite changes in the local anisotropy direction. The weak local anisotropy hardly perturbs the system.

Some ferromagnetic systems such as $Dy_{1-x}Y_xAl_2$ [109] present RMA and cubic

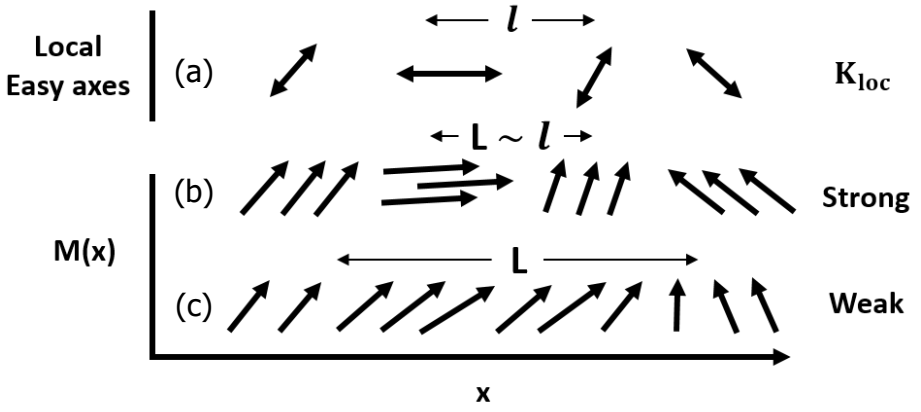

Figure 3.22: Random magnetic anistropy model. (a) Schematic representation of the variation of local anisotropy easy axis with position. l represents the length at which the random axis changes, and L is the correlation length. M(x) indicates the variation of magnetization direction in response to the local anisotropy. (b) When the anisotropy is strong, the magnetization closely follows the local axes. (c) For weak anisotropy, M is smoother. Adapted from [108].

anisotropy. This material shows the presence of a ferromagnetic phase with low remanence for x between 0.63 and 0.87. It can be explained by the increment of the local random centers in the alloy that cause a deviation of **M** from the easy direction. Also, Montecarlo simulation performed on cubic crystals with random anisotropy shows a domain-type ferromagnetic phase for strong random anisotropy [110].

The observed magnetic structures on FeGa can be explained by a weak RMA. The cubic anisotropy dominates the system, but a weak RMA allows the magnetization to wander, enabling the magnetic moment to point out-of-plane. Crystalline materials with RMA and a coherent magnetic anisotropy term can be modelled according to a ferromagnetic wandering axis (FWA) [111]. This model considers that the system is basically aligned, with the RMA providing a perturbation on the aligned state. In the remanent state, the system is not completely ordered. The random anisotropy causes the local magnetization axis to wander as one moves along the system. Three relevant fields are defined in the FWA model [111].

- Exchange field:

$$H_{ex} = \frac{\alpha M_s}{l^2} \tag{3.14}$$

where α is proportional to Ja^2, being J and a the microscopic exchange

constant and the interatomic separation repectively.

- Random anisotropy field:

$$H_r = \beta_r M_s \tag{3.15}$$

where β_r is proportional to microscopic anisotropy.

- Coherent anisotropy field:

$$H_c = \beta_c M_s \tag{3.16}$$

where β_r is proportional to coherent anisotropy.

We consider that FeGa samples have a weak RMA, this is $H_r/H_{ex} < 1$. When an external magnetic field is applied in such a way that $H > H_c$, the magnetization follows the equation:

$$\frac{M_s - M(H)}{M_s} = \frac{1}{15}\frac{H_r^2}{[H_{ex}^3\,(H + H_c)]^{1/2}} \tag{3.17}$$

The magnetization loop of sample $\#^{56}_{28}$ (Fig. 3.17) is studied by using the FWA model . The coherent field is calculated with the cubic anisotropy present in the sample. Considering $\mu_0 H_c M_s = (1/4)K_1$, we obtain $\mu_0 H_c = 2.51\,\mathrm{mT}$ for $\mu_0 M_s = 1.25\,\mathrm{T}$ and $|K_1| = 10\,\mathrm{kJ/m^3}$. The red line in Fig. 3.17 indicates the simulated data of eq. 3.17. We obtain that $H_r^2/H_{ex}^{3/2} = 0.17\sqrt{\mathrm{T}}$. The result indicates that the exchange field dominates over random field. The value obtained is in agreement with weak RMA because is not so small to be negligible.

Another result that can be extracted from the FWA model is the magnetic correlation length l.

$$l = \sqrt{\frac{A_r}{K}} \tag{3.18}$$

With values for $A_r = 15\,\mathrm{pJ/m}$ and $K = K_1$, we obtain that $l = 40\,\mathrm{nm}$. This value is clearly smaller than the ripple observed by MFM. But, MFM images shows the whole landscape of the magnetic state. The transition between regions with different M orientation cannot be performed by sharp domain walls because of the exchange energy cost. Thus, the oscillation of the magnetic signal is the result of the twist of M in several steps, each one with a length of about l. We note that the periodicity of the domain structure in RMA films with values larger than l has been observed previously in $TbFe_2$ amorphous films [112].

The origin of RMA in thin films can be explained by the variation of Ga-Ga pairs distribution in the film, the microstrain in grains and the interface magnetic anisotropy. All of these factors increase the RMA contribution to the energy as Ga content increases.

Ga-Ga pairing mechanism

The magnetic anisotropy of each Ga-Ga pair can be large $\sim 10^7\,\mathrm{J/m^3}$ [26]. However, a spatial averaging results in an effective fourfold anisotropy about 2–3 orders of magnitude smaller. In thin films, an anisotropic distribution of Ga-Ga pairs between the in-plane and the out-of-plane direction is proposed to produce a contribution to the perpendicular anisotropy as large as $\sim 10^5\,\mathrm{J/m^3}$ [113]. Local fluctuations of the Ga-Ga pairs distribution break the translational symmetry assumed in Refs. [26, 113] to obtain the macroscopic values of the anisotropy coefficients.

Let us assume that the local random anisotropy is generated by Ga-Ga pairs. At low Ga content, the Ga-Ga pairs are distributed homogeneously in the phase A2 independently of the grain size, and each grain has a similar contribution to the anisotropy energy, as happens in a single element film. When the Ga content is increased, the phase changes to an ordered one. For the ordered phase $D0_3$, the number of Ga-Ga pairs is null. At a certain concentration of Ga atoms, the material has a metastable phase between the A2 and $D0_3$ phase. There are regions with Ga pairing (A2) while other regions have Ga fixed without pairing ($D0_3$). This inhomogeneous distribution of Ga-Ga pairs can be the source of the RMA proposed.

Grain size and micro-strain

The results obtained by XRD are compared with bulk samples [114]. $\Delta K_{(001)}$ is of the same order of magnitude for both, film and bulk samples. But, $\Delta K_{(002)}$ in the films is at least one order of magnitude smaller with respect to bulk samples. In bulk, the volume of the secondary phase (001) is small compared with the main phase (002). However, in our films the volume of secondary phase is bigger. So, the grains in the film are smaller than the bulk ones. As the secondary phase can act as a center of pinning for domain walls, the increment of grain boundaries in our samples can explain a behavior more random respect to bulk. On the other hand, the observation of an inhomogeneous strain in the film suggests another mechanism to alter locally the magnetic anisotropy through the ME effect in each grain on the film.

Interface magnetic anisotropy

At the interface between thin film and the MgO substrate, local fluctuations of Fe/Ga atoms can introduce randomness. A larger value for K_s is reported for Fe-O layers [115] and the contribution per atom is expected to disappear for the Ga-O bond. A full layer of Fe atoms is satisfied for half of the layers of $D0_3$ and B2 structures. At low %Ga, Fe atoms will fill the interface in an ordered way. But, for higher concentrations of Ga, some Ga atoms will take place at the interface. The values of K_s may fluctuate from its maximum in Fe regions to lower values for Fe/Ga mixed regions. The random values of K_s can be the source of the RMA observed.

3.6 Magnetoelastic stress coefficients in FeGa, FeGaTb, and FeGaCu

This section shows the measurements performed by the cantilever method on FeGa, FeGaTb, and FeGaCu alloys at room temperature. The samples were grown at $T_s = 150\,°C$ to induce metastable structures that may enhance the magnetostriction coupling coefficients. The results in FeGa thin films indicate that the behavior is similar to the bulk samples reported. There is no increase in the magnetostrictive peak reported at $x \sim 19$ [18]. Adding third elements to the binary FeGa alloy is proposed in the literature as a method for increasing λ_{100} [116–118]. To fabricate this kind of samples experimentally, a Knudsen cell was loaded with the chosen element. The cell was evaporating at the same time that e-beam evaporator with Fe, and the other Knudsen cell with Ga. The temperature of the Knudsen cell used to add third elements was calculated by using the pressure vapor of the chosen elements.

To increase the magnetostriction observed for FeGa films, two elements were added: Tb and Cu. We decided to dope with Tb because several studies indicate that a minute Tb atomic content in the range 0.1 – 0.3% can triplicate the magnetostriction [116, 117]. Our results indicate that doping with those low quantities does not change the magnetoelastic coupling of the films. On the other hand, alloying FeGa with Cu, has been reported to double the magnetostriction [118]. We have studied at Cu atomic content 3% because there is a lack of data for this composition experimentally. The results indicate that adding Cu is detrimental for the magnetoelastic stress, which can be explained by the nucleation of the ω phase in the presence of copper. The ω phase was identified by the superlattice peaks observed by analyzing the FFT pattern of the TEM images.

3.6.1 $Fe_{(100-x)}Ga_x$ magnetoelastic coupling

FeGa alloys display two magnetostriction peaks. As shown in Fig. 1.3, at $x \sim 19$, and $x \sim 28$. The origin of the first peak is due to an increment in $|B_1|$, but the second one is due to a softening in the shear modulus [18]. The purpose of this work is to see the effect of working with thin films, and compare its properties with the bulk reported ones. To put in value the direct technological applications of these films, the magnetoelastic coupling measurements were carried out at room temperature.

FeGa alloys quenched present higher magnetostriction than the alloys slow-cooled [18]. For the first peak, the magnetostriction is ~ 350 ppm for slow-cooled, and ~ 400 ppm for quenched samples. In order to achieve experimentally high values of magnetostriction, we fabricated a set of samples at $T_s = 150\,°C$. Using this temperature is similar to grow quenched samples. The atoms are ejected from the Knudsen cell, and e-beam evaporator at temperatures above 1000 °C and are deposited on the surface of the substrate at 150 °C. The thermal energy avaliable to promote atomic diffusion on the surface is reduced and the formation of metastable phases can be favored. The formation of Ga-pairs is pointed as the source of the giant magnetostriction in FeGa alloys [36]. The ordered structure $D0_3$ (Fig. 1.2) does not present Ga-pairs and the magnetostriction decreases [82]. By using low T_s, Ga atoms cannot occupy $D0_3$ sites easily, and more Ga-pairs can be formed, and consequently, increasing the magnetostriction.

The samples grown are characterized by XRR and EDX to quantify its thickness and composition. In order to reduce the number of factors that may influence the magnetostriction, all samples were grown with $t \sim 45$ nm. The measures are carried out by the cantilever method explained in section 2.5. To measure B_1, the long axis of the cantilever needs to be FeGa[100]/MgO[110], and to measure B_2 needs to be FeGa[110]/MgO[100]. Then, from each sample only one magnetoelastic coefficient can be obtained. Both samples were grown simultaneously to obtain films with the same thickness and composition.

Fig. 3.23 shows two examples of measurements performed by the cantilever method with the dipole configuration to determine B_1 in two FeGa films with $x = 18$ and $x = 23$. As each sample has a slightly different thickness (t) and initial state of capacitance (C_0), the variation of capacitance (ΔC_x) is divided by these values to compare cycles between samples. The amplitude for the sample $x = 18$ is higher for the $x = 23$ sample. This is an indicator of a higher value of B_1. Also, both sinusoidal curves are in phase, which indicates that the sign of B_1 is the same for both samples. In this case, B_1 is negative because the motion of the dipole start at a maximum. The calibration of the sign was performed by Fe thin films as explained in section 2.5. On the contrary, for

samples that starts at a minimum, the sign of B is positive.

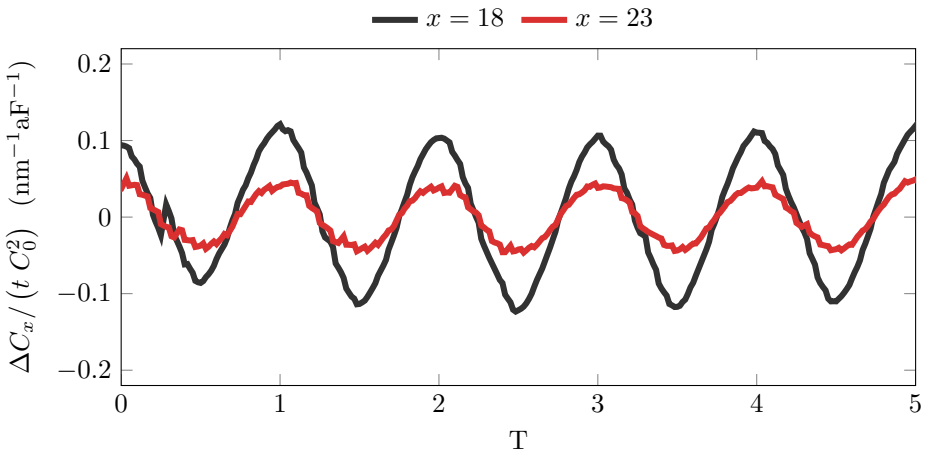

Figure 3.23: Measurements performed by the cantilever method at room temperature to determine B_1 for two samples: $x = 18$ and $x = 23$. The value of ΔC_x is divided by tC_0^2 to compare different measurements.

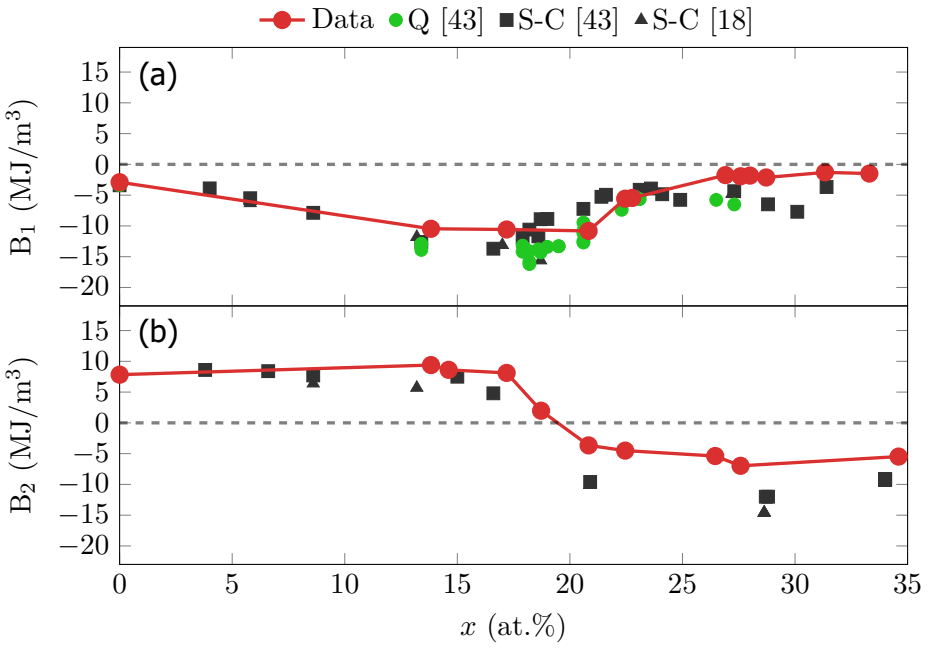

Figure 3.24: Magnetoelastic coupling coefficients for (a) B_1, and (b) B_2 at room temperature. Our data correspond to thin films of FeGa/MgO(001) grown at $T_s = 150\,°C$ with $t \sim 45\,nm$. Reference data for slow-cooled (S-C) and quenched (Q) bulk samples.

Fig. 3.24 shows the results obtained for FeGa thin films grown at $T_s = 150\,°C$ with $t \sim 45\,nm$. Our are data compared to bulk [18], and calculations [43]. For B_1 (Fig. 3.24 a), our data follow the same tendency as the bulk ones. Quenched bulk samples reach a maximum of $B_1 = -15.6\,MJ/m^3$ at $x = 18.7$. Our samples do not display a peak, but a constant $B_1 = -10.5\,MJ/m^3$ for the range $x = 13.8$ – 20.8 is achieved. After that, the magnetoelastic coupling tends to 0 as for the bulk samples. For B_2 (Fig. 3.24 b), our data also follow the same trend of the bulk samples. It is noticeable a change of sign for $x = 19$ which is attributed to a change of phase from the disordered A2 to an ordered superstructure, i.e. $D0_3$ [18]. The value of transition agrees with the obtained previously where the superlattice peaks are observed for $x > 18$.

The trend for both magnetoelastic coefficients in the nanoscale is nearly the same to the reported in the literature for bulk. There are slight changes in our thin films. $|B_1|$ is lower that of the quenched bulk samples, and $|B_2|$ for compositions with $x > 19$ also present lower values.

3.6.2 $(Fe_{83}Ga_{17})_{(100-y)}Tb_y$ magnetoelastic coupling

The origin of the large magnetostriction in FeGa alloys points to the tetragonal distortion produced by Ga-pairs [119–121]. Keeping in mind that the tetragonal distortion plays a crucial role in the magnetostriction, a possible route to enhance the magnetostriction is to add a third element to the alloy that induces a tetragonal distortion in the matrix. Several investigations on adding $3d$ and $4f$ transition elements like V, Cr, Mn, Co, Ni, Cu, Zn, Nb, Mo and Rh [122–126]; and rare-earth elements like Y, La, Ce, Tb, Dy [116, 119, 127–132] were carried out. The results indicate that the doping performed by rare-earth elements was the most effective in order to enhance the magnetostriction [119]. Among rare-earth elements studied, Tb is one of the most popular used to dope FeGa because of its high atomic radius relative to Fe and Ga. The atomic radius for Tb is 1.78 Å, whereas for Fe is 1.27 Å, and for Ga is 1.40 Å. The larger radius of Tb is suggested as the origin of the induced tetragonal distortion that enhances the magnetostriction values of FeGaTb [133].

Fig. 3.25 shows the λ_{100} values for FeGa alloys doped with Tb obtained from [116, 117]. Both curves correspond to bulk polycrystalline samples fabricated by arc-melting at constant Ga atomic content ($x = 17$). The difference between both curves lies in the thermal treatment: quenched [116], and slow-cooled [117]. The composition of these alloys is written as $(Fe_{100-x}Ga_x)_{(100-y)}Tb_y$. As the Ga atomic content is constant, by analyzing the Tb atomic content, y, the effects of doping are clearly visible. For quenched samples, λ_{100} increases from 45 ppm to 135 ppm at $y \sim 0.3$. For

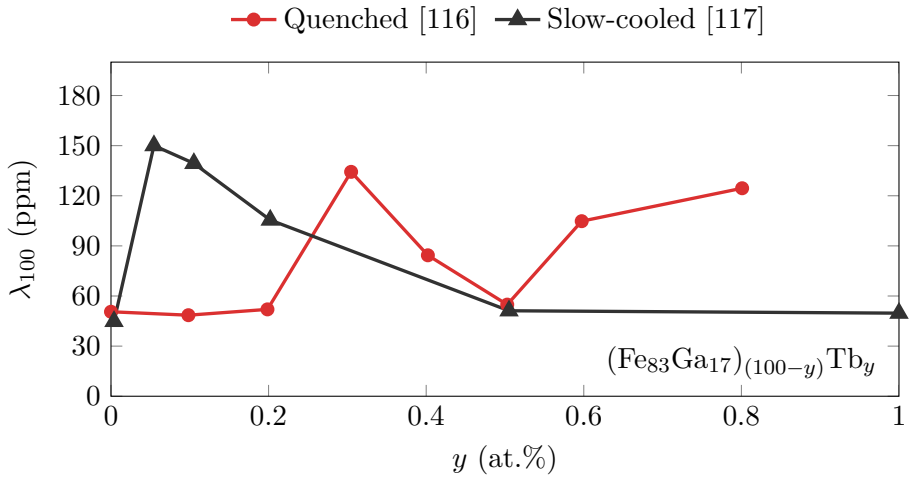

Figure 3.25: Reference data for magnetostriction in polycrystal FeGa doped with Tb. Samples were fabricated by arc-melting at constant Ga atomic content of 17%. Data for quenched [116], and slow-cooled [117] samples.

slow-cooled samples, a maximum magnetostriction of 150 ppm is achieved at $y = 0.05$. The thermal treatment seems to affect the Tb positioning in the matrix, and the maximums occurs at different Tb content. But, it is evident that a minute addition of Tb to FeGa can enhance its magnetostriction, at least in polycrystalline bulk samples.

Experimentally, to fabricate FeGaTb thin films by MBE, we use two Knudsen cells (Ga and Tb), and one e-beam evaporator (Fe). As the amount of Tb in the film is very small, we cannot detect it by EDX means. So, it is calculated by using the vapor pressure of the Fe, Ga and Tb elements. The vapor pressure for each element is calculated as:

$$\mathrm{P(mbar)} = 10^{A-B/T(K)} \tag{3.19}$$

where A and B are: $A_{\mathrm{Fe}} = 10.353$, $B_{\mathrm{Fe}} = 21038\,\mathrm{K}$, $A_{\mathrm{Ga}} = 8.558$, $B_{\mathrm{Ga}} = 14658\,\mathrm{K}$, $A_{\mathrm{Tb}} = 8.388$, and $B_{\mathrm{Tb}} = 17450\,\mathrm{K}$ [79]. Fig. 3.26 shows the vapor pressure curves for each element.

To clearly quantify the influence on the magnetostriction by the addition of Tb to the alloy, the samples are grown with the vapor pressure of Fe and Ga constant. By varying the temperature of the Tb cell we can obtain samples with different doping. The Ga content is fixed at $x = 17$ because it is where B_1 displays its maximum value for our samples (Fig. 3.24 a), and we can compare it with the reference data (Fig. 3.25). By using the eq. 3.19 we can calculate the temperature of the Tb cell to cover the range $y = 0.07$ – 0.50, which

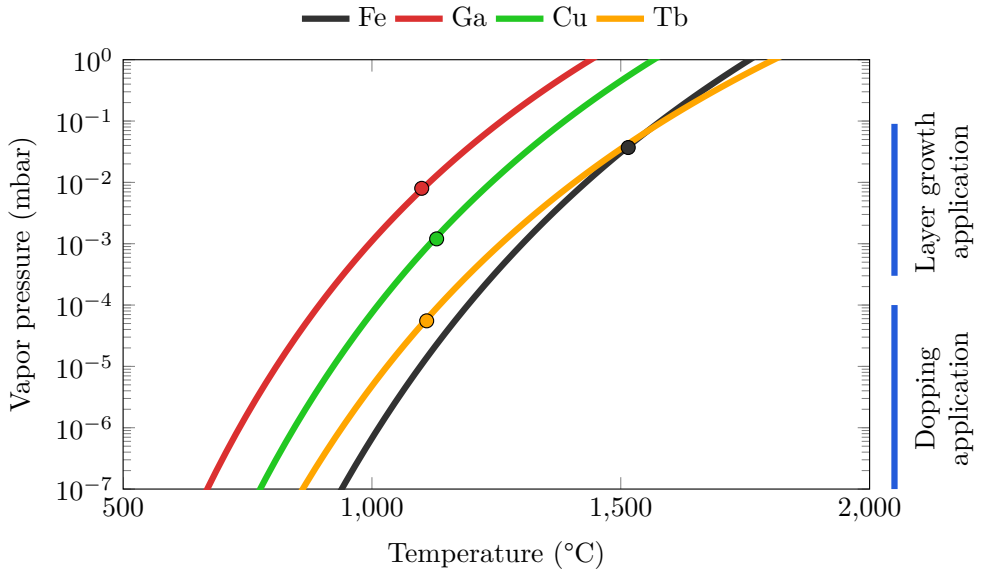

Figure 3.26: Vapor pressure for Fe, Ga, Cu and Tb elements. Calculated from eq. 3.19 with the values from [79]. Dots represent the temperatures of evaporation used in this work for each element.

corresponds to a cell temperature of T= 1050 °C – 1170 °C.

The samples are $(Fe_{83}Ga_{17})_{(100-y)}Tb_y/MgO(001)$ grown at $T_s = 150$ °C with $t \sim 45$ nm. The RHEED images taken during the deposition indicate a single-crystal growth without reconstructions. Ex-situ MOKE loops not display any changes respect to FeGa thin films undoped. Fig. 3.27 shows the magnetoelastic coupling coefficients B_1 and B_2 measured at room temperature by the cantilever method. For B_1 and B_2, the curves are nearly constant for all Tb doping. No changes are seen by the addition of a minute amount of Tb in the alloy except for a slight change in both, B_1 and B_2, at $y = 0.48$. Our results do not agree with the reported data in Fig. 3.25 . However, we should not forget that the reference data are refereed to λ_{100}, which depends on the elastic constants.

Thus, doping traces of rare-earth atoms effectively increase the density of nanoinclusions in the A2 matrix in bulk single-crystals due to the high selectivity of rare-earth atoms, they possess stronger bonding interaction with Fe atoms rather than with Ga atoms. As a consequence, the elastic constant c_{12} significantly increases, as observed by the resonant ultrasound spectroscopy method [134], with the rising density of tetragonal nanoinclusions as opposed to the constant c_{11}, resulting in a remarkable enhancement in magnetostriction due to the immediate relevance between magnetostriction λ_{001} and $c_{11} - c_{12}$.

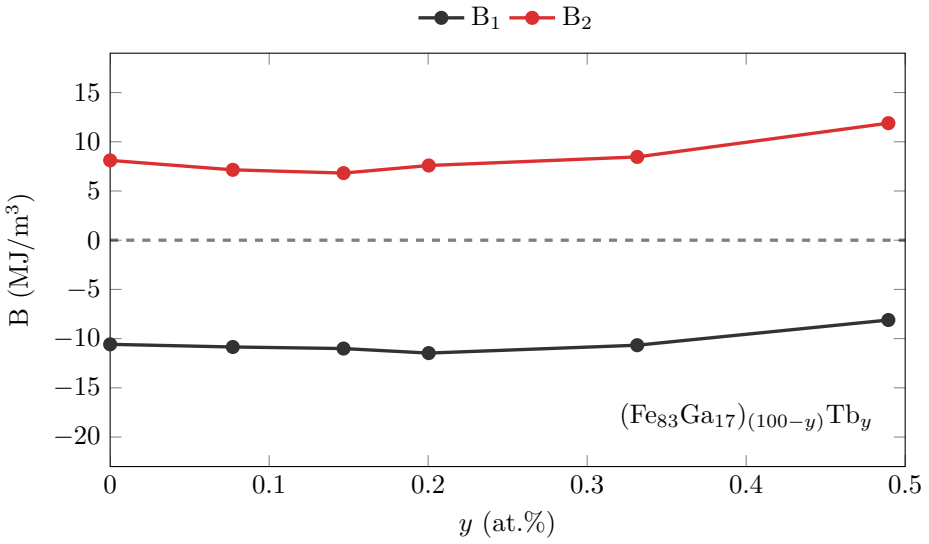

Figure 3.27: Dependence on the magnetoelastic coupling coefficients B_1 and B_2 with the Tb atomic content. Samples are $Fe_{(83-y)}Ga_{17}Tb_y$ grown at T_s = 150 °C with $t \sim 45$ nm measured at room temperature.

The cantilever method provides measurements of the magnetoelastic stress B_1. Thus, if the enhancement of the magnetostriction is due to the softening of the c_{11}-c_{12} effective elastic constant, as suggested by Chen et al. [134], and not enhancement of B_1, the results obtained from this set of experiments is a confirmation of the relevance of the elastic coefficients in FeGaTb alloys.

Another explanation for our results can be discussed in terms of the tetragonal distortions caused by Tb. As we are growing the samples at T_s = 150 °C, the behavior is expected to be similar to the quenched reference [116], and an enhancement of the magnetostriction around $y \sim 0.3$ should be observed. But, in our samples it seems that Tb does not induce any tetragonal distortion, because we do not see such enhancement. This result can be explained by the single-crystal growth achieved. The internal strain in polycrystalline samples can contribute to magnetostriction because of the lattice expansion. Also, TEM and SEM reports indicate that Tb is located preferentially at the grain boundaries [117]. As our samples are single-crystal, the internal stresses are diminished, and few grain boundaries are expected. Thus, Tb is dispersed in our samples without reinforcing the tetragonal distortions at grain boundaries, and no changes in the magnetostriction are observed.

3.6.3 $(Fe_{100-x}Ga_x)_{(100-y)}Cu_y$ magnetoelastic coupling

The effect that a non-magnetic element like Ga caused in the magnetostriction of Fe was surprising. Several investigations were carried out on other Fe binary alloys with non-magnetic elements like Ge, and Si [43]. The results indicate that the magnetostriction is also enhanced, but not as much as with Ga. However, the idea of enhancement of magnetostriction due to nonmagnetic elements brought to ternary FeGa alloys. The non-magnetic Zn was introduced in the FeGa matrix leading to the ternary alloy $Fe_{73}Ga_{18}Zn_9$, which showed a increased magnetostriction with respect to the binary alloy [124, 135]. Addition of Sn and Pb was also studied in nanoribbons, and an increment in the magnetostriction was also found [136]. However, in the same period of periodic table of elements, there are few reports on the non-magnetic transition element Cu.

Ab initio molecular dynamics simulations for the ternary alloy FeGaCu indicate that a small amount of Cu can double the magnetostriction of the FeGa binary alloy [118]. The position of Cu atoms in the matrix plays a crucial role in the enhancement of the magnetostriction. Fig. 3.28 shows the $Fe_{79.7}Ga_{18.7}Cu_{1.6}$ alloy with two different configurations of Cu atoms. The structure in which the enhanced magnetostriction was calculated is shown in Fig. 3.28 a. The nearest neighbors of Cu atoms in this configuration are Fe atoms. But, if among the nearest neighbors are Ga atoms (Fig. 3.28 b), then, the magnetostriction decays to values below of those of the FeGa binary alloy (300 ppm). Depending on the position of Cu atoms, the magnetostriction of this ternary alloy varies in the range $\lambda_{100} = 220$ – 550 ppm. Experimentally, it is a hard task to stabilize the phase with high magnetostriction instead of other phases. Calculations indicate that Cu atoms prefer to stay together or substitute Fe, like Fig. 3.28 b. But, it is pointed that the quenching process can freeze the metastable high-magnetostriction structure. An experimental research on the FeGaCu bulk alloy was performed to clarify the role that Cu plays in the magnetostriction [137]. The result indicates that the magnetostriction of FeGaCu is worse that of FeGa. Adding Cu decreases the magnetoelastic coupling coefficients, and increases the Young's modulus. Therefore, the magnetostriction is worsen doubly.

As there are few experimental data to endorse the calculations performed on $(Fe_{100-x}Ga_x)_{(100-y)}Cu_y$ alloys, we decided to fabricate thin films of this alloy and study its magnetoelastic couplings. Ab initio calculations show an enhancement of magnetostriction at $y = 1.6$ [118], but not other compositions were discussed. Experimentally, we fabricated a set of samples with constant Cu atomic content, while varying the Ga atomic content. Two Knudsen cells (Ga and Cu) and e-beam evaporator (Fe) were used to evaporate the elements.

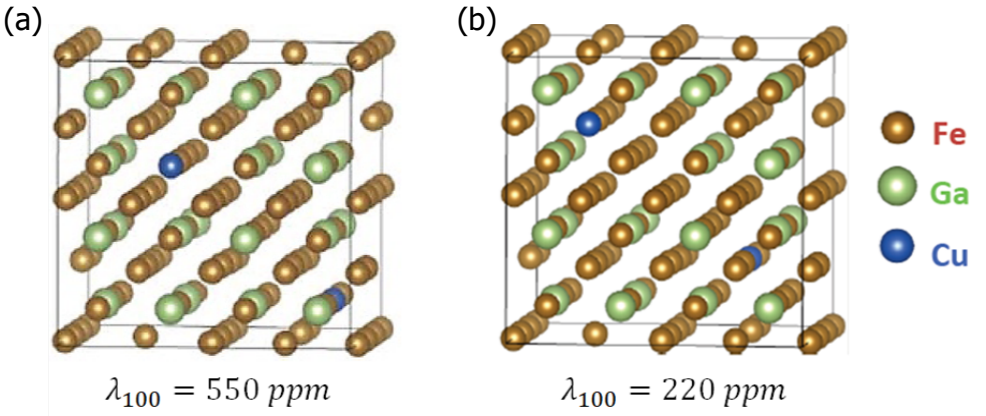

Figure 3.28: Atomic configuration of $Fe_{79.7}Ga_{18.7}Cu_{1.6}$ with two Cu atoms. (a) High magnetostriction configuration with Cu atoms nearest neighbors being Fe atoms. (b) Low magnetostriction configuration with Cu atoms nearest neighbors being Fe and Ga atoms. Brown, green and blue balls represent Fe, Ga, Cu atoms, respectively. Taken from [118].

The vapor pressure of the Knudsen cell for Cu is obtained from the eq. 3.19 where $A_{\mathrm{Cu}} = 8.388$ and $B_{\mathrm{Cu}} = 17450\,\mathrm{K}$. The temperature of Knudsen cell necessary for $y = 1.6$ is $\sim 1110\,^{\circ}\mathrm{C}$. But, due to limitations in ex-situ quantification by EDX, the temperature of the cell was raised to $1140\,^{\circ}\mathrm{C}$. At this temperature, the alloy is $(Fe_{100-x}Ga_x)_{97}Cu_3$, and the Cu content can be detected by EDX. The samples were grown at $T_s = 150\,^{\circ}\mathrm{C}$ with $t \sim 45\,\mathrm{nm}$. The RHEED images taken during the deposition indicate a single-crystal growth.

Fig. 3.29 shows the magnetoelastic coupling stresses B_1 and B_2 for the FeGaCu and FeGa films, the latter data for comparison purpose. For B_1 (Fig. 3.29 a), adding Cu to FeGa decreases its value. The peak $B_1 = -10.81\,\mathrm{MJ/m^3}$ obtained at $x = 20.83$ for FeGa, is not observed for FeGaCu because the curve $|B_1|$ is monotonically decreasing as the Ga content increases. This result is in agreement with the obtained by Zhao et al. [137], which also points that the control of Cu distribution is a hard task to achieve. Comparing our result with the proposed by the calculations [118], the Cu atoms in our samples are surrounded by both Fe and Ga atoms, which is detrimental to the magnetostriction. Nevertheless, the behavior of B_2 presents some singularities. For B_2 (Fig. 3.29 b), all the values are negative, and $|B_2|$ is larger in the series with Cu for compositions with $x > 19$.

To investigate the crystal structure of the ternary alloy FeGaCu, the sample $(Fe_{73}Ga_{27})_{97}Cu_3$ was characterized by TEM. Fig. 3.30 a shows the TEM image, where the atoms for substrate and film are aligned indicating an epitaxial growth. Fig. 3.30 b shows the FFT pattern of the FeGaCu thin film at zone

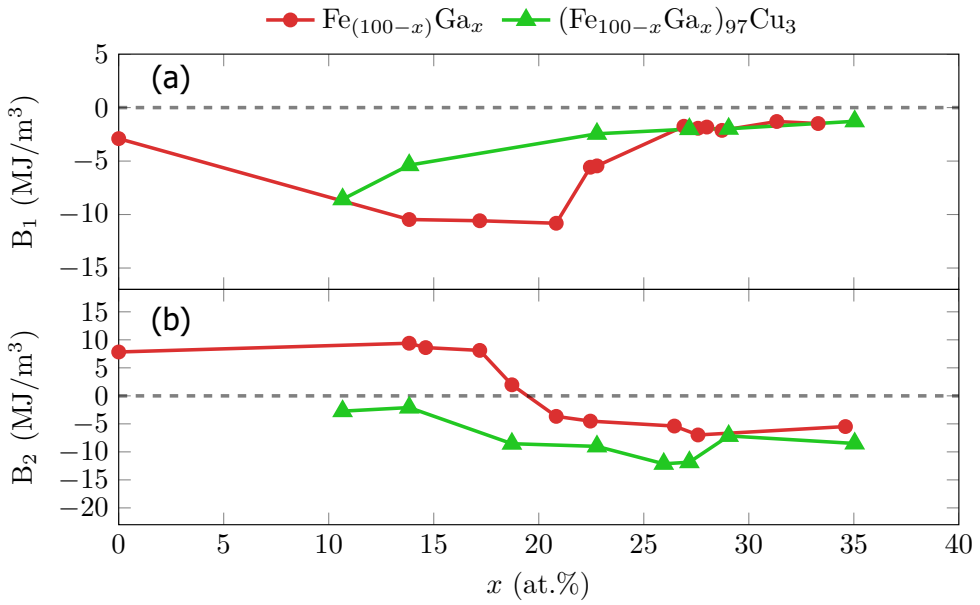

Figure 3.29: Magnetoelastic coupling coefficients for (a) B_1, and (b) B_2 at room temperature. Thin films were grown on MgO(001) at $T_s = 150\,°C$ with $t \sim 45\,nm$. Red circles for $Fe_{(100-x)}Ga_x$ binary alloy, and green triangles for $(Fe_{100-x}Ga_x)_{97}Cu_3$ ternary alloy.

axis [110]. There are several spots indicating a superorder in the lattice. These spots can be explained by an induced hexagonal ω phase in the sample. It has been reported that an ideal ω structure can be found in FeGa polycrystalline at $x = 27$ [138]. The ω structure is obtained from a $D0_3$, where one pairs of {111}-A2 planes collapse to an intermediate position leaving the next plane unaltered [139–144]. The relationships between A2 and ω are $[0\bar{1}1]$-A2 $\parallel$ $[1\bar{2}10]$-ω, $(\bar{1}11)$-A2 $\parallel$ (0001)-ω [142]. This phase is similar to the observed in Ti-Mo alloys [140, 144]. Fig. 3.30 c shows the pathway from $D0_3$ structure to ω structure [138]. The simulated $[1\bar{2}10]$-ω electron diffraction pattern is shown in Fig. 3.30 d, which is consistent with the FFT pattern of Fig. 3.30 b. Two variants of ω phase are found in our sample, ω_1 and ω_2. The pattern in Fig. 3.30 d is simulated for ω_1. The variant ω_2 is symmetric to ω_1 horizontally. The indexed spots of these two variants are marked in Fig. 3.30 b with red circles for ω_1, and green circles for ω_2. The origin of the transition $D0_3$ to ω phase is suggested by a softening in the shear modulus [145]. The reduced shear modulus increases the instability of the lattice, and $D0_3$ phase collapses.

We propose that the ω phase is caused by the Cu atoms collapsing the lattice. If we compare the FFT pattern of $(Fe_{73}Ga_{27})_{97}Cu_3$ (Fig. 3.30 b), and the obtained for $Fe_{76}Ga_{24}$ (Fig. 3.10 b), the superorder lattice spots are only visible

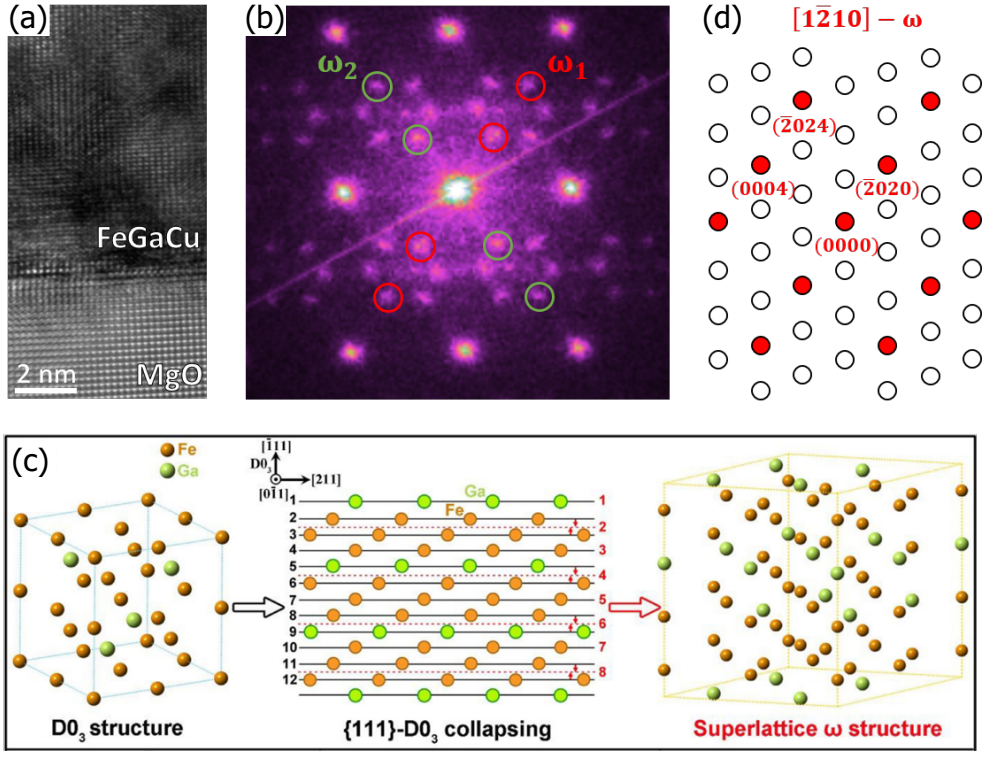

Figure 3.30: (a) TEM image indicating MgO substrate and FeGaCu thin film. (b) FFT pattern of FeGaCu corresponding to zone axis [110]. Spots are indexed according to two variants of the ω phase, ω_1 (red) and ω_2 (green). (c) Pathway explaining the transition from $D0_3$ to ω structure via {111} collapsing. (d) Simulated electron diffraction pattern for [0$\bar{1}$1]-ω zone axis. (c) and (d) taken from [138].

in the FeGaCu FFT pattern. The difference of 3% in Ga content between the previous samples cannot be discarded as the origin of the ω phase, but the only experimental report about the ω phase in FeGa alloys is achieved by directional solidification along with post-grown thermal processing [138]. In our case, the sample is measured as-grown without any post-annealing process. So, it seems plausible to argue that the ω phase observed is caused by the addition of Cu atoms.

3.7 Conclusions

The structural and magnetic characterization of FeGa/MgO(001) samples present dependency with the temperature of the substrate while the deposition is carried out, and the composition of the alloy. *bcc* structure is found at low T_s (150 °C), and *fcc* structure at higher T_s (400 °C). A superlattice order is found for compositions $x > 18$. High-T_s samples present an isotropic magnetic behavior, whereas low-T_s samples present cubic magnetic anisotropy. It is found a reorientation of the magnetic axes for compositions $x > 19$, and the stabilization of $K_1 \sim -22\,\mathrm{kJ/m^3}$ in this range, as opposed to the bulk values of $K_1 < -10\,\mathrm{kJ/m^3}$.

FeGa thin films have shown magnetic domain structures that change from in-plane to a ripple magnetic structure as the Ga content increases. The origin of the magnetic anisotropy associated to the ripple can be due to: a local inhomogeneous distribution of Fe/Ga atoms throughout the film volume, the interface with the MgO substrate, and local strain. Random magnetic anisotropy can distort the magnetization to make it non-uniform in-plane. We propose that a RMA associated with such non-homogeneous distributions can explain the observed magnetic structures.

The study of B_1 and B_2 for FeGa thin films does not show any improvement over bulk material. The tendency of B_1 and B_2 is nearly the same to the bulk ones, including the change of sign for B_2 at $x = 19$. For FeGa doped with Tb, no changes were seen in the magnetoelastic coupling coefficients. The single-crystal growth fabrication process can be behind this behavior. Tb atoms tend to migrate to grain boundaries and induce tetragonal distortions. Polycrystalline films have a great number of grains where Tb can migrate, but for single-crystal films there are few boundaries to migrate and generate distortion. For the ternary FeGaCu samples, the values of $|B_1|$ decrease with respect to FeGa, whereas B_2 are negative for all Ga compositions. An investigation on the sample $(Fe_{73}Ga_{27})_{97}Cu_3$ indicates that a ω phase is formed by adding Cu. Then, the negative values for B_2 may be explained by the superorder lattice ω.

Chapter 4

Straintronic multiferroic heterostructures

4.1 Introduction

Conventional hardware platforms for computing, information processing and information communication are built with electronics based on electric charge-based devices, i.e. transistors, to carry out computational tasks. Charge-based electronics demands a lot of energy to work, and it is still remote that transistors will ever evolve to a point in which they dissipate sub-aJ of energy to process one bit of information [8]. Also, a transistor is volatile, it cannot retain information once powered off. Some alternatives to transistors are being investigated in the field of magnetic devices. The magnetic devices are non-volatile, and can be more efficient energetically than transistors in some circumstances [8]. Materials with interconnected magnetic and electric capacities [146] are arising as a promising candidates to make efficient magnetoelectronic devices. Heterostructures based on ferroelectrics and ferromagnets can control the magnetization actively through the ferroelectric part of the structure at room temperature [147] without magnetic field or electric current [148–151]. One of them is based on the phenomena located at the FE-FM interface: modification of the population of spin-up and spin-down electron density of states [152] and voltage-driven oxygen migration and modification of the oxide ferromagnet [153]. Other mechanisms are based on the strain transferred from the ferroelectric crystal to a ferromagnetic film generating a uniaxial magnetic anisotropy through the magnetoelastic coupling effect [154–156]. This mechanism is called straintronic and is the main topic of this chapter. The field of straintronics presents a low-energy consumption to store bits [10–12], it shows lower heat dissipation per switching cycle [151] and the magnetoelectric

coupling parameter α_E is larger than any other coupling mechanism[148].

A multiferroic structure is based on a magnetostrictive material coupled to a piezoelectric crystal through intermediate strain [13–16]. The magnetization of the magnetostrictive material can be controlled by the electrically generated mechanical strain in the piezoelectric. If the magnetic material can encode two states of magnetization, then it can act as a binary system with bits 0 and 1. A straintronic device can switch between magnetic states consuming $\sim 1\,\mathrm{aJ}$ [157], which is about two orders of magnitude lower than the energy dissipated by a transistor. This devices do not need electric current to switch the bit, this why they are low-energy consumers.

Several groups have investigated the control of magnetization in magnetostrictive films deposited on piezoelectric films by using an external electric field. They have demonstrated the reversible control of nanomagnetic domains [158], and strain assisted reversal of perpendicular magnetization in Co/Ni multilayers [159]. Others have studied straintronic heterostructures based on rare-earth magnetostrictive layers such as lanthanum strontium manganite (LSMO) [160], Tb/Co_2/FeCo multilayers [161], and Terfenol-D [162]. But, rare-earth-free magnetostrictive materials have attracted interest, such as FeGa because of the high magnetostriction that present at compositions $x = 19, 28$, and the control of its magnetization through the strain generated by the substrate has been achieved [163, 164].

4.2 Ferroelectric substrate: PMN-PT

The strain-mediated coupling requires materials with large electrostriction. Relaxor ferroelectric compounds, as $[Pb(Mg_{1/3}Nb_{2/3})O_3]_{0.7}$ – $[PbTiO_3]_{0.3}$ (PMN-PT) [165] are used to induce strain in magnetic thin films with significant magnetoelastic coupling. Many of these films are amorphous [154, 166] or polycrystalline [162, 167–171] to diminish native large magnetocrystalline anisotropy that can conceal the effect due to the ferroelectric domain switching, usually detected by 90° easy axis switching [172]. For instance, when PMN-PT is coupled to a Ni layer, this heterostructure is capable of storing the magnetization orientation of the ferromagnetic layer acting as a non-volatile device [173]. Moreover, its lattice parameter is $a_{\text{PMN-PT}} = 0.402\,\mathrm{nm}$ [174], which is near to $\sqrt{2}a_{\text{FeGa}} = 0.419\,\mathrm{nm}$ and the preparation of FeGa crystalline films is expected. In this thesis, two oriented surfaces of PMN-PT are used as substrate: (001), and (011).

Fig. 4.1 shows the eight possible polarization directions of PMN-PT crystal. The polarization points along the body diagonals of the pseudo-cubic unit cell, which correspond to the four structural (ferroelastic) domains (r1, r2, r3, and

r4) [175]. Fig. 4.1 a shows the polarization switch for PMN-PT(001). When the polarization is switched by applying electric field perpendicular to the surface, PMN-PT[001], it has 3 available routes to switch from $r1^+$ state to an orientation with P pointing downwards, 180°, 71°, and 109°. The switch from $r1^+$ to $r1^-$ is a 180° switch in which the final state is antiparallel to the original polarization vector. The switch $r1^+$ to $r3^-$ is a 71° rotation of $\mathbf{P}$ that leads to a same strain that the 180° switch. The 109° switch, from $r1^+$ to $r2^-/r4^-$ is a ferroelastic switching mode that changes the sign of the distortion in the (001) plane and remains after the application of the electric field. Thus, the 180°, and 71° switches are not desirable in straintronic applications. Fig. 4.1 b shows the polarization switch for PMN-PT(011). When an electric field is applied along [0-1-1] direction, three switch paths are allowed: 71° (from $r1^+$ to $r3^-/r4^+$), 109° (from $r1^+$ to $r2^-$), and 180° (from $r1^+$ to $r1^-$). Only the 71° ferroelastic switching introduces to a strong lattice deformation along the [011] direction. For PMN-PT(011) substrates, the desired switching path is 71°, in opposite to a 109° switch for PMN-PT(001).

PMN-PT(011) commercial substrates (Crystal-Gmbh) were tested prior to thin film deposition. Fig. 4.2 a shows the polarization-electric loop. Several cycles were measured ranging from E = ± 0.25 MV/m to ± 1.25 MV/m along the thickness direction of the PMN-PT single-crystal. The values obtained for remnant polarization and coercive E-field are in agreement with the literature [176], i.e. for the cycle E = ± 0.8 MV/m, the remanence is $\sim 5\,\mu$C/cm^2, and the coercive field is ~ 0.3 MV/m. The substrate before poling is also studied by AFM. Fig. 4.2 b shows the topography of PMN-PT(011). Piezoresponse force microscopy (PFM) let us observe the ferroelectric domains. Fig. 4.2 c-d shows the lateral and vertical piezoresponse images, respectively. For lateral PFM, the color code indicates the in-plane polarization, whereas for vertical PFM, it shows the out-of-plane polarization. The ferroelectric domains size is $< 1\,\mu$m, and are in a random fashion, as expected for substrates before applying electric field.

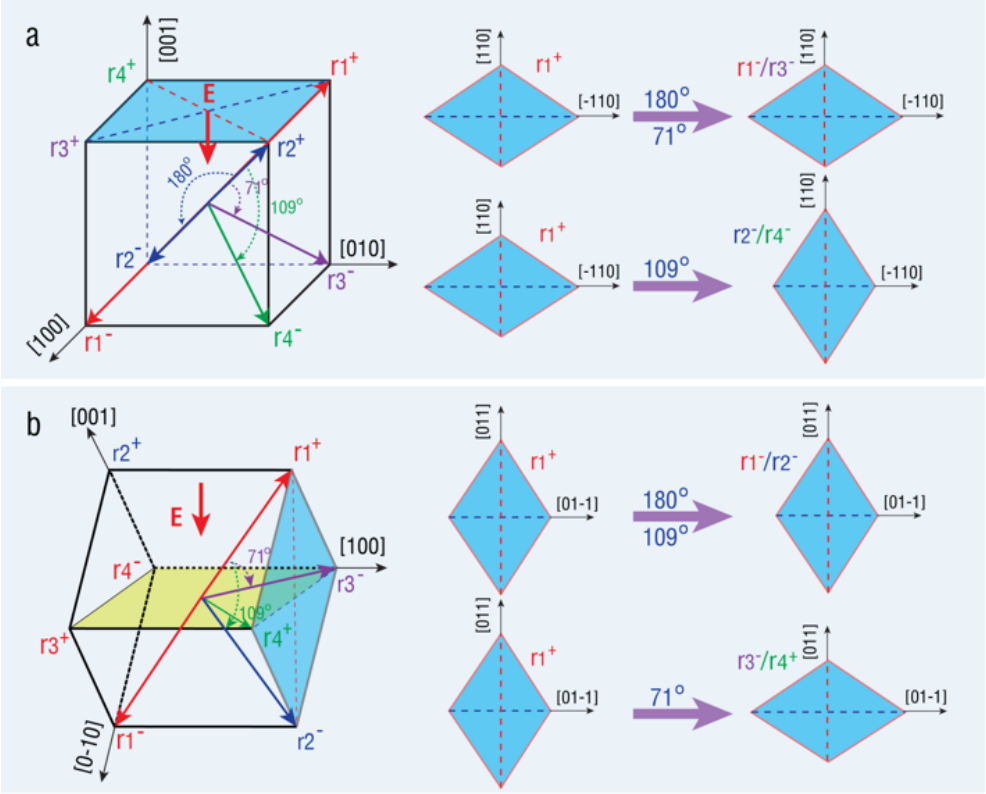

Figure 4.1: Scheme of the different paths that the polarization takes in PMN-PT. (a) PMN-PT(001) with an applied electric field along PMN-PT[001]. (b) PMN-PT(011) with an applied electric field along PMN-PT[011]. The initial state for (a) and (b) is $r1^+$. When the electric field is applied, the pseudo-cubic unit cell can be strained. The switch that causes a strong strain is: (a) 109° from $r1^+$ to $r2^-/r4^-$, and (b) 71° from $r1^+$ to $r3^-/r4^+$. Taken from supplementary [175]

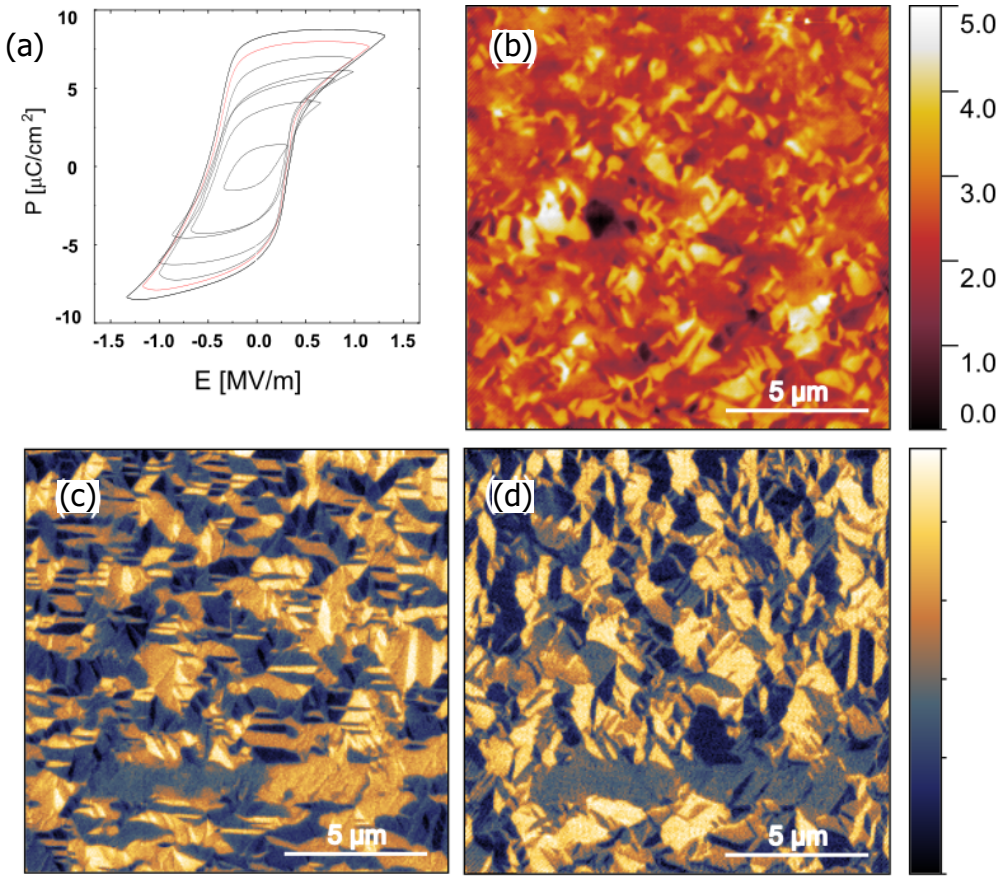

Figure 4.2: Examples of (a) polarization–electric-field hysteresis curves, (b) topography, (c) lateral, and (d) vertical piezoresponse force microscopy images taken on a PMN-PT(110) crystal. The color bars indicate in-plane **P** along the horizontal direction for lateral PFM, and out-of-plane **P** for vertical PFM.

4.3 Fabrication of heterostructures

The first attempt made to obtain crystalline layers was the deposition of FeGa layers on clean PMN-PT crystals. As said in the previous section, this idea is based on the low misfit between PMN-PT[100] and FeGa[110] directions. However, the result is the formation of polycrystalline films for both types of PMN-PT substrates. Another growing route was developed during this investigations to achieve a single-crystal growth at low T_s. This procedure incorporates the deposition of a thin layer of MgO and it is one of the first ever reported FeGa single-crystal growing using PMN-PT as substrate. The use of MgO has two main reasons. First, FeGa growns epitaxially in MgO surfaces and secondly, layers of MgO can be easily grown by e-gun evaporation in ultra high vacuum [177].

Fig. 4.3 shows the temperature scheme used to obtain polycrystal and single-crystal films. Prior to the growth of the film, the PMN-PT crystal was heated up to 800 °C over 2 hours to obtain a clean surface. For a single-crystal FeGa film (Fig. 4.3 a) it is necessary to grow a MgO seed layer. This layer is deposited at substrate temperature of 600 °C using an e-gun at a rate of 1.71 nm/min. The thickness of MgO layer is ~ 1 nm. Then, the sample is annealed at 800 °C for 2 hours. After that, the substrate temperature is decreased at a rate of 5 °C/min until the sample reaches 150 °C. Polycrystalline samples are obtained (Fig. 4.3 b), if the procedure explained about the MgO layer is skipped. For both routes, at 150 °C we grow the FeGa film with a thickness in the range of $5 - 20$ nm with a composition around x ~ 19 (first magnetostrictive peak). To achieve this composition the Ga cell is held at 1120 °C, and the e-gun is evaporating Fe at a rate of 0.76 nm/min controlled with a quartz microbalance. After that, a Mo capping layer of ~ 2 nm is deposited to prevent oxidation by e-gun at 1.5 nm/min.

4.4 Structural characterization

4.4.1 FeGa/MgO/PMN-PT

In situ RHEED images were taken at several stages of the sample fabrication. Fig. 4.4 and Fig. 4.7 shows the RHEED images for PMN-PT(001) and PMN-PT(011) substrates, respectively. After the cleaning process, Kikuchi lines are visible, indicating the cleanness and the flatness of the surface of the substrate. When the MgO is deposited, the patterns are aligned with the substrate evidencing the epitaxial growth between PMN-PT and MgO for both (001) and (011) surfaces. After that, RHEED patterns of FeGa show a crystalline growth, although interesting differences are observed for films grown on (001) and (110) surfaces as will be discussed in the next sections.

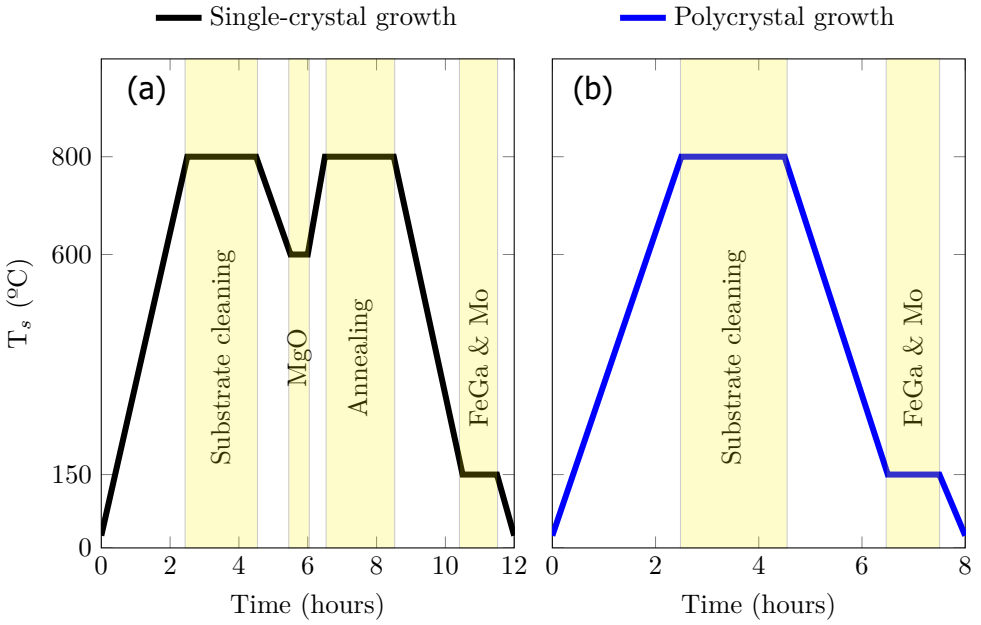

Figure 4.3: Temperature scheme used to obtain (a) single-crystal FeGa, and (b) polycrystal FeGa films using PMN-PT substrates. In yellow is marked the procedure carried out during that time.

The epitaxial growth using MgO as seed layer is achieved, and a single-crystal structure is obtained. The RHEED patterns demonstrate that the growth procedure chosen allows us to fabricate single-crystal heterostructures. The reproducibility of this process was tested, and all of the samples fabricated via this route were single-crystal.

PMN-PT(001) heterostructures

Fig. 4.4 shows RHEED images for the FeGa/MgO/PMN-PT(001) heterostructure. The RHEED images for the three layers are observed every 90°, implying a 4-fold in-plane symmetry. Also, two different RHEED patterns are obtained at an azimuth angles separated by 45° from each one. For the FeGa layer, a simple estimation of the epitaxial relation can be done by analyzing the distance between streaks in images taken at known azimuth angles. Thus, the ratio $d_1/d_2 = \sqrt{2}$ (see Fig. 4.4), which is equivalent to the ratio between the modules of the reciprocal lattice vectors $2\pi/a_{110}$ and $2\pi/a_{100}$. $\sqrt{2}a_{\mathrm{FeGa}}$ matches the lattice parameter of the MgO, so, it can be concluded that the FeGa film grows according to the next epitaxial relationships:

$$\begin{aligned} &\text{PMN-PT[100]} \parallel \text{MgO[100]} \parallel \text{FeGa[110]} \\ &\text{PMN-PT[110]} \parallel \text{MgO[110]} \parallel \text{FeGa[100]} \end{aligned} \tag{4.1}$$

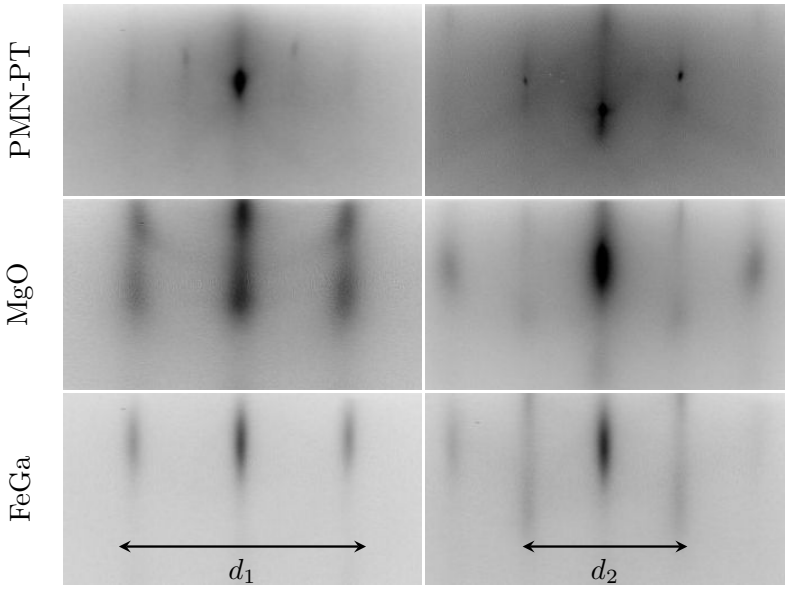

Figure 4.4: RHEED images of FeGa/MgO/PMN-PT(001) samples. For the first column the images are in the PMN-PT[100] direction, and for the second column, in the PMN-PT[110] direction. First row is the RHEED image for the PMN-PT(001), second row for the MgO seed layer, and third row for the FeGa film. The arrow indicates the distance between two symmetrical streaks.

The lattice parameter for each material is $a_{\text{PMN-PT}} = 0.402\,\text{nm}$, $a_{\text{MgO}} = 0.421\,\text{nm}$, and $a_{\text{FeGa}} = 0.290\,\text{nm}$. The misfit η between each layer is:

$$\eta_{\text{MgO/PMN-PT}} = \frac{a_{\text{MgO}} - a_{\text{PMN-PT}}}{a_{\text{PMN-PT}}} = 4.72\% \tag{4.2}$$

$$\eta_{\text{FeGa/MgO}} = \frac{\sqrt{2}a_{\text{FeGa}} - a_{\text{MgO}}}{a_{\text{MgO}}} = -2.58\% \tag{4.3}$$

Fig. 4.5 shows the XRD pattern for the heterostructure FeGa/MgO/PMN-PT(001). The peak FeGa(002) is indexed as a bcc crystal and the plane (002) is the expected result for the epitaxy. The MgO layer is so thin that its peak is not present, but we can consider that if the FeGa(002) peak is present, the MgO layer is growing according to a MgO(001) surface (as observed in RHEED and TEM images). Then, the epitaxy of the heteroestructure is FeGa(001)/MgO(001)/PMN-PT(001). The lattice parameters obtained from the XRD pattern are: $a_{\text{PMN-PT}} = 0.4041\,\text{nm}$, and $a_{\text{FeGa}} = 0.2892\,\text{nm}$. The peak at $2\theta = 33.19\,^\circ$ is indexed as PMN-PT(003/2), which is a peak that sometimes emerges in the measurements due to the presence of radiation with $\lambda_{\text{Cu}}/2$.

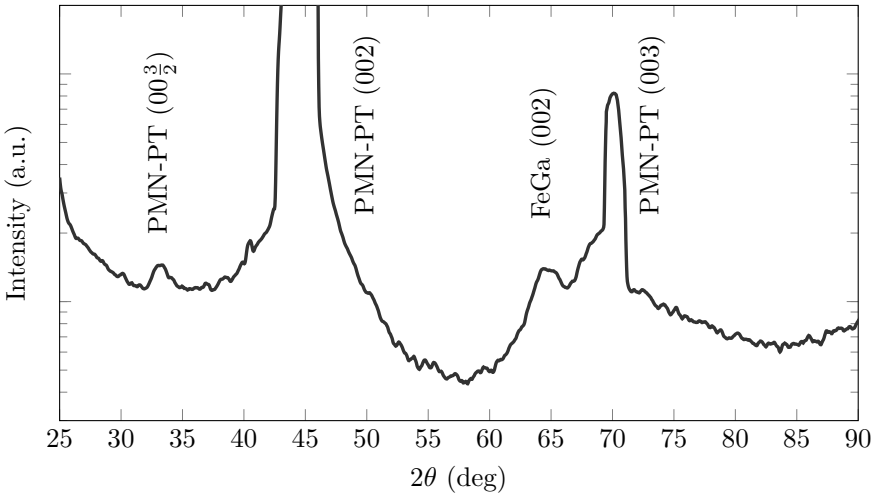

Figure 4.5: XRD pattern for the sample FeGa/MgO/PMN-PT(001).

The sample was characterized by aberration-corrected scanning transmission electron microscopy in combination with electron energy-loss spectroscopy (STEM-EELS). Fig. 4.6 shows a representative high-angle annular dark-field (HAADF) image of the heterostructure along the [100] zone axis of the PMN-PT substrate.

In the TEM images, the intensity of the signal is proportional to the atomic number. The brighter dots corresponding to the substrate in Fig. 4.6 a are the Pb columns. The MgO layer is darker because its atoms are lighter. FeGa and Mo films can be seen as an intermediate grey color. Fig. 4.6 b shows a HAADF image on the area marked on Fig. 4.6 a. This area is taken at higher resolution and the contrast is enhanced locally. The image displays atomic ordering for the MgO and FeGa layers. For the PMN-PT crystal, bright points located at the midpoints of the Pb square lattice are now visible.

Fig. 4.6 c shows the Fast Fourier Transform (FFT) of an area that encloses FeGa film and MgO layer. Analyzing the distance between spots, we can index each spot and establish the epitaxial relationships between FeGa and MgO. The spots of the MgO layer are forming squares, which represents a [100] zone axis. The FeGa film spots are distributed in a rectangle fashion. This distribution can be indexed as a [110] zone axis with the [1-10] direction in the film plane. Fig. 4.6 d shows the FFT image for PMN-PT, which corresponds to a [100] zone axis as identified for the MgO layer. These results support the proposed relations in eq. 4.1 between in-plane directions observed by RHEED.

The composition maps, Fig. 4.6 e,f, show a sharp transition between FeGa and MgO. There is no diffusion between layers. A loss of resolution is noted at the

interface between MgO and PMN-PT. This loss can be due to a projection effect of the steps that ferroelectric surfaces like PMN-PT present [178].

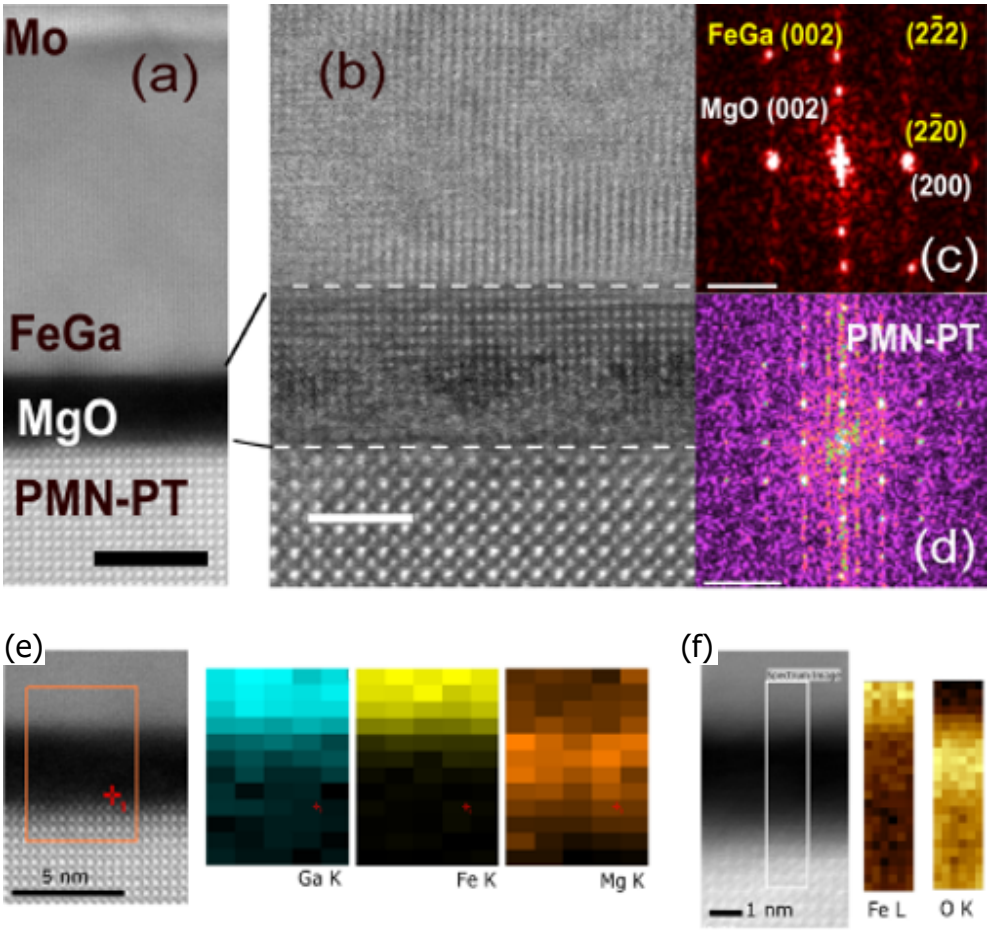

Figure 4.6: (a) Representative high-resolution spherical aberration-corrected STEM image of the structure viewed along the [100] zone axis direction of the PMN-PT substrate. Scale bar length 5 nm. (b) Enlarged area of the FeGa/MgO/PMN-PT structure. Scale bar length 2 nm. Fast Fourier Transforms of (c) FeGa + MgO and (d) PMN-PT areas. Scale bar length 5 nm^{-1}. (e) EDS and (f) EELS maps obtained on the areas marked with rectangles on the HTEM image. The K-edge signal for Ga (blue) and Fe (yellow) and Mg (orange) was used to determine the EDS maps. Fe L-edge and O K-edge were selected to obtain the corresponding EELS maps for which brighter color indicates higher presence of the selected element.

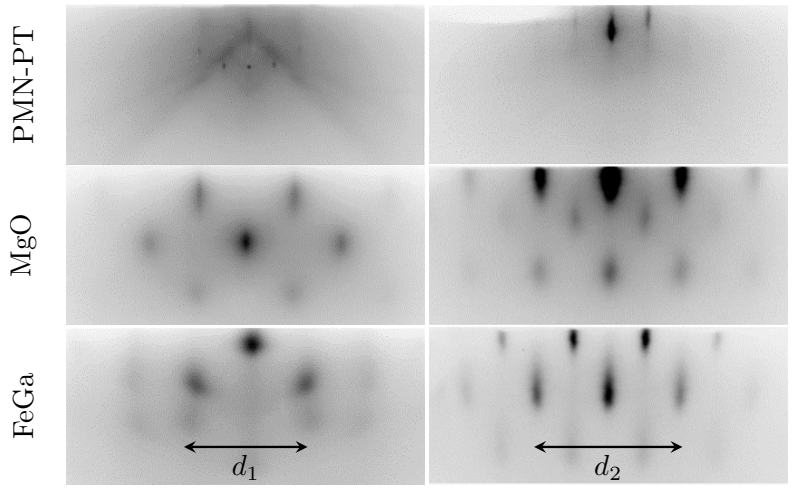

Figure 4.7: RHEED images of FeGa/MgO/PMN-PT(011) samples. For the first column the images are in the PMN-PT[100] direction, and for the second column, in PMN-PT[110] direction. First row is the RHEED image for the PMN-PT(011), second row for the MgO seed layer and third row for the FeGa film. The arrow indicates the distance between two symmetrical streaks.

PMN-PT(011) heterostructures

Fig. 4.7 shows RHEED images for the growing heterostructure using PMN-PT(011) as a substrate. MgO and FeGa grows with nearly the same distances between symmetrical streaks (d_1 and d_2). As the lattice parameter of MgO is similar to the PMN-PT, we can argue that the crystal orientation of MgO is the same as the PMN-PT(011). But, FeGa has a lattice parameter that does not match with a growing surface (011). The ratio d_1/d_2 for FeGa obtained from Fig. 4.7 is ~ 0.8, which is near to the value of $\sqrt{2/3}$. The orthogonal reciprocal vectors which its ratio satisfies the previous relation are $2\pi/a_{110}$ and $2\pi/a_{111}$. As we will see in XRD section, FeGa grows *bcc* (112), whose in-plane vectors are [110] and [111] confirming the relation d_1/d_2 observed in RHEED. For the images taken with the beam along the PMN-PT[100] direction a complex pattern is observed. That arrangement can be explained by the presence of two variants that share the perpendicular [112] direction, a fact observed for iron films grown on MgO(110) crystals [179, 180].

Then, the epitaxial relationships for the orthogonal in-plane axes are:

$$\begin{aligned} &\text{PMN-PT[110]} \parallel \text{MgO[110]} \parallel \text{FeGa[111]} \\ &\text{PMN-PT[100]} \parallel \text{MgO[100]} \parallel \text{FeGa[110]} \end{aligned} \tag{4.4}$$

The misfit along the PMN-PT[100] is the same as the previous section. But,

for PMN-PT[110] direction the misfit changes. If we consider a non-dislocation growing, the misfit is:

$$\eta_{\text{MgO/PMN-PT}} = \frac{\sqrt{2}a_{\text{MgO}} - \sqrt{2}a_{\text{PMN-PT}}}{\sqrt{2}a_{\text{PMN-PT}}} = 4.72\% \tag{4.5}$$

$$\eta_{\text{FeGa/MgO}} = \frac{\sqrt{3}a_{\text{FeGa}} - \sqrt{2}a_{\text{MgO}}}{\sqrt{2}a_{\text{MgO}}} = -15.63\% \tag{4.6}$$

The misfit for $\eta_{\text{FeGa/MgO}}$ is too high to be considered. However, block epitaxy is the method for the accommodation of strain and promotes the crystalline growing. So, the system will tend to minimize the misfit including dislocations. For example, a possible minimization of misfit occurs when 6 FeGa cells match 5 MgO cells:

$$\eta_{\text{FeGa/MgO}} = \frac{6\sqrt{3}a_{\text{FeGa}} - 5\sqrt{2}a_{\text{MgO}}}{5\sqrt{2}a_{\text{MgO}}} = 1.23\% \tag{4.7}$$

A misfit of 1.23% between FeGa and MgO makes more plausible the observed epitaxial growth rather than a non-dislocation growth. However, we cannot determine experimentally the number of cells matching in this system, 6 FeGa and 5 MgO minimize the misfit, but other combinations of cells are still possible by the dislocation model.

Fig. 4.8 shows the XRD pattern for the heterostructure FeGa/MgO/PMN-PT(011). The peaks indicate that *bcc* FeGa(112) is growing over MgO(011) surface. Then, the epitaxy of the heterostructure is FeGa(112)/MgO(011)/PMN-PT(011). The lattice parameters obtained from the XRD pattern are: $a_{\text{PMN-PT}} = 0.4044\,\text{nm}$, and $a_{\text{FeGa}} = 0.2896\,\text{nm}$. These values are nearly the same as the PMN-PT(001) sample. There is no variation in the lattice parameter due to the epitaxy between FeGa and MgO. The peak at $2\theta = 48.46\,^\circ$ is indexed as PMN-PT(0 3/2 3/2), which is a peak that sometimes emerges in the measurements due to the presence of radiation with $\lambda_{\text{Cu}}/2$.

A sample of Fe/MgO/PMN-PT(011) was characterized by TEM. Fe and FeGa have similar lattice parameter $a_{Fe} = 0.286\,\text{nm}$ and $a_{FeGa} = 0.290\,\text{nm}$, so the TEM images are representative for a FeGa specimen. Fig. 4.9 a shows the PMN-PT substrate, MgO layer and Fe film. The atomic order between MgO and Fe is preserved. Note that the image shows the epitaxy between Fe[110] and MgO[100], which generates less misfit than Fe[111] and MgO[110]. Fig. 4.9 b shows the FFT of the MgO. The pattern indicates a [110] zone axis, where the spots are at 35.26° and 54.74° forming a non-regular hexagon [181]. Fig. 4.9 c shows the FFT image of a Fe area. The angle between spots is 60° and displays a regular hexagon. This pattern is characteristic for [111] zone

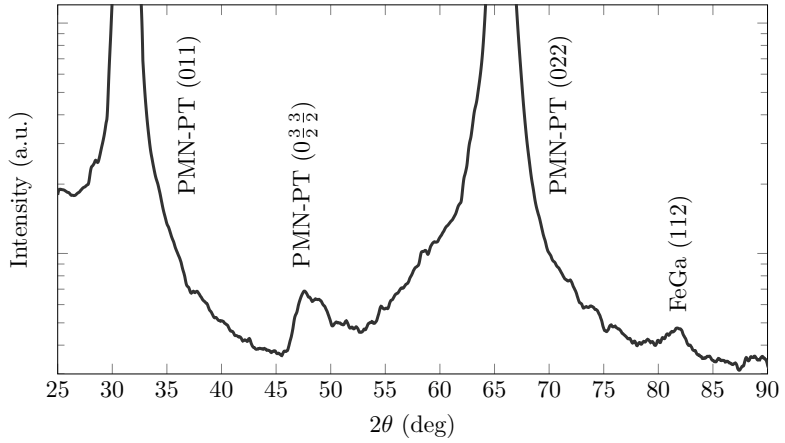

Figure 4.8: XRD pattern for the sample FeGa/MgO/PMN-PT(011).

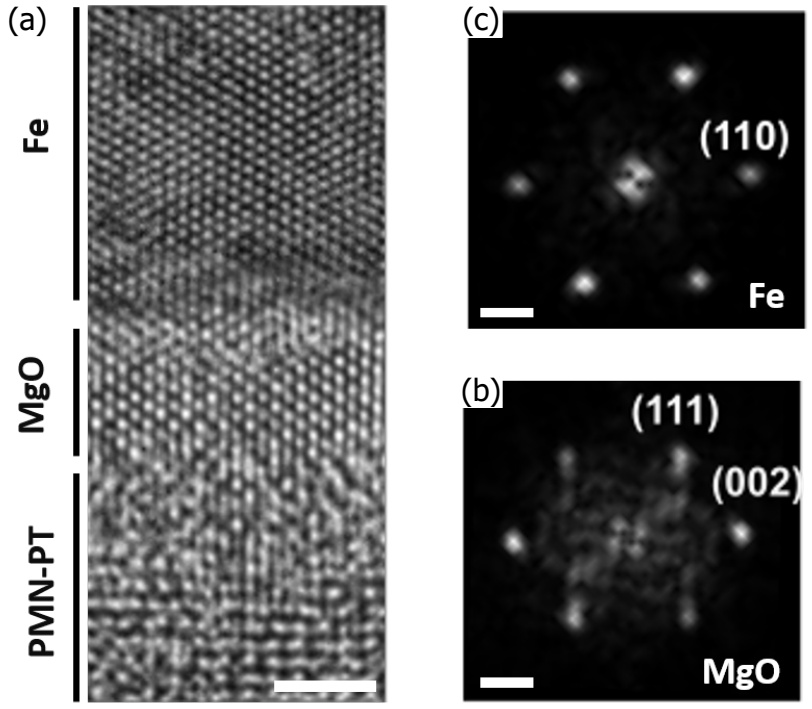

Figure 4.9: (a) TEM image for Fe/MgO/PMN-PT(011) viewed along the [110] zone axis of PMN-PT. Scale bar length 2 nm. Fast Fourier transforms of (b) MgO and (c) Fe. Scale bar length 2 nm^{-1}.

axis [181]. The results obtained from TEM support the proposed relations observed by RHEED.

4.4.2 FeGa/PMN-PT

Fig. 4.10 shows RHEED images that were recorded during the growing of FeGa directly over PMN-PT substrates. The substrate images are omitted because are similar to Fig. 4.4 and Fig. 4.7. When FeGa is deposited over the clean PMN-PT substrate at $T_s = 150\,°\text{C}$, the RHEED patterns become circular indicating a polycrystalline growing (Fig. 4.10 a). No matter the orientation or the substrate chosen, the RHEED pattern is similar in each case.

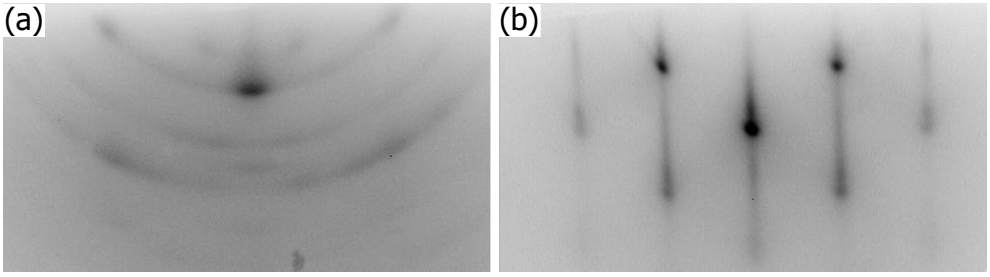

Figure 4.10: RHEED images taken from FeGa deposited over PMN-PT(011) substrates. (a) $T_s = 150\,°\text{C}$, (b) $T_s = 950\,°\text{C}$.

An investigation about the growth of FeGa over PMN-PT substrates was carried out to avoid polycrystal films. The temperature of the substrate was changed from the usual $T_s = 150\,°\text{C}$, utilized in this thesis, to $T_s = 950\,°\text{C}$. Fig. 4.10 b shows the RHEED pattern. As one can see, the pattern indicates a crystalline growth. The increase in temperature allows the atoms to diffuse more over the substrate surface and stabilize a crystalline structure.

The misfit in FeGa[111], including dislocations, and FeGa[110] directions are respectively:

$$\eta_{\text{FeGa/PMN-PT}} = \frac{8\sqrt{3}a_{\text{FeGa}} - 7\sqrt{2}a_{\text{PMN-PT}}}{7\sqrt{2}a_{\text{PMN-PT}}} = 0.97\% \tag{4.8}$$

$$\eta_{\text{FeGa/PMN-PT}} = \frac{\sqrt{2}a_{\text{FeGa}} - a_{\text{PMN-PT}}}{a_{\text{PMN-PT}}} = 2.02\% \tag{4.9}$$

If the film grows without dislocations along FeGa[111] direction, the misfit is -15.63%. This value can explain the polycrystal growth observed in RHEED images when the film is deposited at $T_s = 150\,°\text{C}$. But, at $T_s = 950\,°\text{C}$, the RHEED images indicate epitaxial growth. As the misfit without dislocations

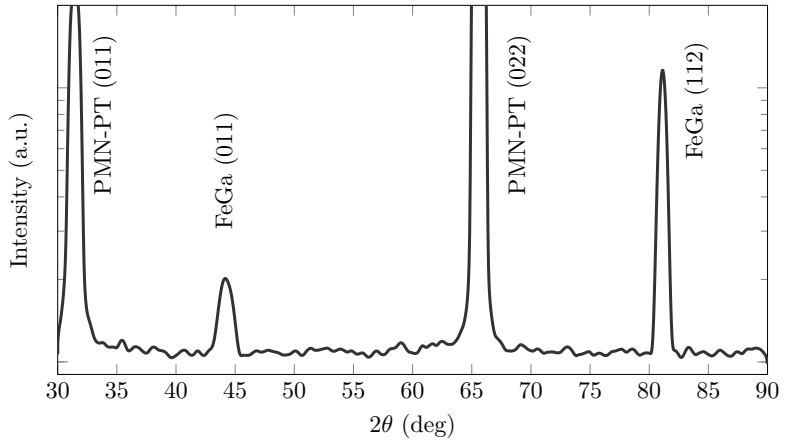

Figure 4.11: XRD pattern for the sample FeGa/PMN-PT(011) grown at $T_s = 950\,°C$.

is too high, we propose that 8 FeGa cells match 7 MgO cells at $T_s = 950\,°C$ minimizing the misfit.

A XRD pattern of the sample FeGa/PMN-PT(011) grown at $T_s = 950\,°C$ is shown in Fig. 4.11 . The peaks corresponding to FeGa indicate *bcc* crystal structure. Two reflections for FeGa are found, (011) and (112). The reflection FeGa(112) is the expected for films grown on PMN-PT(011). But, the reflection FeGa(011) indicates that the film has two textures, being the dominant texture (112) as the intensity shows. The lattice parameters obtained from the XRD pattern are: $a_{\text{PMN-PT}} = 0.4022\,\text{nm}$, and $a_{\text{FeGa}} = 0.2861\,\text{nm}$.

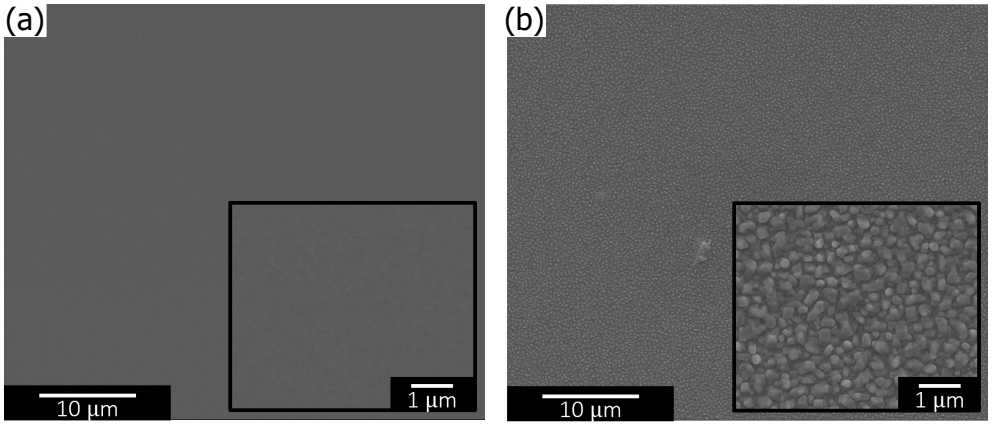

Figure 4.12: SEM images of the FeGa crystalline samples. Both insets correspond to zoomed areas. (a) FeGa/MgO/PMN-PT grown at $T_s = 150\,°C$. (b) FeGa/PMN-PT grown at $T_s = 950\,°C$.

Crystalline films can be grown by using a MgO seed layer or by growing FeGa onto PMN-PT at $T_s = 950\,°C$. However, the flatness of the surface is affected by the deposition temperature. SEM images of both crystalline films are shown in Fig. 4.12. When the MgO seed layer is deposited, the FeGa grows flat at $T_s = 150\,°C$ (Fig. 4.12 a). But, when the FeGa is deposited directly on PMN-PT at $T_s = 950\,°C$, the surface is rugged. The size of the particles which originate this roughness is $\sim 300\,nm$.

4.5 Magnetic characterization

4.5.1 FeGa/MgO/PMN-PT

Fig. 4.13 shows the magnetic behavior of the as-grown samples studied by VSM and MOKE. Thin films grown on MgO/PMN-PT(001) and (011) are analyzed. Fig. 4.13 a,c shows the VSM measurements corresponding to easy and hard axis of each sample. Fig. 4.13 b,d shows the squareness of the samples as a function of the angle of the applied magnetic field obtained by using the analysis of MOKE data described in section 2.4.2.

For FeGa/MgO/PMN-PT(001) samples, the easy and hard axes are FeGa[110] and FeGa[100], respectively (Fig. 4.13 a). The loops suggest that the sample has a cubic magnetic anisotropy with a composition above $x = 18$. This result agrees with the previous ones for this composition ($x = 19$). From VSM measures, the ratio M_r/M_s with H applied along FeGa[100] is $\sim \sqrt{2}/2 \simeq 0.707$. The value agrees with the presence of a square symmetry, $M_r \simeq M_s \cos 45 = M_s\sqrt{2}/2$ if the magnetization rotates from easy to hard axis. The squareness polar plot displays a 4-fold magnetic anisotropy (Fig. 4.13 b) confirming this behavior. The directions in the polar plot are 0° ‖FeGa[100], and 90° ‖FeGa[010].

For FeGa/MgO/PMN-PT(011) samples at $x = 19$, the easy and hard axis are FeGa[111] and FeGa[110], respectively (Fig. 4.13 c). The squareness polar plot displays a strong uniaxial magnetic anisotropy (Fig. 4.13 d). The directions in the polar plot are 0° ‖FeGa[111], and 90° ‖FeGa[110].

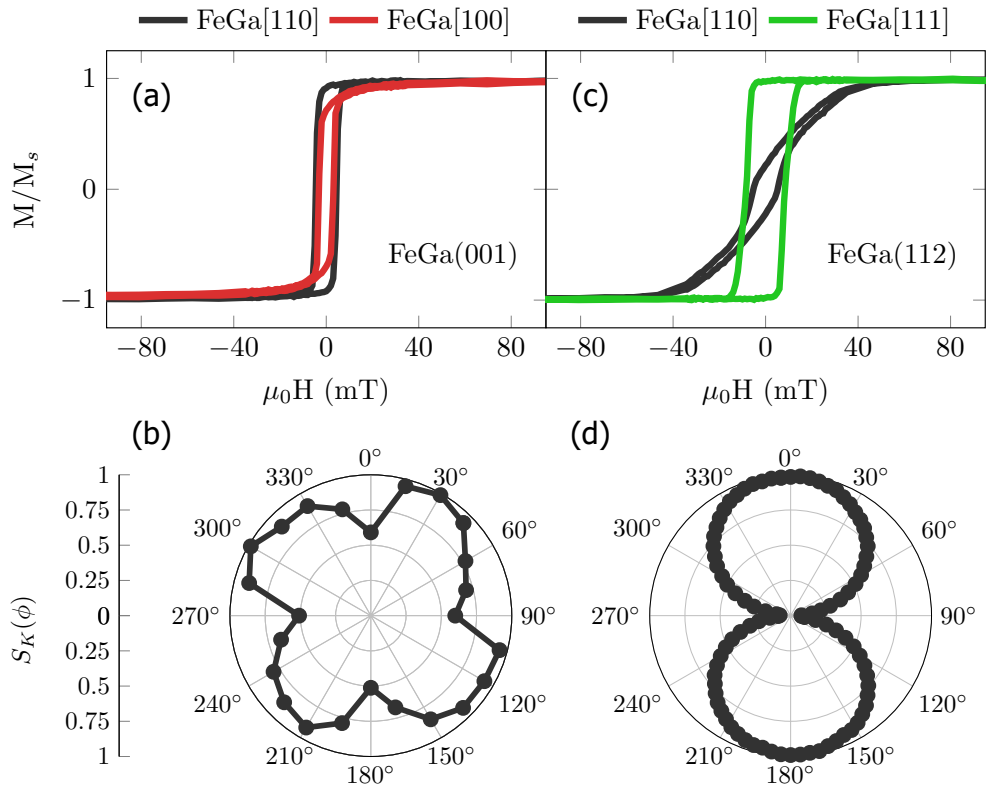

Figure 4.13: Magnetic measures of FeGa thin films. First column (a-b) is for FeGa(001)/MgO(001)/PMN-PT(001), and second column (c-d) for FeGa(112)/MgO(011)/PMN-PT(011). Easy and hard axis in-plane are shown. First row (a-c) is VSM data, and second row (b-d) squareness polar plot obtained by MOKE. The crystal axis that correspond to 0° and 90° in the polar plot are respectively (b) FeGa[100] and FeGa[010], (d) FeGa[111] and FeGa[110].

4.5.2 FeGa/PMN-PT

The crystal structure of the samples grown directly onto PMN-PT depends on the growth temperature, T$_s$. A MOKE study was performed to characterize how the magnetic anisotropies are influenced by T$_s$ in these samples. Fig. 4.14 shows the squareness polar plot of FeGa/PMN-PT(011) at T_s = 150 °C (Fig. 4.14 a) and T_s = 950 °C (Fig. 4.14 b). The shape of the squareness indicates that for both samples, the magneto-crystalline anisotropy is weak. Even the strong uniaxial anisotropy found in FeGa/MgO/PMN-PT(011) samples is hardly noticeable. The origin of this behavior can be found in the structural characterization section. For samples grown at T_s = 150 °C the RHEED images indicate a polycrystalline growth (Fig. 4.10 a). For polycrys-

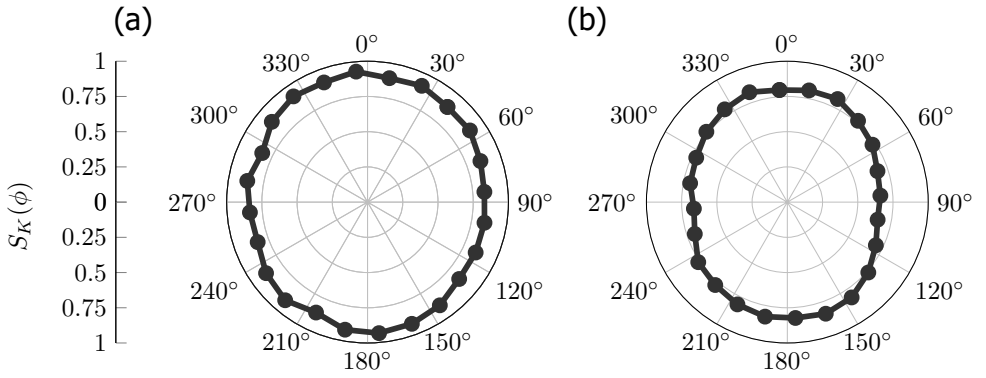

Figure 4.14: Squareness polar plot of FeGa/PMN-PT(011) samples grown at (a) $T_s = 150\,°C$, and (b) $T_s = 950\,°C$. The crystal axis that correspond to 0° and 90° in the polar plot are PMN-PT[110] and PMN-PT[100], respectively.

tals, magnetic anisotropy exists on the scale of a single crystallite. However, at macroscopic scale, the crystallites are oriented randomly and the average magneto-crystalline anisotropy results in an isotropic magnetization [182, 183]. For samples grown at $T_s = 950\,°C$, two crystal textures are found. We can consider that the magnetocristalline anisotropy of both textures in addition to the irregular grain shape (Fig. 4.12 b), may result in an averaged magnetic isotropic behavior [184, 185].

Discussion about the best candidate for straintronic applications

Once the heterostructures are characterized structural and magnetically, we continue on the development of a straintronic device. The need to choose the best candidate is essential, the thesis period does not allow us to investigate all the heterostructures presented. Then, the selection process was made according to the expected applications. In our case, the objective is to manipulate the magnetization of the thin film via an electric voltage applied on the substrate. The magnetic states of the samples need to be well-defined, i.e. to switch between the state 0 and state 1 as a bit system. For the samples FeGa/PMN-PT, the squareness indicates an isotropic behavior of the magnetization. It does not change on the temperature of growing, despite of structural changes seen. Also, the rough surface of samples grown at $T_s = 950\,°C$ can be problematic in nanopattern applications because after the lithography process, it can present irregular shapes making the shape magnetization field different for each pattern. Nevertheless, the samples FeGa/MgO/PMN-PT have flat surfaces and well-defined magnetic states due to the presence of easy and hard axis in cubic anisotropy, for PMN-PT(001), and uniaxial anisotropy, for PMN-PT(011). If the applied voltage in the substrate can change the landscape of the energy,

then, the easy axis can be shifted to another direction. So, we will focus on the heterostructure made by FeGa/MgO/PMN-PT to investigate applications in the field of straintronics.

4.6 Design and fabrication of a platform for voltage application

The samples fabricated are not a device by themselves, we need a device to put the samples in, and apply voltage to measure the changes in the magnetization of the film. The samples need a post-grown preparation before putting into the device. On the other hand, two main requisites are required for the device: to be able to bear voltages of $\sim 400\,\mathrm{V}$, and to let the surface of the sample exposed in order to allow measurements with MOKE and MFM without interference.

To achieve a ferroelectric deformation in PMN-PT, we sandwiched it like a capacitor. The voltage is applied between its surface and base. By this way, the substrate its strained by a perpendicularly applied voltage. Fig. 4.15 a shows a scheme of the heterostructure designed to apply voltage. Then, the Mo/FeGa bilayer acts as a plate of the capacitor. To make the base the other plate, we evaporate $\sim 1\,\mathrm{nm}$ of Ti as an adherent to subsequently evaporate a $\sim 1\,\mathrm{nm}$ of gold to create the metallic plate. The positive voltage is defined when the base of the sample is at ground voltage.

The designed and fabricated device is shown in Fig. 4.15 b. The size is $20 \times 15\,\mathrm{mm}$. The device is a PCB with 10 pads. There are 9 pads to apply voltage on the surface, and the other one is to apply voltage on the base. The surface of the sample is microcontacted to the 9 pads. The other pad occupies the central area of the device. This pad is designed to glue the sample by using silver paint. By this means, the sample is hold on the device, and the electric contact with the base is homogeneous. By PCB header pins, the voltage is applied between the surface and the base of the substrate. The microcontacts are done near to the borders to avoid their destruction while we perform a MFM scan.

The device allows us to measure the sample in different equipment without removing the sample from the PCB. Adapters to the pin headers were designed and fabricated to work in MOKE and MFM equipment by using aluminum and MACOR® .

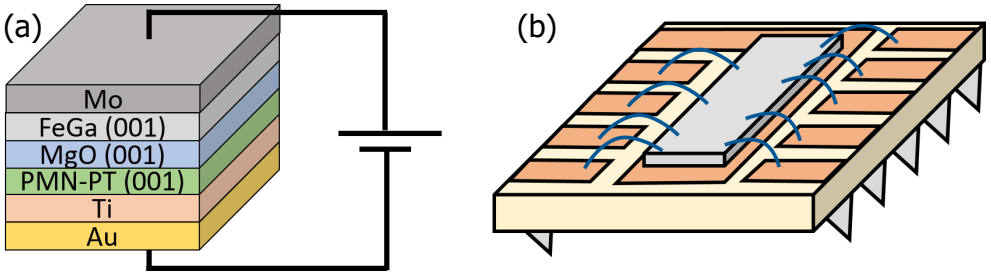

Figure 4.15: (a) Scheme of the sample with the layers deposited post-grown (Ti and Au). The voltage is applied between Mo and Au. Positive voltage is defined when Au acts as ground. (b) Scheme of the PCB device designed and fabricated. The sample is glued to the central pad by using silver paint. The surface is microcontacted to the other 9 pads. The voltage is applied via PCB header pins.

4.7 Straintronic devices

In this section we present the results and analysis for the two proposed heterostructures with straintronic applications: FeGa(112)/MgO(011)/PMN-PT(011) and FeGa(001)/MgO(001)/PMN-PT(001).

The importance of using MOKE in the magnetic characterization of this heterostructures is due to the inhomogeneities that the switching modes of ferroelectric substrates manifest. The laser focus spot diameter is in the micrometer range, so the measure is local respect to VSM, that averages for all the sample. It is essential to focus the spot in an area of the sample where the switching mode of the ferroelectric domain causes a strong strain to maximize the magnetoelastic response. The ferroelectric domains are very inhomogeneous [175], so finding an area with a strong strain switching is not straightforward.

The notation 0+ and 0− used from now on is referred to the state of remanent magnetization after applying electric field with positive and negative polarity, respectively.

4.7.1 FeGa(001) heterostructures

A heterostructure of FeGa(001)/MgO(001)/PMN-PT(001) is studied. The MgO thickness is $t_{\mathrm{MgO}} \sim 3\,\mathrm{nm}$, and the magnetoelastic layer is $Fe_{81}Ga_{19}$ with $t_{\mathrm{FeGa}} = 15\,\mathrm{nm}$.

An initial poling of $E = 0.6\,\mathrm{MV/m}$ was carried out to align the ferroelectric domains. The poling was high enough to ensure that the ferroelectric reaches the saturation. After that, a MOKE scan along several areas of the sample was performed to find an area with the majority of the ferroelectric switching

via 109° to focus the laser spot. In PMN-PT(001) substrates $\sim 23\%$ of the area corresponds to a 109° switch [175]. The results obtained from these areas are shown in this section.

A squareness polar plot of the states 0+ and 0− is shown in Fig. 4.16 a. The as-grown 4-fold magnetic anisotropy is masked by a strong uniaxial magnetic contribution that arises from poling the sample. The easy and hard axis rotates 90° after applying $|E| = 0.3\,\mathrm{MV/m}$. The major changes occur in FeGa[100] and FeGa[010] directions. Fig. 4.16 b,c shows how the M-H loop interchange its easy and hard axis after applying electric field. Clearly, the sample can store two different states, 0+ and 0−, at remanence. After applying an electric field of $E = 0.3\,\mathrm{MV/m}$, the easy magnetic axis is pointing along FeGa[010]. But, if an electric field of $E = -0.3\,\mathrm{MV/m}$ is applied, then, the easy axis is FeGa[100]. In a sample of this size, the voltage needed to switch between states is 150 V. By this result, we can confirm that it is possible to control the magnetic axis of the sample by only applying electric field.

However, for other regions of the film, the configuration of easy and hard magnetic axis remains fixed under the application of electric field. This can be explained by not-109° switching ferroelectric domain areas. Also, an inhomogeneous magnetic response of the FeGa film has been also observed in amorphous CoFeB thin films [186] and mesoscopic discs [187].

The dependency of squareness and electric polarization is studied along FeGa[100] direction. Fig. 4.17 shows the squareness of the sample for an electric loop of amplitude $|E| = 0.5\,\mathrm{MV/m}$. Each point of the main panel is obtained from an individual M-H loop as the red dashed arrows indicate. The curve $S_K(\mathrm{E})$ shows that an electric field of $|E| = 0.3\,\mathrm{MV/m}$ is enough to saturate the ferroelectric substrate because its coercive electric field is $\sim 0.15\,\mathrm{MV/m}$. The magnetic state achieved by the FeGa film when the ferroelectric is saturated, is perfectly detained when there is no electric applied field. There are nearly no losses in magnetization after this process. The amplitude of $\Delta S_K \sim 0.8$ at $\mathrm{E} = 0\,\mathrm{MV/m}$ confirms that a high change in the magnetic states occurs after the saturation of the substrate.

The large jumps of $S_K(\mathrm{E})$ observed for $\mathrm{E} \sim 0.15\,\mathrm{MV/m}$, and $\sim -0.1\,\mathrm{MV/m}$ present an asymmetry with respect to E. An explication for the shift in the $S_K(\mathrm{E})$ curve could be ascribed to the inhomogeneous FE domain switching through the structure. Some areas have fixed magnetic axis that do not switch under applied electric field. Then, the ferromagnetic exchange coupling interaction with these areas favors a parallel orientation of M. The effect of this interaction is an unidirectional anisotropy that can enforce or cease the inversion of M in the reversible area, explaining the observed shift of the $S_K(\mathrm{E})$ loop.

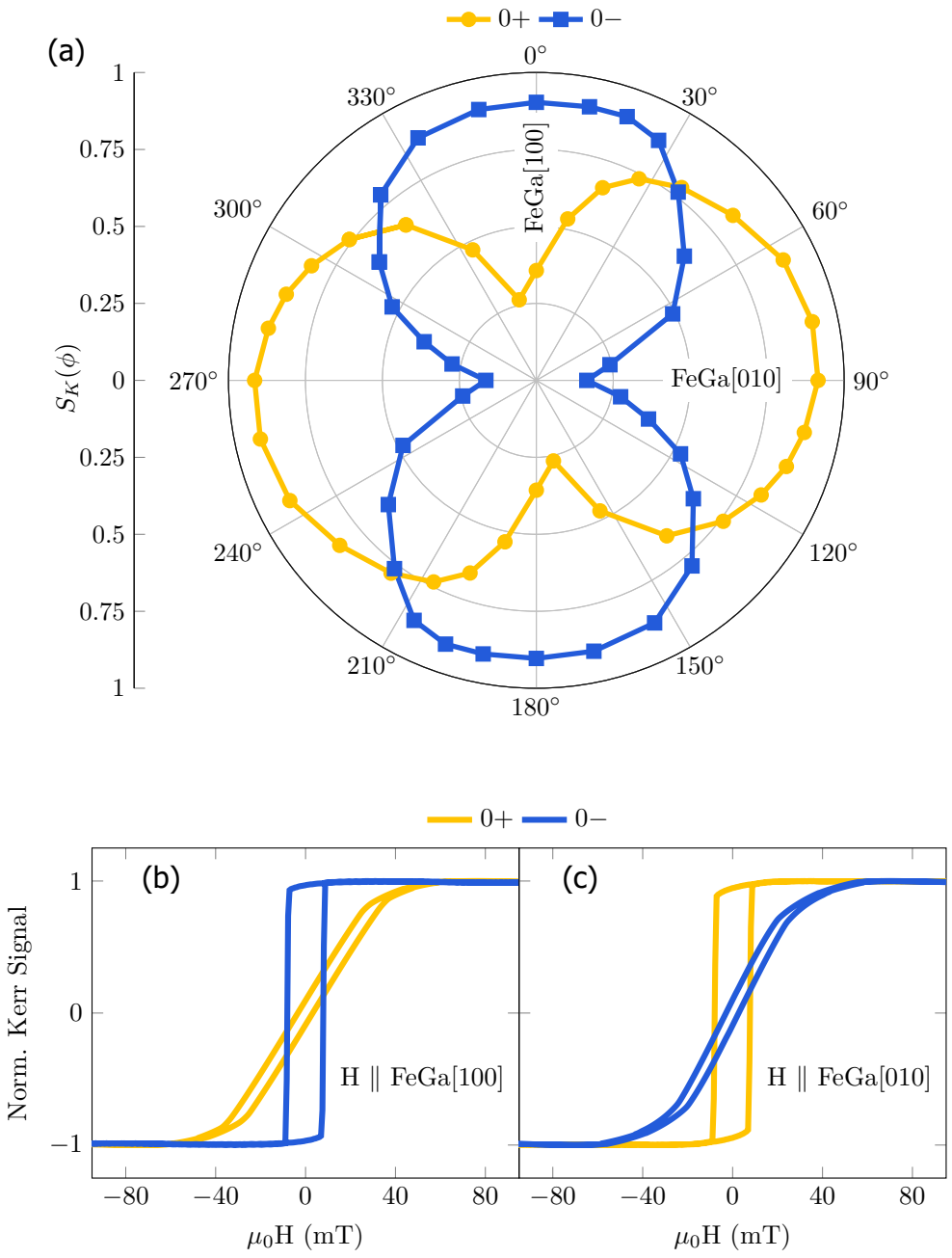

Figure 4.16: (a) Squareness polar plot for 0+ (yellow) and 0− (blue) states. (b) and (c) are the normalized Kerr signal for 0+ and 0− states with H applied along FeGa[100] and FeGa[010] directions, respectively.

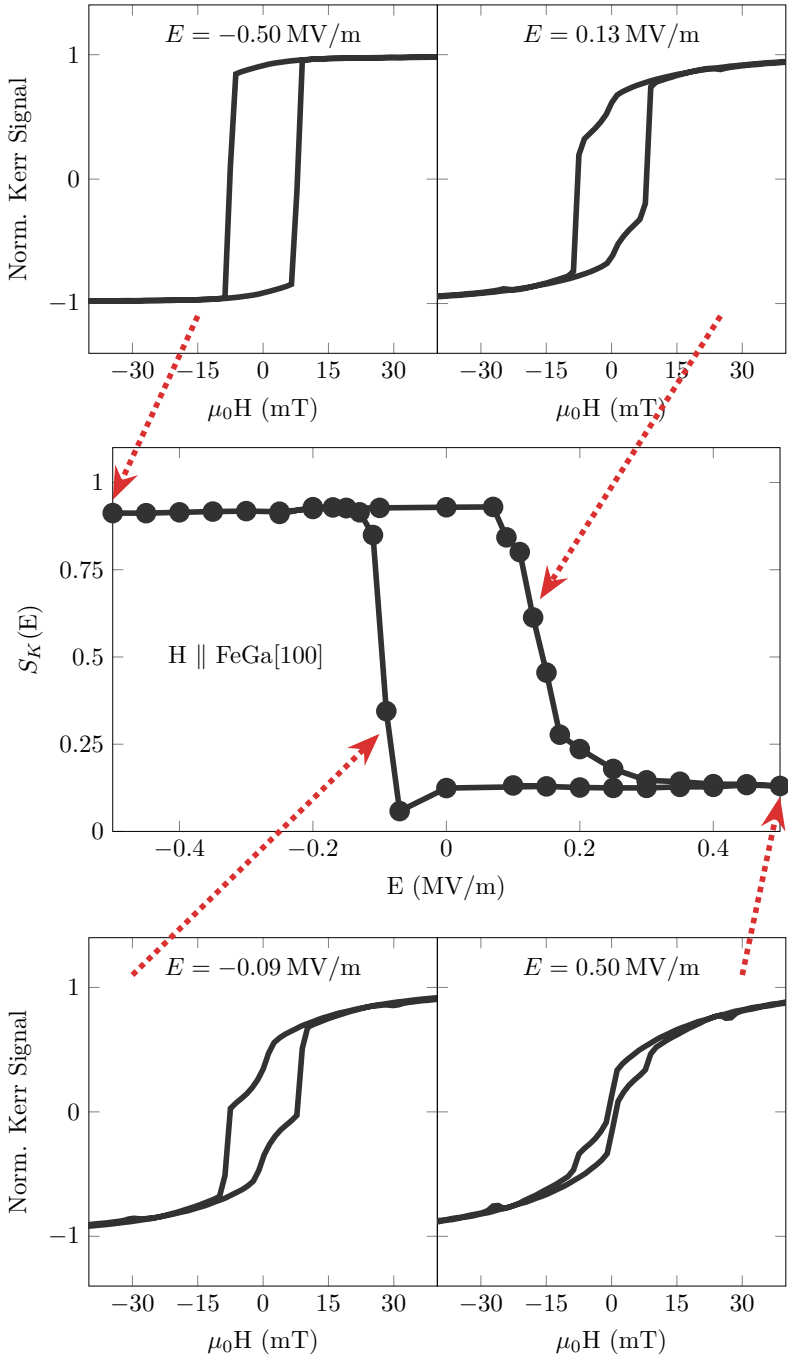

Figure 4.17: Detailed graph showing the representative M-H loops that produce the $S_K(E)$ curve (main panel). Each point of the graph is obtained from MOKE measurements with H ∥ FeGa[100] at several voltages. Some representative M-H loops are shown at electric field E = −0.5 MV/m, E = 0.13 MV/m, E = −0.09 MV/m, and E = 0.50 MV/m.

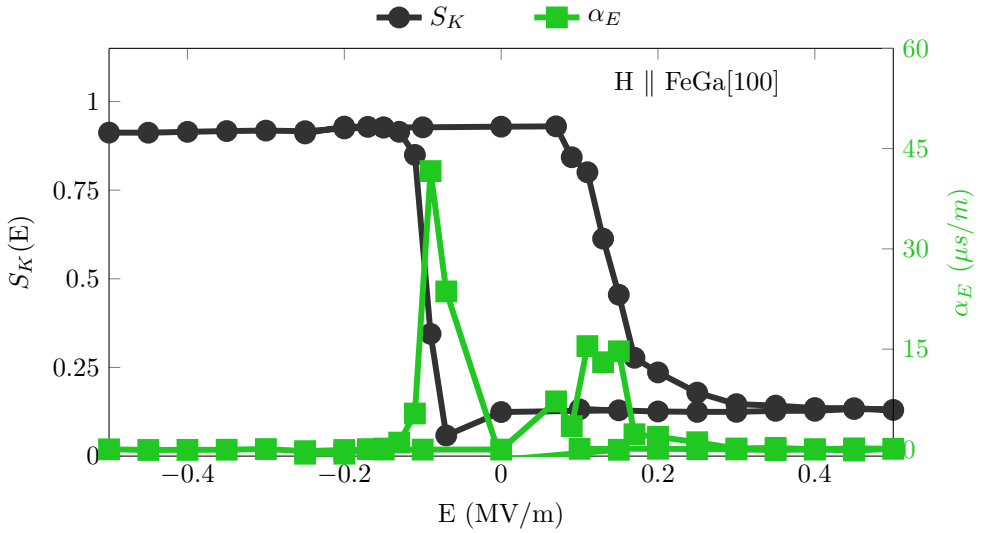

Figure 4.18: Electric loop while H is applied parallel to FeGa[100]. S_K and the effective converse magnetoelectric coefficient, α_E, as a function of the applied electric field. The maximum value of α_E is 41.6 μs/m at $E = -0.09$ MV/m.

The heterostructure fabricated presents a change in its magnetization when an electric field is applied. A relevant parameter used to study how strong is the coupling between magnetization and electric field is the converse magnetoelectric coupling coefficient, α_E.

$$\alpha_E = \mu_0 \frac{\Delta M}{\Delta E} \tag{4.10}$$

For MOKE data, we can consider that $\Delta M = M_s \Delta S_K$. The value of M_s used for a composition of $x = 19$ is $\mu_0 M_s = 1.65$ T [188].

Fig. 4.18 shows α_E obtained for each electrical step (ΔE). The maximum value obtained is $\alpha_E = 41.6\,\mu$s/m at $E = -0.09$ MV/m. In order to give a reasonable value of α_E for this sample, $\alpha_E \simeq 15\,\mu$s/m is more reproducible for positive and negative electric field. The magnetocoupling obtained in this work is, to the best of our knowledge, the highest achieved in the scientific literature. Optimized structures of amorphous films grown on relaxor substrates reach values of $\alpha_E \sim 8\,\mu$s/m [189]. For oxide magnetic layers, $\alpha_E \sim 0.1\,\mu$s/m [190], and for the interfacial oxidation coupling mechanism, α_E decreases to values in the range of $\sim 0.01\,\mu$s/m [191]. The Kerr loops used to calculate α_E were obtained in an area with 90° magnetic switching. In other regions, the maximum of α_E, peak at different E, or have a smaller magnitude because of the integration that Kerr signal performs.

Active control of magnetic domain walls [192–195] is a matter of interest for practical applications [196]. A study of the magnetic domains was performed by MFM. Experimentally, it was not possible to measure positive voltages with the actual MFM configuration. For positive bias, the surface of the sample acts as the positive electrode, and the substrate as ground. However, when the tip of MFM is close to the surface, the tip acts as ground, and the voltage instead of being applied through the sample, goes to the tip. A solution could be to put the tip and surface at the same voltage. The problem is that the electric voltage necessary to switch the ferroelectric is sufficiently high to cause severe damage to the MFM equipment if the internal system reaches that voltage. So, in order to avoid damage to the equipment, positive bias was not measured. For negative bias, the surface acts as ground, and the substrate as positive electrode. So, the tip and surface are at the same voltage (ground) and the image taken is at the maximum definition possible without electric contributions.

Fig. 4.19 shows MFM images taken at different voltages in the area of switching. The colour scale bar is the same for all images. White arrows indicate the easy axis for each image. In Fig. 4.19 b appears the [010] and [100] FeGa directions. In Fig. 4.19 a, the initial magnetic configuration is at $\mathrm{E} = 0\,\mathrm{MV/m}$ after applying $\mathrm{E} = 0.4\,\mathrm{MV/m}$. This is the 0+ state. M lays in the film plane, so the contrast observed corresponds to the domain walls (DWs). The easy direction is along FeGa[010] as Fig. 4.16 indicates. Fig. 4.19 b was taken at $\mathrm{E} = -0.08\,\mathrm{MV/m}$, which is near to the coercive electric field of the heterostructure. Changes in the DWs are becoming noticeable. A set of lines appear in regions that previously were empty, while some DWs disappear from other regions. An increment in the contrast could indicate a nonhomogeneous switch of P. As this voltage is near to the coercive electric field, some ferroelectric domains may be have switched, and the others not. This causes a misalignment of M because the stresses in the film are inhomogeneous. In Fig. 4.19 c, the applied electric field is $\mathrm{E} = -0.14\,\mathrm{MV/m}$. Some of the previous DWs disappear and a new set appear in the FeGa[100] direction. As we know, at this voltage, the electric saturation is almost reached. The 90° rotation of M is completed, and the new magnetic landscape is visible. For the Fig. 4.19 d, $\mathrm{E} = -0.2\,\mathrm{MV/m}$ and the regions are still the same. The ferroelectric is in saturation. In Fig. 4.19 e, the voltage is dropped to $\mathrm{E} = 0\,\mathrm{MV/m}$ (0− state). As we can see, the magnetic domains are stable from the saturation state. This result agrees with the magnetic behavior obtained in the curve $S_K(\mathrm{E})$ (Fig. 4.17). In Fig. 4.19 f, the state 0+ is achieved after applying $\mathrm{E} = 0.4\,\mathrm{MV/m}$ with the tip far from the surface to avoid electrical interference. The domain configuration has some similarities with respect to Fig. 4.19 a. There are some differences between these configurations, that can be explained by the fact that

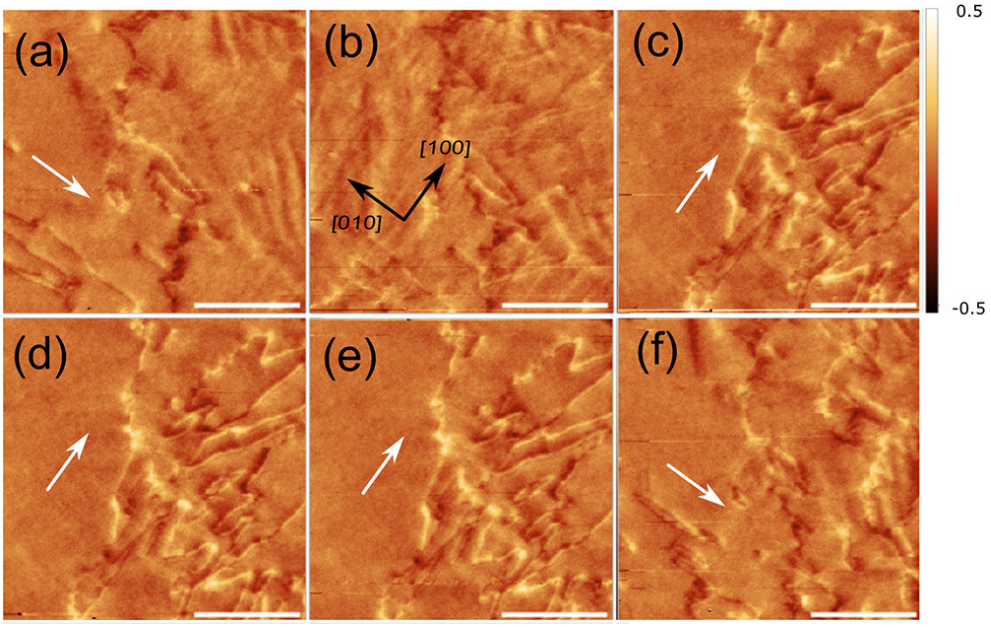

Figure 4.19: Magnetic force microscopy images taken on the film at different values of electric field on the same area: (a) 0+, (b) $-0.08\,\mathrm{MV/m}$, (c) $-0.14\,\mathrm{MV/m}$, (d) $-0.2\,\mathrm{MV/m}$, (e) 0−, and (f) 0+. The arrows in panel b stand for the FeGa [100]/[010] in-plane directions. The white arrows indicate the magnetic easy axis. The units of color code bar are degrees. Scale bar length $10\,\mu\mathrm{m}$.

the low magnetic moment of the tip may modify some soft magnetic domains.

Non-volatile memory

The switch of an easy direction into a hard direction opens the possibility of using this heterostructure as a non-volatile memory. The two states of this memory are 0+ and 0−, i.e. a bit-binary system. To prove that, the heterostructure is subject to several electric pulses to switch between its two states. We use the squareness, S_k, to evaluate how the easy axis is switching while electrical pulses are being applied.

The experiment was carried out by MOKE with the loght incidence direction along the FeGa[010] direction. An initial measurement of a M-H loop was performed to obtain the Kerr amplitude of the loop at easy axis (maximum amplitude). This value is necessary to transform Kerr signal into S_k. An electric field of $|E| = 0.3\,\mathrm{MV/m}$ was used to switch between the states 0+ and 0−. The duration of the electric pulse is $\sim 500\,\mathrm{ms}$. Fig. 4.20 shows the results.

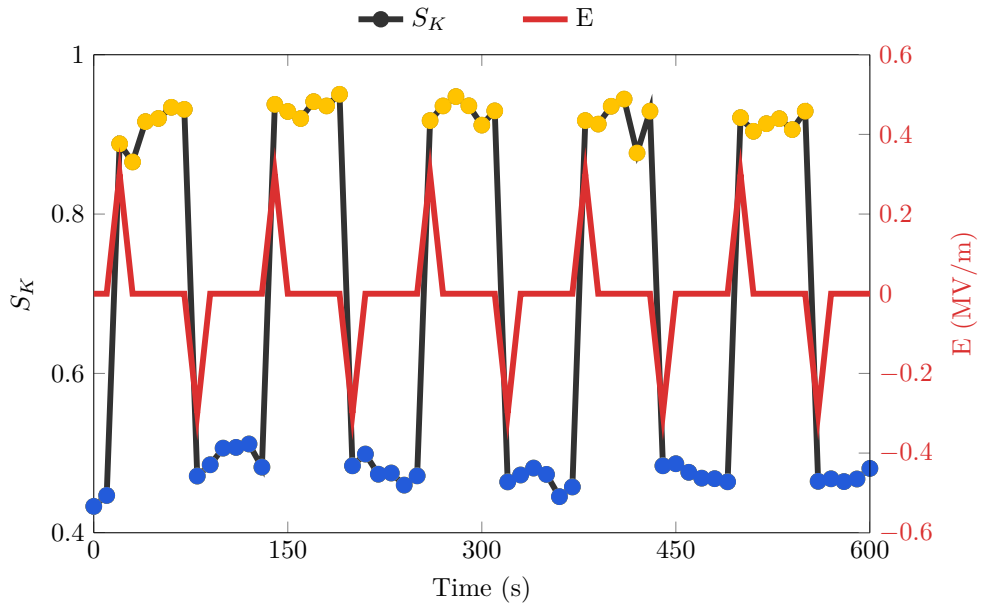

Figure 4.20: S_K measurements (points) along FeGa[010] direction while several electric pulses of alternating polarity are applied (red line). Yellow and blue points indicate 0+ and 0− states, respectively.

It is important to note that no applied magnetic field is used, the origin of the magnetic switch is exclusively due to electrical pulses. Several switches are shown indicating that the heterostructure is able to act as a non-volatile memory. The switch achieved is repeatable and stable. Amplitude is similar in all cycles exposed, even for 30 minutes straight (30 cycles) the heterostructure still able to switch with no losses in the amplitude. The difference in S_k between the two states is large ~ 0.4. Also, the magnetic configuration is stable between electric pulses acting as a possible long-time non-volatile memory.

A rotation of 90° in magnetization is achieved by only applying voltage, but for technological applications a 180° rotation is more interesting. Using this heterostructure we found a route to switch the magnetization from +M to -M by the combination of electric pulses and the assistance of a magnetic field as low as 3 mT. The experiment was performed at FeGa[100] direction measuring the longitudinal Kerr signal. Before the experiment, a M-H loop was recorded to measure the Kerr amplitude in order to normalize the signal during the experiment. In Fig. 4.21 is depicted the route of 180° rotation. In the upper panel appears the Kerr signal normalized. The inset represents the step of the loop that we are moving to. The bottom panel indicates the magnetic field (green) and electric pulses applied (red) along the steps. The route to achieve the 180° is as follows:

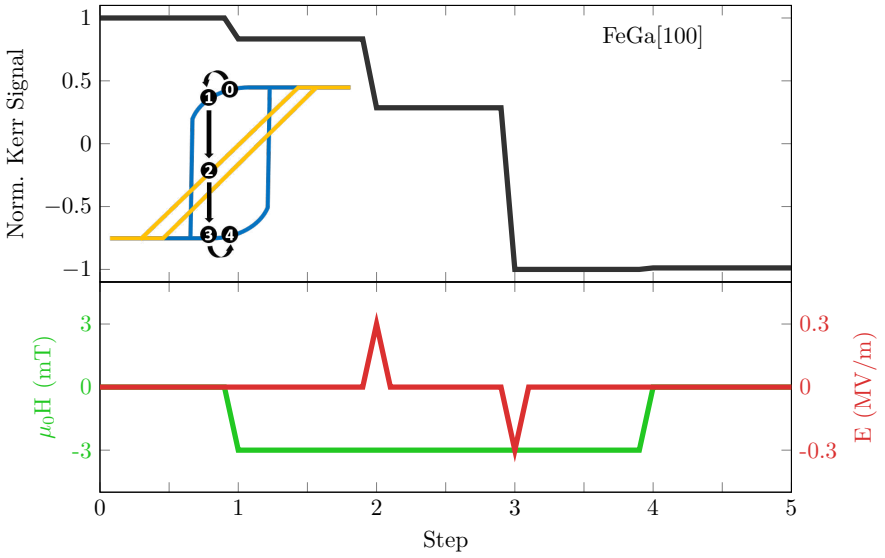

Figure 4.21: 180° rotation of M along FeGa[100] direction. The upper panel indicates the normalized Kerr signal. The inset is a scheme of the steps taken between positive (yellow) and negative (blue) voltage dependent M-H loop. Lower panel shows the magnetic (green) and electric (red) field applied in each step.

- Step 0: Remanence at H = 0 and E = 0 after applying H = 100 mT along FeGa[100] direction and E = 0.3 MV/m.
- Step 1: Application of H = −3 mT, in such a way that H is antiparallel to M. The assistance of H from step 1 to 4 is essential to achieve the rotation.
- Step 2: Electric pulse of E = 0.3 MV/m to switch from the EA (blue M-H loop) to HA (yellow M-H loop).
- Step 3: Electric pulse of E = −0.3 MV/m to switch from the HA (yellow M-H loop) to EA (blue M-H loop). The Kerr signal goes down, indicating that an antiparallel configuration was achieved. If the rotation route fails, the Norm. Kerr Signal goes up to the value of step 2.
- Step 4: Applied magnetic field is switched from H = −3 mT to H = 0 mT.
- Step 5: Final magnetic configuration. There is nor applied magnetic field or electric. The Norm. Kerr Signal evidences a rotation of 180° in the magnetization vector.

Analysis

The as-grown FeGa thin film presents cubic magnetic anisotropy (Fig. 4.13 b). But, when the substrate is poled, a uniaxial contribution emerges, and overcomes the cubic anisotropy. The analysis of the energy terms involving the thin film are discussed to explain two phenomena: the arising of a uniaxial anisotropy, and the 90° rotation of the magnetic axis when an electric field is applied.

The total energy density of the film depends on the cubic magneto-cristalline (e_{mc}), and the magnetoelastic (e_{mel}) terms.

$$e_{mc} = K_1(\alpha_x^2\alpha_y^2 + \alpha_y^2\alpha_z^2 + \alpha_z^2\alpha_x^2) + K_2\alpha_x^2\alpha_y^2\alpha_z^2 \tag{4.11}$$

$$\begin{aligned} e_{mel} = {} & B_1\left(\alpha_x^2\epsilon_{xx} + \alpha_y^2\epsilon_{yy} + \alpha_z^2\epsilon_{zz}\right) + \\ & + B_2\left(\alpha_x\alpha_y\epsilon_{xy} + \alpha_y\alpha_z\epsilon_{yz} + \alpha_z\alpha_x\epsilon_{zx}\right) \end{aligned} \tag{4.12}$$

where K_1 and K_2 are the first and second order magnetocrystalline constants. B_1 and B_2 are the irreducible cubic magnetoelastic coefficients. α_x, α_y, and α_z are the direction of cosines which the magnetization makes relative to the three crystal axes, $\langle 100\rangle$, $\langle 010\rangle$, and $\langle 001\rangle$ respectively. ϵ_{ij} are the strain components relative to the same crystal directions as α_i.

For our film, we can consider that the magnetization lies in-plane, $\alpha_z = 0$, and the cubic axes satisfy that $\alpha_x = \cos\phi$, and $\alpha_y = \sin\phi$, where ϕ is the relative angle to $\langle 100\rangle$ FeGa crystal direction. Taking these assumptions, the total density energy ($e_{mc} + e_{mel}$) of the thin film is:

$$e_{\text{total}} = \frac{K_1}{4}\sin^2(2\phi) + B_1\epsilon_{xx} - B_1\sin^2(\phi)\left(\epsilon_{xx} - \epsilon_{yy}\right) + \frac{B_2}{2}\epsilon_{xy}\sin(2\phi) \tag{4.13}$$

The substrate influences the total energy of the film through the strain. When an electric field is applied to PMN-PT(001) crystal, there are several modes in which **P** switches between different $\langle 111\rangle$ directions (Fig. 4.1). The strain versus E curves of PMN-PT presents an asymmetric butterfly-like shape [197]. The switch of **P** by the 109° mechanism provides ferroelastic jumps that persist at remanence. The value for the strain along directions $\langle 110\rangle$ is $\sim 0.04\%$ [197]. However, the mixture of the switching modes (109° with 71° and 180° mechanisms) in the whole substrate can translate the strain to the film with values that fluctuate [154, 197, 198] and modify locally the magnetic anisotropy coefficients [199]. The proportion of polarization variants with 109° switching varies in crystals with the same nominal composition [197]. Thus, the observation of areas with induced uniaxial anisotropy insensitive to the bias of the electric field is compatible with ferroelectric domains undergoing 71° and 180° switching modes (Fig. 4.1).

The combination of Kerr and scanning electron microscopy with polarization analysis (SEMPA) measurements has linked the shape of $S_K(\phi, \mathrm{E})$ to the presence of single or multidomain ferroelectric switching [187]. In mesoscopic amorphous CoFeB discs, the rotation of 90° of both M, observed directly by SEMPA, and $S_K(\phi)$, measured by Kerr effect, are ascribed to the 109° domain switching of a single variant. $S_K(\phi)$ for the FeGa film rotates by 90° between the 0− and 0+ states (Fig. 4.16 a) in agreement with the data reported for CoFeB amorphous discs [187]. This result suggests that our experiments were carried out in a single ferroelectric domain that undergoes a 109° switching.

Considering that we are in a 109° ferroelectric switching area, and the crystal directions between thin film and substrate are FeGa[100]‖PMN-PT[110], the shear strain produced in the substrate is transmitted to film via FeGa[100] and FeGa[010] directions. Then, the strain components in the film are $\epsilon_{xx} = -\epsilon_{yy}$, and $\epsilon_{xy} = 0$. Assuming this condition, the total energy becomes:

$$e_{\mathrm{total}} = \frac{K_1}{4}\sin^2(2\phi) + B_1\epsilon_{xx} - 2B_1\epsilon_{xx}sin^2(\phi) \tag{4.14}$$

Typically, a uniaxial term has the form $K_{\mathrm{uni}}\sin^2(\phi)$. Looking into eq. 4.14, we can identify this term as $K_{\mathrm{uni}} = -2B_1\epsilon_{xx}$. As we have seen in the previous results, this term overcomes the magneto-cristalline cubic term $K_1/4$.

In order to calculate the uniaxial anisotropy constant, we estimate its value according to the literature. For $Fe_{80}Ga_{20}$, $B_1 = -15\,\mathrm{MPa}$ [19, 188], and the strain generated by PMN-PT is $\epsilon_{xx} = \pm 0.04\%$ [197]. The alternating sign of ϵ_{xx} has its origin in the shear strain produced in the substrate by a 109° ferroelectric switch, which changes its direction according to the polarity of the applied electric field. For positive bias $\epsilon_{xx} = -0.04\%$, and for negative applied electric field $\epsilon_{xx} = 0.04\%$. Then, we can calculate the absolute value of the uniaxial term in our film according to the literature $|K_{\mathrm{uni}}| = 12\,\mathrm{kJ/m^3}$. However, we can estimate the value of K_{uni} from the hard loop shown in Fig. 4.16 b and Fig. 4.16 c. The anisotropy field is $\mu_0 H_a \sim 30\,\mathrm{mT}$. Then, we can calculate K_{uni} as:

$$K_{\mathrm{uni}} = \frac{\mu_0 M_s H_a}{2} \tag{4.15}$$

The magnetic saturation for a $Fe_{80}Ga_{20}$ film is $\mu_0 M_s = 1.65\,\mathrm{T}$ [188]. Then, the experimental value obtained is $|K_{\mathrm{uni}}| = 19.7\,\mathrm{kJ/m^3}$. The K_{uni} obtained experimentally is higher than the predicted by the literature. This fact can be explained by an improved value of B_1 achieved in our sample, and the single ferroelectric domain focused by MOKE.

The cubic anisotropy constant is calculated from the M-H loop shown in Fig. 4.13 a. We obtain $K_1 = -12\,\mathrm{kJ/m^3}$. We can compare both anisotropy con-

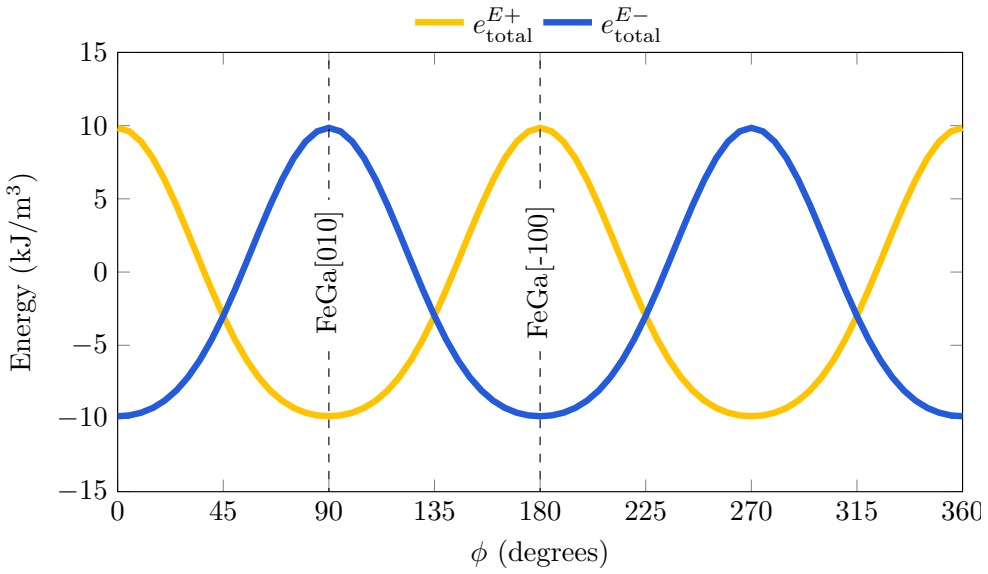

Figure 4.22: Curves obtained from eqs. 4.16 and 4.17. The crystal directions FeGa[010] and FeGa[-110] are marked to analyze how the minimum of energy switch as the polarity of E changes.

stants by the ratio $|K_{\text{uni}}|/|K_1| = 1.64$. The uniaxial anisotropy is higher than the cubic one explaining the overcome of the uniaxial anisotropy observed.

As the uniaxial anisotropy changes its sign with the polarization of the substrate, we define $K^{E+}_{\text{uni}} = -19.7\,\text{kJ/m}^3$, and $K^{E-}_{\text{uni}} = 19.7\,\text{kJ/m}^3$ for positive and negative bias, respectively. The total energy is then, represented as:

$$e^{E+}_{\text{total}} = \frac{K_1}{4}\sin^2(2\phi) + B_1\epsilon_{xx} + K^{E+}_{\text{uni}} sin^2(\phi) \tag{4.16}$$

$$e^{E-}_{\text{total}} = \frac{K_1}{4}\sin^2(2\phi) + B_1\epsilon_{xx} + K^{E-}_{\text{uni}} sin^2(\phi) \tag{4.17}$$

Fig. 4.22 shows the curves obtained from the eqs. 4.16 and 4.17. When the electric field is applied positively, the minimum of energy corresponds to FeGa[010], which is the position of the easy axis observed. For negative electric field, the minimum is at FeGa[100] directions. The analysis done can explain the 90° rotation of the easy axis by a high value of uniaxial anisotropy that changes its sign according to the polarity of the applied electric field.

Discussion about polycrystal FeGa/PMN-PT(001)

Taking into account the previous results and analysis, the strong magnetocoupling between FeGa and PMN-PT could persist even without the MgO layer. A study of the heterostructure $Fe_{80}Ga_{20}$/PMN-PT(001) grown at $T_s = 150\,°C$ with $t = 17\,nm$ is carried out. The as-grown S_k is shown in Fig. 4.14 a, exposing an isotropic magnetization in-plane. As we have seen, when the substrate PMN-PT(001) is poled, a strong uniaxial magnetic anisotropy emerges. This uniaxial anisotropy can break the isotropic configuration and set two states at remanence, 0+ and 0−.

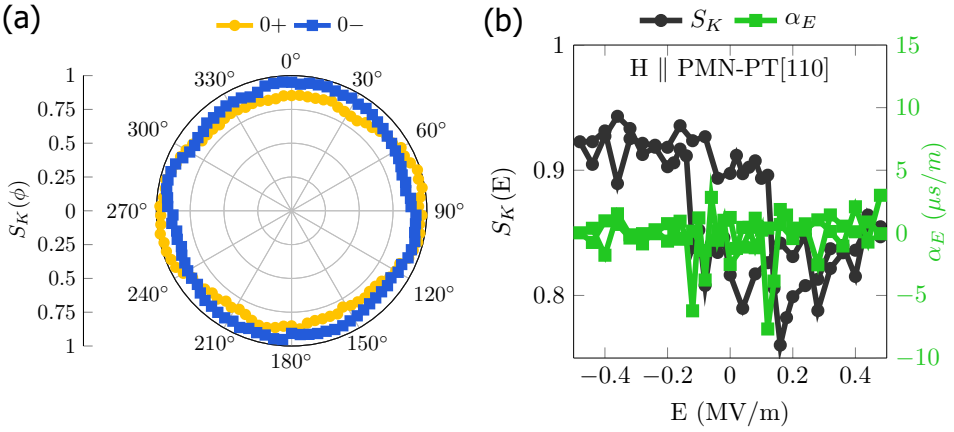

Figure 4.23: Magnetic characterization of sample FeGa/PMN-PT grown at $T_s = 950\,°C$. (a) Squareness polar plot of the states 0+ and 0−. The directions are 0° ∥ PMN-PT[110] and 90° ∥ PMN-PT[100]. (b) Electric loop while H is applied along PMN-PT[110] direction. S_K and α_E as a function of the applied electric field.

Fig. 4.23 a shows the squareness polar plot of the states 0+ and 0−. The MOKE measure was carried out in a switching ferroelectric area. The as-grown isotropic magnetization is hardly modified by the electric field applied to the substrate. The states 0+ and 0− present a similar magnetic landscape. The direction at which the magnetization varies most is PMN-PT[110]. Fig. 4.23 b shows the electric polarization loop carried along PMN-PT[110] direction. The amplitude of S_K is around ~ 0.1, while for the heterostructure with MgO layer is around ~ 0.9. The loop is noisy and the magnetic states are not-so-well stored from saturation to electric remanence. This fact causes a low magnetocoupling, α_E, between film and substrate. The maximum value is $|\alpha_E| = 7.7\,\mu s/m$ at E= 0.12 MV/m. We note that this is the area with a most

significant observed switch. Other switching ferroelectric areas presents values nearly to $\alpha_E \sim 0\,\mu$s/m because of the noisy magnetic behavior of the film when the substrate is poled. For technological applications, the heterostructure FeGa/PMN-PT presents low values of α_E, whereas the heterostructure FeGa/MgO/PMN-PT present higher values of α_E and a non-volatile behavior.

The uniaxial magnetic anisotropy does not emerge in this heterostructure. This fact can be explained by the analysis of the term $K_{\text{uni}} = -2B_1\epsilon_{xx}$. The magnetoelastic coefficient B_1 is similar to the MgO heterostructure. So, the shear strain produced in the PMN-PT substrate is not causing a strain in the magnetostrictive film. As the film is polycrystalline grown, the crystals are in a random fashion. The net strain is averaged and it results in a weak uniaxial magnetic anisotropy.

Other phenomenology observed

The difficult to fabricate magnetic heterostructures with reproducible results is shown in this section. Only ferroelectric domains that switch their polarization via 109 ° are able to modify the strain on the magnetostrictive film. Then, we have measured samples that present some degree of changes when an electric field is applied, but, it seems that there is mixture of ferroelectric domains which switch by other via that cannot reproduce the previous observed rotation of 90 °. In this section, the electric field is applied perpendicularly as the Fig. 4.15 shows. The squareness polar plots analyzed in Fig. 4.24 have the next relationship: 0 ° ∥ PMN-PT[110] and 90 ° ∥ PMN-PT[100].

Sample $Fe_{82}Ga_{18}$/MgO/PMN-PT(001) with $t_{\text{FeGa}} = 18\,$nm and $t_{\text{MgO}} = 1.6\,$nm is studied by MOKE. Fig. 4.24 a shows the squareness polar plot for $E = 0.5\,$MV/m and $E = -0.5\,$MV/m. Measurements indicate the presence of a uniaxial magnetic anisotropy in the thin film. The magnetic easy axis is rotated $\sim 20\,°$ when an electric field of $|E| = 0.5\,$MV/m is applied. A rotation of easy axis less than 90 ° is also observed for CoFeB mesoscopic discs grown on PMN-PT(001) [187]. Also, the easy axis at $E = 0.5\,$MV/m is rotated 45 ° with respect to the direction PMN-PT[110], unlike to point along the orthogonal directions of PMN-PT(001) as seen in the rest of samples. At $E = 0\,$MV/m the states 0+ and 0− are equal (Fig. 4.24 b), being similar to the curve $E = -0.5\,$MV/m shown in Fig. 4.24 a. In this case, the magnetic states are not stored at $E = 0\,$MV/m, and the heterostructure is volatile.

For the sample $Fe_{82}Ga_{18}$/MgO/PMN-PT(001) with $t_{\text{FeGa}} = 8\,$nm and $t_{\text{MgO}} = 2.4\,$nm the squareness plot dependency with electric field is shown in Fig. 4.24 c. In this case, there is no rotation in the magnetization vector, but a change in the magnetic anisotropy is observed. For negative bias, the uniaxial magnetic anisotropy has a 2-fold symmetry, but, for positive bias, a 4-fold

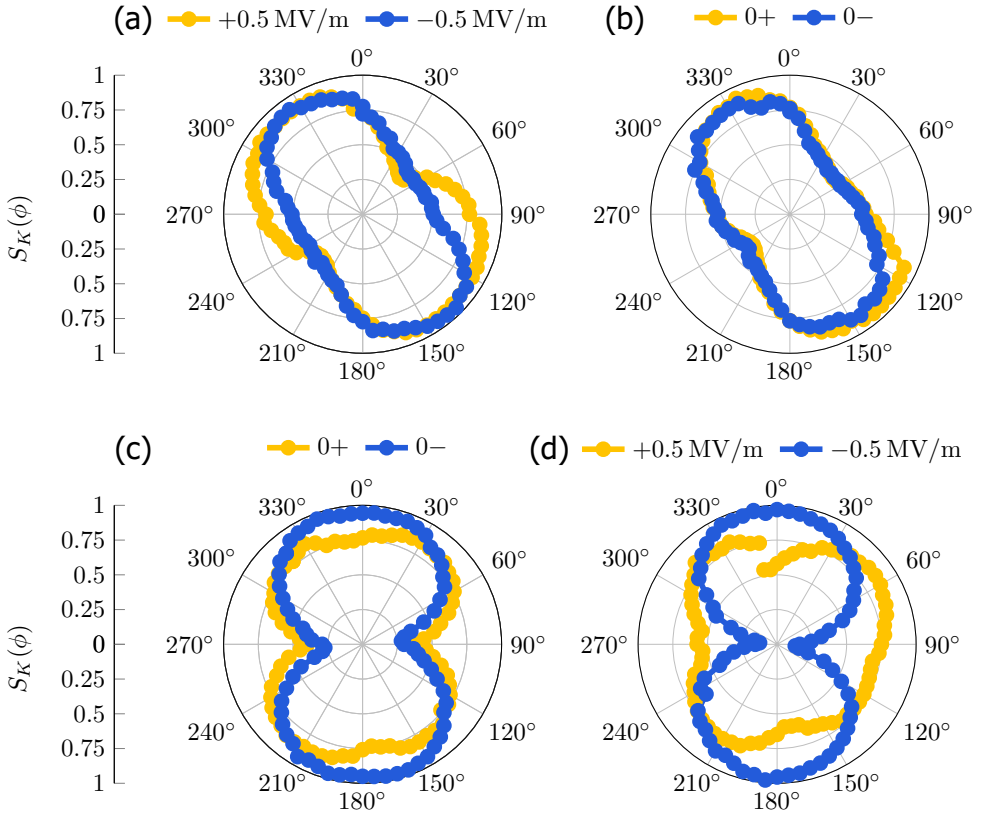

Figure 4.24: Squareness polar plot for FeGa/MgO/PMN-PT(001) samples. (a) and (b) sample with $x = 18$, $t_{\mathrm{FeGa}} = 18\,\mathrm{nm}$ and $t_{\mathrm{MgO}} = 1.6\,\mathrm{nm}$. (c) and (d) sample with $x = 18$, $t_{\mathrm{FeGa}} = 8\,\mathrm{nm}$ and $t_{\mathrm{MgO}} = 2.4\,\mathrm{nm}$.

symmetry is arising and competing with the uniaxial anisotropy. Also, a lose of the ferroelectric character of PMN-PT was observed during a MOKE angular measurement at $E = 0.5\,\mathrm{MV/m}$ (Fig. 4.24 d). The uniaxial anisotropy is reinforced at negative electric field, but the positive bias cannot retain the strain for all the duration of the cycle measurement ($\sim$ 1 hour) and the S_k curve displays a non-closed loop.

4.7.2 FeGa(112) heterostructures

Heterostructures of FeGa(112)/MgO(011)/PMN-PT(001) are studied. An initial poling of E= 0.6 MV/m was carried out to align the ferroelectric domains. PMN-PT(011) has a strong lattice strain when the ferroelectric domains switch via 71 °. By means of MOKE, several areas of the samples are measured to find these switching areas. In the multiple samples fabricated, and in all the areas searched micron by micron, no relevant magnetic switching was found.

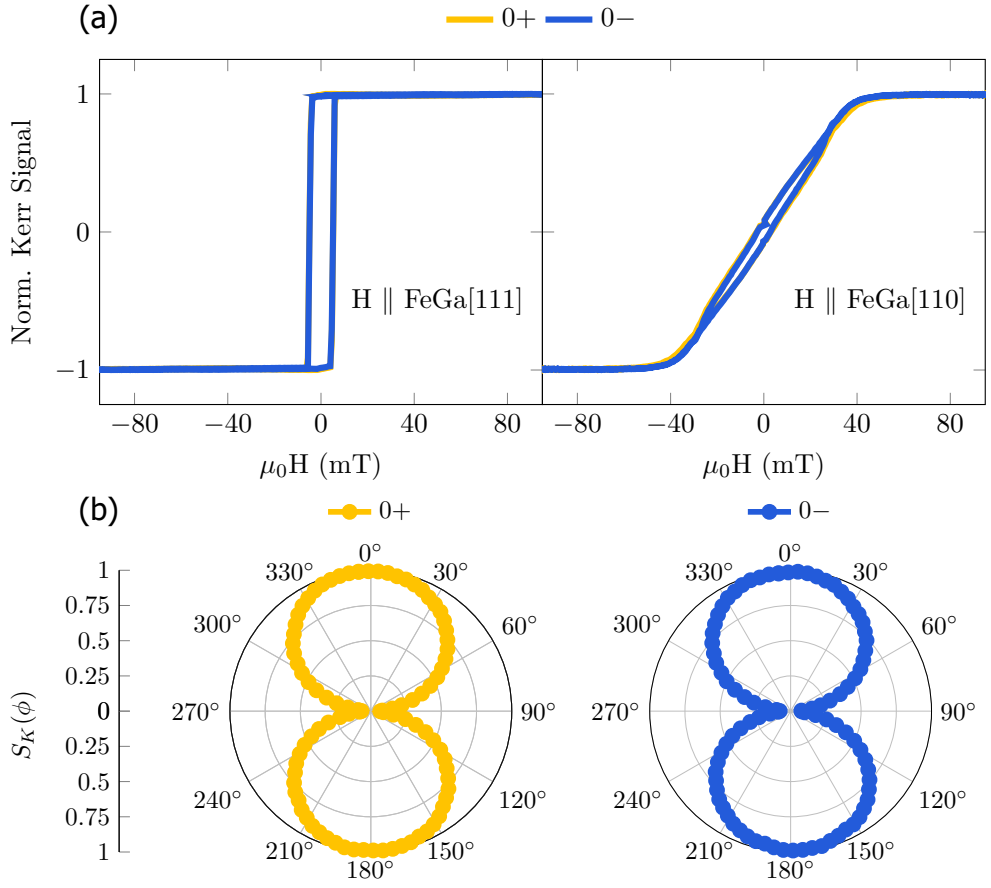

Figure 4.25: Magnetic characterization of FeGa(112)/MgO(011)/PMN-PT(011) heterostructure by MOKE. (a) M-H loops at FeGa[111] and FeGa[110] directions. States 0+ and 0− are shown in each plot. As there is no change, plot of state 0− is overlapping the 0+ state. (b) S_K for 0+ and 0− states where 0° ∥ FeGa[111] and 90° ∥FeGa[110].

The results exposed in this section are for a sample with MgO thickness of $t_{\mathrm{MgO}} = 1\,\mathrm{nm}$, and a thin film of $Fe_{81}Ga_{19}$ with $t_{\mathrm{FeGa}} = 15\,\mathrm{nm}$.

Fig. 4.25 a shows the hysteresis loops performed by MOKE along easy (FeGa[111]), and hard magnetic axis (FeGa[110]) to see the differences between the states after applying the electric field. The result indicates that there is no change between the loop 0+ and 0−. Fig. 4.25 b shows the S_K plots performed to search directions with pronounced switching, but the shape for states 0+ and 0− does not change under applied electric field.

An electric loop along FeGa[110] direction (hard axis) is shown in Fig. 4.26 . At $E = 0\,\mathrm{MV/m}$, M-H loops have nearly the same S_k, as seen in Fig. 4.25 a.

But, at $E = \pm 1\,\mathrm{MV/m}$ some differences arise. From $E = 1\,\mathrm{MV/m}$ to $E = -1\,\mathrm{MV/m}$, the M-H loop broaden and, S_k and the coercive field, increase as the voltage decreases. The amplitude of the electric loop is $\Delta S_k \sim 0.2$, which is lower than the obtained for PMN-PT(001) heterostructures, $\Delta S_k \sim 0.8$. In any case, this is the only straintronic noticeable result obtained for PMN-PT(011) heterostructures. Two separated magnetic states can be stabilized by a continuous electric applied field, i.e. state 0 at $E = 1\,\mathrm{MV/m}$, and state 1 at $E = -1\,\mathrm{MV/m}$. Unfortunately, when the electric field is switched off, the magnetic state is lost. So, these heterostructures can act as volatile memories.

As the samples do not present high changes under applied electric field, it may be possible that the measurement taken on the samples were not performed on the ferroelectric switching area. For substrates PMN-PT(011), the main mechanism of switching is the 71°, that occurs in $\sim 80\%$ of the sample [175]. So, it does not seems plausible not to find an area with ferroelectric switching.

Heterostructures based on PMN-PT(011) have shown its functionality. For example CoPt/PMN-PT(011) presents two differentiated states at $E = \pm 1.4\,\mathrm{MV/m}$ [200]. Volatile magnetization manipulation was reported in $La_{0.7}Sr_{0.3}MnO_3$ [165] and $Co_{40}Fe_{40}B_{20}$/PMN-PT(011) [201] heterostructures with the maximum change of the in-plane $\Delta M/M(0)$ reaching 25% and 83%, respectively. Thin films of Fe/PMN-PT(011) present a non-volatile memory with an amplitude of $\Delta M_r/M_s = 10\%$ between states [202]. Alloys of Fe like FePt/PMN-PT(011) can switch the magnetization $\sim 90°$ in-plane by applying electric field perpendicularly [203]. Also, for FeGa polycrystals it is possible to change M-H loops by applying electric field [204].

As the literature reports, PMN-PT(011)-based heterostructures are able to work as a non-volatile straintronic device. The main difference between our work and literature is the FeGa single-crystal growth achieved via MgO layer. The sample displays a strong uniaxial magnetic anisotropy as-grown (Fig. 4.13 d) that remains after poling. The effect of poling the substrate perpendicularly generates a strain of $\epsilon_{xx} = 0\%$ and $\epsilon_{yy} = 0.19\%$ [205]. In our samples, it generates even more strain along FeGa[111] direction, which reinforces the uniaxial anisotropy seen as-grown. When the substrate switches its polarization, the strain is $\epsilon_{xy} = \pm 0.13\%$ [205], where $\pm$ indicates the polarity. Note that the shear strain produced by the switch in polarization is lower than the poling strain. We propose that, in terms of energy, the term ϵ_{xx} is related to uniaxial energy, and overcomes the rest of contributions due to its reinforcement after poling, including the shear strain, ϵ_{xy}, which is the responsible for the rotation of the magnetic axis.

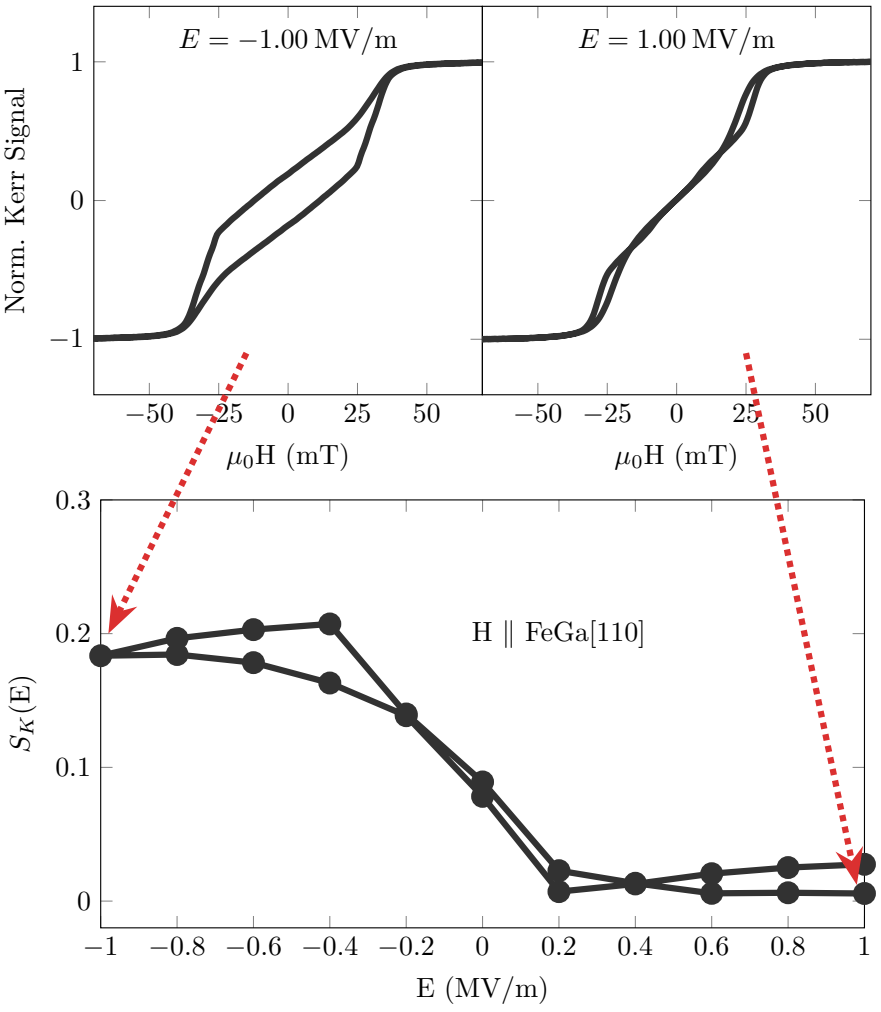

Figure 4.26: S_k *vs* E for FeGa/MgO/PMN-PT(011) heterostructure with H applied parallel to FeGa[110]. S_k values are obtained from M-H loops. The most relevant M-H loops are shown above the main plot: left plot for $-1\,\mathrm{MV/m}$, and right plot for $1\,\mathrm{MV/m}$.

4.8 Conclusions

We have shown a fabrication route to grown FeGa single-crystal using PMN-PT as a substrate by the deposition of an intermediate MgO layer. Structural and magnetic characterizations were performed on FeGa/MgO/PMN-PT and FeGa/PMN-PT heterostructures. The samples with MgO present better characteristics to act as a straintronic device such as flat surface, single-crystal structure and magnetic anisotropy. The samples were characterized magnetically by MOKE under applied electric field. The results for samples with PMN-PT(001) are promising. The electric field can rotate the easy axis of magnetization 90° achieving a giant magnetocoupling factor of $\alpha_E = 15\,\mu$s/m. This fact is reproducible over several cycles proving that the heterostructure fabricated work as a non-volatile memory. On the other hand, the samples with PMN-PT(011) substrate only present changes when an electric field is applied continuously. When the electric field is switched off, the magnetic states are lost.

Summary and conclusions

This thesis is focused on the study and characterization of structural and magnetic properties of iron-gallium alloys at the thin film scale. The interest in studying FeGa alloys relies on its high magnetostriction. For a composition of $Fe_{81}Ga_{19}$, the magnetostriction λ_{100} is 10 times that of the pure Fe [18]. These alloys are rare-earth free, machinable [24], ductile, weldable, and they can be deposited over crystalline substrates [25]. Also, they present high Curie temperature [19] (675 °C for Ga 19%), small magnetic anisotropy coefficients [26] and are corrosion resistant [27], as well as biodegradable [28]. These magnetostrictive alloys have many applications like: active and passive vibration control, spintronic devices, energy harvesting, and torque sensing [17]. Another application of magnetostrictive materials is in the straintronics field. Straintronics is based on the control of the magnetization **M** via strain. In this thesis, we have shown the rotation of the magnetization in FeGa thin films by applying electric field to a ferroelectric substrate. As no electric current is used, the rotation of **M** is more efficient energetically than the used in the nowadays current devices.

The summary and conclusions for each chapter are indicated below.

Chapter 2: The experimental methods used in this thesis are: molecular beam epitaxy, reflection high-energy electron diffraction, transmission electron microscopy, x-ray diffraction, x-ray reflectivity, energy-dispersive x-ray spectroscopy, vibrating-sample magnetometry, magneto-optic Kerr effect magnetometry, magnetic force microscopy, and the cantilever method. Among these methods, we want to highlight the work done in magneto-optic Kerr effect (MOKE) and the cantilever method. For MOKE, a procedure to obtain hysteresis loops along any crystallographic direction was developed by conjugating longitudinal and transverse Kerr signals. By using this method we can plot the squareness from each loop into a polar plot to identify magnetic anisotropies in the film without the need of rotate the sample. For the cantilever method, a capacitance cell was built to measure the magnetoelastic (ME) coupling coefficients of FeGa/MgO samples. The capacitance cell fabricated can measure

changes of capacitance in the order of aF. Also, a magnetic dipole made of two ferrite permanent magnets was mounted over a rotary platform to apply magnetic field to the capacitance cell. As the magnetic field rotates around the cell, several measurements of parallel and perpendicular magnetic configurations can be performed and, in this way, the values of the magnetoelastic coefficients can be precisely determined by averaging.

Chapter 3: Epitaxial thin films of FeGa/MgO(001) were grown by MBE and studied by structural and magnetic characterization techniques according to two variables: growth temperature (T_s) and Ga content (x). The samples growth at $T_s = 150\,°C$ present *bcc* crystal structure and cubic magnetic anisotropy. However, samples with $x = 24$ grown at $T_s > 400\,°C$ can present *bcc* or *fcc* structure, and magnetically are isotropic. AFM images indicate that samples grown at $T_s = 150\,°C$ present a flat surface, whereas samples grown at $T_s = 600\,°C$ present 3D island growth. From the study of FeGa thin films *vs* Ga atomic content we have obtained that for $x > 18$ a superorder structure is formed, as RHEED and XRD measurements indicate. The presence of the superorder *bcc* (001) peak is attributed to a Ga ordering in the matrix. Respect to the magnetic characterization, VSM and MOKE results indicate that the magnetic easy axis rotates from FeGa[100] at $x < 19$ to FeGa[110] for $x > 19$. This spin-reorientation occurs at the same range of compositions in which the superorder is observed. It is argued that the Ga ordering may be behind the spin-reorientation. Another change was found in MFM measurements, a corrugated magnetic structure arises for $x > 20$. An analysis of the M-H loops with the ferromagnetic wandering axis model is made to conclude that the origin of the corrugated magnetic structure may be a random magnetic anisotropy. The influence on the ME coupling coefficients by adding third elements to the binary alloy is also studied. The literature reports that adding Tb or Cu to FeGa can double the λ_{100} [116–118]. Our results indicate that doping with Tb has no influence on the magnetoelastic stress coefficients. On the other hand, alloying with Cu is detrimental to B_1 and B_2. TEM measurements indicate that a ω phase is formed in the ternary FeGaCu alloy. The presence of the ω phase could explain the weakening of the ME coupling coefficients.

Chapter 4: Heterostructures based on the magnetostrictive layer FeGa and the ferroelectric substrate PMN-PT are presented as candidate for straintronic devices. The use of PMN-PT as substrate has been reported for straintronic applications due to the high strain that present when the polarization is switched. In this thesis two surface oriented substrates are used: PMN-PT(001) and PMN-PT(011). For FeGa grown directly on PMN-PT at $T_s = 150\,°C$, the RHEED indicates polycrystalline growth. But, for $T_s = 950\,°C$ the RHEED indicates crystalline growing. A deposition route to achieve

single-crystal FeGa was carried out by using a MgO seed layer. This route is reproducible and the films have good crystallinity according to RHEED, XRD and TEM measurements. As-grown magnetic characterization indicates that FeGa/MgO/PMN-PT(001) present cubic magnetic anisotropy, whereas FeGa/MgO/PMN-PT(011) present uniaxial anisotropy. FeGa grown directly on PMN-PT at $T_s = 150\,°C$ and $T_s = 950\,°C$ present magnetic isotropy. A PCB platform was designed and fabricated to hold the samples and lead a perpendicular electric field to polarize the ferroelectric substrate. The results for FeGa/MgO/PMN-PT(001) are promising, we have shown that a magnetic easy axis rotation of 90 ° can be achieved by applying $|E| = 0.2\,MV/m$. A giant converse magnetoelectric coupling coefficient of $\alpha_E = 15\,\mu s/m$ was measured and the non-volatile character of the device is proved. Also, a 180 ° rotation of the magnetic easy axis can be achieved by the assistance of a magnetic field as low as 3 mT. For FeGa/MgO/PMN-PT(011) the results indicate that the strong uniaxial magnetic anisotropy does not rotate under applied electric field. However, changes in the hysteresis loops along the hard magnetic axis are observed for $E = \pm 1\,MV/m$. The squareness and coercive field increase for negative bias, but at $E = 0\,MV/m$ the magnetic state is lost. Then, the heterostructures based on PMN-PT(011) are volatile.

Outlook

Here the large value of the converse magnetoelectric coupling coefficient has been observed in FeGa(001) films. This large value makes this material appealing for new low-energy consumption and adequate to be integrated in spintronic devices to realize efficient logic or neuromorphic computing. A major drawback in the use of PMN-PT substrates is the inhomogeneity of the ferroelectric inversion mechanisms. Small magnets with nanometric lateral dimensions will be used for applications with strain and electric field concentrated in the magnetic element. In general, the strain applied by the ferroelectric in that geometry is volatile and induces also volatile electric control of the magnetic properties. Recently, non-reversible states have been reported in trilayers comprising two magnetic layers separated by a non-magnetic spacer, with opposite sign for the magnetostricition coefficients in each magnetic layer and dipolar coupling between them [206]. Thus, the FeGa alloy may be part of that trilayer structure.

Besides the large magnetoelastic stress and giant converse magnetoelectric coupling coefficient observed for the A2 structure, the ordered $D0_3$ phase presents a stark giant anomalous Nernst effect at room temperature suitable for recollecting energy using thermal variations [207]. Controlling the crystal structure via the growth temperature and/or flux rate may also generate structures with complementary properties.

Resumen y conclusiones

Esta tesis está centrada en el estudio y caracterización de propiedades estructurales y magnéticas de la aleación hierro-galio en películas delgadas. El interés del estudio del FeGa reside en su alta magnetostricción. Para la composición $Fe_{81}Ga_{19}$, la magnetostricción λ_{100} es 10 veces superior a la del Fe puro [18]. Estas aleaciones además de no poseer tierras raras, son mecanizables [24], dúctiles, soldables y pueden depositarse sobre sustratos cristalinos [25]. También presentan una alta temperatura de Curie [19] (675 °C para Ga 19%), una baja anisotropía magnética [26], son resistentes a la corrosión [27] y además son biodegradables [28]. Estas aleaciones magnetostrictivas tienen diversas aplicaciones: control activo y pasivo de vibración, dispositivos espintronicos, recolección de energía y detección de par [17]. Otra aplicación de los materiales magnetostrictivos es en el campo de la deformatrónica. La deformatrónica se basa en el control de la imanación **M** mediante deformaciones. En esta tesis hemos mostrado la rotación de la imanación en películas delgadas de FeGa mediante la aplicación de campo eléctrico a un sustrato ferroeléctrico. Como no se utiliza corriente eléctrica, la rotación de **M** es más eficiente energéticamente que la usada en los dispositivos actuales.

El resumen y conclusiones de cada capítulo se indican a continuación.

Capítulo 2: Los métodos experimentales usados en esta tesis son: crecimiento epitaxial por haces moleculares, reflexión por difracción de electrones de alta energía, microscopía electrónica de transmisión, difracción de rayos-x, reflectividad de rayos-x, fluorescencia de rayos-x por energía dispersiva, magnetómetro de muestra vibrante, magnetómetro de efecto Kerr magneto-óptico, microscopía de fuerza magnética y el método de la viga en voladizo. De estos métodos, queremos destacar el trabajo realizado con el magnetómetro de efecto Kerr magneto-óptico (MOKE) y con el método de la viga en voladizo. Para el MOKE, se ha desarrollado un procedimiento para obtener ciclos de histéresis a lo largo de cualquier dirección cristalográfica conjugando las señales longitudinales y transversales Kerr. Mediante este método podemos graficar la cuadratura de cada ciclo en una gráfica polar para identificar las anisotropías

magnéticas de la película sin la necesidad de rotar la muestra. En cuanto al método de la viga en voladizo, se ha construido una celda capacitiva para medir los coeficientes de acoplamiento magnetoelástico (ME) de las muestras FeGa/MgO. La celda capacitiva se ha fabricado para poder medir cambios de capacidad del orden de los aF. Además, a partir de dos imanes permanentes de ferrita se ha construido un dipolo magnético montado sobre una plataforma rotatoria para poder aplicar campo magnético a la celda capacitiva. Como el campo magnético rota alrededor de la celda, se obtienen varias medidas en configuración paralela y perpendicular para poder determinar con mayor precisión los coeficientes magnetoelásticos.

Capítulo 3: Se han crecido y estudiado películas delgadas epitaxiales de FeGa/MgO(001) estructural y magnéticamente atendiendo a dos variables: temperatura de crecimiento (T_s) y contenido de Ga (x). Las muestras crecidas a $T_s = 150\,°C$ muestran una estructura cristalina tipo *bcc* y anisotropía magnética cúbica. Sin embargo, las muestras con $x = 24$ crecidas a $T_s = 400\,°C$ pueden presentar estructuras tipo *bcc* o *fcc*, y son magnéticamente isótropas. Las imágenes de AFM indican que las muestras crecidas a $T_s = 150\,°C$ tienen la superficie plana, mientras que las muestras crecidas a $T_s = 600\,°C$ presentan crecimiento por islas. Del estudio de películas delgadas de FeGa respecto a su contenido en Ga hemos obtenido que para $x > 18$ se forma una estructura superordenada, tal y como las medidas de RHEED y XRD indican. La presencia del pico de superorden *bcc* (001) se atribuye a un ordenamiento de los átomos de Ga en la matriz. En cuanto a la caracterización magnética, los resultados de MOKE y VSM indican que el eje fácil magnético rota de la dirección FeGa[100], para $x < 19$, hacia la dirección FeGa[110], para $x > 19$. Esta reorientación de espín ocurre en el mismo rango de composiciones a las cuales se observa el superorden. Se puede argumentar que el ordenamiento del Ga puede estar detrás de la reorientación de espín. En las medidas de MFM se ha encontrado otro cambio para $x > 20$, el surgimiento de una estructura magnética corrugada. El análisis de ciclos de histéresis, junto al modelo del ferromagnético de ejes errantes, permite concluir que una anisotropía magnética aleatoria puede ser el origen de la estructura magnética corrugada. También se ha estudiado la influencia en los coeficientes magnetoelásticos al añadir un tercer elemento a la aleación binaria FeGa. La literatura indica que añadir Tb o Cu al FeGa puede doblar el valor de λ_{100} [116–118]. Nuestros resultados indican que dopar con Tb no tiene influencia en los coeficientes magnetoelásticos. Por otro lado, alear con Cu es perjudicial para B_1 y B_2. Las medidas de TEM indican la formación de una fase ω en la aleación ternaria FeGaCu. La presencia de la fase ω podría explicar el emperoramiento de los coeficientes magnetoelásticos.

Capítulo 4: Se presentan las heteroestructuras basadas en una capa magne-

tostrictiva de FeGa y el sustrato ferroeléctrico PMN-PT como candidatos para crear dispositivos deformatrónicos. Se ha utilizado el PMN-PT como sustrato debido a la alta deformación que presenta cuando se cambia su polarización. En esta tesis se han utilizado dos tipos de orientaciones para los sustratos: PMN-PT(001) y PMN-PT(011). Para el FeGa crecido directamente sobre PMN-PT a $T_s = 150\,°C$, las imágenes de RHEED indican un crecimiento policristalino. Pero, para muestras crecidas a $T_s = 950\,°C$, el RHEED indica crecimiento cristalino. Se ha logrado obtener FeGa monocristal mediante una ruta de depósito en la cual está involucrada una capa intermedia de MgO. Esta ruta es reproducible y las películas crecen con buena cristalinidad de acuerdo a las medidas de RHEED, XRD y TEM. La caracterización magnética de la muestra virgen indica que la heteroestructura FeGa/MgO/PMN-PT(001) presenta anisotropía magnética cúbica, mientras que FeGa/MgO/PMN-PT(011) presenta anisotropía uniaxial. Las muestras de FeGa crecido directamente sobre PMN-PT a $T_s = 150\,°C$ y $T_s = 950\,°C$ son isótropas magnéticamente. Se ha diseñado y fabricado una plataforma PCB para sujetar las muestras y poder aplicar campo eléctrico perpendicular para polarizar el sustrato ferroeléctrico. Los resultados de FeGa/MgO/PMN-PT(001) son prometedores, se ha mostrado cómo puede conseguirse una rotación de 90 ° mediante la aplicación de $|E| = 0.2\,MV/m$. Se ha medido un coeficiente de acoplo magnetoeléctrico inverso gigante de $\alpha_E = 15\,\mu m/s$ y también se ha mostrado el carácter no volátil del dispositivo. Además, puede conseguirse una rotación de 180 ° del eje magnético fácil mediante la asistencia de un campo magnético tan bajo como 3 mT. Para FeGa/MgO/PMN-PT(011), los resultados indican que la fuerte anisotropía uniaxial no rota cuando se aplica campo eléctrico. Sin embargo, sí que se observan cambios en los ciclos de histéresis a lo largo del eje magnético difícil para $E = \pm 1\,MV/m$. La cuadratura y campo coercitivo incrementan para campos eléctricos negativos, pero a campo nulo, el estado magnético se pierde. Entonces, las heteroestructuras basadas en PMN-PT(011) son volátiles.

Perspectivas

Se ha observado un valor alto del coeficiente de acoplo magnetoeléctrico inverso para las películas FeGa(001). Este valor tan alto lo hace atractivo para su uso en dispositivos de bajo consumo energético y poder ser integrado en dispositivos espintrónicos para realizar tareas lógicas o de computación neuromórfica. El gran inconveniente de usar sustratos PMN-PT es la inhomogeneidad de los mecanismos de inversión ferroeléctrica. Cualquier aplicación tecnológica requerirá el uso de pequeños elementos magnéticos con dimensiones nanométricas en las que se concentra la deformación y campo eléctrico. En general, la deformación aplicada por los ferroeléctricos en esa geometría

es volátil, e induce también un control eléctrico volátil de las propiedades magnéticas. Recientemente, se han reportado estados no reversibles en tricapas compuestas por dos capas magnéticas separadas por un espaciador no magnético con el signo de los coeficientes magnetoelásticos opuesto en cada capa magnética, y acopladas dipolarmente entre ellas [206]. Por tanto, la aleación FeGa podría formar parte de esa estructura tricapa.

Además de los altos valores magnetoelásticos, y del acoplo magnetoeléctrico inverso gigante observado para la estructura A2, la fase ordenada $D0_3$ presenta un efecto Nernst anómalo gigante a temperatura ambiente, lo cual es ideal para recolectar energía de variaciones térmicas [207]. Controlar la estructura cristalina a través de la temperatura de crecimiento y/o el flujo de evaporación también puede generar estructuras con propiedades complementarias.

Publications

- Ciria, M.; Proietti, M. G.; Corredor, E. C.; Coffey, D.; Begué, A.; de la Fuente, C.; Arnaudas, J. I.; Ibarra, A. Crystal structure and local ordering in epitaxial $Fe_{100-x}Ga_x$/MgO(001) films. *Journal of Alloys and Compounds* **2018**, *767*, 905-914.
- Begué, A.; Proietti, M. G.; Arnaudas, J. I.; Ciria, M. Magnetic ripple domain structure in FeGa/MgO thin films. *Journal of Magnetism and Magnetic Materials* **2019**, *498*, 166135.
- Bartolomé, P.; Begué, A.; Muñoz-Noval, A.; Ciria, M.; Ranchal, R. Unveiling the different physical origins of magnetic anisotropy and magnetoelasticity in Ga-rich FeGa thin films. *The Journal of Physical Chemistry C* **2020**, *124*, 4717-4722.
- Begué, A.; Ciria, M. Strain-mediated giant magnetoelectronic coupling in a crystalline multiferroic heterostructure. *ACS Applied Materials & Interfaces* **2021**, *13*, 6778-6784

Bibliography

(1) Knell, M. In *Nanotechnology and the Challenges of Equity, Equality and Development*, Cozzens, S. E., Wetmore, J., Eds.; Springer Netherlands: 2011.

(2) Feynman, R. P. In Annual Meeting of the American Physical Society: 1959.

(3) Bader, S.; Parkin, S. Spintronics. *Annual Review of Condensed Matter Physics* **2010**, *1*, 71–88.

(4) M. H. Falk, R. D. I. Hyperthermia in oncology. *International Journal of Hyperthermia* **2001**, *17*, 1–18.

(5) Wang, Z. L.; Wu, W. Nanotechnology-Enabled Energy Harvesting for Self-Powered Micro-/Nanosystems. *Angewandte Chemie International Edition* **2012**, *51*, 11700–11721.

(6) Akyildiz, I. F.; Jornet, J. M. The Internet of nano-things. *IEEE Wireless Communications* **2010**, *17*, 58–63.

(7) Wellise, C. In Hewlett Packard Enterprise Discover More Conference: 2019.

(8) D'Souza, N.; Biswas, A.; Ahmad, H.; Fashami, M. S.; Al-Rashid, M. M.; Sampath, V.; Bhattacharya, D.; Abeed, M. A.; Atulasimha, J.; Bandyopadhyay, S. Energy-efficient switching of nanomagnets for computing: straintronics and other methodologies. *Nanotechnology* **2018**, *29*, 442001.

(9) Bandyopadhyay, S.; Atulasimha, J.; Barman, A. Magnetic straintronics: Manipulating the magnetization of magnetostrictive nanomagnets with strain for energy-efficient applications. *Applied Physics Reviews* **2021**, *8*, 041323.

(10) Matsukura, F.; Tokura, Y.; Ohno, H. Control of magnetism by electric fields. *Nature Nanotechnology* **2015**, *10*, 209–220.

(11) Bandyopadhyay, S.; Atulasimha, J., *Nanomagnetic and Spintronic Devices for Energy-Efficient Memory and Computing*, 1st Ed.; John Wiley & Sons Inc: United States of America, 2016.

(12) Klimov, A.; Tiercelin, N.; Dusch, Y.; Giordano, S.; Mathurin, T.; Pernod, P.; Preobrazhensky, V.; Churbanov, A.; Nikitov, S. Magnetoelectric write and read operations in a stress-mediated multiferroic memory cell. *Applied Physics Letters* **2017**, *110*, 222401.

(13) Spaldin, N. A.; Fiebig, M. The Renaissance of Magnetoelectric Multiferroics. *Science* **2005**, *309*, 391–392.

(14) Fiebig, M. Revival of the magnetoelectric effect. *Journal of Physics D: Applied Physics* **2005**, *38*, R123–R152.

(15) Eerenstein, W.; Mathur, N. D.; Scott, J. F. Multiferroic and magnetoelectric materials. *Nature* **2006**, *442*, 759–765.

(16) Bibes, M.; Barthélèmy, A. Towards a magnetoelectric memory. *Nature Materials* **2008**, *7*, 425.

(17) Emdadi, A.; Palacheva, V. V.; Balagurov, M.; Bobrikov, I. A.; Cheverikin, V. V.; Cifre, J.; Golovin, I. S. Tb-dependent phase transitions in Fe-Ga functional alloys. *Intermetallics* **2018**, *93*, 55–62.

(18) Clark, A. E.; Hathaway, K. B.; Wun-Fogle, M.; Restorff, J. B.; Lograsso, T. A.; Keppens, V. M.; Petculescu, G.; Taylor, R. A. Extraordinary magnetoelasticity and lattice softening in bcc Fe-Ga alloys. *Journal of Applied Physics* **2003**, *93*, 8621–8623.

(19) Clark, A. E.; Restorff, J. B.; Wun-Fogle, M.; Lograsso, T. A.; Schlagel, D. L. Magnetostrictive properties of body-centered cubic Fe-Ga and Fe-Ga-Al alloys. *IEEE Transactions on Magnetics* **2000**, *36*, 3238–3240.

(20) Du Trémolet de Lacheisserie, E.; Gignoux, D.; Schlenker, M., *Magnetism: II-Materials and Applications*; Springer Science+Business Media: Switzerland, 2012.

(21) Kellogg, R. A. Development and Modeling of Iron–gallium Alloys, Ph.D. Thesis, Engineering Mechanics Iowa State University, 2003.

(22) Kellogg, R. A.; Flatau, A. B.; Clark, A. E.; Wun-Fogle, M.; Lograsso, T. A. Temperature and stress dependencies of the magnetic and magnetostrictive properties of $Fe_{0.81}Ga_{0.19}$. *Journal of Applied Physics* **2002**, *91*, 7821–7823.

(23) Kellogg, R.; Russell, A.; Lograsso, T.; Flatau, A.; Clark, A.; Wun-Fogle, M. Tensile properties of magnetostrictive iron–gallium alloys. *Acta Materialia* **2004**, *52*, 5043–5050.

(24) Ueno, T.; Summers, E.; Higuchi, T. Machining of iron–gallium alloy for microactuator. *Sensors and Actuators A: Physical* **2007**, *137*, 134–140.

(25) Weston, J.; Butera, A.; Lograsso, T.; Shamsuzzoha, M.; Zana, I.; Zangari, G.; Barnard, J. Fabrication and characterization of $Fe_{81}Ga_{19}$ thin films. *IEEE Transactions on Magnetics* **2002**, *38*, 2832–2834.

(26) Cullen, J.; Zhao, P.; Wutting, M. Anisotropy of crystalline ferromagnets with defects. *Journal of Applied Physics* **2007**, *101*, 123922.

(27) Jayaraman, T. V.; Srisukhumbowornchai, N.; Guruswamy, S.; Free, M. L. Corrosion studies of single crystals of iron–gallium alloys in aqueous environments. *Corrosion Science* **2007**, *49*, 4015–4027.

(28) Wang, H.; Zheng, Y.; Liu, J.; Jiang, C.; Li, Y. In vitro corrosion properties and cytocompatibility of Fe-Ga alloys as potential biodegradable metallic materials. *Materials Science and Engineering: C* **2017**, *71*, 60–66.

(29) Kittel, C. Physical Theory of Ferromagnetic Domains. *Reviews of Modern Physics* **1949**, *21*, 541–583.

(30) Du Trémolet de Lacheisserie, E. Definition and measurement of the surface magnetoelastic coupling coefficients in thin films and multilayers. *Physical Review B* **1995**, *51*, 15925–15932.

(31) Ikeda, O.; Kainuma, R.; Ohnuma, I.; Fukamichi, K.; Ishida, K. Phase equilibria and stability of ordered b.c.c. phases in the Fe-rich portion of the Fe-Ga system. *Journal of Alloys and Compounds* **2002**, *347*, 198–205.

(32) Okamoto, H., *Binary Alloy phase diagrams*, 2nd Ed.; Materials Information Society: 1992.

(33) Kawamiya, N.; Adachi, K.; Nakamura, Y. Magnetic properties and Mössbauer investigations of Fe-Ga alloys. *Journal of the Physical Society of Japan* **1972**, *33*, 1318–1327.

(34) Xing, Q.; Du, Y.; McQueeney, R. J.; Lograsso, T. A. Structural investigations of Fe-Ga alloys: Phase relations and magnetostrictive behavior. *Acta Materialia* **2008**, *56*, 4536–4546.

(35) Summers, E. M.; Lograsso, T. A.; Wun-Fogle, M. Magnetostriction of binary and ternary Fe-Ga alloys. *Journal of Materials Science* **2007**, *42*, 9582–9594.

(36) Wu, R.; Yang, Z.; Hong, J. First-principles determination of magnetic properties. *Journal of Physics: Condensed Matter* **2003**, *15*, S587–S598.

(37) Khachaturyan, A.; Viehland, D. Structurally Heterogeneous Model of Extrinsic Magnetostriction for Fe-Ga and Similar Magnetic Alloys: Part II. Giant Magnetostriction and Elastic Softening. *Metallurgical and Materials Transactions A* **2007**, *38*, 2317.

(38) Wang, H.; Zhang, Y. N.; Yang, T.; Zhang, Z. D.; Sun, L. Z.; Wu, R. Q. Ab initio studies of the effect of nanoclusters on magnetostriction of $Fe_{1-x}Ga_x$ alloys. *Applied Physics Letters* **2010**, *97*, 262505.

(39) Marchant, G. A.; Patrick, C. E.; Staunton, J. B. Ab initio calculations of temperature-dependent magnetostriction of Fe and *A*2 $Fe_{1-x}Ga_x$

within the disordered local moment picture. *Physical Review B* **2019**, *99*, 054415.

(40) Lograsso, T.; Ross, A.; Schlagel, D.; Clark, A.; Wun-Fogle, M. Structural transformations in quenched Fe–Ga alloys. *Journal of Alloys and Compounds* **2003**, *350*, 95–101.

(41) Lograsso, T.; Summers, E. Detection and quantification of D03 chemical order in Fe–Ga alloys using high resolution X-ray diffraction. *Materials Science and Engineering: A* **2006**, *416*, 240–245.

(42) Liu, L.; Fu, S.; Liu, G.; Wu, G.; Sun, X.; Li, J. Transmission electron microscopy study on the microstructure of $Fe_{85}Ga_{15}$ alloy. *Physica B-Condensed Matter* **2005**, *365*, 102–108.

(43) Restorff, J. B.; Wun-Fogle, M.; Hathaway, K. B.; Clark, A. E.; Lograsso, T. A.; Petculescu, G. Tetragonal magnetostriction and magnetoelastic coupling in Fe-Al, Fe-Ga, Fe-Ge, Fe-Si, Fe-Ga-Al, and Fe-Ga-Ge alloys. *Journal of Applied Physics* **2012**, *111*, 023905.

(44) Ciria, M.; Proietti, M. G.; Corredor, E. C.; Coffey, D.; Begué, A.; de la Fuente, C.; Arnaudas, J. I.; Ibarra, A. Crystal structure and local ordering in epitaxial $Fe_{100-x}Ga_x$/MgO(001) films. *Journal of Alloys and Compounds* **2018**, *767*, 905–914.

(45) Browning, R.; Li, T. Z.; Chui, B.; Ye, J.; Pease, R. F.; Czyzewski, Z.; Joy, D. C. Empirical forms for the electron/atom elastic scattering cross sections from 0.1 to 30 keV. *Journal of Applied Physics* **1994**, *76*, 2016–2022.

(46) Hubbell, J. H.; Veigele, W. J.; Briggs, E. A.; Brown, R. T.; Cromer, D. T.; Howerton, R. J. Atomic Form Factors, Incoherent Scattering Functions, and Photon Scattering Cross Sections. *Journal of Physical and Chemical Reference Data* **1975**, *4*, 471–538.

(47) Hasegawa, S. In *Characterization of Materials*, Kaufmann, E. N., Ed.; John Wiley & Sons, Inc: 2012; Chapter Reflection high-energy electron diffraction, pp 1925–1938.

(48) Wang, G. C.; Lu, T. M. In *RHEED Transmission Mode and Pole Figures: Thin Film and Nanostructure Texture Analysis*; Springer Science+Business Media: New York, 2014; Chapter RHEED Transmission Mode and RHEED Pole Figure, pp 73–106.

(49) Kainuma, Y. The Theory of Kikuchi patterns. *Acta Crystallographica* **1955**, *8*, 247–257.

(50) Deepak, F. L.; Mayoral, A.; Arenal, R., *Advanced Transmission Electron Microscopy: Applications to Nanomaterials*; Springer Science+Business Media: Switzerland, 2015.

(51) Hecht, E., *Optics*, 2nd Ed.; Addison Wesley: 1989, p 95.

(52) Ali, M. Growth and study of magnetostrictive FeSiBC thin films for device applications, University of Sheffield, 1999.

(53) Osgood III, R. M.; Clements, B. M.; White, R. L. Asymmetric magneto-optic response in anisotropic thin films. *Physical Review B* **1997**, *55*, 8990–8996.

(54) Liang, J. H.; Cao, J. Z.; Li, J. X.; Wu, Y. Z. Asymmetric magneto-optic response in anisotropic thin films. *Journal of Applied Physics* **1997**, *117*, 1–5.

(55) Liang, J. H.; Xiao, X.; Li, J. X.; Zhu, B. C.; Zhu, J.; Bao, H.; Zhou, L.; Wu, Y. Z. Quantitative study of the quadratic magneto-optical Kerr effects in Fe films. *Optics express* **2015**, *23*, 11357–11366.

(56) Rafique, S.; Cullen, J. R.; Wuttig, M.; Cui, J. Magnetic anisotropy of FeGa alloys. *Journal of Applied Physics* **2004**, *95*, 6939–6941.

(57) Jiles, D., *Introduction to magnetism and magnetic materials*, 1st Ed.; Springer-Science+Business Media: 1991.

(58) Cullity, B. D.; Graham, C. D., *Introduction to Magnetic Materials*, 2nd Ed.; John Wiley & Sons Inc: United States of America, 2008.

(59) Kerr, J. On rotation of the plane of polarization by reflection from the pole of a magnet. *The London, Edinburgh, and Dublin Philosophical Magazine and Journal of Science* **1877**, *3*, 321–343.

(60) Abelmann, L., *Magnetic force microscopy*, 3rd Ed.; Elsevier Ltd.: 2016, pp 675–684.

(61) Dreyer, M.; Gomez, R. D.; Mayergoyz, I. D. Resolution enhancement by applying MFM under UHV conditions. *IEEE Transactions on Magnetics* **2000**, *36*, 2975–2977.

(62) Klokholm, E. The measurement of magnetostriction in ferromagnetic thin films. *IEEE Transactions on Magnetics* **1976**, *12*, 819–821.

(63) B. Hetnarski, R.; Ignaczak, J., *Mathematical theory of elasticity*, 2nd Ed.; CRC Press: 2003.

(64) Timoshenko, S.; Woinowsky-Krieger, S., *Theory of plates and shells*, 2nd Ed.; MacGraw-Hill: 1959.

(65) Landau, L. D.; Lifshizt, E. M., *Curso de física teórica*; Reverté: 1973.

(66) Dubrovin, B. A.; Fomenko, A. T.; Novikov, S. P., *Modern geometry - Methods and applications*, 2nd Ed.; Springer: 1991.

(67) Clark, A. E. In *Handbook of Ferromagnetic Materials*, Wohlfarth, E. P., Ed.; North-Holland: 1980; Chapter 7.

(68) Nye, J. F., *Physical properties of crystals: Their representation by tensors and matrices*; Oxford University Press: 1985.

(69) Anton, H.; Rorres, C., *Elementary linear algebra*, 11th Ed.; Wiley: 1973.

(70) Fu, J.; Bernard, F.; Kamali-Bernard, S. First-principles calculations of typical anisotropic cubic and hexagonal structures and homogenized moduli estimation based on the Y-parameter: Application to CaO,

MgO, CH and Calcite $CaCO_3$. *Journal of Physics and Chemistry of Solids* **2017**, *101*, 74–89.

(71) Ciria, M. Magnetoelasticidad de superredes de tierras raras con lutecio e itrio, Ph.D. Thesis, Universidad de Zaragoza, 1997.

(72) Abadía, C. Magnetismo de monocristales y películas delgadas de intermetálicos fuertemente anisotropos de tierra rara con hierro y zinc, Ph.D. Thesis, Universidad de Zaragoza, 1998.

(73) Benito, L. Anisotropía y magnetoelasticidad en superredes de tierras raras, Ph.D. Thesis, Universidad de Zaragoza, 2004.

(74) Jones, R. V.; Richards, J. C. S. The design and some applications of sensitive capacitance micrometers. *Journal of Physics E: Scientific Instruments* **1973**, *6*, 589–600.

(75) Scott, A. H.; Curtis, H. L. Edge correction in the determination of dielectric constant. *Journal of Research of the National Bureau of Standards* **1939**, *22*, 747–775.

(76) Huang, S. M.; Stott, A. L.; Green, R. G.; Beck, M. S. Electronic transducers for industrial measurement of low value capacitances. *Journal of Physics E: Scientific Instruments* **1988**, *21*, 242–250.

(77) Manual de referencia del puente AH2500A Andeen-Hagerling, 1994.

(78) Zhang, Y.; Zhan, Q.; Zuo, Z.; Yang, H.; Zhang, X.; Yu, Y.; Liu, Y.; Wang, J.; Wang, B.; Li, R.-W. Magnetic Anisotropy and Reversal in Epitaxial FeGa/MgO(001) Films Deposited at Oblique Incidence. *IEEE Transactions on Magnetics* **2015**, *51*, 1–4.

(79) Eberl, K. Vapor pressure elements `https://www.mbe-komponenten.de/selection-guide/element.php`.

(80) JEOL Ltd. Energy table for EDS analysis `https://www.unamur.be/services/microscopie/sme-documents/Energy-20table-20for-20EDS-20analysis-1.pdf`.

(81) Martínez-Boubeta, C.; Costa-Krämer, J. L.; Cebollada, A. Epitaxy, magnetic and tunnel properties of transition metal/MgO(001) heterostructures. *Journal Of Physics: Condensed Matter* **2003**, *15*, R1123–R1167.

(82) Du, Y.; Huang, M.; Chang, S.; Schlagel, D. L.; Lograsso, T. A.; McQueeney, R. J. Relation between Ga ordering and magnetostriction of Fe-Ga alloys studied by x-ray diffuse scattering. *Physical Review B* **2010**, *81*, 054432.

(83) Van Dyck, D.; Van Tendeloo, G.; Amelinckx, S. Diffraction effects due to a single translation interface in a small crystal. *Ultramicroscopy* **1984**, *15*, 357–370.

(84) Kuz'min, M.; Richter, M. In *Encyclopedia of Materials: Science and Technology*, Buschow, K. J., Cahn, R. W., Flemings, M. C., Ilschner,

B., Kramer, E. J., Mahajan, S., Veyssière, P., Eds.; Elsevier: Oxford, 2007, pp 1–7.

(85) Tudu, B.; Tiwari, A. Recent Developments in Perpendicular Magnetic Anisotropy Thin Films for Data Storage Applications. *Vacuum* **2017**, *146*, 329–341.

(86) Atulasimha, J.; Flatau, A. B.; Cullen, J. R. Analysis of the effect of gallium content on the magnetomechanical behavior of single-crystal FeGa alloys using an energy-based model. *Smart Materials and Structures* **2008**, *17*, 025027.

(87) Sun, L.; Hao, Y.; Chien, C. L.; Searson, P. C.; Searson, P. C. Tuning the properties of magnetic nanowires. *IBM Journal of Research and Development* **2005**, *49*, 79–102.

(88) Mudivarthi, C.; Na, S.-M.; Schaefer, R.; Laver, M.; Wuttig, M.; Flatau, A. B. Magnetic domain observations in Fe–Ga alloys. *Journal of Magnetism and Magnetic Materials* **2010**, *322*, 2023–2026.

(89) He, Y.; Coey, J. M. D.; Schaefer, R.; Jiang, C. Determination of bulk domain structure and magnetization processes in bcc ferromagnetic alloys: Analysis of magnetostriction in $Fe_{83}Ga_{17}$. *Physical Review Materials* **2018**, *2*, 014412.

(90) Cao, D.; Wang, Z.; Pan, L.; Feng, H.; Cheng, X.; Zhu, Z.; Wang, J.; Liu, Q.; Han, G. Controllable magnetic and magnetostrictive properties of FeGa films electrodeposited on curvature substrates. *Applied Physics A* **2016**, *122*, 938.

(91) Tacchi, S.; Fin, S.; Carlotti, G.; Gubbiotti, G.; Madami, M.; Barturen, M.; Marangolo, M.; Eddrief, M.; Bisero, D.; Rettori, A.; Pini, M. G. Rotatable magnetic anisotropy in a $Fe_{0.8}Ga_{0.2}$ thin film with stripe domains: Dynamics versus statics. *Physical Review B* **2014**, *89*, 024411.

(92) Marioni, M. A.; Pilet, N.; Ashworth, T. V.; O'Handley, R. C.; Hug, H. J. Remanence due to wall magnetization and counterintuitive magnetometry data in 200-nm films of Ni. *Physical Review Letters* **2006**, *97*, 027201.

(93) Frömter, R.; Stillrich, H.; Menk, C.; Oepen, H. P. Imaging the Cone State of the Spin Reorientation Transition. *American Physical Society* **2008**, *100*, 207202.

(94) Williamson, G. K.; Hall, W. H. X-ray line broadening from filed aluminium and wolfram. *Acta Metallurgica* **1953**, *1*, 22–31.

(95) Landolt-Börnstein In *II-VI and I-VII Compounds; Semimagnetic Compounds*, Madelung, O., Rössler, U., Schulz, M., Eds.; Springer Materials: 1999.

(96) Johnson, M. T.; Bloemen, P. J. H.; den Broeder, F. J. A.; de Vries, J. J. Magnetic anisotropy in metallic multilayers. *Reports on Progress in Physics* **1996**, *59*, 1409–1458.

(97) Hubert, A.; Schäfer, R. In *Magnetic Domains*; Springer: 1998; Chapter Domain Theory.

(98) Dennis, C. L.; Borges, R. P.; Buda, L. D.; Ebels, U.; Gregg, J. F.; Hehn, M.; Jouguelet, E.; Ounadjela, K.; Petej, I.; Prejbeanu, I. L.; Thornton, M. J. The defining length scales of mesomagnetism: a review. *Journal Of Physics: Condensed Matter* **2002**, *14*, 1175–1262.

(99) Atulasimha, J.; Flatau, A. B. A review of magnetostrictive iron-gallium alloys. *Smart Materials and Structures* **2011**, *20*, 1–15.

(100) Bormio-Nunes, C.; Tirelli, M. A.; Sato-Turtelli, R.; Grössinger, R.; Müller, H.; Wiesinger, G.; Sassik, H.; Reissner, M. Volume magnetostriction and structure of copper mold-cast polycrystalline Fe–Ga alloys. *Journal of Applied Physics* **2005**, *97*, 033901-1–6.

(101) Balogh, J.; Dézsi, I.; Fetzer, C.; Korecki, J.; Kozioł-Rachwał, A.; Mły ńczak, E.; Nakanishi, A. Magnetic properties of the Fe-MgO interface studied by Mössbauer spectroscopy. *Physical Review B* **2013**, *87*, 174415.

(102) Kawauchi, T.; Miura, Y.; Zhang, X.; Fukutani, K. Interface-driven noncollinear magnetic structure and phase transition of Fe thin films. *Physical Review B* **2017**, *95*, 014432–.

(103) Yang, H. X.; Chshiev, M.; Dieny, B.; Lee, J. H.; Manchon, A.; Shin, K. H. First-principles investigation of the very large perpendicular magnetic anisotropy at Fe|MgO and Co|MgO interfaces. *Physical Review B* **2011**, *84*, 54401–54406.

(104) Liu, T.; Zhang, Y.; Cai, J. W.; Pan, H. Y. Thermally robust Mo/CoFeB/MgO trilayers with strong perpendicular magnetic anisotropy. *Scientific Reports* **2014**, *4*, 5895.

(105) O'Handley, R. C.; Woods, J. P. Static magnetization direction under perpendicular surface anisotropy. *Physical Review B* **1990**, *42*, 6568–6573.

(106) Thiaville, A.; Fert, A. Twisted spin configurations in thin magnetic layers with interface anisotropy. *Journal of Magnetism and Magnetic Materials* **1992**, *113*, 161–172.

(107) Imry, Y.; Ma, S.-k. Random-Field Instability of the Ordered State of Continuous Symmetry. *Physical Review Letters* **1975**, *35*, 1399–1401.

(108) O'Handley, R. C., *Modern Magnetic Materials: Principles and Applications*, 1st Ed.; John Wiley & Sons Inc: United States of America, 2000.

(109) Del Moral, A.; Arnaudas, J. I.; Gehring, P. M.; Salamon, M. B.; Ritter, C.; Joven, E.; Cullen, J. Magnetic first-order phase transition and crossover associated with random anisotropy in crystalline $Dy_xY_{1-x}Al_2$. *Physical Review B* **1993**, *47*, 7892–7896.

(110) Fisch, R. Phase transitions in cubic models with random anisotropic exchange. *Physical Review B* **1995**, *51*, 6358–6363.

(111) Chudnovsky, E. M.; Saslow, W. M.; Serota, R. A. Ordering in ferromagnets with random anisotropy. *Physical Review B* **1986**, *33*, 251–261.

(112) Hellman, F.; Shapiro, A. L.; Abarra, E. N.; Robinson, R. A.; Hjelm, R. P.; Seeger, P. A.; Rhyne, J. J.; Suzuki, J. I. Long ferromagnetic correlation length in amorphous $TbFe_2$. *Physical Review B* **1999**, *59*, 11408–11417.

(113) Barturen, M.; Milano, J.; Vásquez-Mansilla, M.; Helman, C.; Barral, M. A.; Llois, A. M.; Eddrief, M.; Marangolo, M. Large perpendicular magnetic anisotropy in magnetostrictive $Fe_{1-x}Ga_x$ thin films. *Physical Review B* **2015**, *92*, 054418.

(114) Du, Y.; Huang, M.; Lograsso, T. A.; McQueeney, R. J. X-ray diffuse scattering measurements of chemical short-range order and lattice strains in a highly magnetostrictive $Fe_{0.813}Ga_{0.187}$ alloy in an applied magnetic field. *Physical Review B* **2012**, *85*, 214437.

(115) Odkhuu, D.; Yun, W. S.; Rhim, S.; Hong, S. C. Theory of perpendicular magnetocrystalline anisotropy in Fe/MgO (001). *Journal of Magnetism and Magnetic Materials* **2016**, *414*, 126–131.

(116) Jiang, L.; Yang, J.; Hao, H.; Zhang, G.; Wu, S.; Chen, Y.; Obi, O.; Fitchorov, T.; Harris, V. G. Giant enhancement in the magnetostrictive effect of FeGa alloys doped with low levels of terbium. *Applied Physics Letters* **2013**, *102*, 222409.

(117) Meng, C.; Wang, H.; Wu, Y.; Liu, J.; Jiang, C. Investigating enhanced mechanical properties in dual-phase Fe-Ga-Tb alloys. *Scientific Reports* **2016**, *6*, 1–9.

(118) Wang, H.; Zhang, Y. N.; Wu, R. Q.; Sun, L. Z.; Xu, D. S.; Zhang, Z. D. Understanding strong magnetostriction in $Fe_{100-x}Ga_x$ alloys. *Scientific Reports* **2013**, *3*, 3521.

(119) He, Y.; Jiang, C.; Wu, W.; Wang, B.; Duan, H.; Wang, H.; Zhang, T.; Wang, J.; Liu, J.; Zhang, Z.; Stamenov, P.; Coey, J.; Xu, H. Giant heterogeneous magnetostriction in Fe–Ga alloys: Effect of trace element doping. *Acta Materialia* **2016**, *109*, 177–186.

(120) Han, Y.; Wang, H.; Zhang, T.; He, Y.; Jiang, C. Exploring structural origin of the enhanced magnetostriction in Tb-doped $Fe_{83}Ga_{17}$ ribbons: Tuning Tb solubility. *Scripta Materialia* **2018**, *150*, 101–105.

(121) He, Y.; Ke, X.; Jiang, C.; Miao, N.; Wang, H.; Coey, J. M. D.; Wang, Y.; Xu, H. Interaction of Trace Rare-Earth Dopants and Nanoheterogeneities Induces Giant Magnetostriction in Fe-Ga Alloys. *Advanced Functional Materials* **2018**, *28*, 1800858.

(122) Restorff, J. B.; Wun-Fogle, M.; Clark, A. E.; Lograsso, T. A.; Ross, A. R.; Schlagel, D. L. Magnetostriction of ternary Fe–Ga–X alloys (X=Ni,Mo,Sn,Al). *Journal of Applied Physics* **2002**, *91*, 8225–8227.

(123) Li, J.; Gao, X.; Zhu, J.; He, C.; Qiao, J.; Zhang, M. Texture evolution and magnetostriction in rolled $(Fe_{81}Ga_{19})_{99}Nb_1$ alloy. *Journal of alloys and compounds* **2009**, *476*, 529–533.

(124) Lograsso, T. A.; Jones, N. J.; Schlagel, D. L.; Petculescu, G.; Wun-Fogle, M.; Restorff, J. B.; Clark, A. E.; Hathaway, K. B. Effects of Zn additions to highly magnetoelastic FeGa alloys. *Journal of Applied Physics* **2015**, *117*, 17E701.

(125) Clark, A.; Restorff, J.; Wun-Fogle, M.; Hathaway, K.; Lograsso, T. A.; Huang, M.; Summers, E. Magnetostriction of ternary fe–ga–x (x= c, v, cr, mn, co, rh) alloys. *Journal of applied physics* **2007**, *101*, 09C507.

(126) Li, J.; Gao, X.; Zhu, J.; Li, J.; Zhang, M. Ductility enhancement and magnetostriction of polycrystalline Fe–Ga based alloys. *Journal of Alloys and Compounds* **2009**, *484*, 203–206.

(127) Wu, W.; Liu, J.; Jiang, C.; Xu, H. Giant magnetostriction in Tb-doped $Fe_{83}Ga_{17}$ melt-spun ribbonss. *Applied Physics Letters* **2013**, *103*, 262403.

(128) Wu, W.; Liu, J.; Jiang, C. Tb solid solution and enhanced magnetostriction in $Fe_{83}Ga_{17}$ alloys. *Journal of Alloys and Compounds* **2015**, *622*, 379–383.

(129) Fitchorov, T. I.; Bennett, S.; Jiang, L.; Zhang, G.; Zhao, Z.; Chen, Y.; Harris, V. G. Thermally driven large magnetoresistance and magnetostriction in multifunctional magnetic FeGa–Tb alloys. *Acta materialia* **2014**, *73*, 19–26.

(130) Jin, T.; Wu, W.; Jiang, C. Improved magnetostriction of Dy-doped $Fe_{83}Ga_{17}$ melt-spun ribbons. *Scripta Materialia* **2014**, *74*, 100–103.

(131) Yao, Z.; Tian, X.; Jiang, L.; Hao, H.; Zhang, G.; Wu, S.; Zhao, Z.; Gerile, N. Influences of rare earth element Ce-doping and melt-spinning on microstructure and magnetostriction of $Fe_{83}Ga_{17}$ alloy. *Journal of Alloys and Compounds* **2015**, *637*, 431–435.

(132) Jiheng, L.; Ximing, X.; Chao, Y.; Xuexu, G.; Xiaoqian, B. Effect of yttrium on the mechanical and magnetostrictive properties of $Fe_{83}Ga_{17}$ alloy. *Journal of Rare Earths* **2015**, *33*, 1087–1092.

(133) Ma, T.; Hu, S.; Bai, G.; Yan, M.; Lu, Y.; Li, H.; Peng, X.; Ren, X. Structural origin for the local strong anisotropy in melt-spun Fe-Ga-Tb: Tetragonal nanoparticles. *Applied Physics Letters* **2015**, *106*, 112401.

(134) Chen, Y.; Fu, Z.; Wu, Y.; Xu, Y.; Xiao, Y.; Wang, J.; Zhang, R.; Jiang, C. Giant heterogeneous magnetostriction induced by charge accumulation-mediated nanoinclusion formation in dual-phase nanostructured systems. *Acta Materialia* **2021**, *213*, 116975.

(135) Lin, Y.-C.; Lin, C.-F. Effects of phase transformation on the microstructures and magnetostriction of Fe-Ga and Fe-Ga-Zn ferromagnetic shape memory alloys. *Journal of Applied Physics* **2015**, *117*, 17A920.

(136) Liu, H.; Wang, Y.; Dong, L.; Wang, H.; Zhang, Y.; Zhang, Z.; Tan, W. Structure and magnetic properties of Fe–Ga ribbons doped by Sn. *Journal of Materials Science: Materials in Electronics* **2021**, *32*, 745–751.

(137) Zhao, X.; Tian, X.; Yao, Z. Q.; Zhao, L. J.; Wang, R.; Yan, J. The tetragonal-like distortion of Fe–Ga alloys interstitial doped with Cu. *Rare Metals* **2021**, *40*, 1851–1857.

(138) Gou, J.; Ma, T.; Qiao, R.; Yang, T.; Liu, F.; Ren, X. Dynamic precipitation and the resultant magnetostriction enhancement in [001]-oriented Fe-Ga alloys. *Acta Materialia* **2021**, *206*, 116631.

(139) Sikka, S.; Vohra, Y.; Chidambaram, R. Omega phase in materials. *Progress in Materials Science* **1982**, *27*, 245–310.

(140) Li, T.; Kent, D.; Sha, G.; Stephenson, L. T.; Ceguerra, A. V.; Ringer, S. P.; Dargusch, M. S.; Cairney, J. M. New insights into the phase transformations to isothermal ω and ω-assisted α in near β-Ti alloys. *Acta Materialia* **2016**, *106*, 353–366.

(141) Yang, Y.; Castany, P.; Bertrand, E.; Cornen, M.; Lin, J.; Gloriant, T. Stress release-induced interfacial twin boundary ω phase formation in a β type Ti-based single crystal displaying stress-induced α" martensitic transformation. *Acta Materialia* **2018**, *149*, 97–107.

(142) Lai, M.; Tasan, C.; Zhang, J.; Grabowski, B.; Huang, L.; Raabe, D. Origin of shear induced β to ω transition in Ti–Nb-based alloys. *Acta Materialia* **2015**, *92*, 55–63.

(143) Bendersky, L.; Boettinger, W.; Burton, B.; Biancaniello, F.; Shoemaker, C. The formation of ordered ω-related phases in alloys of composition Ti_4Al_3Nb. *Acta Metallurgica et Materialia* **1990**, *38*, 931–943.

(144) Nag, S.; Devaraj, A.; Srinivasan, R.; Williams, R. E. A.; Gupta, N.; Viswanathan, G. B.; Tiley, J. S.; Banerjee, S.; Srinivasan, S. G.; Fraser, H. L.; Banerjee, R. Novel Mixed-Mode Phase Transition Involving a Composition-Dependent Displacive Component. *Physical Review Letter* **2011**, *106*, 245701.

(145) Narsu, B.; Wang, G.-S.; Johansson, B.; Vitos, L. Large magneto-chemical-elastic coupling in highly magnetostrictive Fe-Ga alloys. *Applied Physics Letters* **2013**, *103*, 231903.

(146) Curie, P. Sur la symétrie dans les phénomènes physiques, symétrie d'un champ électrique et d'un champ magnétique. *Journal de Physique Théorique et Appliquée* **1894**, *3*, 393.

(147) Heron, J. T.; Bosse, J. L.; He, Q.; Gao, Y.; Trassin, M.; Ye, L.; Clarkson, J. D.; Wang, C.; Liu, J.; Salahuddin, S.; Ralph, D. C.; Schlom, D. G.; Iñiguez, J.; Huey, B. D.; Ramesh, R. Deterministic switching of ferromagnetism at room temperature using an electric field. *Nature* **2014**, *516*, 370–373.

(148) Hu, J.-M.; Duan, C.-G.; Nan, C.-W.; Chen, L.-Q. Understanding and designing magnetoelectric heterostructures guided by computation: progresses, remaining questions, and perspectives. *npj Computational Materials* **2017**, *3*, 18.

(149) Song, C.; Cui, B.; Li, F.; Zhou, X.; Pan, F. Recent progress in voltage control of magnetism: Materials, mechanisms, and performance. *Progress in Materials Science* **2017**, *87*, 33–82.

(150) Meisenheimer, P. B.; Novakov, S.; Vu, N. M.; Heron, J. T. Perspective: Magnetoelectric switching in thin film multiferroic heterostructures. *Journal of Applied Physics* **2018**, *123*, 240901.

(151) Hu, J.-M.; Nan, C.-W. Opportunities and challenges for magnetoelectric devices. *APL Materials* **2019**, *7*, 080905.

(152) Duan, C.-G.; Velev, J. P.; Sabirianov, R. F.; Zhu, Z.; Chu, J.; Jaswal, S. S.; Tsymbal, E. Y. Surface Magnetoelectric Effect in Ferromagnetic Metal Films. *Physical Review Letters* **2008**, *101*, 137201.

(153) Bauer, U.; Yao, L.; Tan, A. J.; Agrawal, P.; Emori, S.; Tuller, H. L.; van Dijken, S.; Beach, G. S. D. Magneto-ionic control of interfacial magnetism. *Nature Materials* **2015**, *14*, 174–181.

(154) Zhang, S. et al. Electric-Field Control of Nonvolatile Magnetization in $Co_{40}Fe_{40}B_{20}/Pb(Mg_{1/3}Nb_{2/3})_{0.7}Ti_{0.3}O_3$ Structure at Room Temperature. *Physical Review Letters* **2012**, *108*, 137203.

(155) Kim, J.-Y.; Yao, L.; van Dijken, S. Coherent piezoelectric strain transfer to thick epitaxial ferromagnetic films with large lattice mismatch. *Journal of Physics: Condensed Matter* **2013**, *25*, 082205.

(156) Bhattacharya, D.; Bandyopadhyay, S.; Atulasimha, J. Review: Voltage induced strain control of magnetization: computing and other applications. *Multifunctional Materials* **2019**, *2*, 032001.

(157) Roy, K.; Bandyopadhyay, S.; Atulasimha, J. Energy dissipation and switching delay in stress-induced switching of multiferroic nanomagnets in the presence of thermal fluctuations. *Journal of Applied Physics* **2012**, *112*, 023914.

(158) Brintlinger, T.; Lim, S.-H.; Baloch, K. H.; Alexander, P.; Qi, Y.; Barry, J.; Melngailis, J.; Salamanca-Riba, L.; Takeuchi, I.; Cumings, J. In Situ Observation of Reversible Nanomagnetic Switching Induced by Electric Fields. *Nano Letters* **2010**, *10*, 1219–1223.

(159) Gopman, D. B.; Dennis, C. L.; Chen, P. J.; Iunin, Y. L.; Finkel, P.; Staruch, M.; Shull, R. D. Strain-assisted magnetization reversal in

Co/Ni multilayers with perpendicular magnetic anisotropy. *Scientific Reports* **2016**, *6*, 27774.

(160) Gopman, D. B.; Dennis, C. L.; Chen, P. J.; Iunin, Y. L.; Finkel, P.; Staruch, M.; Shull, R. D. Manipulating magnetism in $La_{0.7}Sr_{0.3}MnO_3$ via piezostrain. *Physical Review B* **2015**, *91*, 024406.

(161) Dusch, Y.; Tiercelin, N.; Klimov, A.; Giordano, S.; Preobrazhensky, V.; Pernod, P. Stress-mediated magnetoelectric memory effect with uni-axial TbCo2/FeCo multilayer on 011-cut PMN-PT ferroelectric relaxor. *Journal of Applied Physics* **2013**, *113*, 17C719.

(162) Shen, J.; Cong, J.; Chai, Y.; Shang, D.; Shen, S.; Zhai, K.; Tian, Y.; Sun, Y. Nonvolatile Memory Based on Nonlinear Magnetoelectric Effects. *Physical Review Applied* **2016**, *6*, 021001.

(163) Rementer, C. R.; Fitzell, K.; Xu, Q.; Nordeen, P.; Carman, G. P.; Wang, Y. E.; Chang, J. P. Tuning static and dynamic properties of FeGa/NiFe heterostructures. *Applied Physics Letters* **2017**, *110*, 242403.

(164) Dai, G.; Zhan, Q.; Liu, Y.; Yang, H.; Zhang, X.; Chen, B.; Li, R.-W. Mechanically tunable magnetic properties of Fe81Ga19 films grown on flexible substrates. *Applied Physics Letters* **2012**, *100*, 122407.

(165) Thiele, C.; Dörr, K.; Bilani, O.; Rödel, J.; Schultz, L. Influence of strain on the magnetization and magnetoelectric effect in $La_{0.7}A_{0.3}MnO_3$/PMN−PT(001) ($A = \mathrm{Sr}, \mathrm{Ca}$). *Physical Review B* **2007**, *75*, 054408.

(166) Lou, J.; Reed, D.; Pettiford, C.; Liu, M.; Han, P.; Dong, S.; Sun, N. X. Giant microwave tunability in FeGaB/lead magnesium niobate-lead titanate multiferroic composites. *Applied Physics Letters* **2008**, *92*, 16–19.

(167) Wu, T.; Bur, A.; Wong, K.; Zhao, P.; Lynch, C. S.; Amiri, P. K.; Wang, K. L.; Carman, G. P. Electrical control of reversible and permanent magnetization reorientation for magnetoelectric memory devices. *Applied Physics Letters* **2011**, *98*, 262504.

(168) Brandlmaier, A.; Geprägs, S.; Woltersdorf, G.; Gross, R.; Goennenwein, S. T. B. Nonvolatile, reversible electric-field controlled switching of remanent magnetization in multifunctional ferromagnetic/ferroelectric hybrids. *Journal of Applied Physics* **2011**, *110*, 043913.

(169) Nan, T. et al. Quantification of strain and charge co-mediated magnetoelectric coupling on ultra-thin Permalloy/PMN-PT interface. *Scientific Reports* **2014**, *4*, 3688.

(170) Zhang, S.; Chen, Q.; Liu, Y.; Chen, A.; Yang, L.; Li, P.; Ming, Z. S.; Yu, Y.; Sun, W.; Zhang, X.; Zhao, Y.; Sun, Y.; Zhao, Y. Strain-Mediated Coexistence of Volatile and Nonvolatile Converse Magnetoelectric Ef-

fects in Fe/Pb($Mg_{1/3}Nb_{2/3}$)$_{0.7}$$Ti_{0.3}O_3$ Heterostructure. *ACS Applied Materials & Interfaces* **2017**, *9*, 20637–20647.

(171) Jahjah, W.; Jay, J.-P.; Le Grand, Y.; Fessant, A.; Prinsloo, A.; Sheppard, C.; Dekadjevi, D.; Spenato, D. Electrical Manipulation of Magnetic Anisotropy in a $Fe_{81}Ga_{19}$/Pb($Mg_{1/3}Nb_{2/3}$)O_3-Pb(Zr_xTi_{1-x})O_3 Magnetoelectric Multiferroic Composite. *Physical Review Applied* **2020**, *13*, 034015.

(172) Buzzi, M.; Chopdekar, R. V.; Hockel, J. L.; Bur, A.; Wu, T.; Pilet, N.; Warnicke, P.; Carman, G. P.; Heyderman, L. J.; Nolting, F. Single Domain Spin Manipulation by Electric Fields in Strain Coupled Artificial Multiferroic Nanostructures. *Physical Review Letters* **2013**, *111*, 027204.

(173) Overby, M.; Chernyshov, A.; Rokhinson, L. P.; Liu, X.; Furdyna, J. K. GaMnAs-based hybrid multiferroic memory device. *Applied Physics Letters* **2008**, *92*, 192501.

(174) Bai, F.; Wang, N.; Li, J.; Viehland, D.; Gehring, P. M.; Xu, G.; Shirane, G. X-ray and neutron diffraction investigations of the structural phase transformation sequence under electric field in 0.7Pb(Mg1/3Nb2/3)-0.3PbTiO3 crystal. *Journal of Applied Physics* **2004**, *96*, 1620–1627.

(175) Liu, M.; Nan, T.; Hu, J. M.; Zhao, S. S.; Zhou, Z.; Wang, C. Y.; Jiang, Z. D.; Ren, W.; Ye, Z. G.; Chen, L. Q.; Sun, N. X. Electrically controlled non-volatile switching of magnetism in multiferroic heterostructures via engineered ferroelastic domain states. *NPG Asia Materials* **2016**, *8*, e316.

(176) Wu, T.; Zhao, P.; Bao, M.; Bur, A.; Hockel, J. L.; Wong, K.; Mohanchandra, K. P.; Lynch, C. S.; Carman, G. P. Domain engineered switchable strain states in ferroelectric (011) [$Pb(Mg_{1/3}Nb_{2/3})O_3$]$_{(1-x)}$-[$PbTiO_3$]$_x$ (PMN-PT, x$\sim$0.32) single crystals. *Journal of Applied Physics* **2011**, *109*, 1–8.

(177) Singh, J.; Gupta, L. Annealing Effects on MgO Films Grown using e-beam Evaporation. *International Journal of Mathematical, Engineering and Management Sciences* **2019**, *4*, 619–626.

(178) Ziss, D.; Martín-Sánchez, J.; Lettner, T.; Halilovic, A.; Trevisi, G.; Trotta, R.; Rastelli, A.; Stangl, J. Comparison of different bonding techniques for efficient strain transfer using piezoelectric actuators. *Journal of Applied Physics* **2017**, *121*, 135303.

(179) Yaegashi, S.; Kurihara, T.; Segawa, H. Epitaxial growth and magnetic properties of Fe(211). *Journal of Applied Physics* **1993**, *74*, 4506–4512.

(180) Serizawa, K.; Ohtake, M.; Kawai, T.; Futamoto, M.; Kirino, F.; Inaba, N. Influence of crystal orientation on the magnetostriction behavior of Fe films formed on MgO single-crystal substrates. *Journal of Magnetism and Magnetic Materials* **2019**, *477*, 420–426.

(181) Liao, Y., *Practical electron microscopy and database*; www.globalsino.com/EM/: www.globalsino.com/EM/, 2006.

(182) Biasi, R.; Cardoso, L. A simple model for the magnetocrystalline anisotropy in mixed ferrite nanoparticles. *Physica B: Condensed Matter* **2012**, *407*, 3893–3896.

(183) Pinto, M. A. Morphology of micromagnetics. *Physical Review B* **1988**, *38*, 6824–6831.

(184) Téllez-Blanco, J.; Kou, X.; Estevez-Rams, E.; Fidler, J.; Ma, B. Coercivity and magnetic anisotropy of sintered Sm_2Co_17-type permanent magnets. *Journal of Applied Physics* **1997**, *82*, 3928–3933.

(185) Li, D.; Garmestani, H.; Yan, S.; Elkawni, M.; Bacaltchuk, C.; Schneider-Muntau, H.; Liu, J.; Saha, S.; Barnard, J. Effects of high magnetic field annealing on texture and magnetic properties of FePd. *Journal of Magnetism and Magnetic Materials* **2004**, *281*, 272–275.

(186) Li, P. et al. Spatially Resolved Ferroelectric Domain-Switching-Controlled Magnetism in $Co_{40}Fe_{40}B_{20}/Pb(Mg_{1/3}Nb_{2/3})_{0.7}Ti_{0.3}O_3$ Multiferroic Heterostructure. *ACS Applied Materials & Interfaces* **2017**, *9*, 2642–2649.

(187) Ba, Y. et al. Spatially Resolved Electric-Field Manipulation of Magnetism for CoFeB Mesoscopic Discs on Ferroelectrics. *Advanced Functional Materials* **2018**, *28*, 1706448.

(188) Clark, A. E.; Wun-Fogle, M.; Restorff, J.; Lograsso, T.; Cullen, J. Effect of quenching on the magnetostriction on $Fe_{1-x}Ga_x$ (0.13<x<0.21). *IEEE Transactions on Magnetics* **2001**, *37*, 2678–2680.

(189) Wang, J.; Pesquera, D.; Mansell, R.; van Dijken, S.; Cowburn, R. P.; Ghidini, M.; Mathur, N. D. Giant non-volatile magnetoelectric effects via growth anisotropy in $Co_{40}Fe_{40}B_{20}$ films on PMN-PT substrates. *Applied Physics Letters* **2019**, *114*, 092401.

(190) Eerenstein, W.; Wiora, M.; Prieto, J. L.; Scott, J. F.; Mathur, N. D. Giant sharp and persistent converse magnetoelectric effects in multiferroic epitaxial heterostructures. *Nature Materials* **2007**, *6*, 348–351.

(191) Hu, J.-M.; Duan, C.-G.; Nan, C.-W.; Chen, L.-Q. Giant sharp and persistent converse magnetoelectric effects in multiferroic epitaxial heterostructures. *npj Computational Materials* **2017**, *3*, 18.

(192) Chung, T.-K.; Carman, G. P.; Mohanchandra, K. P. Reversible magnetic domain-wall motion under an electric field in a magnetoelectric thin film. *Applied Physics Letters* **2008**, *92*, 112509.

(193) Lahtinen, T. H. E.; Franke, K. J. A.; van Dijken, S. Electric-field control of magnetic domain wall motion and local magnetization reversal. *Scientific Reports* **2012**, *2*, 258.

(194) Parkes, D. E.; Cavill S. A.. andCavill, S. A. T.; Wadley, P.; McGee, F.; Staddon, C. R.; Edmonds, K. W.; Campion, R. P.; Gallagher, B. L.;

Rushforth, A. W. Non-volatile voltage control of magnetization and magnetic domain walls in magnetostrictive epitaxial thin films. *Applied Physics Letters* **2012**, *101*, DOI: 10.1063/1.4745789.

(195) Lei, N.; Devolder, T.; Agnus, G.; Aubert, P.; Daniel, L.; Kim, J.-V.; Zhao, W.; Trypiniotis, T.; Cowburn, R. P.; Chappert, C.; Ravelosona, D.; Lecoeur, P. Strain-controlled magnetic domain wall propagation in hybrid piezoelectric/ferromagnetic structures. *Nature Communications* **2013**, *4*, 1378.

(196) Parkin, S. S. P.; Hayashi, M.; Thomas, L. Magnetic Domain-Wall Racetrack Memory. *Science* **2008**, *320*, 190–194.

(197) Yang, L.; Zhao, Y.; Zhang, S.; Li, P.; Gao, Y.; Yang, Y.; Huang, H.; Miao, P.; Liu, Y.; Chen, A.; Nan, C. W.; Gao, C. Bipolar loop-like non-volatile strain in the (001)-oriented $Pb(Mg_{1/3}Nb_{2/3})O_3$-$PbTiO_3$ single crystals. *Scientific Reports* **2014**, *4*, 4591.

(198) Qiao, K. et al. Regulation of phase transition and magnetocaloric effect by ferroelectric domains in FeRh/PMN-PT heterojunctions. *Acta Materialia* **2020**, *191*, 51–59.

(199) Lo Conte, R.; Xiao, Z.; Chen, C.; Stan, C. V.; Gorchon, J.; El-Ghazaly, A.; Nowakowski, M. E.; Sohn, H.; Pattabi, A.; Scholl, A.; Tamura, N.; Sepulveda, A.; Carman, G. P.; Candler, R. N.; Bokor, J. Influence of Nonuniform Micron-Scale Strain Distributions on the Electrical Reorientation of Magnetic Microstructures in a Composite Multiferroic Heterostructure. *Nano Letters* **2018**, *18*, 1952–1961.

(200) Yang, Y. T.; Li, J.; Peng, X. L.; Wang, X. Q.; Wang, D. H.; Cao, Q. Q.; Du, Y. W. Electric field mediated non-volatile tuning magnetism in CoPt/PMN-PT heterostructure for magnetoelectric memory devices. *Journal of Applied Physics* **2016**, *119*, 1–5.

(201) Zhang, S.; Zhao, Y.; Xiao, X.; Wu, Y.; Rizwan, S.; Yang, L.; Li, P.; Wang, J.; Zhu, M.; Zhang, H.; Jin, X.; Han, X. Giant electrical modulation of magnetization in $Co_{40}Fe_{40}B_{20}/Pb(Mg_{1/3}Nb_{2/3})_{0.7}Ti_{0.3}O_3(011)$ heterostructure. *Scientific Reports* **2014**, *4*, 2045–2322.

(202) Zhang, C.; Wang, F.; Dong, C.; Gao, C.; Jia, C.; Jiang, C.; Xue, D. Electric field mediated non-volatile tuning magnetism at the single-crystalline $Fe/Pb(Mg_{1/3}Nb_{2/3})_{0.7}Ti_{0.3}O_3$ interface. *Nanoscale* **2015**, *7*, 4187–4192.

(203) Leiva, L.; Ampuero Torres, J.; Gómez, J.; Velázquez Rodriguez, D.; Milano, J.; Butera, A. Electric field control of magnetism in FePt/PMN-PT heterostructures. *Journal of Magnetism and Magnetic Materials* **2022**, *544*, 168619.

(204) Jiménez, M. J.; Cabeza, G.; Gómez, J. E.; Velázquez Rodriguez, D.; Leiva, L.; Milano, J.; Butera, A. Thickness dependence of the magnetoelectric coupling in Fe89Ga11 thin films deposited on ferroelectric

PMN-PT single crystals. *Journal of Magnetism and Magnetic Materials* **2020**, *501*, 166361.

(205) Ghidini, M.; Mansell, R.; Maccherozzi, F.; Moya, X.; Phillips, L.; Yan, W.; Pesquera, D.; Barnes, C.; Cowburn, R.; Hu, J.; Dhesi, S.; Mathur, N. Shear-strain-mediated magnetoelectric effects revealed by imaging. *Nature Materials* **2019**, *18*, 840–845.

(206) Chen, A.; Piao, H.-G.; Ji, M.; Fang, B.; Wen, Y.; Ma, Y.; Li, P.; Zhang, X.-X. Using Dipole Interaction to Achieve Nonvolatile Voltage Control of Magnetism in Multiferroic Heterostructures. *Advanced Materials* **2021**, 2105902.

(207) Sakai, A.; Minami, S.; Koretsune, T.; Chen, T.; Higo, T.; Wang, Y.; Nomoto, T.; Hirayama, M.; Miwa, S.; Nishio-Hamane, D.; Ishii, F.; Arita, R.; Nakatsuji, S. Iron-based binary ferromagnets for transverse thermoelectric conversion. *Nature* **2020**, *581*, 53–57.